



Polytechnic University of Marche
Ph.D. School in Engineering Science
Curriculum in Civil-Environmental, Building Engineering and Architecture

Applications of OMA techniques in civil engineering: automatization of methods for long-term monitoring of structures

Ph.D. Dissertation of:
Gianluca Standoli

Advisor:

Prof. Francesco Clementi

Co-Advisor:

Prof. Stefano Lenci

Curriculum supervisor:

Prof. Francesco Fatone



Università Politecnica delle Marche
Scuola di Dottorato di Ricerca in Scienze dell'Ingegneria
Curriculum in Ingegneria Civile-Ambientale, Edile e Architettura

Tecniche OMA applicate all'ingegneria civile: automatizzazione dei metodi per il monitoraggio continuo delle strutture

Tesi di Dottorato di:
Gianluca Standoli

Tutor:

Prof. Francesco Clementi

Co-Tutor:

Prof. Stefano Lenci

Coordinatore del Corso:

Prof. Francesco Fatone

XXXIV ciclo - 2018/2021

Università Politecnica delle Marche
Dipartimento di Ingegneria Civile-Ambientale, Edile e Architettura
Via Brecce Bianche — 60131 - Ancona, Italy

Acknowledgements

The PhD school are coming to their end and the time has come to draw conclusion on another important part of my life. It has been three years that I'll always remember and I'll keep dear because of all the beautiful experiences I lived and all the people I met.

I wish to thank my academic tutor Prof. Francesco Clementi for the incredible opportunity he gave me and for his guidance both in the professional than everyday life. It has been an unrepeatable experience that allowed me to know new people, places and new ways of thinking.

A special thank to Novatest S.r.l. for co-financing my PhD and for the support provided in these three years, and to my co-tutor Prof. Stefano Lenci for the beautiful experience.

Thanks to my parents and to my sister. I can seem repetitive, but I could not reach all these milestones without your support and your love. Thanks to all of my family, my aunts, uncles, grandparents and all the cousins for always believing in my capacities and for all the time you dedicated to me during my life.

A special thanks to the friends, those I know from my childhood, like Mario, Stefano, Luca, Daniele, Pierluigi who have always been by my side and who are practically part of my family, and to all the new people that entered my life in the last years and that accompanied me and will accompany me in the future: thank you Chiara, Alfredo, Viola, Lorenzo, Pier Francesco, for been present every day.

Another special thanks goes to Giulia, Francesco and Clara, for all the kindness and the beautiful moments you donate me. I cannot express with word how important you are to me.

Thank you to all the people I met as colleagues during my PhD, which became wonderful friends. Giorgio, Ersilia, Angela, Mattia, Francesca, Marina, Valentina, Davide thanks for all the moments we spent together.

And at last thanks for the friends of Wakeland for all the time we spent together in these three years: you also become incredible friends.

Abstract

Evolution of technologies both in the fields of in situ investigations and Finite Element modeling strongly enhanced the possibility to understand the dynamic behavior of structures, allowing a periodic or continuous analysis of their response to environmental, anthropic, and exceptional actions and the formulation of accurate hypotheses about their future behavior, which is fundamental for ensuring their safety.

In particular, this thesis is focused on the application of a non-destructive methodology for structural health assessment which has become quite popular nowadays, which is based on the acquisition of vibrational data and the extraction of the modal parameters applying Operational Modal Analysis techniques. These methods result very effective and also very suited in case of historic masonry structures, due to the non-invasiveness and cheapness of the instrumentation necessary for the monitoring activity.

Different examples of operational modal analysis applied for the evaluation of the health state of concrete and masonry structures are proposed into this work in order to highlight the potentiality of method. Moreover, they constitute the basis for the main theme of the thesis, which is the acquisition and interpretation of the results of over one year of continuous monitoring of the two symmetrical bell towers of the Cathedral of Santa Maria Annunziata of Camerino (Central Italy).

The monitoring activity target is the evaluation of the dynamic behavior of the two towers after the damages occurred during the seismic events of 2016 and the consequent reinforcement interventions. The experimental data are acquired in continuous using four triaxial MEMS accelerometers installed, two for each structure, on two opposite corners of the bell cells. Data processing is managed with an automatic system, purposely implemented in Matlab© environment, which elaborates the time histories and executes OMA analysis to track the modal characteristics of the structures and their evolution in time. Correlation with environmental factors allows to discern the effect of climatic conditions on the variations of modal frequencies and damping.

Abstract

L'evoluzione tecnologica, sia nel campo delle indagini in situ che della modellazione agli elementi finiti, ha fortemente aiutato nella comprensione del comportamento dinamico delle strutture, consentendo un'analisi periodica o continua della loro risposta ad azioni ambientali, antropiche ed eccezionali e la formulazione di previsioni accurate sul loro comportamento futuro, aspetti fondamentali per garantirne la sicurezza.

Questa tesi, in particolare, si concentra sull'applicazione di una metodologia non distruttiva per la valutazione della salute strutturale che è diventata molto popolare oggi, basata sull'acquisizione di dati vibrazionali e sull'estrazione dei parametri modali tramite l'applicazione delle tecniche identificative dell'Analisi Modale Operativa. Questi metodi risultano molto efficaci e molto adatti anche nel caso di strutture murarie storiche, per la non invasività e l'economicità della strumentazione necessaria per l'attività di monitoraggio.

In questo lavoro vengono proposti diversi esempi di analisi modale operativa applicata per la valutazione dello stato di salute delle strutture in calcestruzzo e muratura al fine di evidenziare le potenzialità del metodo. Inoltre, costituiscono la base per lo sviluppo di quello che è il tema principale della tesi, ovvero la raccolta e l'interpretazione dei dati derivanti da oltre un anno di monitoraggio continuo dei due campanili simmetrici della Cattedrale di Santa Maria Annunziata di Camerino (Italia centrale).

L'obiettivo dell'attività di monitoraggio è la valutazione del comportamento dinamico delle due torri a seguito dei danni avvenuti durante gli eventi sismici del 2016 e dei conseguenti interventi di rinforzo. I dati sperimentali vengono acquisiti in continuo utilizzando quattro accelerometri MEMS triassiali installati, due per ogni struttura, su due angoli opposti delle celle a campana. L'elaborazione dei dati è gestita con un sistema automatico, appositamente implementato in ambiente Matlab®, che elabora le cronologie ed esegue analisi OMA per tracciare le caratteristiche modali delle strutture e la loro evoluzione nel tempo. La correlazione con i fattori ambientali permette di discernere l'effetto delle condizioni climatiche sulle variazioni delle frequenze modali e dello smorzamento.

Contents

Acknowledgements.....	i
Abstract.....	i
Abstract.....	ii
Contents	i
List of Figures.....	i
List of Tables	i
1 Introduction	3
1.1 Research context.....	3
1.2 Objectives and main contributions	4
1.3 Organization of the thesis	5
2 Structural Health Monitoring (S.H.M.): Background and Tools	7
2.1 Introduction to SHM.....	7
2.2 SHM Classifications	8
2.3 SHM applications	9
2.4 The measurement processes	10
2.4.1 Instrumentation	11
2.4.2 Data Acquisition Hardware.....	12
2.4.3 Transducers	13
2.4.3.1 Piezoelectric accelerometers.....	13
2.4.3.2 MEMS accelerometers	15
2.4.4 Signal Processing	15
3 Operational Modal Analysis: Methodologies.....	18
3.1 Modelling of the dynamic behavior of linear systems	18

3.1.1	Spatial and modal models	18
3.1.1.1	Spatial formulation	18
3.1.1.2	Modal formulation.....	19
3.1.2	Frequency response models	22
3.1.2.1	Frequency response models	22
3.1.2.2	Frequency response models in the Modal Space	24
3.1.3	State-Space models	25
3.1.3.1	Continuous-time state-space model.....	27
3.1.3.1.1	<i>State equation</i>	28
3.1.3.1.2	<i>Observation equation</i>	29
3.1.3.1.3	<i>State-Space Model</i>	29
3.1.3.2	Discrete-time state-space model	30
3.1.3.3	Stochastic processes	31
3.1.3.4	Stochastic discrete-time state-space model.....	32
3.1.4	Auto-spectra and cross-spectra functions.....	33
3.2	Output-only modal identification techniques.....	35
3.2.1	Identification methods developed in the frequency domain	36
3.2.1.1	Peak Picking method	36
3.2.1.1.1	<i>Identification of the natural frequencies</i>	36
3.2.1.1.2	<i>Identification of vibration modes</i>	37
3.2.1.2	Frequency Domain Decomposition method	38
3.2.1.2.1	<i>Singular Value Decomposition</i>	39
3.2.1.3	Enhanced Frequency Domain Decomposition method.....	40
3.2.2	Identification techniques implemented in the time domain	42
3.2.2.1	Covariance-driven Stochastic Subspace Identification method	42
3.2.2.2	Data-driven Stochastic Subspace Identification method	45
3.2.2.2.1	<i>Kalman filter</i>	46

3.2.2.2.2	<i>Factorization and Projection matrix</i>	47
4	Short-term monitoring and OMA identification for assess the health status of operative structures	51
4.1	Identification procedure	51
4.1.1	Data acquisition and pre-processing	51
4.1.2	Modal parameters extraction	52
4.1.3	Mode shapes representation and validation	53
4.2	Modal Identification of the Arch Bridge on Garigliano River after damage of its strays	53
4.2.1	Description of the case study	53
4.2.2	Sensors layout and photographic documentation	54
4.2.3	Identification process	56
4.2.3.1	Preliminary evaluation of the frequency contents of signals	56
4.2.3.2	Identification of Frequencies and Damping ratios	58
4.2.3.3	Mode shapes representation and validation	60
4.2.4	Dynamic identification of the stays	62
4.3	Modal Identification of Hangar Morandi Cover	64
4.3.1	Description of the case study	64
4.3.2	Sensors layout and photographic documentation	65
4.3.2.1	Monitoring campaign on 26.06.2020	65
4.3.2.2	Monitoring campaign on 23.07.2020	67
4.3.3	Identification process	72
4.3.3.1	Preliminary evaluation of the frequency contents of signals acquired on 26.06.2020	72
4.3.3.2	Preliminary evaluation of the frequency contents of signals acquired on 23.07.2020	73

4.3.4 Identification of Frequencies and Damping ratios through Analysis of Data Acquired on 26.06.2020	76
4.3.4.1 Mode shapes representation and validation	77
4.3.5 Dynamic identification of the stays monitored on 26.06.2020	78
4.3.6 Identification of Frequencies and Damping ratios through Analysis of Data Acquired on 23.07.2020	79
4.3.6.1 Mode shapes representation and validation	81
4.3.7 Dynamic identification of the stays monitored on 23.07.2020	83
5 OMA Identification for Model Updating of Finite Elements models of historical buildings	84
5.1 Manual calibration approach: the case study of four bell towers in Ferrara (FE) province, struck by Emilia Earthquake in 2016	85
5.1.1 Geometrical and historical description of the case studies	86
5.1.1.1 San Giorgio Cathedral Belfry	86
5.1.1.2 San Benedetto Belfry	87
5.1.1.3 Matildea Tower	88
5.1.1.4 Pomposa Abbey Belfry	90
5.1.2 Ambient vibration testing	91
5.1.2.1 Acceleration sensors layout and data acquisition settings	92
5.1.2.2 AVT Data processing	93
5.1.2.3 Enhanced Frequency Domain Decomposition	94
5.1.2.4 Stochastic Subspace Identification	96
5.1.2.5 Comparison and validation of the experimental results	97
5.1.3 Model updating process	103
5.1.3.1 Preliminary FE modeling	103
5.1.3.2 Calibration process	108
5.1.3.2.1 <i>San Giorgio Cathedral Belfry</i>	108

5.1.3.2.2	<i>San Benedetto Belfry</i>	109
5.1.3.2.3	<i>Matildea Tower</i>	111
5.1.3.2.4	<i>Pomposa Abbey Belfry</i>	113
5.1.3.3	Validation of mode shape through CrossMAC matrix	114
5.2	Automatic calibration approach via Genetic Algorithms: the case study of Ostra Civic Tower	116
5.2.1	Ostra Civic Tower: description of the case study	116
5.2.1.1	Historical survey	116
5.2.1.2	Geometrical and material survey	118
5.2.2	Ambient vibration testing	121
5.2.2.1	Field testing procedure	122
5.2.2.2	Operational modal analysis	125
5.2.2.2.1	<i>Data processing</i>	125
5.2.2.2.2	<i>Theoretical background on SSI-based methods</i>	125
5.2.2.2.3	<i>Modal results</i>	127
5.2.3	Numerical modelling and updating via Genetic Algorithm	131
5.2.3.1	Preliminary FE model	132
5.2.3.2	GA-based model updating	135
5.2.3.3	Calibration process	137
5.2.3.3.1	<i>Twelve-group discretization approach</i>	137
5.2.3.3.2	<i>Model updating results</i>	140
5.2.4	Discussion	146
6	Automatic OMA identification process for long-time monitoring	148
6.1	The case study: Camerino Dome twin bell towers	148
6.1.1	Localization and History	149
6.1.2	Geometrical and Material Survey	150
6.2	Preliminary Finite Elements Model	151

6.3	Ambient Vibration Testing - Instrumentation and sensors layouts.....	152
6.4	The automatic identification procedure	153
6.4.1	Flow-chart of the method	153
6.4.2	Preliminary modal identification.....	156
6.4.3	Pre-Processing of long-term monitoring data	158
6.4.4	Automatic modal parameters identification process	159
6.4.4.1	Stable poles identification.....	159
6.4.4.1.1	<i>SSI-cov method and stabilization diagram.....</i>	<i>159</i>
6.4.4.1.2	<i>Elimination of spurious poles.....</i>	<i>161</i>
6.4.4.1.3	<i>Validation criteria.....</i>	<i>162</i>
6.4.4.2	“k-means” clustering analysis.....	163
6.4.4.3	Preliminary modal tracking results	164
6.5	Environmental effects on modal parameters	166
6.5.1	Multiple Regression Analysis	167
6.6	Monitoring activity results.....	173
Conclusions		174
References		176

List of Figures

Fig. 1-1 - Classic workflow for OMA process	4
Fig. 1-2 - Main processing steps of a classical vibration-based health monitoring system	5
Fig. 2-1 - Data acquisition system setup	11
Fig. 2-2 - Dynamic data acquisition system	12
Fig. 2-3 - Piezoelectric sensor from PCB 393B12 series	13
Fig. 2-4 - MEMS accelerometers: MonoDAQ-E-gMeter (a) and internal configuration (b)	15
Fig. 2-5 - Aliasing. True signal (3.5kHz), Aliased signal (0.5kHz)	16
Fig. 3-1 - Genesis of the stochastic state-space-model used for general applications	26
Fig. 3-2 - Typical modal domains associated to structural modes [43]	41
Fig. 3-3 - Example of stabilization diagram to differentiate between stable poles (blue points) and unstable poles (purple crosses)	45
Fig. 4-1 - Arch Bridge on Garigliano River	54
Fig. 4-2 - Denomination of stays	54
Fig. 4-3 - First sensors layout	55
Fig. 4-4 - Second sensors layout	55
Fig. 4-5 - Third sensors layout	55
Fig. 4-6 - Orientation of the sensors placed on the stays	56
Fig. 4-7 - FFT of the signals of the first acquisition	56
Fig. 4-8 - FFT of the signals of the second acquisition	57
Fig. 4-9 - FFT of the signal of the third acquisition	57
Fig. 4-10 - Stabilization diagram - sample rate 50 Hz	58
Fig. 4-11 - Complexity plot of the estimated modes	59
Fig. 4-12 - Experimental model indicating the measurement positions	60
Fig. 4-13 - AUTOMAC of the estimated frequencies	60
Fig. 4-14 - Mode shapes	61
Fig. 4-15 - Morandi Hangar Nr.3 in Fiumicino Airport	64
Fig. 4-16 - Naming of the elements and layout of the systems monitored on 26.06.2020 (in red) and on 23.07.2020 (in blue)	65
Fig. 4-17 - First sensors layout for 26.06.2020 monitoring	66
Fig. 4-18 - Second sensors layout for 26.06.2020 monitoring	67
Fig. 4-19 - First Sensors Layout for 23.07.2020 monitoring	68
Fig. 4-20 - Second sensors layout for 23.07.2020 monitoring	69

Fig. 4-21 - Third sensors layout for 23.07.2020 monitoring	70
Fig. 4-22 - Fourth sensors layout for 23.07.2020 monitoring	71
Fig. 4-23 - FFT of the signals of the first acquisition on 26.06.2020	72
Fig. 4-24 - FFT of the signals of the second acquisition on 26.06.2020	73
Fig. 4-25 - FFT of the signals of the first acquisition on 23.07.2020	74
Fig. 4-26 - FFT of the signals of the second acquisition on 23.07.2020	74
Fig. 4-27 - FFT of the signals of the third acquisition on 23.07.2020	75
Fig. 4-28 - FFT of the signals of the fourth acquisition on 23.07.2020	75
Fig. 4-29 - Stabilization diagram - sample rate 6.25 Hz	76
Fig. 4-30 - Complexity plot of the estimated modes	77
Fig. 4-31 - Experimental model indicating the measurement positions of 26.06.2020: sensor diagram n.1 (a) sensor diagram n.2 (b)	77
Fig. 4-32 - Mode shapes	78
Fig. 4-33 - AUTOMAC of the estimated frequencies	78
Fig. 4-34 - Stabilization diagram - sample rate 6.25 Hz	79
Fig. 4-35 - Complexity plots of the estimated modes	80
Fig. 4-36 - Experimental model indicating the measurement positions of 23.07.2020: sensor diagram n.1 (a) sensor diagram n.2 (b) sensor diagram n.3 (c) sensor diagram n.4 (d)	81
Fig. 4-37 - Mode shapes	82
Fig. 4-38 - AUTOMAC of the estimated frequencies	82
Fig. 5-1 - Towers location - Ferrara Province	85
Fig. 5-2 - Geometrical configuration of San Giorgio church belfry in Ferrara	87
Fig. 5-3 - Geometrical configuration of San Benedetto church tower in Ferrara	88
Fig. 5-4 - Geometry configuration of Matildea tower in Bondeno	89
Fig. 5-5 - Geometry configuration of Pomposa abbey tower in Codigoro	91
Fig. 5-6 - Wired accelerometric sensors schemes	93
Fig. 5-7 - Graphs for EFDD method	95
Fig. 5-8 - SVD graphs for SSI method	97
Fig. 5-9 - San Giorgio Belfry - Comparison between EFDD and SSI mode shapes	100
Fig. 5-10 - San Benedetto Belfry - Comparison between EFDD and SSI mode shapes	101
Fig. 5-11 - Matildea Tower - Comparison between EFDD and SSI mode shapes	102
Fig. 5-12 - Pomposa Abbey Belfry - Comparison between EFDD and SSI mode shapes	103
Fig. 5-13 - Towers NMs: a) prospective views; b) section views	104
Fig. 5-14 - Mode shapes of towers preliminary model	106

Fig. 5-15 - San Giorgio Belfry - Comparison between experimental and numerical mode shapes after calibration.....	109
Fig. 5-16 - San Benedetto Belfry - Comparison between experimental and numerical mode shapes after calibration	111
Fig. 5-17 - Matildea Tower - Comparison between experimental and numerical mode shapes after calibration.....	112
Fig. 5-18 - Pomposa Abbey Belfry - Comparison between experimental and numerical mode shapes after calibration	114
Fig. 5-19 - Ostra Civic Tower localization.....	117
Fig. 5-20 - San Francesco Church and the Tower before bombardments (a) and a view of the central square to the present days (b).	118
Fig. 5-21 - Geometrical survey of the investigated tower: front views (top) and CAD sections (bottom).....	120
Fig. 5-22 - Excerpts from the photographic survey of the tower:(1) trapdoor accessing the upper level and connecting iron ladder; (2) close-up of the 4th level brickwork; (3) concrete slab of the 3rd floor with ladder opening;(4) particular of the reinforcement intervention with tie rods; (5) close-up of the 2nd level internal brickwork; (6) external brickwork of the 1st level; (7) basement brickwork; (8) spiral staircase at the entrance level.	121
Fig. 5-23 - Instrumentation used for the ambient vibration tests.....	123
Fig. 5-24 - Sensor layouts and corresponding acceleration time series for 2018 and 2019 dynamic testing campaigns (blue, green and red colours indicate signals in x, y and z direction, respectively).	124
Fig. 5-25 - Complexity plots of the identified experimental modes for EM 2018 (a) and EM 2019 (b).	128
Fig. 5-26 - Mode shapes of 2018 and 2019 EMs identified with SSI method (in blue) and cross-comparison with the respective mode shapes identified with EFDD method (in red).	129
Fig. 5-27 - Comparison between mode shapes of EM 2018 (in blue) and the corresponding ones of EM 2019 (in red).	131
Fig. 5-28 - FE modelling of the Civic Tower of Ostra: (a) Assonometric view, (b) Bottom view at foundation level.....	133
Fig. 5-29 - Frequencies values and mode shapes resulting from modal analysis operated on the preliminary FE model.	134
Fig. 5-30 - Workflow for the projection of the experimental data onto the NM for the genetic algorithm updating, with measured nodes highlighted.	136
Fig. 5-31 - GA-based model updating flowchart.....	137

Fig. 5-32 - Updating variables for the twelve-group discretization of the FE model. Each material group is named as “X” followed by a subscript composed by a number (from 00 to 12) which stands for the group and a letter (“M” is masonry, “C” is concrete and “F” is the filling material).	138
Fig. 5-33 - Numerical mode shapes after calibration using isotropic material modelling.	144
Fig. 5-34 - Numerical mode shapes after calibration using orthotropic material modelling.	145
Fig. 6-1 - Localization of the city of Camerino (a) and a view of Santissima Maria Annunziata Cathedral (b)	149
Fig. 6-2 - Crack patterns and material surveys	150
Fig. 6-3 - Mode shapes resulting from modal analysis over non calibrated FE model	151
Fig. 6-4 - Sensors layouts: respectively the continuous monitoring system (in green) and the short-time monitoring system (in blue).	152
Fig. 6-5 - Example of acquisition in trigger modality: Cartoceto (PU) seismic event on 29.10.21 at 12:53:10 - Magnitude 4.1	153
Fig. 6-6 - Geometrical model with highlighted reference nodes.	154
Fig. 6-7 - Flowchart of the proposed methodology	155
Fig. 6-8 - Target frequencies and mode shapes obtained from short-time monitoring data analysis .	157
Fig. 6-9 - Example of detrending of data acquired with one triaxial sensor.....	158
Fig. 6-10 - Low-pass filter with cut-off frequency at 12.5 Hz (a); Kaiser Window (b)	159
Fig. 6-11 - Stabilization diagrams	161
Fig. 6-12 - Damping check for removal of spurious poles (b) from the ones identified (a).	162
Fig. 6-13 - Reduction of poles after application of validation criteria (b) after removal of spurious poles with damping check (a).....	163
Fig. 6-14 - k-mean cluster and centroids	164
Fig. 6-15 - Modal tracking of the frequencies associated to the first four modes: left tower (a), right tower (b).....	165
Fig. 6-16 - Freezing condition in correspondence of the minimum temperature value on 15.02.2021	166
Fig. 6-17 - Correlation of frequencies with environmental data	171
Fig. 6-18 - Correlation of damping with frequencies and environmental data	172
Fig. 6-19 - Modal tracking of frequencies after removal of environmental effects (in black)	173

List of Tables

Table 3-1 - The variant weighting matrices in: PC - main component, CVA - canonical analysis	50
Table 4-1 - Main experimental frequencies of the bridge and related modal dampings	58
Table 4-2 - Frequencies identified for the various stays	62
Table 4-3 - Main experimental frequencies of Antennas 09 and 10 and related modal dampings	76
Table 4-4 - Frequencies identified for the various stays connected to Antennas 09 and 10.....	79
Table 4-5 - Main experimental frequencies of the bridge and related modal dampings	80
Table 4-6 - Frequencies identified for the various stays	83
Table 5-1 - San Giorgio Belfry - Modal Identification results	99
Table 5-2 - San Benedetto Belfry - Modal Identification results	100
Table 5-3 - Matildea Tower - Modal Identification results	101
Table 5-4 - Pomposa Abbey Belfry - Modal Identification results	102
Table 5-5 - Key features of the meshed solids	105
Table 5-6 - Elastic parameters of the preliminary models.....	105
Table 5-7 - Modal properties of towers preliminary NMs	107
Table 5-8 - Comparison between experimental and preliminary numerical models' frequencies	107
Table 5-9 - San Giorgio Belfry - Comparison between experimental and calibrated NMs frequencies	108
Table 5-10 - San Benedetto Belfry - Comparison between experimental and calibrated NMs frequencies	110
Table 5-11 - Matildea Tower - Comparison between experimental and calibrated NMs frequencies	112
Table 5-12 - Pomposa Abbey Belfry - Comparison between experimental and calibrated NMs frequencies	113
Table 5-13 - Cross-MAC between experimental and numerical mode shapes after calibration	115
Table 5-14 - Global modal parameters identified for EM 2018 and EM 2019.....	127
Table 5-15 - MAC between mode shapes identified with SSI and EFDD methods: (a) EM 2018 and (b) EM 2019.....	129
Table 5-16 - Percentage variation between modal frequencies and damping ratios of EM2018 and EM2019.....	130
Table 5-17 - MAC between EMs mode shapes identified with SSI method.....	131
Table 5-18 - Elastic properties of the initial FE model.....	133
Table 5-19 - Preliminary numerical results (NM0) and differences with the experimental frequency values (EM).....	134

Table 5-20 - MAC between numerical and experimental mode shapes: (a) NM0-EM 2018 and (b)NM0-EM 2019. NM0 stands for preliminary numerical model.	135
Table 5-21 - Lower and upper bounds for isotropic elastic properties (E is the Elastic Young's Modulus, ν is the Poisson's ratio and γ is the mass density).	139
Table 5-22 - Lower and upper bounds for orthotropic elastic properties (G is the shear Modulus, while the subscripts L, N and T indicate Longitudinal, Normal and Tangential components respectively). (*) Concrete stayed as isotropic material.	139
Table 5-23 - Optimal values for the material parameters of the isotropic FE models after calibration and successive updating.	140
Table 5-24 - Optimal values for the material parameters of the orthotropic FE model after calibration against 2018 EM modal data. (*) Concrete stayed as isotropic material.	141
Table 5-25 - Optimal values for the material parameters of the orthotropic FE model after updating with 2019 EM modal data. (*) Concrete stayed as isotropic material.	141
Table 5-26 - Comparison between 2018 experimental (EM) and numerical (NM) frequencies for different material modelling approaches and different updating parameters.	142
Table 5-27 - Comparison between 2019 experimental (EM) and numerical (NM) frequencies for different material modelling approaches and different updating parameters.	143
Table 5-28 - CrossMAC between EMs and calibrated NMs considering isotropic and orthotropic materials: (a)NM 2018 with isotropic material, (b) NM 2019 with isotropic material, (c) NM 2018 with orthotropic material, (d) NM 2019 with orthotropic material.	146
Table 6-1 - Comparison of the modal frequencies of the towers identified from preliminary monitoring data.	157
Table 6-2 - Modal parameters identified for the bell towers and comparison.	165
Table 6-3 - Comparison of the twin towers modal parameters after removal of environmental effects	173

1 Introduction

1.1 Research context

In the recent years Italy has been struck by numerous catastrophic seismic events, which strongly affected the country at economic level but also from human point of view [1–5]. The severity of the situation strongly sensitizes the public opinion and especially the technicians towards the necessity to reach a higher level of security of structures and infrastructures. Italy is famous throughout the world because of its enormous cultural heritage, which is composed in large part of masonry historical buildings of the more different typologies (churches, towers, arch bridges...). Unfortunately, this constructive field is also the one which results the more affected by seismic events, because of the intrinsic characteristics of the masonry structures, which usually leads to their cracking and, often, collapse [6–9].

The first step in the process of preservation and consequent interventions is obviously a deep knowledge of the health status of the constructions, in order to highlight eventual vulnerabilities linked to aging of materials, lack of connections, localized or diffused damage...[10,11]. The engineering branch which focuses over these features is known as Structural Health Monitoring (SHM). It can be defined as a systemic approach whose objective is that to identify and locate eventual anomalies of the structures and evaluate their evolution over time.

Among the variety of techniques which have been proposed into this field, in the last years, thanks to the technological progress, a non-destructive method emerged over the others, because of the countless advantages it offers in terms of economy of the investigations and practicality: Ambient Vibration Testing (AVT). This is an SHM methodology based on the evaluation of the dynamic response of a structure based on the acquisition and analysis of the vibration of the structure itself.

It is based on the concept that, when a particular occurrence modifies the structural configuration, this modification influences the modal response, and so a variation occurs in the modal properties (modal frequencies, damping ratio and mode shapes). Vibration data can be acquired following two dynamic test approaches: Experimental Modal Analysis (EMA), where the source of the vibrations is known and measured [12], and Operational Modal Analysis (OMA), which is the main theme of this discussion, and it is based on the concept of vibration induced by white noise (caused by environmental agents or human activities) [13–15]. Different methodologies and algorithms are proposed in this context and are finalized to threat acceleration data and extract modal characteristics in frequency [16] or time domains [17,18].

A classical approach is the one summarized in Fig. 1-1:

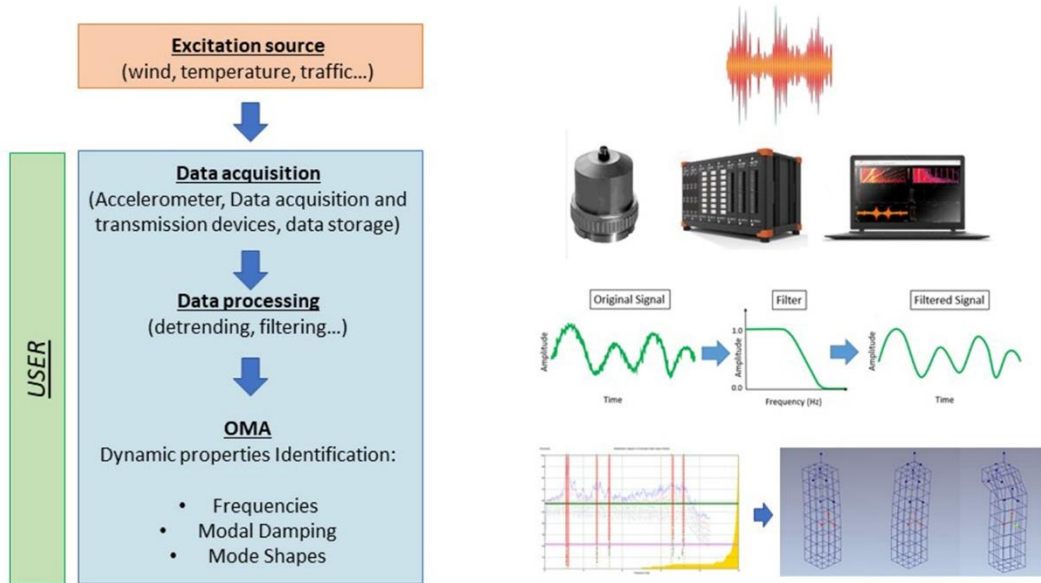


Fig. 1-1 - Classic workflow for OMA process

This scheme allows a quite rapid identification of the parameters of a structure, able to describe its actual condition. Nowadays civil engineering is focusing on the possibility to apply a continuous monitoring of the buildings, with the installation of fixed systems which acquire vibration data during the entire life of the structure, so that, in case of new constructions (especially the strategic ones) it is spreading the custom of designing monitoring system integrated into the structure itself [10,19].

These scenarios require the elaboration of automatic systems [20], able to manage enormous quantities of data, evaluating the variation in the modal parameters practically in real-time, with the idea of sending alerts when a significant change occurs.

1.2 Objectives and main contributions

The theme discussed in this thesis regards the different applications of OMA techniques to assist civil engineering in the context of SHM. Different techniques are presented and analyzed, always showing their utility in practical cases.

The discussion is developed starting from the classic application of this methodology to operative structures in order to evaluate their health state, analyzing both the case of a damaged structure than the one where no particular anomalies are evident.

Then the possibility to couple dynamic tests to the classic method of Finite Element modelling has been analyzed, in order to evaluate the potentiality of this method and the possibility to integrate clustering procedure in the context of modal updating, where the validation criteria has been established from vibration analysis results.

At least, from all the previous experiences, an automatic procedure for the management of continuous monitoring of structure is proposed. This system is based on the acquisition of data through a particular type of accelerometric sensors, which is recently developing, and which interprets the the excitation in a completely electronic way: MEMS accelerometers. The system, installed on the two bell towers of Camerino Dome, in Macerata Province, is acquiring data from over a year. The automatic procedure, developed in Matlab, elaborates data in order to execute a modal tracking of the main modal parameters. The effects of environmental agent is considered and their influence is removed from the results, in order to make a prevision of the evolution of the main modal characteristics to be compared with the real behavior and so highlight eventual anomalies. The main steps are illustrated in Fig. 1-2.

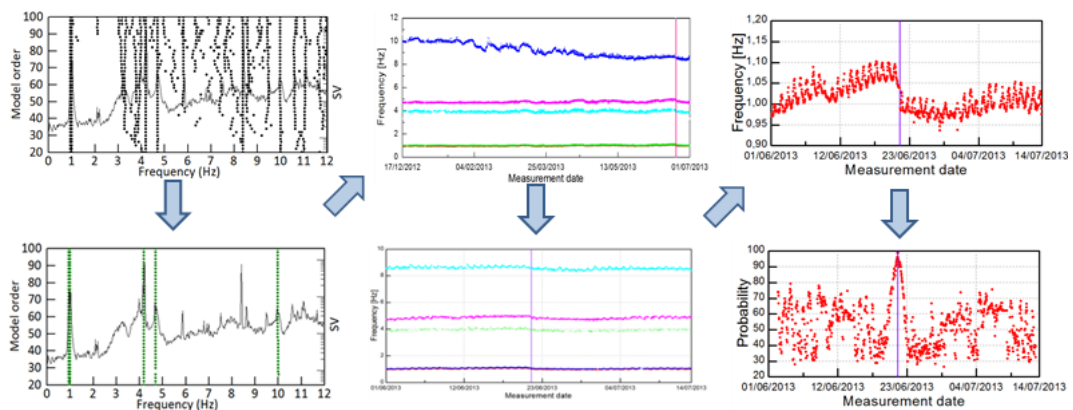


Fig. 1-2 - Main processing steps of a classical vibration-based health monitoring system

1.3 Organization of the thesis

Here is a summary of how the discussion is organized:

Chapter 1 consists in the introduction, where an overview of the context of the thesis is described in order to show the state of the art and present the main themes for the field. The main objectives and contribution are listed.

Chapter 2 provides an introduction to SHM, considering the fields of application, the main techniques adopted and a brief description of the dynamic monitoring instrumentation (sensors and converters) and introducing some concept of signal theory necessary for data elaboration.

Chapter 3 presents a brief review of the mathematical models of dynamic systems and the theoretical basis of the modal identification analysis implemented. So, the most known algorithms are explicated both for frequency domain analysis (Peak Picking, Frequency Domain Decomposition, Enhanced Frequency Domain Decomposition) than time domain (Stochastic Subspace Identification in the Covariance based and Data-Driven forms).

Chapter 4 presents two practical cases where an arch bridge and the cover of Fiumicino Airport have been monitored in order to determine their main dynamic characteristics in operative conditions. In particular the stays of the arch bridge were damaged because of a car accident, so the assessment of the health conditions of the structure were necessary.

Chapter 5 presents a methodology particularly used nowadays in the context of Finite Element Modeling, which consists in the tuning of the material parameters of a structure by comparison with the dynamic data elaborated through OMA techniques. The first part of the chapter considers the case of a manual procedure of model updating of four bell towers damaged during Emilia seismic events of 2012. The second case proposes an automatic calibration process based on Genetic Algorithms (GA) to update the model of Ostra Civic Tower on the basis of the data coming from two different monitoring campaigns.

Chapter 6 describes the main theme of the research and consists in the analysis of the data of the continuous monitoring of the bell towers of Camerino Dome, with acquisition of data using MEMS sensors. The automatic data processing algorithm, implemented in Matlab®, is described in all of its step. The algorithm processes data, then two clustering procedure are used one after the other to extrapolate the modal characteristics from each of the acquisitions files. These data are then correlated with environmental parameters and an autoregressive method is applied in order to filter these effects from the tracked modal characteristics. Modal tracking of frequencies and damping ratios for the first four modes of both the towers are successfully implemented.

2 Structural Health Monitoring (S.H.M.): Background and Tools

2.1 Introduction to SHM

Structural Health Monitoring (SHM) is a field of engineering whose aim is the identification and evaluation of *damage*, which can be defined as a modification occurred into a system which compromise its current and future performances [1].

From the above definition, it appears clear that the identification process, and the successive interventions strategies, presuppose the knowledge of two different temporal states of the investigated system, an initial one, where damage is absent or in the early stages, to be compared with the condition in which damage occurs or is evolving. Therefore, the structure or mechanical system status needs to be checked during time, through periodical monitoring activities, executed with different methodologies depending on the different operative factors and necessities, whose purpose is that of supplying information useful to assess the health status of the object. These features make SHM a multidisciplinary field, involving the collaboration of different actors (structural engineering, electronics and computer sciences, ...) in order to produce the technologies for acquisition and management of information, analysis of the data and establishment of the intervention strategy.

In civil and earthquake engineering, the target is to provide a structure with an adequate margin of safety against damage, in particular against of significant events such as earthquakes. For this reason, a control of the health condition of the structure becomes advisable and necessary for the safety of buildings [7]. Among the multiple possible approaches present in SHM world, this thesis is focused on one methodology, nowadays particularly popular in the civil engineering field, because of the numerous advantages it gives in terms of economy and operativity: Ambient Vibration Testing (AVT).

This discipline, that found its first application in industrial and aerospace engineering, approached civil field during the '80s, when vibration-based system started to be installed for the assessment of structures like bridges and buildings. AVT uses the analysis of the vibrations caused on structure by different factors (anthropological or environmental) in order to extract the properties useful to describe the dynamic behavior of the system. The basic idea is that modal parameters, such as frequencies, mode shapes and modal damping, are based on the physical properties of the whole

structure such as mass, damping and stiffness. Subsequently, when damage occurs and diffuses it modifies also the corresponding modal properties.

Possible application of SHM vibration-based techniques, which will be practically shown in Chapter 4 and Chapter 6, are:

- maintenance or structural safety evaluation of existing structures;
- rapid evaluation of conditions of damaged structures after an earthquake;
- estimation of residual life of structures;
- repair and retrofitting of structures;
- maintenance, management or rehabilitation of historical structures, thanks to the non-invasiveness of the instrumentation and the possibility to not interrupt the activities in the building;

2.2 SHM Classifications

According to Rytter (1993) the procedure for evaluation of damaged condition of a system is composed of five steps [5]:

1. Assessment of damage existence;
2. Localization of damage;
3. Evaluation of damage typology;
4. Measurement of damage extension;
5. Estimation of residual life of the system.

Monitoring activity can produce results able to satisfy the previous five points. On the basis of the followed approach monitoring can be categorized in three ways:

1. Strategies dependent on time [8], comprising:
 - Short-term monitoring, in which measurements are executed at a specific moment, in order to evaluate changes in structural behavior, due to deficiency or damage occurrence. The repetition of short-time monitoring campaigns takes the name of periodic long-term monitoring.
 - Long-term monitoring definition states that continuous monitoring of a structure is considered to be “long term” when the monitoring is carried out over a period of years-to-decades. Preferably, long term monitoring should be carried out over the life of the structure. Recent advances in sensor technology, data acquisition, computer power, communication systems, data and technologies now make it

possible to construct this type of system. Long-term monitoring should be considered if the monitored quantity changes slowly (e.g. temperature) or if the loads are not predictable (e.g. natural hazards such as floods, hurricanes or earthquakes).

- Triggered monitoring defines an activity where data are collected in case a specific event manifests, usually recognized because a particular parameter exceeds a fixed threshold (e.g. the level of acceleration surpasses a specific value in case of earthquakes). The sampling interval for each data collection depends on the dynamic nature of the studied phenomena.

2. Strategies dependent on structural size:

- Local monitoring is the observation of local phenomenon, such as strain or crack opening. Local monitoring is not able to determine the health of the whole structure. Still, in combination with global monitoring methods, local monitoring approach can be a useful to evaluate the severity of detected damages.
- Global monitoring is defined as the observation of global phenomena of structures. A typical application is the monitoring of modal parameters, such as frequencies, mode shapes and damping of the structure and to correlate the test results with the outcome of FE-analysis. The challenge is then to create a “damaged” FE-model so that the monitored results comply with the FE-analysis.

3. Strategies dependent on sampling rate:

- Static monitoring is used for measurements of phenomena such as deflection, inclination, settlements, crack widths, temperature, and humidity. These are quasi-static since they vary slowly over the time.
- Dynamic monitoring is performed with a much higher sampling rate compared to static monitoring. It is usually used for measurements of accelerations in order to control the dynamic structural response.

2.3 SHM applications

Nowadays an always major interest towards SHM methodology, testified by technical literature and practical applications, due to the technological evolution, comports the miniaturization and a lowering of the costs for digital instrumentation, and the always growing diffusion and development of internet which allows the remote control of the systems and data exchange.

In recent times a popular implementation of SHM provide for the installation of specifically designed systems integrated in the structures since construction stage, in order to monitor the structure during

the works. In this way, monitoring become a tool to manage safety risks during construction, as incomplete structural systems are typically vulnerable and exposed to accidents and hazards. Moreover, the validity of the assumptions made during design calculations regarding the forces, reactions, displacements, and drifts that a structure is expected to experience during its construction can be checked and confirmed. Feedback regarding the behavior of the new structure are constantly provided so that, if necessary, it is possible to modify the projects before the completion of works. Once integrated the system will assess the health status of the structure for all its lifetime, with the possibility, in case of smart system, of sending alert messages in case of alteration of the condition or immediately check the safety conditions so far as an exceptional event (such as earthquake) happens.

Apart for the case of new buildings, the main adoption of SHM regards the health assessment for existing structures, and in particular Cultural Heritage buildings, whose preservation is one of the main objectives in the structural engineering field nowadays. In these sense possible examples of SHM usage are short-time monitoring with the purpose of evaluating the current capacities of investigated structure from the dynamic characteristics extracted. The analysis and interpretation of such data would provide critical information about the current load and responses as well as remaining fatigue life. A particular type of application is the calibration of Finite Elements models, especially in case of historical buildings: in this case the data analysis is oriented towards the definition of the material parameters of the structure, which are tuned in order to reproduce the structural response. Once the models are correctly updated they can be subdued to linear and non-linear analysis in order to verify/identify damage mechanism and evaluate the state of the building, with the possibility of planning of interventions.

In this context, a great innovation can be represented by a coupled system of continuous monitoring, with automatic interpretation of data, providing the actual dynamic characteristics of the structure in real-time, and systematic process of model updating, so that the health status of the building is always checked.

2.4 The measurement processes

SHM comprises a large variety of techniques, everyone of them specifically designed to analyze a particular phenomenon, consequently the monitoring system need to be designed to adapt to the different purposes.

For all of the possible cases, being the monitoring short time or continuous, static or dynamic, the instrumentation is always composed of a certain number of sensors (different typologies can be

coupled if required), data acquisition devices, a storage unit and at last a data processing system to visualize, analyze and interpret the acquired data.

In Fig. 2-1 the typical scheme of a monitoring system is presented. As it is observable, the first step consists in the choice of the correct instrumentation: high-quality measurements represent the first fundamental step for a successful modal identification.

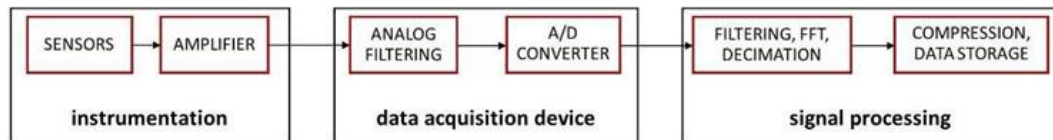


Fig. 2-1 - Data acquisition system setup

The second branch is constituted from the acquisition device: the function of any sensor is the conversion of a physical quantity into an electrical one, typically voltage. Then, the electrical signal in the form of voltage is transferred to the data acquisition hardware for digitization.

At last, there is the data processing, for which different techniques are available. In general, this step is composed of a pre-processing phase, where data are checked and eventual disturbances (linked to the instrumentation itself or to errors in the measurement process) are removed, and then the real analysis of the data with extraction of the interested parameters.

From now on, being the thesis focused on the dynamic monitoring, reference will be made only to the equipment and the techniques used in this context.

2.4.1 Instrumentation

Instrumentation includes deciding on the quantities to be measured and the selection of the type of network (wired vs. wireless), the choice of the transducers and their positions. The last decade has been characterized by substantial effort in the development of wireless sensor networks for structural testing and health monitoring. Even if a number of wireless sensing solutions are currently available, offering attractive advantages such as the reduction of costs and installation time associated to the use of cables, they have not fully replaced wired systems. Nowadays a wired solution is the best way for a continuous monitoring system because of the absence of problems related to power consumption.

The sensor type depends on the application. Typical sensors are accelerometers, strain gauges, fiber optics, and laser. The measured motion is typically very small at a low frequency. Therefore, the sensitivity of the sensor has to be high.

2.4.2 Data Acquisition Hardware

Sensors data, that usually acquire an input analog signal expressed in terms of electric voltage, need to be converted in digital format in order to be stored and processed. Different types of A/D converters can be found on the market, and a first distinction can be made between dedicated solutions (Fig. 2-2a), where the instrumentation is practically ready for use and equipped with an acquisition software, and customizable solutions (Fig. 2-2b), based on programmable hardware and usually adopted by expert users.

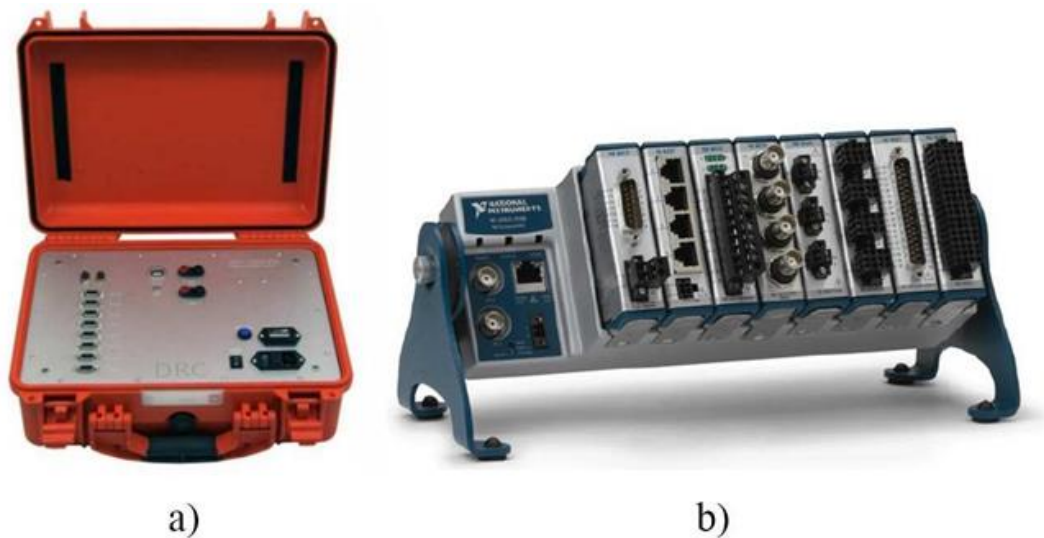


Fig. 2-2 - Dynamic data acquisition system

As already said, Analog-to-Digital Converters (ADC) are devices whose function is that of transform a continuous signal registered by sensors into digital sequences representing the signal in terms of its amplitude. The conversion is based on the discretization of time (sampling) and signal amplitude (quantization).

The main characteristics to consider for an ADC device are:

- *resolution*, defined as number of bits the converter can use for signal representation;
- *noise level*, computing the number of bits noise occupies for zero input (e.g. only the last two bits are typically corrupted by noise in good quality 24-bit digitizers);
- *dynamic range*, usually expressed in dB, and defined as the ratio between the largest and the smallest value the ADC can acquire without significant distortion;
- *The sampling rate (f_s)* is the number of samples acquired per second, where the frequency range investigable is defined as the maximum rate of the ADC. Usually, in civil applications,

being the interesting range for these structures comprised between 0 and 100 Hz, a maximum sampling rate 200 Hz can result satisfactory.

2.4.3 Transducers

Dynamic vibration-based tests data are usually acquired using accelerometric sensors. Among the different types of accelerometers available on the market in the following two subsections, the two main categories will be presented: piezoelectric accelerometers and MEMS.

The choice of the sensors is usually based on a series of considerations:

- the expected amplitude of the motion to be measured;
- the type of investigated structure (e.g., masonry, reinforced concrete, steel, etc.);
- the available budget.

For the case studies proposed in this dissertation, both the typologies of accelerometers are used, in particular, in the short-term monitoring applications piezoelectric ones are adopted, due to the major precision, while in the continuous case triaxial MEMS accelerometers have been experimented.

2.4.3.1 Piezoelectric accelerometers

Piezoelectric sensors are devices with the function of converting a mechanical quantity into an electrical quantity. This characteristic is due to the use of specific materials having piezoelectric properties, so the ability to accumulate electrical charges when subjected to some form of external excitation, with the number of charges proportional to the applied shock. The origin of the piezoelectric component can be natural (quartz) or man-made (polycrystalline ceramics, such as barium titanate) [25].



Fig. 2-3 - Piezoelectric sensor from PCB 393B12 series

In piezoelectric accelerometers the crystal is coupled to a mass, so, when an input acceleration is applied at the base of the sensor, the inertia force associated to the mass causes a deformation of the crystal. The piezoelectric material generates an electric charge, proportional to its deformation, which is transmitted to a signal conditioner which read the input in terms of voltage. This object can be remote, such as in charge-mode sensors, or built-in as for the Integrated Electronics Piezo-Electric (IEPE) accelerometers. IEPE accelerometers offer a number of advantages, in respect to charge mode, such as simplified operation, lower cost, resolution virtually unaffected by cable type and length (long cables can be used without increase in noise, loss of resolution, or signal attenuation), and therefore, nowadays, they are the more used in the piezoelectric category. For this kind of sensors the signal cables is also entrusted with the power supply function, therefore, the signal is high-pass filtered to remove the frequencies close to DC.

For selecting the most appropriate sensor for the required application, the main characteristics to be considered are reported below:

- *Sensitivity* which is the smallest variation detectable in measurement; because of the low amplitude of motion and the limited frequency range of the structure under test, high-sensitivity accelerometers are necessary. Sensitivity is usually defined by the gain of the sensor, so the possibility to amplify the signal before digitalization (for example, 10 V/g), to minimize the limitative effects of electrical noise over the detection of the smallest signals. In fact, electrical noise limits the smallest detectable signal, so a high gain should be preferred since an amplified signal minimizes the noise effects associated to the transmission over cables;
- *dynamic range* (DR) of a sensor (often expressed in dB), which is the ratio between the largest and the smallest measurable signal:

$$DR = 10 \cdot \log \left(\frac{V_{max,s}}{V_{n,s}} \right)^2 \quad (2.1)$$

where $V_{max,s}$ and $V_{n,s}$ respectively represent the maximum voltage signal and the noise floor of the sensor. A 120–140 dB dynamic range is usually very suitable, since it well adapts itself with the average resolution at 24-bit most of the digitizers are equipped with;

- *resolution*, that represents the smallest variation in the input physical quantity perceived in the sensor output, usually expressed in absolute terms or as a percentage of the full-scale range. It indicates the maximum and minimum physical values the sensor can;
- *linearity*, that is the trend there should be in the conversion between the input and output measurement: ideal sensor should behave linearly, but a deviation component is always

present. Such deviation should be as limited as possible and it is expressed by the percentage of nonlinearity, that for high performances accelerometers should be lower than 1%.

2.4.3.2 MEMS accelerometers

Thanks to the fast evolution of the micro-machining in the last decade, enabling the creation of mechanical components with sizes of few micrometers, new devices, known as Micro Electro Mechanical Systems (MEMS), have been developed. This technology rapidly diffused also in the vibration analysis field, leading to the diffusion of MEMS accelerometers. Compared to the classical piezoelectric sensors, MEMS has the advantage of smaller dimensions and cheaper prices [21].

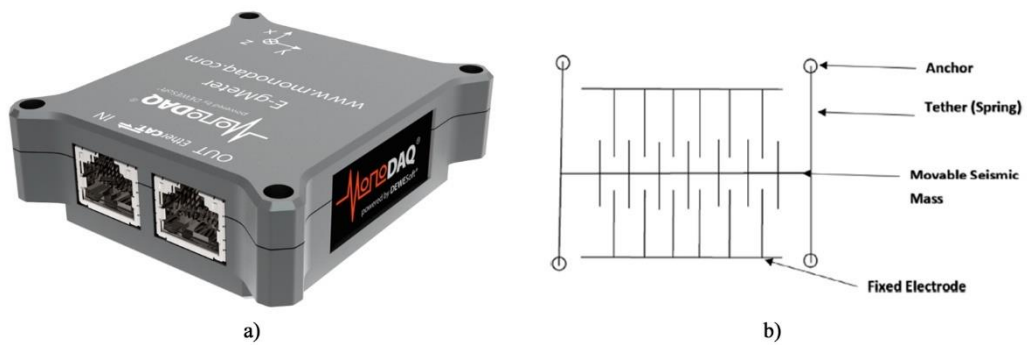


Fig. 2-4 - MEMS accelerometers: MonoDAQ-E-gMeter (a) and internal configuration (b)

This type of sensor (Fig. 2-4) is constituted of a moving mass, linked to flexible tethers, creating an electronic system equivalent to the spring mass system of piezoelectric technology. When the mass moves, the displacement is measured through the variation of the differential capacitance registered between three electrodes, two of which are fixed, and one is moving. The moving electrode, in quite conditions, stand fixed in mid position between the other two components, and so the output differential results zero. Instead, when an acceleration intervenes, the mass displaces because of inertia modifying the distance in respect to the fixed electrodes. The output capacitance is converted in terms of accelerations, for example, if the MEMS is oriented vertically and therefore subdued to gravity, the offset in that direction will be equal to 1g.

As concerns the accelerometers present on the market, the triaxial version is pretty common, and their reliability is assured from different studies in literature [21,22], also when they are configured in arrays [23].

2.4.4 Signal Processing

The quality of signals is very important for a satisfactory analysis and a good identification of the dynamic behavior of a structure. Good quality of the acquisitions requires a correct setting of the

instrumentation before executing the measurements and an appropriate processing of acquired data before the application of identification methods.

The first fundamental step consists in the definition of a correct value for the sampling frequency. Representing the number of samples acquired in one second, sampling frequency must fit the examined structure. Known the frequency range of interest for the structure under analysis, the *Nyquist Theorem* establish:

$$f_s > 2 \cdot f_M \quad (2.2)$$

where f_s is the sampling frequency and f_M is the maximum frequency in the sampled signal, and

$$f_N = f_s/2 \quad (2.3)$$

is the so-called *Nyquist frequency*.

Fig. 2-5 shows the phenomenon of aliasing, caused by a too low value of the sampling frequency, that causes the reconstruction of a “false” waveform after digitization of the continuous signal (e.g. a high-frequency signal appearing as a low-frequency one). Because it is not possible to correct the erroneous effect of aliasing after conversion, usually A/D converter are equipped with an *anti-aliasing filter*.

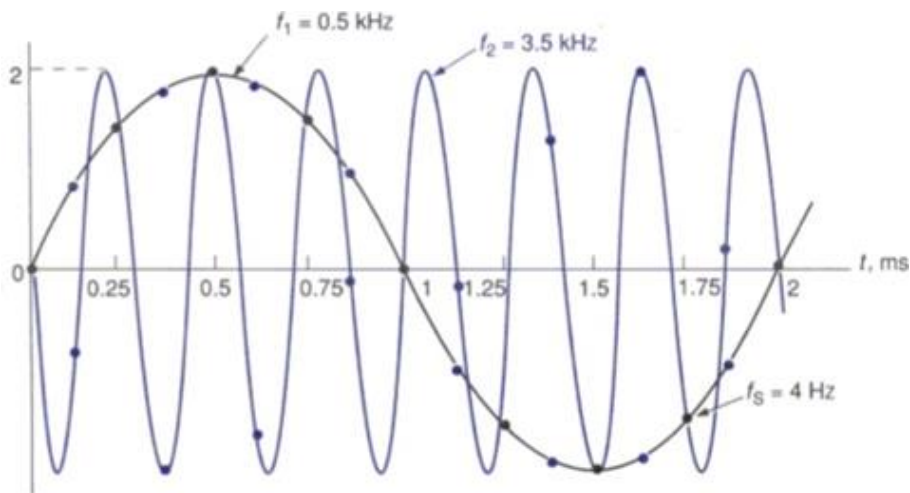


Fig. 2-5 - Aliasing. True signal (3.5kHz), Aliased signal (0.5kHz)

Among the so-called pre-processing operations, necessary to clean the signal before identification, the most common are *filtering* and *decimation*.

Filtering operations are often necessary to remove unwanted frequency components from signals. Digital filters are usually classified as:

- *low-pass*, which excludes all frequencies above a certain threshold;

- *high-pass*, that eliminate the frequencies below a fixed values (e.g. remotion of frequencies near DC);
- *band-stop*, excluding the frequencies defined in the filter band;
- *band-pass*, cleaning the frequencies outside the range established for the filter.

As already stated, signals are acquired with a sampling rate higher than the range of interest for the analysis. Decimation (or down-sampling) is therefore used to resample the acquired signals to a lower sampling frequency. Assuming, for example, that data are acquired with a sampling frequency of 100hz, using a *Decimation Factor* of 2 transforms the signal in a time history with 50 data per second (50 Hz).

3 Operational Modal Analysis: Methodologies

3.1 Modelling of the dynamic behavior of linear systems

3.1.1 Spatial and modal models

3.1.1.1 Spatial formulation

The *Spatial Model* of a multi-degree of freedom (MDOF) system can be described through the well-known second order differential equation (Eq. 3.1):

$$M\ddot{q}(t) + C\dot{q}(t) + Kq(t) = F(t) = B \cdot f(t) \quad (3.1)$$

Where M , K and C are respectively the *Mass*, *Stiffness* and *Damping* matrices, and $\ddot{q}(t)$, $\dot{q}(t)$, $q(t)$ are the vectors of *accelerations*, *velocities* and *displacements*, associated to each of the single degrees of freedom (SDOF) composing the system. $F(t)$ is the vector of the exciting forces, acting over the considered system, which can be written as the product of a matrix B , containing all of the inputs, and a vector $f(t)$, where the application points are listed. It is assumed that the system is formed of planar rigid bodies, so that the matrices are squared [N -by- N], and all the functions are expressed in continuous time domain and referred to the same instant t .

Due to the uncertainties linked to damping and its modelling, it is common practice to assume a proportional approach in the evaluation of the decaying responses, considering a linear relationship between mass and stiffness, as proposed by Rayleigh. The following simplifications allow to express damping as a linear combination between M and K (Eq. 3.2) [24]:

$$C = M \cdot \sum_b a_b \cdot [M^{-1} \cdot K]^b \rightarrow C = \alpha M + \beta K \quad (3.2)$$

This system of second-order differential equations finds its solution in time domain applying *Duhamel integral*.

Due to the complexity of solving the problem associated to MDOF system in time domain, being the solution dependent from the dynamic responses of the single SDOF components, a SDOF oscillator will be considered to illustrate the representation of the *Spatial Model*, which is described by Eq. 3.3:

$$m \cdot \ddot{q}_1(t) + c \cdot \dot{q}_1(t) + k \cdot q_1(t) = f_1(t) \quad (3.3)$$

where $q_1(t)$ is the response of the oscillator subjected to an arbitrary force $f_1(t)$, and $\dot{q}_1(t)$ and $\ddot{q}_1(t)$ are the two derivatives (first and second) of $q_1(t)$, respectively. The application of *Duhamel convolution integral* (Eq. 3.4) together with the imposition of null values for the initial displacement and velocity, allows to find a solution of the problem.

$$q_1(t) = \int_0^t f_1(t) \cdot h_1(t - \tau) \cdot d\tau, \quad \tau > 0 \quad (3.4)$$

In the Eq. 3.4 the function $h_1(t - \tau)$, defined by following relation, is the response of the system in the instant $t - \tau$, caused by a unitary impulse generated in the instant τ (Eq. 3.5):

$$h_1(t - \tau) = \frac{1}{m \cdot \omega_{1d}} \cdot e^{-\omega_1 \xi (t - \tau)} \cdot \sin[\omega_{1d} \cdot (t - \tau)], \quad t > \tau \quad (3.5)$$

Where ω_{1d} is the damped frequency, defined in Eq. 3.6:

$$\omega_1 = \sqrt{k/m} \rightarrow \omega_{1d} = \omega_1 \cdot \sqrt{1 - \xi^2} \quad (3.6)$$

The *damping value* (c) in Eq. 3.3 is related to the known *damping coefficient* (ξ) of the system by the following equation:

$$c = 2 \cdot \xi \cdot m \cdot \omega_1 \quad (3.7)$$

Duhamel integration procedure practically consists in dividing the force the system is subdued as a sequence of impulses (or better of impulsive functions) and then summing the responses calculated for every single impulse. However, being the dynamic response dependent from the responses of the various SDOF systems, a more convenient strategy is to solve the problem transferring it into frequency domain and so using the *Modal Domain*, as it is usually named.

3.1.1.2 Modal formulation

Modal formulation is a methodology which allows the conversion of a system, composed by N coupled second order differential equations, into an equivalent set of the same number of independent differential equations, representing the displacements as a linear combination of N independent vectors, usually named modes of vibrating, that will be indicated as φ_k from now on.

Considering a non-damped system having the same mass and stiffness characteristics of the previous one, whose behavior is expressed in Eq. 3.8 and whose solution takes the form of Eq. 3.9, it is observable that its vibration modes are similar to those of the system where proportional damping hypothesis is assumed.

$$M\ddot{q}(t) + Kq(t) = 0 \quad (3.8)$$

$$q(t) = \varphi_k \cdot e^{\lambda_k \cdot t} \quad (3.9)$$

Solving the eigenvalue problem, it is possible to extract the eigenvalues $-\lambda_k^2$ and their corresponding eigenvectors φ_k (Eq. 3.10):

$$\lambda_k^2 \cdot M \cdot \varphi_k + K \cdot \varphi_k = 0 \Leftrightarrow K \cdot \varphi_k = -\lambda_k^2 \cdot M \cdot \varphi_k \quad (3.10)$$

These quantities, are strictly linked to the dynamic properties of the system, being λ_k correlated to the non-damped angular frequencies (ω^2) (Eq. 3.11), and being the eigenvectors intimately related to the structure vibration modes, usually corresponding to the columns of the so-called *Modal Matrix* (Φ) (Eq. 3.12).

$$\lambda_k = i \cdot \omega_k \quad (3.11)$$

$$\Phi = [\cdots \quad \varphi_k \quad \cdots], \quad k = 1 \dots N \quad (3.12)$$

Introducing the orthogonality property of Φ in respect to the mass and stiffness matrices (Eq. 3.13), it becomes possible to separate the equations of the MDOF non-damped system of Eq. 3.8. Moreover, by multiplying Eq. 3.8 for Φ^T leads to the transformation of matrices M and K into diagonal matrices (Eq. 3.13), respectively called *Modal Mass Matrix* (M_d) and *Modal Stiffness Matrix* (K_d), and with m_k and k_k indicating the elements of the matrices associated to the k -th DOF.

$$\Phi^T \cdot M \cdot \Phi = \begin{bmatrix} \ddots & & \\ & m_k & \\ & & \ddots \end{bmatrix} \quad \Phi^T \cdot K \cdot \Phi = \begin{bmatrix} \ddots & & \\ & k_k & \\ & & \ddots \end{bmatrix} \quad (3.13)$$

So, the non-damped angular frequency for one of the SDOF of the MDOF system is obtainable like in the case of the free response of the 1-DOF oscillator (Eq. 3.14):

$$\omega_k = \sqrt{\frac{k_k}{m_k}} \quad (3.14)$$

Extending the discussion to the more general case of damped vibration systems, the orthogonality property must be extended also to the *Damping Matrix* (C) and also under the assumption of proportional distributed damping in the whole system. These leads to the expression of Eq. 3.15:

$$\Phi^T \cdot C \cdot \Phi = \begin{bmatrix} \ddots & & \\ & c_k & \\ & & \ddots \end{bmatrix} = \begin{bmatrix} \ddots & & \\ & 2\xi_k m_k \omega_k & \\ & & \ddots \end{bmatrix} \quad (3.15)$$

It is observable that, under the previous hypothesis, the *Modal Damping Matrix* (C_d) comes from a linear combination of modal matrices M_d and K_d .

From Eq. 2.9, the free dynamic response problem for proportional damped MDOF systems takes the form of a series of individual equations like in Eq. 3.16:

$$\lambda_k^2 + 2\xi_k \omega_k \lambda_k + \omega_k^2 = 0 \quad (3.16)$$

Solving these N expressions associated to the liner system of Eq. 3.8, and relating the obtained eigenvalues to those of non-damped angular frequencies and to the damping coefficients leads to:

$$\lambda_k, \lambda_k^* = -\xi_k \omega_k \pm i \sqrt{1 - \xi_k^2} \cdot \omega_k \quad (3.17)$$

This makes possible to express the general solution of Eq. 3.1. for the system $q(t)$ as a linear combination of the modes of vibration in *Modal Space* (Eq. 3.18).

$$q(t) = \sum_{k=1}^N \varphi_k \cdot \eta_k(t) \quad (3.18)$$

Applying the *superposition of the effects* principle it is possible to convert a linear equation system with proportional damping into a system of independent second-order differential equations, whose solution derives from a linear combination of the singular vibration modes (Eq. 3.19):

$$m_k \cdot \ddot{\eta}_k(t) + c_k \cdot \dot{\eta}_k(t) + k_k \cdot \eta_k(t) = f_k(t), \quad k = 1 \dots N \quad (3.19)$$

Where:

- $\dot{\eta}_k(t)$ and $\eta_k(t)$ are the first and second derivative of the modal coordinate $\eta(t)$;
- m_k, k_k and c_k are the modal components of the modal matrices described in Eq. 3.13 and 3.15, respectively;
- f_k is the modal component of the input excitation associated to k -th DOF, expressed in Eq. 3.20.

$$f_k(t) = \varphi_k^T \cdot (B \cdot f(t)) \cdot I \quad (3.20)$$

By reconnecting to what was expressed in Eq. 3.13, the relation existing between the *modal matrix* and the transformation of M and K in their diagonal version is explicable by the follows:

$$[M_d] \ddot{\eta}(t) + [K_d] \eta(t) = f_\eta(t) \quad \begin{cases} \eta(t) = \Phi^{-1} \cdot q(t) \\ f_\eta(t) = \Phi^T \cdot B f(t) \cdot I \end{cases} \quad (3.21)$$

Consequentially, the vibration modes, solution of the eigenvalues problem, can be defined introducing a scale factor, which allows to obtain the *Unit Modal Mass Matrix* (Eq. 3.27):

$$\ddot{\eta}(t) + \begin{bmatrix} \ddots & & \\ & \omega_\eta^2 & \\ & & \ddots \end{bmatrix} \eta(t) = \Gamma_\eta(t) \rightarrow \ddot{\eta}(t) + \omega_\eta^2 \cdot \eta(t) = \Gamma_\eta(t) \quad (3.22)$$

In which $\Gamma_\eta(t)$ is the *Participation coefficient* used to recognize the modal component equivalent to each SDOF in the normalization process.

From what emerges from the introduction to the *Modal Model*, the relations found applying the *Duhamel Integral* in the *Spatial Space* (Eq. 3.3) can be formulated as follows:

$$\eta(t) = \int_0^t f_\eta(\tau) \cdot h(t - \tau) \cdot d\tau, \quad t > 0 \quad (3.23)$$

$$h(t - \tau) = \frac{1}{m_k \cdot \omega_{dk}} \cdot e^{-\omega_k \xi(t - \tau)} \cdot \sin[\omega_{dk} \cdot (t - \tau)], \quad t > \tau \quad (3.24)$$

The function $h(t - \tau)$, in parallel with what emerged from Eq. 3.4 and Eq. 3.5, makes possible to interpret the output response in the *Modal Space* as a filter, formed by the sum of the history of input $f_\eta(\tau)$, which allows to obtain an impulse response function completely defined by the mass (m_k), the *natural frequency* (ω_k), and the *damping ratio* (ξ_k), that are defined as in Eq. 3.25.

$$\begin{aligned} \omega_{dk} &= \omega_k \cdot \sqrt{1 - \xi^2} \\ \xi_k &= \frac{c}{2m_k \omega_d} \quad \text{and} \quad \omega_k = \sqrt{\frac{k_k}{m_k}} \end{aligned} \quad (3.25)$$

3.1.2 Frequency response models

Operating in frequency domain instead of the time one is an alternative and simpler way to approach the dynamic problem expressed by Eq. 3.1. This methodology consists in the application of the Fourier Transform in order to convert the system of second order-differential equations into a set of algebraic equations.

3.1.2.1 Frequency response models

Starting from the 1-DOF system represented through Eq. 3.3, the application of *Fourier Transform* leads to:

$$-m \cdot \omega^2 \cdot Q_1(\omega) + c \cdot i \cdot \omega \cdot Q_1(\omega) + k \cdot Q_1(\omega) = F_1(\omega) \quad (3.26)$$

in which the functions $Q_1(\omega)$ and $F_1(\omega)$ are the *Fourier transforms* functions of $q_1(t)$ and $f_1(t)$.

The structural response of the system is written in its explicit form as:

$$Q_1(\omega) = \frac{F_1(\omega)}{-\omega^2 \cdot m + i \cdot \omega \cdot c + k} = H_1(\omega) \cdot F_1(\omega) \quad (3.27)$$

where $H_1(\omega)$, corresponding to the Fourier Transform of the impulse function $h_1(t - \tau)$ in Eq. 3.5, is the *Frequency Response Function* (FRF) of SDOF system, which can be alternatively expressed as:

$$H_1(\omega) = \frac{1}{-\omega^2 \cdot m + i \cdot \omega \cdot c + k} = \frac{1/m}{\omega_1^2 - \omega^2 + 2 \cdot i \cdot \xi \cdot \omega \cdot \omega_1} \quad (3.28)$$

The division of the numerator and denominator for the mass (m), and substituting the terms $\omega_1 = \sqrt{(k/m)}$ and $c = 2 \cdot \xi \cdot m \cdot \omega_1$, allow to rewrite Eq. 3.28 in the form of Eq. 3.29, highlighting once again that the FRF results a complex function, with amplitude ($A = \sqrt{(Re^2 + Im^2)}$) and phase ($f = \tan^{-1}(Im/Re)$), where Re stands for the real part and Im for the imaginary one.

$$H_1(\omega) = \frac{1/k}{1 + 2i\xi \left[\frac{\omega_1}{\omega} \right] - \left[\frac{\omega_1}{\omega} \right]^2} \quad (3.29)$$

It can be observed that:

- for low level of damping, the FRF has its maximum amplitude in $\omega = \omega_1 \cdot \sqrt{1 - \xi^2}$, which can represent an acceptable natural frequency;
- when excitation is low, inertial mass and damping results negligible, the FRF tending to the value of $1/k$; this fact implies a quite constant trend of the amplitude plot and a value of phase close to zero.
- for values of exciting frequency close to the natural one, a peak is found (with phase value which jumps from 0° to 180°), and the phenomenon is called *Resonance*. In this case the response is totally imaginary and practically related only to damping forces. Sharper shapes of the amplitude curves correspond to lower damping levels (Figure 1).

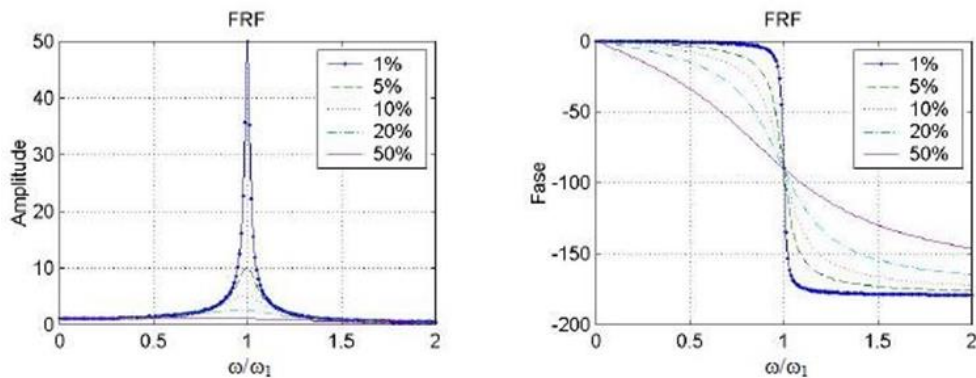


Figure 1 - Amplitude and phase of the Frequency Response Function of 1-DOF system

The relation between input forces and the system response can be defined through the application of Fourier Transform to the terms $q_i(t)$ and $f_i(t)$ in Eq. 3.1, transforming them in the $[N\text{-by-}1]$ vectors $Q_N(\omega)$ and $F_N(\omega)$ of Eq. 3.30:

$$Q_N(\omega) = H(\omega) \cdot F_N(\omega) \quad (3.30)$$

The components $H_{ij}(\omega)$ of the $[N\text{-by-}N]$ matrix $H(\omega)$, appearing in the above equation, represents the FRF corresponding to the response of a coordinate i when subdued to a generic force applied in a coordinate j of the system. This matrix is related to the structural characteristics of the system by Eq. 3.31:

$$H(\omega) = [-\omega^2 \cdot M + i \cdot \omega \cdot C + K]^{-1} \quad (3.31)$$

3.1.2.2 Frequency response models in the Modal Space

Extending the concepts expressed by Eq. 3.30, the structural response of a MDOF system can be rapidly evaluated in frequency domain, by rewriting the afore-mentioned expression as follows:

$$Q_{\eta k}(\omega) = H_{\eta k}(\omega) \cdot F_k(\omega) \quad (3.32)$$

and considering that in the Modal Domain the elements $H_{\eta k}(\omega)$ of the FRF matrix can be written as:

$$H_{\eta k}(\omega) = \frac{1}{\omega_k^2 - \omega^2 + 2 \cdot i \cdot \xi_k \cdot \omega \cdot \omega_k} \quad (3.33)$$

So, the complete FRF matrix can be expressed with generalized coordinates recurring to the vibration modes (Eq. 3.34):

$$H(\omega) = \Phi \cdot H_{\eta}(\omega) \cdot \Phi^T = \sum_{k=1}^N H_{\eta k} \cdot \varphi_k \cdot \varphi_k^T \quad (3.34)$$

in which H_{η} is a diagonal matrix composed by FRFs calculated in the Modal Space, normalized respect to the modal mass matrix. This process leads to the construction of a FRF matrix which is related to the principal modes of vibration of the system, as it is marked by Eq. 3.35:

$$H_{\eta(i,j)}(\omega) = \sum_{k=1}^N \frac{[\varphi_i]_k \cdot [\varphi_j]_k}{\omega_k^2 - \omega^2 + 2 \cdot i \cdot \xi_k \cdot \omega \cdot \omega_k} \quad (3.35)$$

One of the advantages which emerges from the use of the Modal Domain formulation, apart for the lower computational cost, stands in the possibility to reduce the number of vibration modes necessary for the analysis of the structural response, considering only the modes associated to lower frequencies, which are also the more interesting for the characterization of the dynamic behavior of the structure.

Moreover, combining the results regarding the response of the system for the model space (Eq. 3.18) and the ones described by Eq. 3.33, it is possible to write the output response of the MDOF linear system, when known forces acts over it, as:

$$Q(\omega) = \sum_{k=1}^N \varphi_k \cdot H_{\eta k}(\omega) \cdot F_k(\omega) \quad (3.36)$$

Considering that the FRF can be also seen as the Fourier Transform of the impulse response function (IRF) defined by *Duhamel integral* in Eq. 3.4, the $H(\omega)$ matrix can be written as the ratio of the spectrum of the output data $Q(\omega)$ and the spectrum of the input force system $F(\omega)$. Consequently, a system composed by a SDOF system excited by several harmonic inputs, whose nominal frequency is ω_p , it is possible to express the FRF as follows:

$$H(\omega) = \frac{Q(\omega)}{F(\omega)} = \frac{1/k}{1 + 2i\xi \left(\frac{\omega_p}{\omega_n}\right) - \left(\frac{\omega_p}{\omega_n}\right)^2} \quad (3.37)$$

It can be observed that when ω_p tends to nominal natural frequency ω_n of the system, the *Resonance phenomenon* takes place, with the phase which jumps from the 0 to π and the response which becomes purely imaginary and related to the damping forces. Matrix $H_{ij}(\omega)$ is expressed as:

$$H_{ij}(\omega) = \sum_{r=1}^N H_{ijr} = \sum_{r=1}^N \frac{R_{ijr}}{j\omega_p - \lambda_r} + \frac{R_{ijr}^*}{j\omega_p - \lambda_r^*} \quad (3.38)$$

$$\lambda_r = -\xi\omega_n \mp j\omega_n\sqrt{1 - \xi^2} \text{ and } R_{ijr} = \frac{\varphi_{ir}\varphi_{jr}}{j2\omega_{dr}m_r} \quad (3.39)$$

in which the complex roots of the equation, so the values λ_r , are the system poles, furnishing information about the damped frequencies (imaginary part) and damping ratios (real part), while R_{ijr} are the so-called residuals containing the mode shapes coefficients. Due to the symmetry of the matrix $H_{ij}(\omega)$, it is possible to extract the mode shape associated to a specific frequency just knowing one row or one column associated to that defined natural frequency [25].

3.1.3 State-Space models

Linear-time invariant (L.T.I.) systems dynamic problem, under the assumption of proportional damping and the consequent orthogonality of the eigenvectors, can be solved operating a separation of the differential equations describing the problem, whose solution produces a set of vibration modes which are equal to those characterizing a non-damped structure. In real cases, it appears obvious, that

these conditions are not met, being the damping distribution not proportional to mass and stiffness and sometimes even occurring the case of localized damping.

The application of identification method in order to extract modal parameters in operational conditions, where also noise disturbance in data acquisition is to be considered, requires an adaptation of the formulation, which pass through the construction of a stochastic state-space model.

All the steps, starting from equation of motion, passing for the discretization of collected time series, until arriving to the formulation of a discrete stochastic model, which allows to execute modal identification also in systems affected by random noise and subjected to unknown input forces, are synthetized in the scheme of Fig. 3-1.

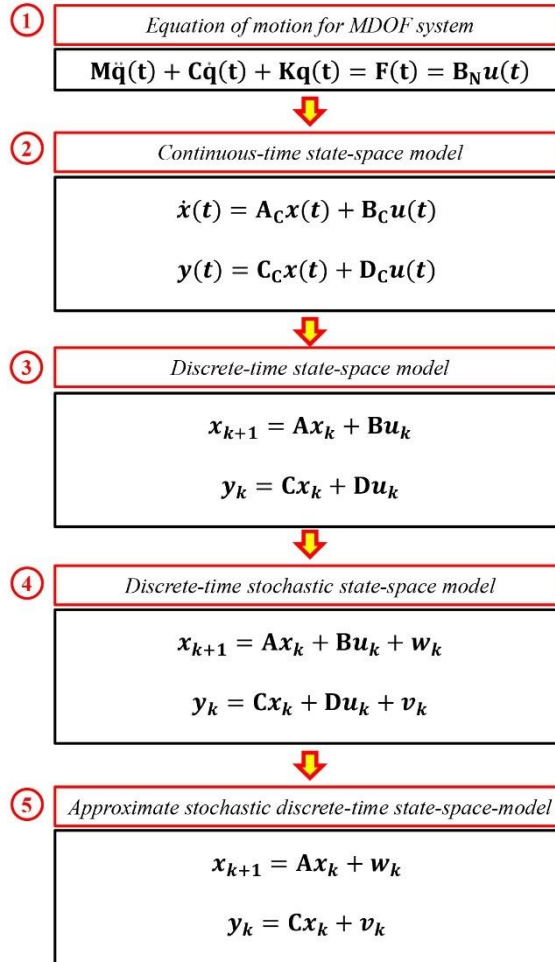


Fig. 3-1 - Genesis of the stochastic state-space-model used for general applications

3.1.3.1 Continuous-time state-space model

The description of a N dofs structural system in state-space is formulated with the well-known Eq. 3.40:

$$M\ddot{q}(t) + C\dot{q}(t) + Kq(t) = F(t) = B_N u(t) \quad (3.40)$$

In which:

- M , C and K are respectively the $[N\text{-by-}N]$ matrices of mass, damping and stiffness;
- $F(t)$ is the $[N\text{-by-}1]$ vector of external forces, that can be seen as the product of the input matrix (B) for the vector of points of application (u), both of them continuous in time. This product takes into account the possibility, which often occurs, that not all of the N dofs of the system are excited, so the $u(t)$ vector of dimension $m < N$, reduces the number of considered nodes, and the presence of an active force over them is indicated by the zero and ones elements matrix B_N of size $[N\text{-by-}m]$.

Defining a state vector $x(t)$, composed by the vectors of displacements and velocities, and the matrices P and Q (Eq. 3.41), it is possible to transform the MDOF system formed by N second-order differential equations into an equivalent set of $n = 2N$ first order differential equations, independent among themselves.

$$x(t) = \begin{bmatrix} q(t) \\ \dot{q}(t) \end{bmatrix}; \quad P = \begin{bmatrix} C & M \\ M & C \end{bmatrix}; \quad Q = \begin{bmatrix} K & 0 \\ 0 & -M \end{bmatrix}; \quad F(t) = B_N(t) \cdot u(t) \quad (3.41)$$

Matrices P and Q , which are *modal matrices*, result orthogonal, as it is seen in Eq. 3.42, so that the property of mass, damping and stiffness are not affected by the transformation produced by the next steps:

$$\Psi^T \cdot P \cdot \Psi = \begin{bmatrix} \ddots & & \\ & a_k & \\ & & \ddots \end{bmatrix}; \quad \Psi^T \cdot Q \cdot \Psi = \begin{bmatrix} \ddots & & \\ & b_k & \\ & & \ddots \end{bmatrix} \quad (3.42)$$

The compact form of Eq. 3.40 after these substitutions is formulated as such:

$$P \cdot \dot{x}(t) + Q \cdot x(t) = \begin{bmatrix} B_N \\ 0 \end{bmatrix} \cdot u(t) \quad (3.43)$$

Applying the classical solution for $q(t)$, as expressed in Eq. 3.9, [17,26] the problem is written as follows:

$$Q \cdot \Psi = -P \cdot \Psi \cdot \Lambda_C \quad (3.44)$$

Λ_C is the matrix of eigenvalues while Ψ is the matrix of eigenvectors (the (*) symbol indicates the *complex conjugate* of the found values).

$$\Lambda_C = \begin{bmatrix} \Lambda & 0 \\ 0 & \Lambda^* \end{bmatrix}, \quad \Psi = \begin{bmatrix} \theta & \theta^* \\ \theta \cdot \Lambda & \theta^* \cdot \Lambda^* \end{bmatrix} \quad (3.45)$$

For which the relation with the vibration modes is expressed as:

$$\Lambda = \begin{bmatrix} \ddots & & \\ & \lambda_k & \\ & & \ddots \end{bmatrix}; \quad \theta = [\cdots \quad \varphi_k \quad \cdots], \quad k = 1 \dots N \quad (3.46)$$

Applying the orthogonality condition also to matrix Λ_C the form is clearly that of a diagonal matrix.

$$\Lambda_C = - \begin{bmatrix} \ddots & & \\ & 1/a_k & \\ & & \ddots \end{bmatrix} \cdot \begin{bmatrix} \ddots & & \\ & b_k & \\ & & \ddots \end{bmatrix} \quad (3.47)$$

3.1.3.1.1 State equation

State-space model is well known system in the field of Civil Engineering, often adopted for the identification of modal parameters in structure where viscous damping approach is assumed.

At the base of the model, where time is assumed as *continuous* (as symbolized by subscripts “C”), it is necessary to define a *state equation* (Eq. 3.48), which can be obtained multiplying both terms of Eq. 3.44 for the inverse matrix P^{-1} :

$$\dot{x}(t) = A_C \cdot x(t) + B_C \cdot u(t) \quad (3.48)$$

- Matrix A_C , of size $[n\text{-by-}n]$ with $n = 2N$, is named *state matrix*, while B_C is the *input matrix*, of size $[n\text{-by-}m]$, which are defined as follows:

$$A_C = -P^{-1} \cdot Q = \begin{bmatrix} 0 & I \\ -M^{-1}K & -M^{-1}C \end{bmatrix} \quad (3.49)$$

$$B_C = P^{-1} \cdot \begin{bmatrix} B_N \\ 0 \end{bmatrix} = \begin{bmatrix} 0 \\ M^{-1}B_N \end{bmatrix}$$

- $x(t)$ is the *state vector* with dimensions n .

The relation between A_C and matrices Λ_C and Ψ is expressed in Eq. 3.50 and, due to the equality with the results of Eq. 3.44, it emerges that it is possible to extract every modal characteristic regarding a system from matrix A_C :

$$A_C = -P^{-1} \cdot Q = -\Psi \cdot \text{diag}[1/a_k] \cdot \Psi^{-T} \cdot \Psi^T \cdot \text{diag}[b_k] \cdot \Psi^{-1} \quad (3.50)$$

$$A_C = \Psi \cdot \Lambda_C \cdot \Psi^{-1} \leftrightarrow A_C \cdot \Psi = \Psi \cdot \Lambda_C$$

3.1.3.1.2 Observation equation

In operational conditions, it results impossible to directly measure the responses of every dof of the structure, so it is common practice to acquire data regarding l points (with $l < n$), and then assume these points as reference for the analysis. In regard of state-space formulation this means that a second equation is required in order to correlate the output of the generalized N -DOFs system with the measured values coming from data collection.

This second equation, expressed in Eq. 3.51, is usually called *observation equation*:

$$y(t) = C_a \ddot{q}(t) + C_v \dot{q}(t) + C_d q(t) \quad (3.51)$$

Where:

- $y(t)$ is the measurement vector with dimensions l ;
- C_a, C_v, C_d are respectively the output location matrices (of size $[l\text{-by-}N]$) for accelerations, velocities and displacements; these matrices, whose role is to map the instrumented DOFs, are composed by zeros or ones elements;

From Eq. 3.40, remembering the definition of the state vector $x(t)$, observation equation can be written in its compact form as:

$$y(t) = C_c \cdot x(t) + D_c \cdot u(t) \quad (3.52)$$

Where the $[1\text{-by-}n]$ output matrix C_c and the $[1\text{-by-}m]$ direct transmission matrix D_c are:

$$\begin{aligned} C_c &= [C_d - C_a M^{-1} K \quad C_v - C_a M^{-1} C_N] \\ D_c &= C_a M^{-1} B_N \end{aligned} \quad (3.53)$$

3.1.3.1.3 State-Space Model

Once the state-space equation (Eq. 3.48) and observability equation (Eq. 3.52) are defined, it is possible to elaborate the State-Space model, described by Eq. 3.54. From this model it is possible to correlate the response $y(t)$ of a system when subdued to a deterministic excitation $u(t)$. From the previous considerations it is highlighted the importance of the state matrix A_C , containing all the modal information, and of the state vector $x(t)$, from which the model order is established as twice the number of DOFs of the considered system.

$$\dot{x}(t) = A_C \cdot x(t) + B_C \cdot u(t)$$

$$y(t) = C_c \cdot x(t) + D_c \cdot u(t) \quad (3.54)$$

3.1.3.2 Discrete-time state-space model

Experimental campaigns consist in storage of data in operational conditions, using different transducers, which acquire analog signal, that are then converted in digital ones through A/D converters in order to be stored and analyzed by calculators. Due to the working modalities of the instrumentation, it is obvious that the continuous time hypothesis, assumed up till now, needs to be substituted considering time as discrete, in order for the model to better fit the nature of the data.

The continuous time function $x(t)$, $y(t)$ and $u(t)$ of Eq. 3.54 are so replaced by series of values x_k , y_k and u_k , which are defined in the discrete time instant $k\Delta t$, with $k \in \mathbb{N}$ and Δt is the adopted sampling interval: $x_k = x(k \cdot \Delta t)$.

Discrete-time state-space model is represented by the following equation:

$$\begin{aligned} x_{k+1} &= Ax_k + Bu_k \\ y_k &= Cx_k + Du_k \end{aligned} \quad (3.55)$$

Because of *Zero Order Hold assumption* (ZOH) [27], which impose constant values of two consecutive discrete time interval, the continuous-time model matrices A_c , B_c , C_c , D_c are related with their owns discrete-time matrices A , B , C , D by the Eq. 3.56:

$$\begin{aligned} A &= e^{A_c \Delta t} & B &= \int_0^{\Delta t} e^{A_c \tau} d\tau B_c \\ C &= C_c & D &= D_c \end{aligned} \quad (3.56)$$

Applying McLaurin decomposition over the second term of A definition in Eq. 3.56, the relation with the continuous time matrix A_c can be expressed as follows:

$$A = e^{A_c \Delta t} = I + (A_c \cdot \Delta t) + \frac{(A_c \cdot \Delta t)^2}{2!} + \frac{(A_c \cdot \Delta t)^3}{3!} + \dots \quad (3.57)$$

and substituting the eigenvalues decomposition of Eq. 3.50, it is evident that eigenvectors of matrix A are equal to the eigenvectors of matrix A_c (Eq. 3.58):

$$\begin{aligned} A_c &= \Psi \cdot \Lambda_c \cdot \Psi^{-1} \\ A &= e^{A_c \Delta t} = e^{\Psi \cdot \Lambda_c \cdot \Psi^{-1} \cdot \Delta t} = \Psi \cdot e^{\Lambda_c \Delta t} \cdot \Psi^{-1} = \Psi \cdot \Lambda_c \cdot \Psi^{-1} \end{aligned} \quad (3.58)$$

Being the matrix Λ_D composed by the eigenvalues of the *state matrix* A (Eq. 3.59).

$$\Lambda_D = \begin{bmatrix} \ddots & & \\ & \mu_k & \\ & & \ddots \end{bmatrix}; \mu_k = e^{\lambda_k \Delta t} \leftrightarrow \lambda_k = \frac{\ln(\mu_k)}{\Delta t} \quad (3.59)$$

3.1.3.3 Stochastic processes

In the context of Operational Modal Analysis, the assumption of known input excitation often decays, so it becomes impossible to express them in deterministic form, and it is necessary to apply a stochastic process, which also allows to consider the effects of noise into the model.

Considering a certain variable, time dependent, which assumes different values during a process at different time instant t , a stochastic process allows to describe the variable through a set of n (with $n \rightarrow \infty$) random time dependent functions which are designed on the basis of the different realizations of the given variable during the observation process.

In practical applications [28], stochastic processes are considered:

- *stationary*, the statistical properties staying constant during time;
- *zero-mean*, being the average values of the residuals equal to zero, thanks to the de-trending process raw data are subdued; this property involves that in operational modal analysis application covariance functions and correlation functions coincide;
- *ergodic*, because the statistical averages of the properties of the measured signals converge practically everywhere with the temporal averages. *Stationarity* becomes a necessary condition for ergodicity. This property A necessary condition for ergodicity is therefore stationarity. *Ergodicity* can also be a property of correlation when there is convergence between the temporal and statistical *autocorrelation* function.

The *autocorrelation* function furnishes a measure of the similarity between the original signal with its time-shifted version, so it provides the correlation of the time signal with its past and future values. When *stationarity* of the process is considered, the *autocorrelation* is only linked with the time-lag and practically gives information of the rapidity of the evolution of the process in time.

The *correlation matrix* stochastic process $y(t)$ with n_y components, under the assumption of continuous time, can be expresses as:

$$E_{yy}(\tau) = E[y(t)(t + \tau)^T] = \lim_{T \rightarrow \infty} \frac{1}{T} \int_{-T/2}^{+T/2} y(t)(t + \tau)^T dt \quad (3.60)$$

where $E_{yy}(\tau)$ is a $[n_y\text{-by-}n_y]$ square matrix depending on considered time-lag (τ) and with *autocorrelation* or *cross-correlation* values as elements in the diagonal

Transferring the signal in discrete time, the *correlation* function is only defined for $t \geq 0$, and the Eq. 3.60 takes the form:

$$E_{yy}(\tau) = E[y_k \cdot y_{k+\tau}^T] = \lim_{n_t \rightarrow \infty} \frac{1}{n_t} \int_{t=0}^{n_t-1} y_k \cdot y_{k+\tau}^T \quad (3.61)$$

where:

- $E[\bullet]$ is the expected value of correlation for the $y(t)$ time history, which converge to the average value for $t \rightarrow \infty$;
- y_k is the value of $y(t)$ at the time instant $k \cdot \Delta t$.

A particular characteristic of the *autocorrelation* function is its natural tendence to zero value in relation to the irregularity of the time series involved, where to a higher level of irregularity corresponds a faster decay. *Autocorrelation* functions for zero mean stationary stochastic processes are symmetrical functions with maximum value equal to the standard deviation of the process and centered in the origin ($\tau = 0$).

Cross-correlation function, instead, provides the information about the level of correlation between two different time signals $y(t)$ and $x(t)$ (the limit in Eq. 3.62 is necessary because in real application the number of samples is limited):

$$E_{yx}(\tau) = E[y_k \cdot x_{k+\tau}^T] = \lim_{n_t \rightarrow \infty} \frac{1}{n_t} \int_{t=0}^{n_t-1} y_k \cdot x_{k+\tau}^T \quad (3.62)$$

3.1.3.4 Stochastic discrete-time state-space model

Due to the presence of noise in data acquisition, and due to the impossibility of deterministically measure this agent, it become necessary to consider this stochastic component in the discrete-time state-space model. Practically two vectors w_k and v_k , representing noise, are added to the Eq. 3.55, so the model is written as follows:

$$\begin{aligned} x_{k+1} &= Ax_k + Bu_k + w_k \\ y_k &= Cx_k + Du_k + v_k \end{aligned} \quad (3.63)$$

Both of the added components are assumed to be *zero-mean*, implying the following properties for the covariance matrices, calculated for two arbitrary time instants p and q :

$$\begin{pmatrix} w_p \\ v_p \end{pmatrix} \begin{pmatrix} w_p^T & v_p^T \end{pmatrix} = \begin{bmatrix} Q & S \\ R & S^T \end{bmatrix} \quad (3.64)$$

$$E \left(\begin{bmatrix} w_p \\ v_p \end{bmatrix} \begin{bmatrix} w_q^T & v_q^T \end{bmatrix} \right) = 0 \quad p \neq q$$

Correlation matrices associated to the vectors w_k and v_k are assumed to be equal to zero, for every time instant $\tau = q - p \neq 0$. So this means that every new observation is not linked to the previous one. Random stochastic process like this is defined *white noise*.

Another important aspect of the stochastic process is that, during experimental tests, the excitation working over the structure is non deterministically measured, and so the discrete vector u_k cannot be known. From here a very strong hypothesis is made, which consists in including the unknown action into the white noise term, approximating the stochastic discrete-time state-space model as in Eq. 3.65:

$$\begin{aligned} x_{k+1} &= Ax_k + w_k \\ y_k &= Cx_k + v_k \end{aligned} \tag{3.65}$$

A necessary clarification regarding white noise assumption should be made: without this hypothesis, when the input excitation contains some dominant frequency components, these values will be identified as poles of the state matrix A and it will result indistinguishable in respect to the effective natural frequencies of the system.

3.1.4 Auto-spectra and cross-spectra functions

The hypothesis of *zero-mean* value and *normal distribution* of the input excitation, at the basis of stochastic process theory, is a property that very commonly manifests itself in different natural phenomena and also finds confirmation also in the *Central Limit Theorem*, asserting the tendency to the Gaussian distribution of the sum of high number of independent random variables with independent distribution. Adding the *stationarity* and *ergodicity* conditions assures the dependency of the *autocorrelation* function only from the time interval $\tau = t_j - t_i$, but its independence from the time instants t_i and t_j . So, *auto-correlation* function is defined as:

$$R_{xx}(\tau) = \lim_{T \rightarrow \infty} \frac{1}{T} \int_{-T/2}^{+T/2} x_e(t) \cdot x_e(t + \tau) dt \tag{3.66}$$

where $x_e(t)$ is a realization of the stochastic process depending only on time-lag.

Transposition of the *autocorrelation* function in the frequency domain, by mean of the *Fourier Transform*, produces the so-called *auto-spectrum* function, which quantifies how the energy content of the signal, expressed in frequency terms, is distributed :

$$S_{xx}(\omega) = \int_{-\infty}^{+\infty} R_{xx}(\tau) \cdot e^{-i\omega\tau} d\tau \quad (3.67)$$

In particular, in case of *white noise*, the energy value coincides with the variance.

Same considerations are valid in the definition of the *cross-correlation* (Eq. 3.68) and the *cross-spectrum* functions (or *cross-spectral density* function) (Eq. 3.69):

$$R_{x_1x_2}(\tau) = \lim_{T \rightarrow \infty} \frac{1}{T} \int_{-T/2}^{+T/2} x_{1e}(t) \cdot x_{2e}(t + \tau) dt \quad (3.68)$$

$$S_{x_1x_2}(\omega) = \int_{-\infty}^{+\infty} R_{x_1x_2}(\tau) \cdot e^{-i\omega\tau} d\tau \quad (3.69)$$

It is worth to mention that the auto-spectrums are function with real components coming from the product between a complex number and its *complex conjugate*. The *cross-spectrums*, on the contrary, are complex functions.

Considering a vector $y(t)$ containing various stationary stochastic processes, the *correlation matrix* can be defined by the follows:

$$R_y(\tau) = E[y(t)y(t + \tau)^T] = \lim_{T \rightarrow \infty} \frac{1}{T} \int_{-T/2}^{+T/2} y(t) y(t + \tau)^T dt \quad (3.70)$$

That, under the assumption of white noise as input excitation source can be written as:

$$R_y(\tau) = R_y \cdot \delta(\tau) \quad (3.71)$$

in which R_y in a $[n_i\text{-by-}n_i]$ constant matrix and $\delta(r)$ is the *Dirac Delta Function* characterized by the following properties:

$$\delta(\tau) = 0 \text{ if } t = 0$$

$$\delta(\tau) = 0 \text{ elsewhere} \quad (3.72)$$

$$\int_{-\infty}^{+\infty} f(t) \cdot \delta(t - a) \cdot dt = f(a)$$

This property of the $\delta(r)$ function implies the input spectrum is a constant matrix equal to R_y and subsequently the energy of input signal results distributed with uniformity along the frequency axis. The concept previously described is summarized in Eq.3.73, which links the spectrum of input response S_{uu} and the output one S_{yy} .

$$S_{yy}(\omega) = H(\omega) \cdot S_{uu}(\omega) \cdot H^H(\omega) \quad (3.73)$$

The system *transfer function* $H(\omega)$ and the constant matrix becomes the only variable influencing the output spectrum of a *white noise* input process (Eq. 3.74):

$$S_{yy}(\omega) = H(\omega) \cdot R_p(\omega) \cdot H^H(\omega) \quad (3.74)$$

Moreover, if the *cross-correlation* are zero, which means the statistic independence between the input signals, the constant matrix becomes a diagonal matrix and so the contribution provided by a general k -mode on any elements of the output spectrum results from the following expression (Eq. 3.75):

$$S_{q(i,j)}^k(\omega) = \sum_{k=1}^N \frac{[\varphi_i]_k \cdot [\varphi_j]_k}{\omega_k^2 - \omega^2 + 2 \cdot i \cdot \xi_k \cdot \omega \cdot \omega_k} \cdot R_p \cdot \frac{[\varphi_i]_k \cdot [\varphi_j]_k}{\omega_k^2 - \omega^2 + 2 \cdot i \cdot \xi_k \cdot \omega \cdot \omega_k} \quad (3.75)$$

In [26] it was introduced the formulation of Eq. 3.76 which links the output spectral matrix, written as a superposition of the structural modes, and the vector g_k , called *operational reference vector*, which depends on all modal parameters, the input location and the input correlation matrix:

$$S_{yy}(\omega) = \sum_{k=1}^N \frac{\varphi_k \cdot g_k^T}{i\omega - \lambda_k} + \frac{\varphi_k^* \cdot g_k^H}{i\omega - \lambda_k} + \frac{g_k^* \cdot \varphi_k^T}{-i\omega - \lambda_k^*} + \frac{g_k \cdot \varphi_k^H}{-i\omega - \lambda_k^*} \quad (3.76)$$

Decomposing the output spectrum can produce four different poles ($\lambda_k, -\lambda_k, \lambda_k^*$ and $-\lambda_k^*$) for every structural mode. A solution to this problem consists in the use of the *Positive* or *Half-Spectrum function*, resulting from the limitation of the *Discrete Fourier Transfer* (DFT) function only to positive time-lags, when applied to correlation matrix:

$$S_{yy}^+(\omega_j) = \frac{R_{yy}(0)}{2} + \sum_{k=1}^j R_{yy}(k \cdot \Delta t) \cdot e^{-i\omega_j k \Delta t} \quad (3.77)$$

Similarly to the case of the FRF or the transfer function, even the Positive Spectrum can be subdued to modal decomposition [29], assuming the following structure:

$$S_{yy}^+(\omega) = \sum_{k=1}^N \frac{\varphi_k \cdot g_k^T}{i\omega - \lambda_k} + \frac{\varphi_k^* \cdot g_k^H}{i\omega - \lambda_k} \quad (3.78)$$

3.2 Output-only modal identification techniques

Identification of modal parameters, as already stated, can be performed in accordance with two different approaches: the first, known as EMA, where the excitation causing the measured structural

response is known, and the second, known as OMA, where it is hypothesized that the unknown excitation is assimilable with white noise, allowing all the simplification previously exposed.

In particular, taking into account that usually the measured vibrations during experimental campaigns are provoked by environmental agents (wind, temperature variations, earthquakes...) or anthropogenic activities (like traffic, ...) which can be assumed as white noise process, and due to the advantages OMA instrumentation offers in terms of economy and practicality of use, the output-only techniques is usually preferred.

In the following paragraphs the output-only methodologies [25,28,30–36] used in the study of the structures presented in this thesis, developed both in frequency domain (based on the spectral estimation of the structural response) than time domain (based on the correlations or on the projections of the collected output responses), will be explained.

3.2.1 Identification methods developed in the frequency domain

3.2.1.1 *Peak Picking method*

Peak Picking (PP) method is the first among modal identification technique for characterization of civil structures. It is a methodology developed in frequency domain, whose theoretical basis was introduced for the first time in [25] and then implemented for practical applications [37], confirming the effectiveness of ambient vibration test in the study of dynamical behavior of civil structures [38].

Two conditions are at the basis of a successful identification of the modal parameters recurring to PP method:

- structural modes associated to well-separated natural frequencies;
- slightly damping of modes;

The estimation process practically consists of a visual inspection of the magnitude of the power spectrum of the process, plotted over a magnitude vs. frequency chart. So, when structural modes frequencies are close, the method is not able to distinguish between the contributions of different modes [25].

3.2.1.1.1 Identification of the natural frequencies

The construction of the spectral matrix of a MDOF system excited by *white noise* requires the knowledge of the FRF matrix, standing Eq. 3.79:

$$S_q(\omega) = H(\omega) \cdot R_p \cdot H^H(\omega) \quad (3.79)$$

When damping is low, the corresponding natural frequencies are well approximated by the damped resonant frequencies of the system, found in correspondence of maxima of the FRF matrix.

Due to the nature of *white noise* processes, it is quite clear that it is possible to extract natural frequencies from the analysis of the *auto-spectra* function (or *power spectral density* function), defined in Eq. 3.80:

$$PSD_i(\omega_k) = \sum_{k=1}^N PSD_i(\omega_k) \quad (3.80)$$

In particular, in order to assure the identification of all natural frequencies during dynamic tests, in [37] it is suggested the use of the *averaged normalized power spectrum density* (ANPSD) of all measurement points, as expressed in Eq. 3.81:

$$ANSPD(\omega) = \frac{1}{l} \sum_{i=1}^l NPSD_i(\omega) = \frac{1}{l} \sum_{i=1}^l \left[\frac{PSD_i(\omega)}{\sum_{i=1}^N PSD_i(\omega)} \right] \quad (3.81)$$

in which l is the number of instrumented DOFs and $NPSD_i$ are the normalized spectrum associated to each DOF obtained by Eq. 3.80. In fact, averaging the elements in the of the *spectrum matrix* $S^+(\omega)$, as suggested, eliminate the risk of not identifying all of the resonant frequencies, in case of the presence of a reference DOF on one of the nodes of a vibration mode, condition which does not allow mode identification.

3.2.1.1.2 Identification of vibration modes

In case of well-separated natural frequencies and low damping values, the diagonal elements of FRF matrix, formulated in modal domain (Eq. 3.82), in proximity of resonant frequencies are characterized by high values.

$$H(\omega) = \Phi \cdot H_\eta(\omega) \cdot \Phi^T = \sum_{k=1}^N H_{\eta k} \cdot \varphi_k \cdot \varphi_k^T \quad (3.82)$$

$$H_\eta(\omega) = \text{diag} \left[\frac{1}{\omega_k^2 - \omega^2 + 2 \cdot i \cdot \xi_k \cdot \omega \cdot \omega_k} \right]$$

Consequently, near a natural frequency ω_k , k -th element of H_η , can be approximated to the contribute given by the corresponding k -th mode as expressed in Eq. 3.83:

$$H_\eta(\omega) = \varphi_k \cdot \frac{1}{\omega_k^2 - \omega^2 + 2 \cdot i \cdot \xi_k \cdot \omega \cdot \omega_k} \cdot \varphi_k^T = \varphi_k \cdot c_1 \cdot \varphi_k^T \quad (3.83)$$

So, this element of the FRFs matrix is scalar complex value c_1 which is function of the natural frequency, damping and mode shape. Taking Eq. 3.79 and considering Eq. 3.83, it is possible to write the spectrum as follows:

$$S_y(\omega_k) = \varphi_k \cdot c_1 \cdot \varphi_k^T \cdot R_u \cdot \varphi_k \cdot c_1^* \cdot \varphi_k^T = c_1 \cdot c_1^* \cdot \varphi_k \cdot c_2 \cdot \varphi_k^T \quad (3.84)$$

with the complex $c_2 = \varphi_k^T \cdot R_u \cdot \varphi_k$. Compacting the coefficients, Eq. 3.84 becomes:

$$S_y(\omega_k) = c_3 \cdot \varphi_k \cdot \varphi_k^T \quad (3.85)$$

which highlights the mutuality for a given frequency ω_k between the columns of the *spectral matrix* and the configuration of the mode associated to ω_k .

This means that for a reference DOF the property of Eq. 3.86 is valid:

$$S_y(\omega_k)_{(ref,ref)} = c \cdot (\varphi_{ref})_k \cdot (\varphi_{ref})_k^T \quad (3.86)$$

and the same can be applied also to the other components:

$$S_y(\omega_k)_{(j,ref)} = c \cdot (\varphi_j)_k \cdot (\varphi_{ref})_k^T \quad (3.87)$$

At least the ratio between the previous expression is calculated (Eq. 3.88), producing a complex number which allows the calculation (in instrumented DOFs) of the components of the structural modes, corresponding to a frequency ω_k , through the use of just two sensors.

$$T_{j,ref} = \frac{S_y(\omega_k)_{(j,ref)}}{S_y(\omega_k)_{(ref,ref)}} = \frac{(\varphi_j)_k}{(\varphi_{ref})_k} \quad (3.88)$$

Because of the complex nature of the *cross-spectrum*, it is possible to establish, from the value of the phase, if the *i-th* and *ref-th* move in the same or in the opposite direction, where the first condition manifests for phase equal to 0° , while the second for phase equal to 180° .

3.2.1.2 Frequency Domain Decomposition method

As already mentioned in the previous paragraphs, an identification process based on Peak Picking method can incur in some limitations:

- difficulty in the detection of the spectrum peaks;
- separation of closely spaced modes;
- the estimation of the modal damping ratio with higher accuracy.

In order to overcome these problems, in a new method, called *Frequency Domain Decomposition* (FDD) [32,39], then improved in [16]. The method assimilated the concept of *Modal Domain*,

producing a strong improvement to other already effective techniques, proposed in the past for the analysis of dynamic behavior of structures subjected to environmental inputs and the modal parameters extraction from FRF through *Complex Mode Indication Function* (CMIF) [40].

The FDD method consists of a frequency domain non-parametric technique operating through the factorization of the output spectrum matrices constructed with the *Welch method* [41]welch and practically it identifies, for each frequency, the single contribution given by the vibration modes associated to the spectral amplitude for that given frequency.

As already stated in the previous chapter regarding modal analysis, the general response $y(t)$ of an excited structure can be seen as the superposition of n vibration modes (each one with its mode shape ϕ_i), where η_i designates the modal coordinate:

$$y(t) = \phi_1\eta_1(t) + \phi_2\eta_2(t) + \dots + \phi_n\eta_n(t) = [\Phi]\{\eta(t)\} \quad (3.89)$$

After computing the *correlation* function $R_{\eta\eta}(\tau)$ according to Eq. 3.90, in which it is expressed in its modal coordinate in time domain, the *Spectral matrix* $S_{yy}(\omega)$ is calculated through the FFT of the response $y(t)$ (Eq. 3.91):

$$R_{\eta\eta}^+(\tau) = E[q(t+\tau)]q(t)^T = E[\Phi\eta(t+\tau)]\eta(t)^T\Phi^T = [\Phi]S_{\eta\eta}^+(t)[\Phi]^T \quad (3.90)$$

$$S_{yy}(\omega) = [\Phi]S_{\eta\eta}(\omega)[\Phi]^H \quad (3.91)$$

Thanks to the orthogonality property of the *modal matrix* Φ (and subsequently of the mode shapes contained in it) and to the assumption of *white noise* excitation, the modal coordinates are uncorrelated and the *power spectral density* matrix $S_{yy}(\omega)$ results diagonal, allowing the factorization through *Singular Value Decomposition* (SVD) [26,32].

3.2.1.2.1 Singular Value Decomposition

Singular Value Decomposition (SVD) is an algorithm allowing the decomposition of a generic matrix $A \in \mathbb{C}^{n \times m}$ (with $n > m$) as product of three matrices as follows:

$$A = [U][S][V]^H \quad \text{with} \quad S = \begin{bmatrix} S_1 \\ 0 \end{bmatrix} \quad (3.92)$$

where:

- $U \in \mathbb{C}^{n \times n}$ and $V \in \mathbb{C}^{m \times m}$ are matrices containing the right and left singular vectors of matrix A ; in particular, the columns of U contain the eigenvectors of $A^T A$, while in V are contained the eigenvectors of AA^T ;

- $S \in \mathbb{C}^{n \times m}$ is a rectangular matrix, from where the diagonal matrix $S_1 \in \mathbb{C}^{n \times n}$ can be extracted; into S_1 non-null singular values, defining the rank of matrix A and so the number of linearly non-dependent rows and columns, are positioned in decreasing order.

Standing the hypothesis posed in [39]:

- excitation constitutes by white noise;
- orthogonality between mode shapes;
- lightly damping of the structure

it is possible to apply FFD method starting from the estimation of the *half positive spectral* matrix (Eq. 3.93), based on the measured data; executing the SVD on the $S_{yy}^+(\omega)$ matrix, allows to decompose the *spectral* matrix as a combination of *auto-spectral density* functions, each one associated to an SDOF. Consequently, the first singular value ordinate is the *auto-spectrum* of the dominant mode for the considered frequency. The other SVs result negligible, and all the k dominant modes can be detected through the peak of the first SV.

$$S_{yy}^+(\omega) = [U(\omega)] \cdot [S_n] \cdot [U(\omega)] \quad (3.93)$$

In case of modes associated to well-separated frequencies, the most important *auto-spectra* segments will be located near the resonant frequencies, while the plots of other SVs will not show significant peaks. In case of near modes, instead, there will be more SVs presenting well visible peaks in proximity of the resonant frequencies.

After definition of a natural frequency, the first singular vector u_1 , coming from matrix U , defines the mode shape of the dominant mode (Eq. 3.94), while it is possible to neglect the contributions given by other modes.

$$\hat{\phi} = u_1 \quad (3.94)$$

3.2.1.3 Enhanced Frequency Domain Decomposition method

Enhanced Frequency Domain Decomposition (EFDD) is an identification technique specially designed in order to surpass the limitation of FDD linked to the estimation of damping, proposed by [32,42]. Even if the main purpose of the method development was to increase the accuracy in damping ratio evaluation, also the confidence in natural frequency estimation improved, thanks to the definition of an interval frequency range where the frequency peaks associated to the first singular value results dominant.

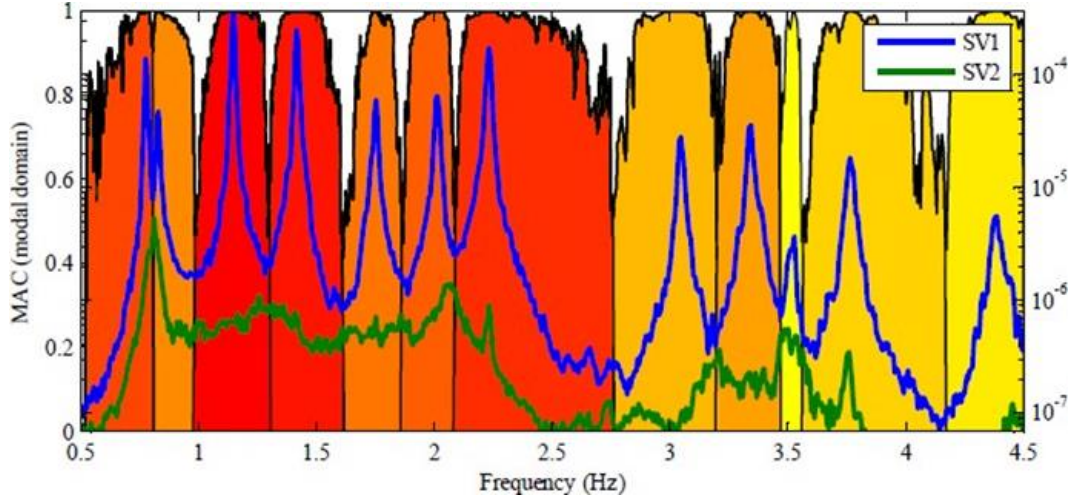


Fig. 3-2 - Typical modal domains associated to structural modes [43]

Once a resonant peak is detected, its modal domain is defined through the *auto-spectral density* of the correspondent SDOF system in the domain. Then *Modal Assurance Criterion* (MAC) [44,45] is adopted as index (Eq. 3.95) in order to evaluate the consistency of the singular vectors of the values around the peak and the mode shape of the resonant peak itself.

$$MAC = \frac{(\phi_1^T \cdot \phi_2)^2}{(\phi_1^T \cdot \phi_1)(\phi_2^T \cdot \phi_2)} \quad (3.95)$$

The MAC index, which variates between 0 and 1, furnishes an evaluation of consistency between two mode shapes, where the value 0 indicates orthogonality between the tested mode shapes, while 1 indicates perfect similarity between two mode shapes, which differ only for a scale factor.

When MAC, calculated between the mode shape of the resonant peak and the other test vectors, is close to unity, all these tested points can be included into the *modal domain*. In order to not discard mode, having very high correspondence with the resonant mode shape but not equal to 1, a threshold of the MAC values should be fixed [32].

After the modal domain definition, mode shape estimation is executed through averaging of the singular vector present into the domain. Applying the reverse FFT function to reconvert the selected given modes to time domain, allows to extract damping ratios from the *auto-correlation* functions calculated for a structure composed of a set of SDOF systems.

In fact, the *auto-correlation* function of a SDOF system excited by *white noise* is proportional to its impulse response, defined as [24]:

$$h(t) = ce^{-\xi_k \omega_k t} \sin(\omega_k t) \quad (3.96)$$

where c is a constant and ξ_k and ω_k represent respectively the damping ratio and the circular frequency.

3.2.2 Identification techniques implemented in the time domain

After the description of the identification techniques developed in frequency domain, in the next paragraphs the most popular time domain identification technique will be presented: the *Stochastic Subspace Identification* (SSI) method [26,28,33]. Two algorithms, based on this method, will be analyzed, both operating under the assumption of discrete-time state-space representation: are parametric identification techniques developed in the time domain: the *Covariance-driven* SSI (SSI-Cov), as described in [33] based on the construction of the correlation matrix, and the *Data-driven* SSI (SSI-Data) introduced in [28] based on the projection of the recorded response time series.

3.2.2.1 Covariance-driven Stochastic Subspace Identification method

The SSI-Cov method is a parametric technique, operating in time domain, which operates the dynamic identification adopting the *state-space* model to fit the behavior of the investigated structure, under the hypothesis of *white noise* excitation and linear time-invariant property of the representing system. This task is performed estimating the *system matrix* A , the *output matrix* C and the *model order* n from the output responses [33], as also described in the practical application reported in [46].

Because the dynamic tests are quite often performed in “multi-setups” configuration, the responses on acquired for the instrumented DOFs are measured with different times. Moreover, some DOFs remains constant for the different acquisitions, and are the so-called *reference channels* (in number pair to l), while r other positions are variable. The choice of the *reference sensors* is very important and must be evaluated, before the installation, on the basis of the level of redundance of information provided by the sensors themselves: sensors located in positions which results symmetrical to the nodes of an expected mode tend to produce the same information in terms of frequencies and damping ratios to those extracted from sensors posed on the nodes of a mode; in these cases it is possible to not use these acquisition in the building of *correlation* matrices, in order to decrease the computational weight.

So, during acquisitions, for each instant k , a column vector y_k^{ref} of the accelerations registered for l reference DOFs, and a column vector y_k of the responses for the r instrumented DOFs needs to be defined. Then it is possible to proceed with the definition of the *covariance* matrix of output $y(t)$:

$$E \left[y_{k+i} \cdot y_k^{refT} \right] \quad (3.97)$$

Eq. 3.98 display the *Toeplitz* matrix, which is composed of $[n_{0i}\text{-by-}n_{ri}]$ blocks, where n_0 is the number of the selected outputs and n_r corresponds to all channels:

$$T_{1|i}^{ref} = \begin{bmatrix} R_i^{ref} & R_{i-1}^{ref} & \cdots & R_1^{ref} \\ R_{i+1}^{ref} & R_i^{ref} & \cdots & R_2^{ref} \\ \vdots & \vdots & \ddots & \vdots \\ R_{2i-1}^{ref} & R_{2i-2}^{ref} & \cdots & R_i^{ref} \end{bmatrix} \quad (3.98)$$

Each block is formed of the correlation functions, associated to positive time-lags whose values variate from $l\Delta t$ to $(2i - l)\Delta t$, and represented by R_1^{ref} to R_{2i-1}^{ref} .

Through factorization, which can be executed recurring to the SVD algorithm (Eq. 3.99)

$$T_i = U \cdot S \cdot V^T = [U_1 \quad U_2] \cdot \begin{bmatrix} S_1 & 0 \\ 0 & 0 \end{bmatrix} \cdot \begin{bmatrix} V_1^T \\ V_2^T \end{bmatrix} = U_1 \cdot S_1 \cdot V_1^T \quad (3.99)$$

the *Toeplitz* matrix (Eq. 3.98) is written as:

$$T_{1|i}^{ref} = \begin{bmatrix} CA^{i-1}G^{ref} & CA^{i-2}G^{ref} & \cdots & CA^0G^{ref} \\ CA^iG^{ref} & CA^{i-1}G^{ref} & \cdots & CA^1G^{ref} \\ \vdots & \vdots & \ddots & \vdots \\ CA^{2i-2}G^{ref} & CA^{2i-3}G^{ref} & \cdots & CA^{i-1}G^{ref} \end{bmatrix} \quad (3.100)$$

but the single block alone is not sufficient to solve the identification problem. Due to the redundance of system $T_{1|i}^{ref}$, but being the single block not enough for the resolution of the identification problem, the *Toeplitz* matrix is decomposed as follows:

$$T_i = \begin{bmatrix} C \\ C \cdot A \\ \vdots \\ C \cdot A^{i-1} \end{bmatrix} \cdot [A^{i-1} \cdot G^{ref} \quad \cdots \quad A \cdot G^{ref} \quad G^{ref}] = O_i \cdot \Gamma_i^{ref} \quad (3.101)$$

in which:

- O_i is the *observability* matrix, formed by a column of i blocks with $[n_0\text{-by-}n_r]$ size;
- Γ_i^{ref} is the *controllability* matrix, composed by a row of i blocks with $[n_0\text{-by-}n_r]$ size.

Comparison between Eq. 3.99 and Eq. 3.102 highlights the possibility to deduce the *observability* and the *controllability* matrices splitting the outputs of the SVD into two parts:

$$\begin{aligned} O_i &= U_1 \cdot S_1^{1/2} \\ \Gamma_i &= S_1^{1/2} \cdot V_1^T \end{aligned} \quad (3.102)$$

The expressions of Eq. 3.102 leads to the extraction of matrix C , obtainable from the first n_0 lines of the *observability* matrix O_i , and matrix A , which derives from resolving the least squares problem expressed in Eq. 3.103, Eq. 3.104 and Eq. 3.105:

$$\begin{bmatrix} C \\ C \cdot A \\ \vdots \\ C \cdot A^{i-2} \end{bmatrix} \cdot A = \begin{bmatrix} C \cdot A \\ C \cdot A^2 \\ \vdots \\ C \cdot A^{i-1} \end{bmatrix} \leftrightarrow \bar{O} \cdot A = \underline{Q} \quad (3.103)$$

$$A = \begin{bmatrix} C \\ C \cdot A \\ \vdots \\ C \cdot A^{i-2} \end{bmatrix}^\dagger \cdot \begin{bmatrix} C \cdot A \\ C \cdot A^2 \\ \vdots \\ C \cdot A^{i-1} \end{bmatrix} \leftrightarrow A = \bar{O}^\dagger \cdot \underline{Q} \quad (3.104)$$

$$\text{where } \bar{O} = \begin{bmatrix} C \\ C \cdot A \\ \vdots \\ C \cdot A^{i-2} \end{bmatrix}, \quad \underline{Q} = \begin{bmatrix} C \cdot A \\ C \cdot A^2 \\ \vdots \\ C \cdot A^{i-1} \end{bmatrix} \quad (3.105)$$

Where:

- \bar{O} contains the first $l \cdot (i - 1)$ lines of O_i ;
- \underline{Q} contains the last $l \cdot (i - 1)$ lines of O_i ;
- the symbol $(\bullet)^\dagger$ represents the Moore-Penrose pseudo-inverse operational function.

Subsequently, the modal parameters can be extracted with easiness from matrices A and C , performing the eigenvalue decomposition of the obtained system matrix A (Eq. 3.106):

$$\lambda_k = \frac{\ln(\mu_k)}{\Delta t} \rightarrow f_k = \frac{|\lambda_k|}{2\pi}; \quad \xi_k = -\frac{Re(\lambda_k)}{|\lambda_k|} \quad (3.106)$$

In conclusion, the mode shapes ϕ_k are calculated as the product of matrix C and the corresponding eigenvectors ψ_k of the matrix A , as shown below:

$$V = C\Psi \leftrightarrow \phi_k = C\psi_k \quad (3.107)$$

Being the solutions of the *state-space model* represented by complex conjugate pairs, only the eigenvectors of matrix A associated to eigenvalues with positive imaginary components are chosen for mode shape extraction. Subsequently, for a state-space model having model order equal to n , a maximum of $n/2$ solutions are possible.

The establishment of a correct *model order* for the state-space is a crucial step of the method. In fact, due the presence of residual values of singular values associated to higher modes, caused by inaccuracy in the measurement process or the manifestation of non-linear effects, and because the SVD of *Toeplitz* matrix does not allow to decide the model order a priori, the most used strategy consists in the building many models, with increasing *model orders* (where the maximum is chosen as

two times the number of expected physical modes) and extract the modal parameters from each model until arriving to the maximum *order*.

The negative effect of this procedure stays in the fact that high *model orders* comport the possible estimation of modes with no physical meaning (called *noise* or *spurious modes*), because caused by the noise content in the acquisitions. To solve this problem, the common practice consists in recurring to a chart, where all the natural frequencies extracted from the various model for all the considered order are reported, in order to be compared: this plot is called *stabilization diagram* (Fig. 3-3).

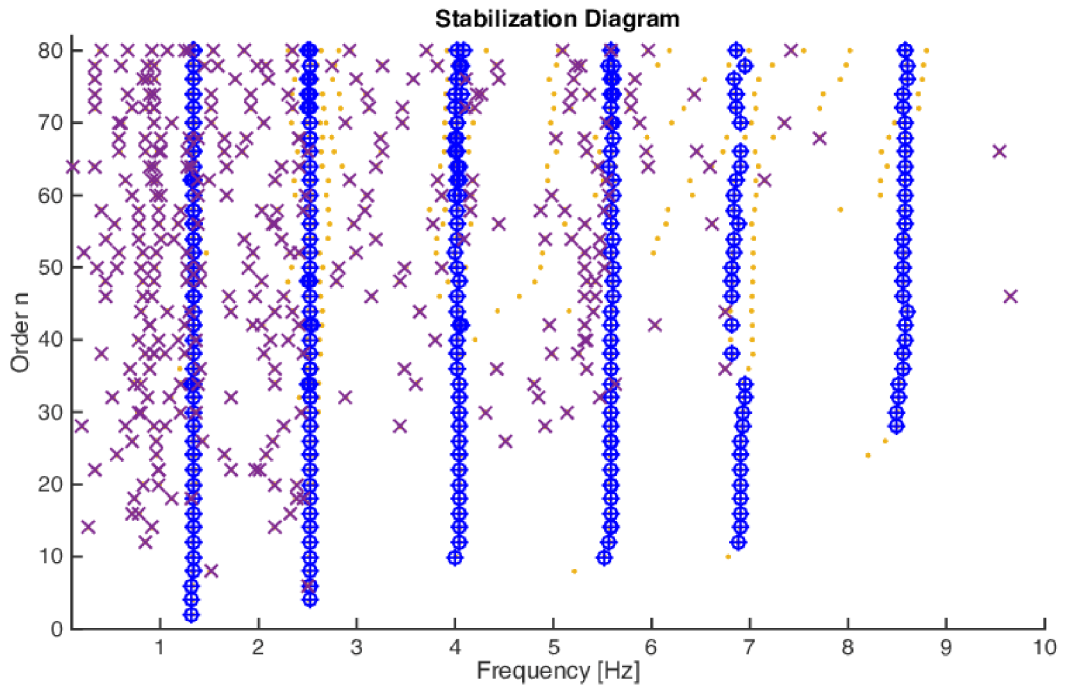


Fig. 3-3 - Example of stabilization diagram to differentiate between stable poles (blue points) and unstable poles (purple crosses)

Inspection of this diagram allows to separate the *stable* modes, recognizable because of the alignment of the poles having consistent parameters, from the *unstable* ones.

3.2.2.2 Data-driven Stochastic Subspace Identification method

The second implementation of SSI method is the *Data-driven Stochastic Subspace Identification* (SSI-Data) method [28,47], which is an algorithm implemented in two different commercial softwares: MACEC [48], a toolbox developed in Matlab© environment by University of Leuven, and ARTeMIS [49], a commercial program implemented by research group in the University of Aalborg.

SSI-Data method estimates the *state-space model* directly from the acquired accelerations time series, substituting the step in which the *covariance* matrix is built, with the projection of the row space of “future” outputs into the row space of “past” outputs, after its reorganization into the *Hankel* matrix.

The algorithm assumes the application of the *non-stationary Kalman Filter* and then develops following the next steps:

1. organization of the collected responses into a *Hankel* matrix;
2. estimation of the *observability* matrix in two consecutive time instants;
3. extraction of the modal parameters after the definition of the *system matrix* A and the *output matrix* C .

3.2.2.2.1 Kalman filter

The *Kalman filter* plays a fundamental role on the development of *SSI-Data* method, but, because of the complexity of the theory regarding this theme, it will be illustrated only examining the main concepts necessary for implementation of the time domain method.

No steady *Kalman filter* is meant to provide an optimal estimation of the state vector \hat{x}_{k+1} applying the expressions of the Eq. 3.108 in an iterative way considering the observation of the outputs (matrix A and C), the statistical properties (G and R_0) up at time instant k , the initial state estimate $\hat{x}_0 = 0$ and the initial covariance of the state estimates $P_0 = E[\hat{x}_k \hat{x}_k^T] = 0$.

$$\begin{aligned}\hat{x}_{k+1} &= A \cdot \hat{x}_k + K_k \cdot (y_k - C \cdot \hat{x}_k) \\ K_k &= (G - A \cdot P_k \cdot C^T) \cdot (R_0 - C \cdot P_k \cdot C^T)^{-1}\end{aligned}\tag{3.108}$$

$$P_{k+1} = A \cdot P \cdot A^T + (G - A \cdot P_k \cdot C^T) \cdot (R_0 - C \cdot P_k \cdot C^T)^{-1} \cdot (G - A \cdot P_k \cdot C^T)^T$$

in which K and P are the *Kalman filter gain matrix* and the *Kalman state covariance matrix*, respectively [28,50,51].

The column of past outputs *block-Hankel* matrix Y_p can be analyzed simultaneously through a set of non-steady *Kalman filters* and the estimated state vectors can be organized into an archive. The past measured responses, contained into this bank, can be linearly combined and then used to construct *Kalman filter state sequence* \hat{X}_i [28,51]:

$$\hat{X}_i = (\hat{x}_i \quad \hat{x}_{i+1} \quad \cdots \quad \hat{x}_{i+N+1}) \in R^{n \times N}\tag{3.109}$$

3.2.2.2.2 Factorization and Projection matrix

Starting from the sensors configuration, it is possible to express the matrix y_k with ($k = 0, 1 \dots N, N \rightarrow \infty$) containing the discrete samples as follows:

$$y_k = [y_m^n] = \begin{bmatrix} y_1^n \\ y_2^n \\ \vdots \\ y_l^n \end{bmatrix} = \begin{bmatrix} y_1^0 & y_1^1 & \dots & y_1^N \\ y_2^0 & y_2^1 & \dots & y_2^N \\ \vdots & \vdots & \ddots & \vdots \\ y_l^0 & y_l^1 & \dots & y_l^N \end{bmatrix} \quad (3.110)$$

After the data are organized as shown in Eq. 3.110, it is possible to build the *block-Hankel* matrix (H), which is a matrix constant along its anti-diagonal elements, having size $[2i\text{-by-}N]$. In practical application, the i value is set as $N = j - (2i - 1)$ (with j is the total number of collected points) so that all the available data can be used during the following projection phase.

Indicating with l the number of available channels, *Hankel* matrix sizes are $2 \cdot i \cdot l \cdot N$, and it is possible to subdivide it into two parts (Eq. 3.111): the *past matrix* (Y_p^{ref}) and the *future matrix* (Y_f).

$$H_{0|2i-1} = \frac{1}{\sqrt{N}^*} \begin{bmatrix} y_0 \\ y_1 \\ \vdots \\ y_{i-1} \\ y_i \\ y_{i+1} \\ \vdots \\ y_{2i-1} \end{bmatrix} = \frac{1}{\sqrt{N}^*} \begin{bmatrix} y_0 & y_1 & \dots & y_{N-1} \\ y_1 & y_2 & \dots & y_N \\ \vdots & \vdots & \ddots & \vdots \\ y_{i-1} & y_i & \dots & y_{i+N-2} \\ y_i & y_{i+1} & \dots & y_{i+N-1} \\ y_{i+1} & y_{i+2} & \dots & y_{i+N} \\ \vdots & \vdots & \ddots & \vdots \\ y_{2i-1} & y_{2i} & \dots & y_{2i+N-2} \end{bmatrix} = \begin{bmatrix} Y_{0|i-1} \\ Y_{i|2i-1} \end{bmatrix} = \begin{bmatrix} Y_p \\ Y_f \end{bmatrix} \quad (3.111)$$

The subscripts of $Y_{0|i-1}$ and $Y_{i|2i-1}$ indicate the first and last block-element in the first column of the H matrix used to define the *past* and *future* matrices dimension. A second separation is operated neglecting the first block-row from the *future matrix* $Y_{0|2i-1}$ and moving this block at the end of the *past matrix* $Y_{0|i}$, as shown in Eq. 3.112

$$H_{0|2i-1} = \frac{1}{\sqrt{N}^*} \begin{bmatrix} y_0 \\ y_1 \\ \vdots \\ y_i \\ y_{i+1} \\ y_{i+1} \\ \vdots \\ y_{2i-1} \end{bmatrix} = \frac{1}{\sqrt{N}^*} \begin{bmatrix} y_0 & y_1 & \dots & y_{N-1} \\ y_1 & y_2 & \dots & y_N \\ \vdots & \vdots & \ddots & \vdots \\ y_i & y_{i+2} & \dots & y_{i+N-1} \\ y_{i+1} & y_{i+2} & \dots & y_{i+N} \\ y_{i+2} & y_{i+3} & \dots & y_{i+N+1} \\ \vdots & \vdots & \ddots & \vdots \\ y_{2i-1} & y_{2i} & \dots & y_{2i+N-2} \end{bmatrix} = \begin{bmatrix} Y_{0|i} \\ Y_{i+1|2i-1} \end{bmatrix} = \begin{bmatrix} Y_p^+ \\ Y_f^- \end{bmatrix} \quad (3.112)$$

The system matrices for the *state-space model* can now be estimated.

Following data organization, the projection, which make the information contained in the *past matrix* useful for future prediction, is so defined:

$$P_i = \left[\frac{Y_{i|2i-1}}{Y_{0|i-1}} \right] = \frac{Y_f}{Y_p} = Y_f Y_p^T (Y_p Y_p^T)^{\dagger} Y_p \quad (3.113)$$

From Eq. 3.113 it is highlighted the function of removing uncorrelated noise, carried out, in a similar way, by projection and covariance. Moreover, the projection matrix can be also assimilated with the product of the extended *observability matrix* O_i and the *Kalman filter state sequence* \hat{X}_i .

$$P_i = O_i \cdot \hat{X}_i \quad (3.114)$$

Due to the difficulties in computation, in practical applications this step is numerically computed through *QR-factorization* of the H matrix as described in [33], which shortly consists in decomposing the H matrix and compressing it (Eq. 3.116) into smaller triangular matrix R , containing the information about the system.

$$H_{0|2i-1} = \begin{bmatrix} Y_p \\ Y_f \end{bmatrix} = R \cdot Q^T \quad (3.115)$$

$$H_{0|2i-1} = \begin{matrix} l & \updownarrow & \\ li & \updownarrow & \\ l(i-1) & \updownarrow & \end{matrix} \begin{pmatrix} R_{11} & 0 & 0 \\ R_{21} & R_{22} & 0 \\ R_{31} & R_{32} & R_{33} \end{pmatrix} \cdot \begin{pmatrix} Q_1^T \\ Q_2^T \\ Q_3^T \end{pmatrix} \begin{matrix} \updownarrow & l \\ \updownarrow & li \\ \updownarrow & l(i-1) \end{matrix} \quad (3.116)$$

$$\begin{matrix} \leftrightarrow & \leftrightarrow & \leftrightarrow & \leftrightarrow \\ li & i & l(i-1) & N \end{matrix}$$

Substitution of Eq. 3.116 in Eq. 3.114 makes the projection matrix P_i expressed as follows:

$$P_i = \begin{pmatrix} R_{21} \\ R_{31} \end{pmatrix} Q_1^T \quad (3.117)$$

And subsequently the *Projection matrix* P_{i-1} is computed as:

$$P_{i-1} = (R_{31} \quad R_{32}) \begin{pmatrix} Q_1^T \\ Q_2^T \end{pmatrix} \quad (3.118)$$

The *projection matrices* P_i and P_{i-1} once available decrease considerably the *QR-Factorization* computational cost, making the system matrices and the modal parameters easy to estimate.

From [28], P_i can be factorized as:

$$P_i = \begin{bmatrix} C \\ C \cdot A \\ \vdots \\ C \cdot A^{i-1} \end{bmatrix} [\hat{x}_i \quad \hat{x}_{i+1} \quad \cdots \quad \hat{x}_{i+N+1}] = O_i \cdot \hat{X}_i \quad (3.119)$$

where the SVD of P_i matrix is:

$$P_i = U \cdot S \cdot V^T = [U_1 \quad U_2] \cdot \begin{bmatrix} S_1 & 0 \\ 0 & 0 \end{bmatrix} \cdot \begin{bmatrix} V_1^T \\ V_2^T \end{bmatrix} = U_1 \cdot S_1 \cdot V_1^T \quad (3.120)$$

P_i matrix order results n , coming from the product of the n columns matrix O_i by a n rows matrix \hat{X}_i , and so result the *order* of the problem and the dimensions of matrix A (being also n the number of different non-zero after decomposition of matrix P_i).

Factorization of matrices O_i and \hat{X}_i produces:

$$\begin{aligned} O_i &= U_1 \cdot S_1^{1/2} \\ \hat{X}_i &= O_i^\dagger \cdot P_i \end{aligned} \quad (3.121)$$

The definition of a new projection, moving down a block row from past matrix to the one of future outputs, is needed for the identification of matrices A and C (Eq. 3.122):

$$P_{i-1} = \frac{Y_f^-}{Y_p^+} = O_{i-1} \cdot \hat{X}_{i+1} \quad (3.122)$$

And its decomposition gives:

$$P_{i-1} = \begin{bmatrix} C \\ C \cdot A \\ \vdots \\ C \cdot A^{i-2} \end{bmatrix} [\hat{x}_i \quad \hat{x}_{i+1} \quad \cdots \quad \hat{x}_{i+N}] = O_{i-1} \cdot \hat{X}_{i+1} \quad (3.123)$$

From which the *Kalman filter state sequence* \hat{X}_{i+1} is obtained:

$$\hat{X}_{i+1} = O_{i-1}^\dagger \cdot P_{i-1} \quad (3.124)$$

From the computation of the successive sequences, only based on data, a system with more equations than unknown variables are obtained, where the system matrices can be extracted from, fixing the time instants to i and $i+N-I$:

$$\begin{bmatrix} \hat{X}_{i+1} \\ Y_{i|i} \end{bmatrix} = \begin{bmatrix} A \\ C \end{bmatrix} \hat{X}_i + \begin{bmatrix} W_i \\ V_i \end{bmatrix} \quad (3.125)$$

where $Y_{i|i}$ is a *Hankel* matrix with only one block row and W_i , V_i can be treated as the residuals of an optimization problem. Since the *Kalman state sequences* and the outputs are known, and the residuals are uncorrelated with X_i , the set of equations can be solved for A and C in a least square sense:

$$\begin{bmatrix} A \\ C \end{bmatrix} = \begin{bmatrix} \hat{X}_{i+1} \\ Y_{i|i} \end{bmatrix} \hat{X}_i^\dagger \quad (3.126)$$

The identification problem is now theoretically solved, with the modal parameters which can be deduced following the procedure described for the *SSI-Cov* technique.

One last consideration can be appointed: in operative conditions, sometimes it is useful to introduce two *weighting* matrices W_1 and W_2 (Table 3-1) which are multiplied by the value of the data to be decomposed into singular values of the *SSI-Data* method (Eq. 3.127):

$$\bar{P}_i = W_1 \cdot P_i \cdot W_2 \quad (3.127)$$

This weighting operation introduces a transformation of state vector coordinates which lead to identical identification results of the process.

Table 3-1 - The variant weighting matrices in: PC - main component, CVA - canonical analysis

Variation	$W_1(\text{il} \cdot \text{il})$	$W_2(\text{N} \cdot \text{N})$
UPC	I	I
PC	I	$Y_p^T \cdot (Y_p \cdot Y_p^T)^{-1/2} \cdot Y_p^T$
CVA	$(Y_f \cdot Y_f^T)^{-1/2}$	I

4 Short-term monitoring and OMA identification for assess the health status of operative structures

In the previous sections, the main concept regarding SHM and one of its most popular technique have been exposed. Into this chapter two practical cases, where dynamic monitoring and OMA identification techniques have been successfully applied for the assessment of health status of operative structures, will be presented, in order to show the potentiality and most of all the versatility of this methodology. The examined structures are respectively an arch bridge and the cover of an airport hangar, both realized in concrete. In the first case, the purpose of the activity was the evaluation of the capacities of the bridge after it was damaged due to a car accident. In the second case, the antenna supporting the hangar cover have been monitored to extract the modal parameters, describing their dynamic behavior, in order for these data to be compared with the ones relative to the experimentation of a new type of sensors, which are being tested on this structure.

4.1 Identification procedure

4.1.1 Data acquisition and pre-processing

The monitoring activities have been executed through a sensor network was composed 21 monoaxial piezoelectric accelerometers characterized by a maximum measurement range of 8 g, a sensitivity of 1000 mV/g and a bandwidth range from 0.8 to 100 Hz. The digitization process and synchronization of measurements was automated through 7 A/D converter with 24 bits of resolution, 120 dB of dynamic range and provided with anti-aliasing filter. Every registration had a duration between 30 to 60 minutes, and data were collected with a sampling frequency of 1000 Hz.

Once all the time histories have been acquired, the data are processed as follows:

- Evaluation of the frequency content of the signals through FFT algorithm;
- Application of 0.5Hz-100Hz bandpass filter in order to eliminate frequencies that are not of interest for the characterization of the building;
- Elimination of time sequences with anomalous peaks;

- Data resampling, the frequency of which is reduced from 1000 Hz to 100 Hz (field in which the frequencies of interest for civil structures are usually found), with the application of a decimation factor of 10.

In the subsequent phases of the dynamic identification the decimation process was repeated in order to identify the most significant modes for the analyzed structures.

The data are then processed through an identification software capable of extracting the dynamic parameters of the structure, natural frequencies and modal shapes, making an estimate of the damping associated with the selected modes.

4.1.2 Modal parameters extraction

The identification software operates through the SSI (Stochastic Subspace Identification) algorithm in the time domain [33], estimating the Frequency Response Function (FRF) of the system from which the modal parameters are extracted.

The procedure for selecting the real modes is based on the values of the modal parameters obtained for each order of the chosen model; it provides for the introduction of comparison parameters, of which an acceptance threshold value can be cautiously established. Three parameters are introduced, corresponding to the three modal parameters, namely frequency (f), modal form (φ) and damping ratio (ξ), to which a criterion for comparison of the modes is associated.

$$\Delta f = \frac{|f_1 - f_2|}{f} < 1\% \quad (4.1)$$

$$\Delta \xi = \frac{|\xi_1 - \xi_2|}{\xi} < 5\% \quad (4.2)$$

$$MAC(\varphi_1, \varphi_2) = \frac{|\varphi_1^T \cdot \varphi_2^*|^2}{(\varphi_1^T \cdot \varphi_1^*)(\varphi_2^T \cdot \varphi_2^*)} > 95\% \quad (4.3)$$

where the M.A.C. (Modal Assurance Criterion) allows you to compare the modal forms calculated at the different orders of the model.

If all the selection criteria are exceeded, the pole is defined as stable. At each order of the model this estimate is made and, through the stabilization diagram, the structural modes are aligned, eliminating the purely numerical modes.

4.1.3 Mode shapes representation and validation

For each of the examined structures, a modal model was created in order to schematically represent the structure in question. This model does not contain any information on materials and boundary conditions but allows to detect how each monitored point moves at each natural frequency.

Each point is associated with information relating to the modulus and phase of each modal vector, in order to identify how the various sensors, move each other reciprocally (in phase or counterphase)

In the plotting of the modal forms the following assumptions were made:

- Rigid behavior in the plane of the various decks;
- Modal forms referring only to the x and y axes (plane);
- The points at the base of the building that were not monitored were assumed with zero displacement (wedged at the base).

Validation of mode shapes was ascertained through M.A.C., in accordance with the expression of Eq. 4.3.

4.2 Modal Identification of the Arch Bridge on Garigliano River after damage of its strays

4.2.1 Description of the case study

The structure object of the dynamic experimentation is an arched bridge (Fig. 4-1) with an inferior road built in Minturno on the Garigliano river km 156-250 S.S. 7 "Via Appia". The bridge is made of reinforced concrete. and it is composed of a central span with span of about 50.85 m, and two shore spans, with spans of about 12m, for a total length of about 75m; the width of the deck is about 9 m.



Fig. 4-1 - Arch Bridge on Garigliano River

The convention adopted for naming the stays is shown in Fig. 4-2. By convention, the words "Right Arch" are adopted for the arch where the damaged forestay is located, and "Left Arch" for the other.

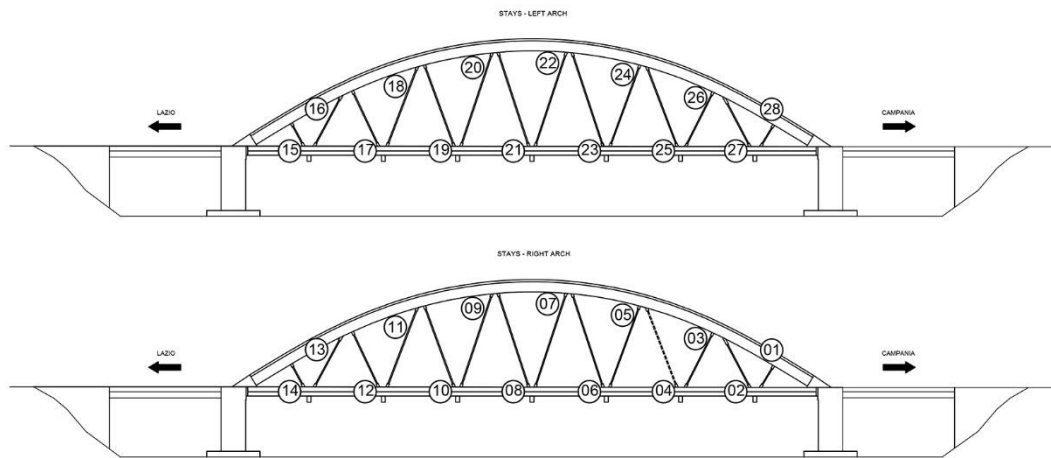


Fig. 4-2 - Denomination of stays

4.2.2 Sensors layout and photographic documentation

The first part of the monitoring activity has been focused on the evaluation of the global behavior of the bridge. The test was carried out by varying the position of the sensors as indicated in Fig. 4-3÷Fig. 4-5, and finally made synchronous in order to maximize the information obtained. In particular, the synchronization is made possible through three sensors always left in the same positions during the

various tests, such as Nr. 15, Nr. 18, Nr. 43.

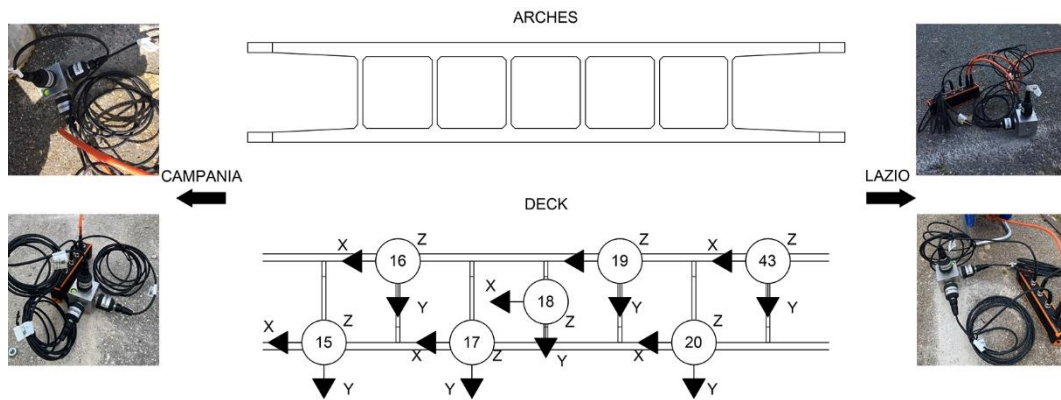


Fig. 4-3 - First sensors layout

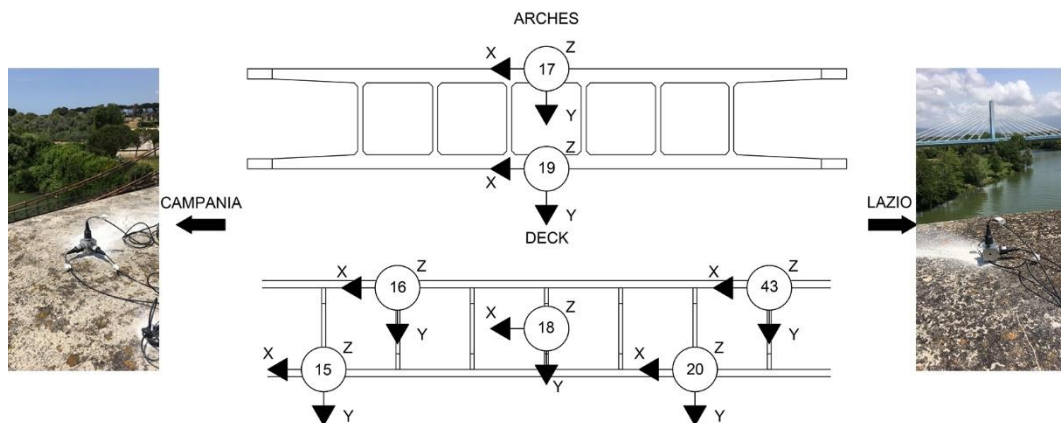


Fig. 4-4 - Second sensors layout

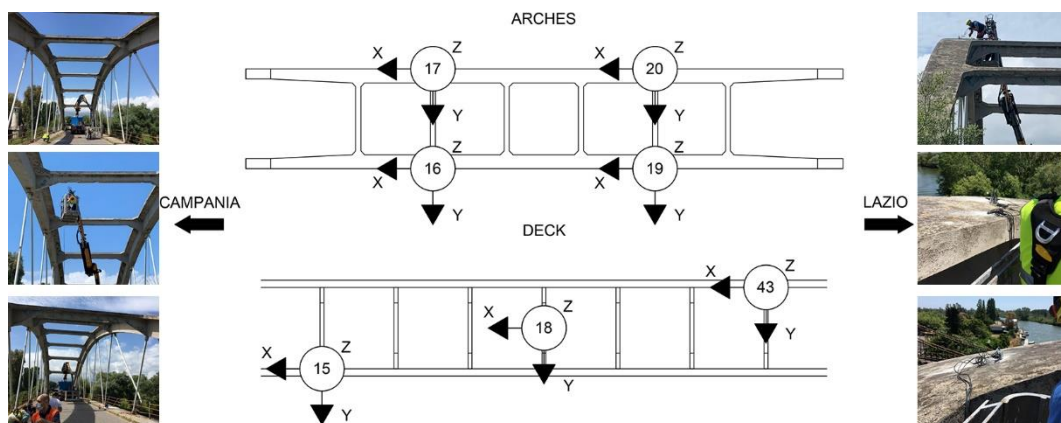


Fig. 4-5 - Third sensors layout

Then the dynamic behavior of the single stays has been investigated, positioning an orthogonal triad of sensors on each of the stays and acquiring vibration data. The orientation of the sensors that form the measurement triad is shown, as a function of the inclination of the stays (Fig. 4-6).

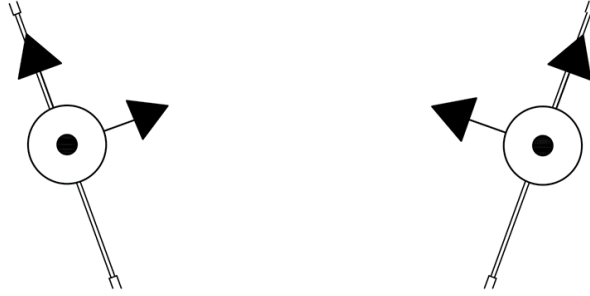


Fig. 4-6 - Orientation of the sensors placed on the stays

4.2.3 Identification process

4.2.3.1 Preliminary evaluation of the frequency contents of signals

The frequency contents of the signals, extrapolated through the FFT algorithm are shown below (Fig. 4-7÷Fig. 4-9):

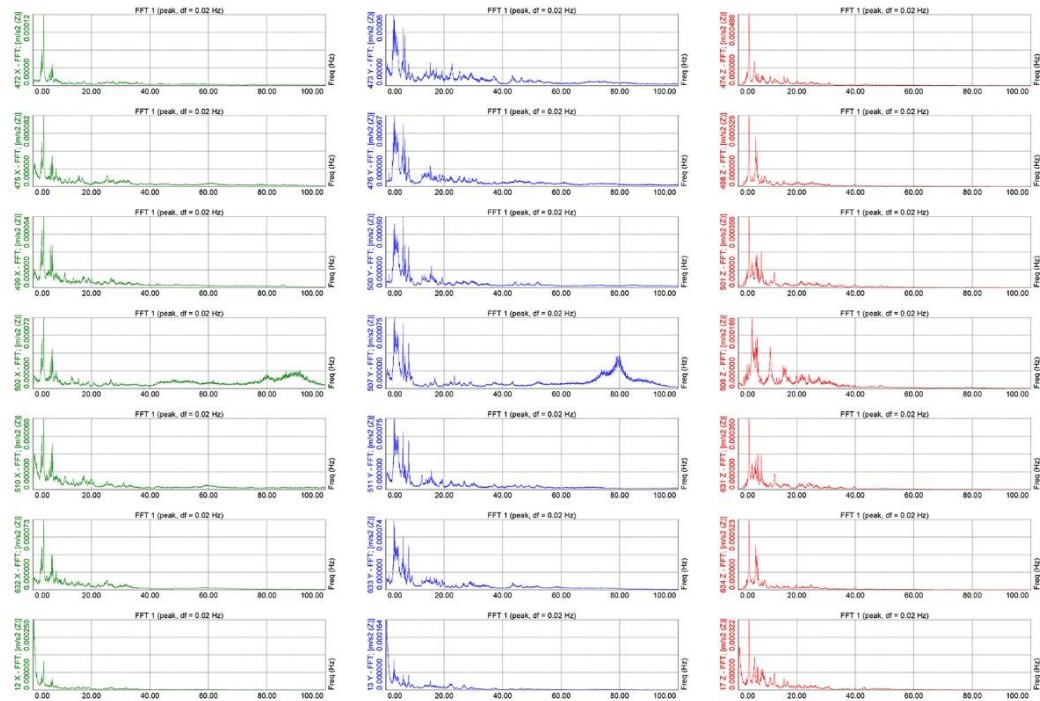


Fig. 4-7 - FFT of the signals of the first acquisition

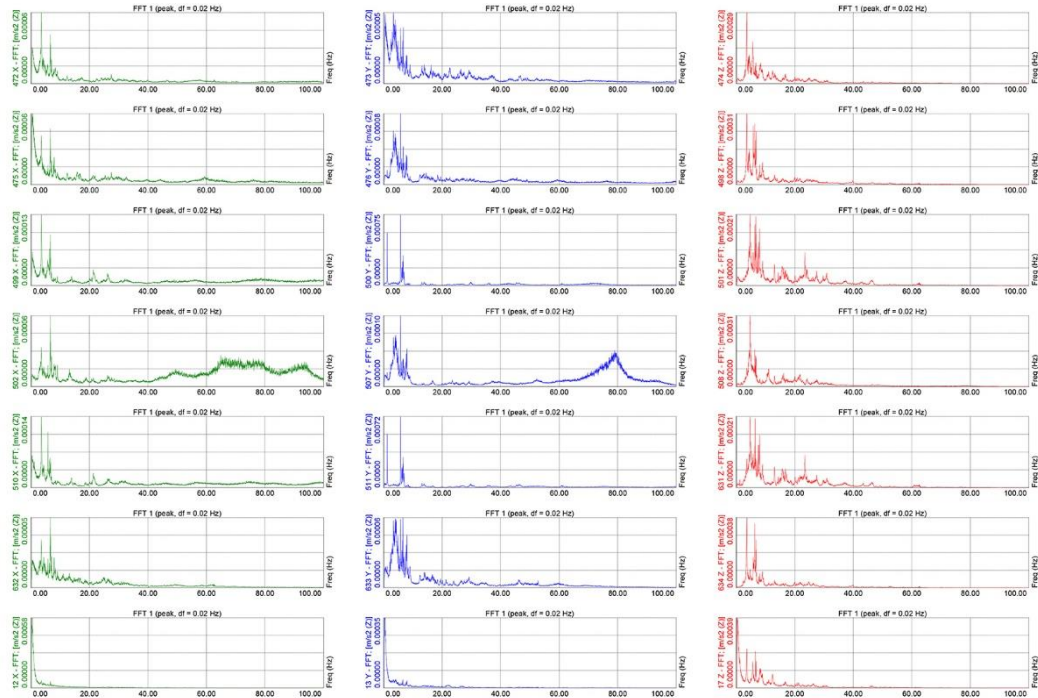


Fig. 4-8 - FFT of the signals of the second acquisition

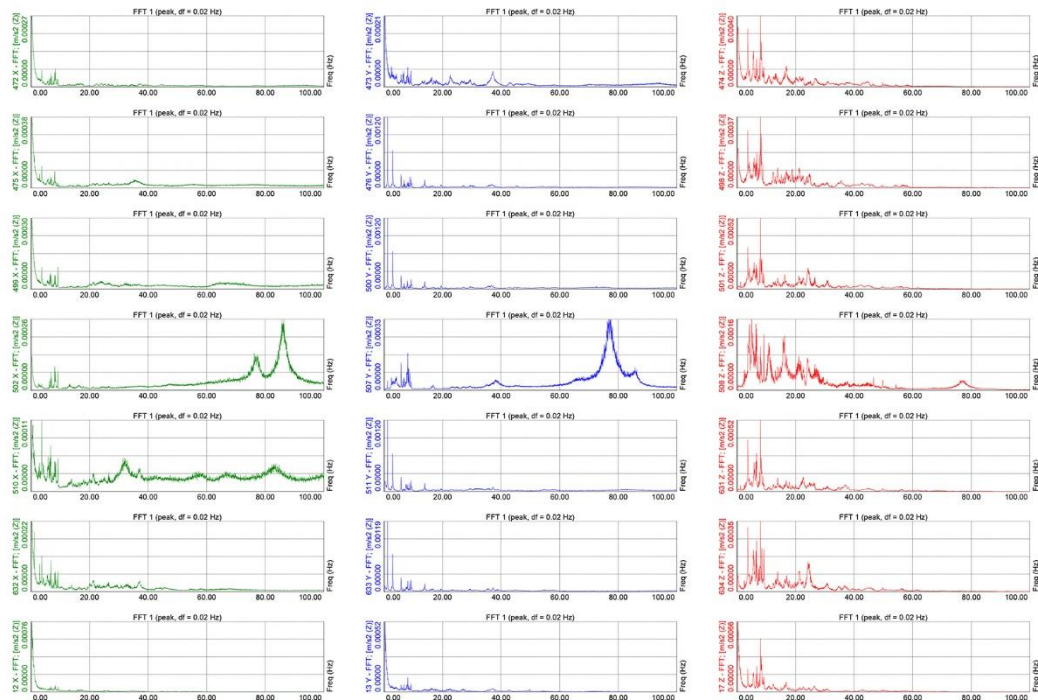


Fig. 4-9 - FFT of the signal of the third acquisition

From these elaborations it is possible to notice that the predominant frequencies, for the global structure, are located in the 0-20 Hz range, which is the interval where the analysis focus.

4.2.3.2 Identification of Frequencies and Damping ratios

The first part of the analysis is focused on the identification of the modal parameters describing the global structural behavior of the bridge. By applying the previously described identification algorithm (SSI) over the acquisitions acquired for the schemes of Fig. 4-7÷Fig. 4-9, the following stabilization diagram is obtained (Fig. 4-10).

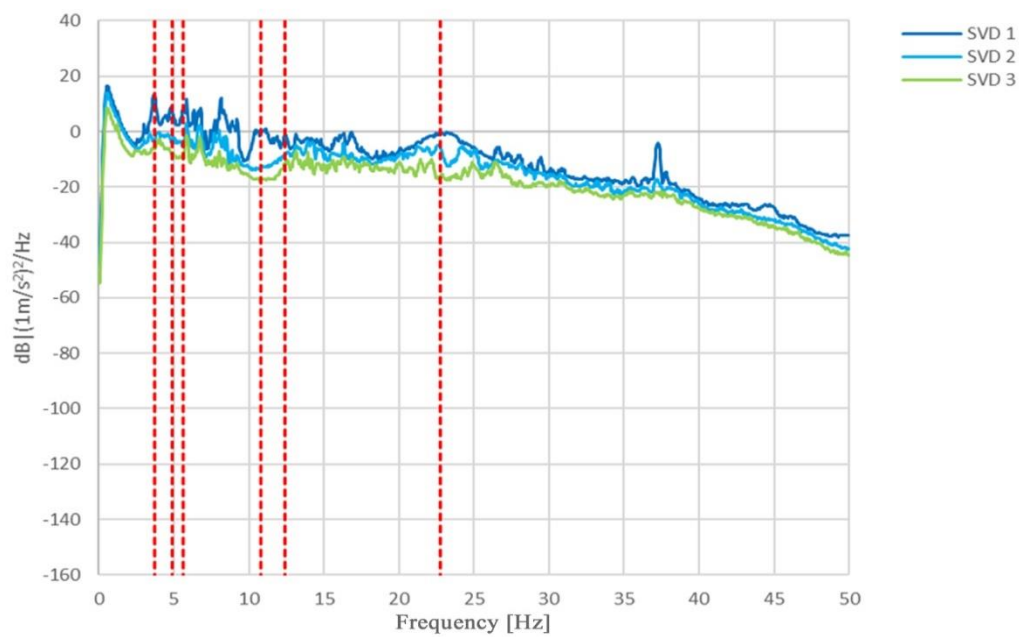


Fig. 4-10 - Stabilization diagram - sample rate 50 Hz

Table 4-1 shows the main natural frequencies identified while Fig. 4-11 **Errore. L'origine riferimento non è stata trovata.** shows the complexity plot of the estimated frequencies.

Table 4-1 - Main experimental frequencies of the bridge and related modal dampings

Frequency [Hz]	Damping [%]
3.689	2.106
4.909	1.905
5.641	1.293
10.760	1.894

12.428	0.983
22.774	1.598

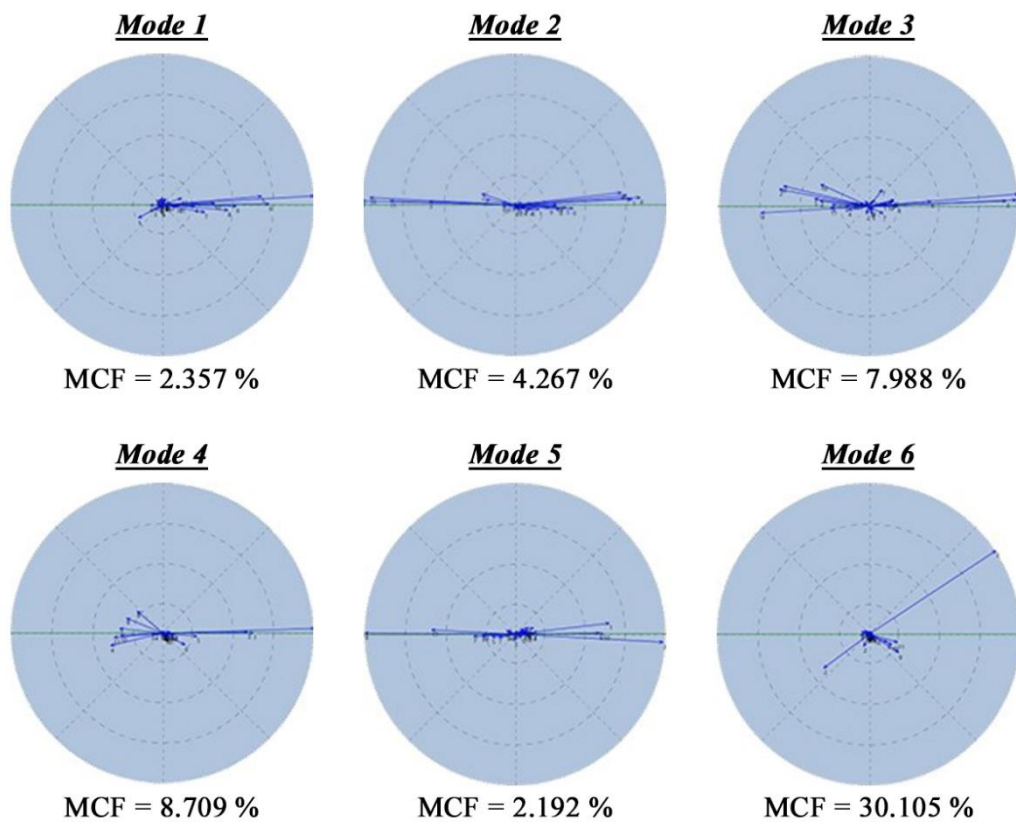


Fig. 4-11 - Complexity plot of the estimated modes

4.2.3.3 Mode shapes representation and validation

The modal model that schematically represents the structure is shown in Fig. 4-12:

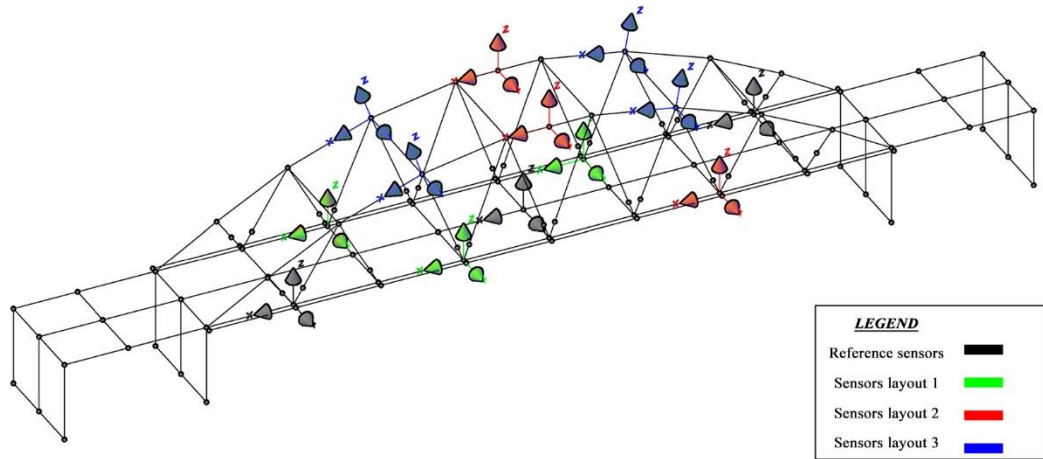


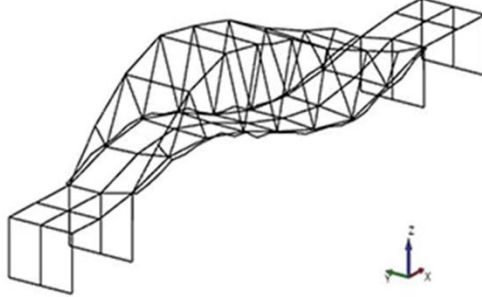
Fig. 4-12 - Experimental model indicating the measurement positions

By overlapping the results, obtained by applying the analysis techniques described in Section 4.1.3 to the acquired data, it was possible to identify mode shapes illustrated in Fig. 4-14, whose validation is assured by the results shown into the AUTOMAC diagram (Fig. 4-13). This matrix, correlating the obtained mode shapes with themselves, confirms their consistency modes and the decoupling of resulting modes, as it is evident looking at the low values of the terms outside the principal diagonal of the matrix.

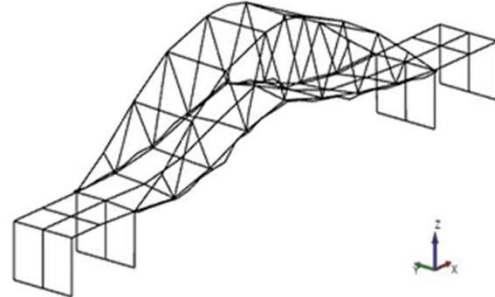
MAC	3.689 Hz	4.909 Hz	5.641 Hz	10.76 Hz	12.43 Hz	22.77 Hz
3.689 Hz	1	0.013	0.014	0.004	0.002	0.002
4.909 Hz	0.013	1	0.236	0.068	0.005	0.033
5.641 Hz	0.014	0.236	1	0.007	0.000	0.005
10.76 Hz	0.004	0.068	0.007	1	0.163	0.024
12.43 Hz	0.002	0.005	0.000	0.163	1	0.005
22.77 Hz	0.002	0.033	0.005	0.024	0.005	1

Fig. 4-13 - AUTOMAC of the estimated frequencies

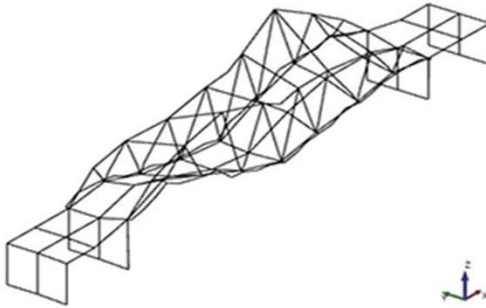
Mode 1 - $f = 3.869$ Hz



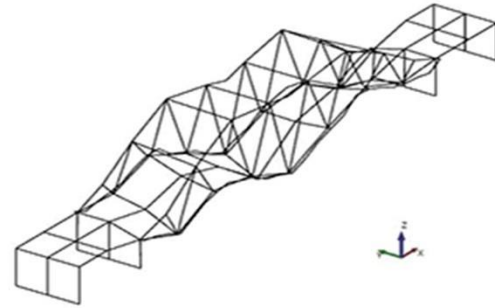
Mode 2 - $f = 4.909$ Hz



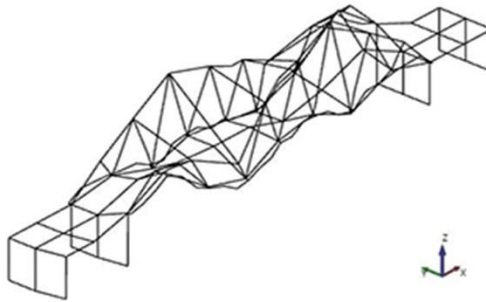
Mode 3 - $f = 5.641$ Hz



Mode 4 - $f = 10.760$ Hz



Mode 5 - $f = 12.428$ Hz



Mode 6 - $f = 22.774$ Hz

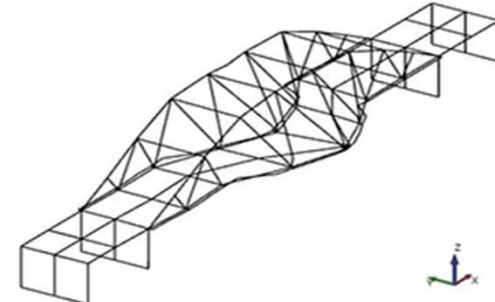


Fig. 4-14 - Mode shapes

The visualization of the mode shapes, as expectable, highlights a predominance of the vertical flexural behavior, as it is possible to observe for the first five modes, while, for modes linked to frequencies higher than 20 Hz a transversal displacement component starts to manifest.

4.2.4 Dynamic identification of the stays

The second part of the analysis focused on the evaluation of the single stays state, with Table 4-2 which shows the frequencies relating to the first modes of vibration of the stays, obtained through the dynamic identification techniques illustrated in the previous paragraphs. The numbering is that indicated in Fig. 4-2.

Table 4-2 - Frequencies identified for the various stays

Stay	Mode	f [Hz]	ξ [%]	Complexity [%]
01	1	60.626	0.544	0.884
	2	63.505	0.636	0.656
02	1	16.445	0.693	0.033
	2	17.105	0.445	0.282
03	1	14.346	1.631	0.000
	2	35.962	0.893	0.000
04	DAMAGED			
05	1	6.445	1.674	0.686
	2	28.944	0.164	0.241
06	1	8.305	0.213	0.781
	2	20.566	0.277	0.036
07	1	30.622	0.493	3.703
	2	48.731	0.427	1.398
08	1	6.851	0.933	0.029
	2	31.222	3.069	1.194
09	1	49.314	3.320	0.000
	2	66.718	1.182	0.000
10	1	6.541	2.200	0.363
	2	16.138	0.404	0.004
11	1	9.162	2.441	0.000
	2	22.273	1.284	0.000
12	1	7.668	1.645	0.000
	2	20.324	0.878	0.000

13	1	9.191	1.505	0.366
	2	16.136	1.067	0.003
14	1	14.903	1.267	0.001
	2	16.776	3.526	0.112
15	1	15.598	6.193	0.006
	2	16.932	1.593	0.013
16	1	9.907	8.987	0
	2	15.893	2.899	0.008
17	1	15.962	1.665	0.465
	2	18.576	3.288	0.010
18	1	14.195	0.935	4.721
	2	15.912	2.081	0.023
19	1	8.012	1.744	2.711
	2	38.865	0.628	0.104
20	1	49.351	3.554	0.000
	2	66.910	0.839	0.000
21	1	6.411	2.925	0.104
	2	16.785	0.286	0.000
22	1	6.719	3.291	0.669
	2	30.757	0.453	0.000
23	1	6.403	1.584	1.549
	2	16.084	0.287	0.256
24	1	6.445	1.674	0.686
	2	15.364	0.892	0.254
25	1	8.746	0.494	1.113
	2	20.870	0.188	0.052
26	1	13.98	1.295	0.015
	2	38.558	0.729	0.123
27	1	15.119	0.421	3.309
	2	15.491	0.402	0
28	1	59.099	0.400	9.824

2	60.676	0.402	0.016
---	--------	-------	-------

A part for some cases, a certain correspondence is observable in the frequencies values associated to the symmetrical stays, with values of frequencies which tend to decrease with the increment of stays length.

The mode shapes, instead, are all of the flexural type, perpendicular to the direction of development of the forestay.

4.3 Modal Identification of Hangar Morandi Cover

4.3.1 Description of the case study



Fig. 4-15 - Morandi Hangar Nr.3 in Fiumicino Airport

The structure that is the subject of the dynamic experimentation is the roof of the 3 Hangar of Fiumicino Airport, designed by the engineer Riccardo Morandi (Fig. 4-15**Errore. L'origine riferimento non è stata trovata.**). It is a roof with dimensions of approximately 200m x 85m, made with reinforced concrete beams. with curvilinear development. From the extrados of the latter stand out, for a height of about 15 m, 37 reinforced concrete antennas, which act as a support for the roof, to which they are connected by three stays made in cap. The antennas are connected in pairs by means of a beam at the top, with the exception of the trio of antennas on the left of the diagram shown in Fig. 4-16. The diagram highlights the monitored antennas. In this report the antennas are identified, with convention starting from the right side, with a number from 01 to 37, while the stays are indicated

with a letter.

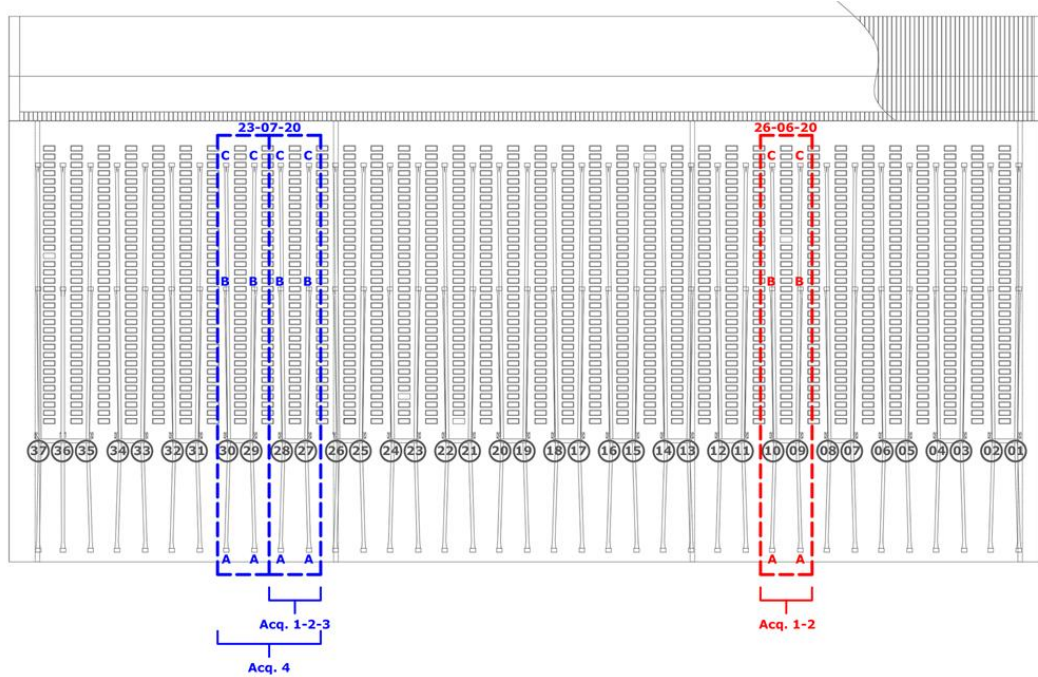


Fig. 4-16 - Naming of the elements and layout of the systems monitored on 26.06.2020 (in red) and on 23.07.2020 (in blue)

4.3.2 Sensors layout and photographic documentation

4.3.2.1 Monitoring campaign on 26.06.2020

The test was carried out by positioning the sensors as indicated in Fig. 4-17 and Fig. 4-18, and subsequently synchronizing the acquired time histories, in order to maximize the information obtained. In particular, the synchronization is made possible through some sensors always left in the same positions during the various tests, such as those connected to the control units C15, C16, C17 and C43. Some images of the sensor installation are shown in and.

In the case of the first scheme, shown in Fig. 4-17, the sensors were positioned at the head of Antenna 10 and at the base of the individual stays, at a variable altitude between 0.85 and 1.30 m.

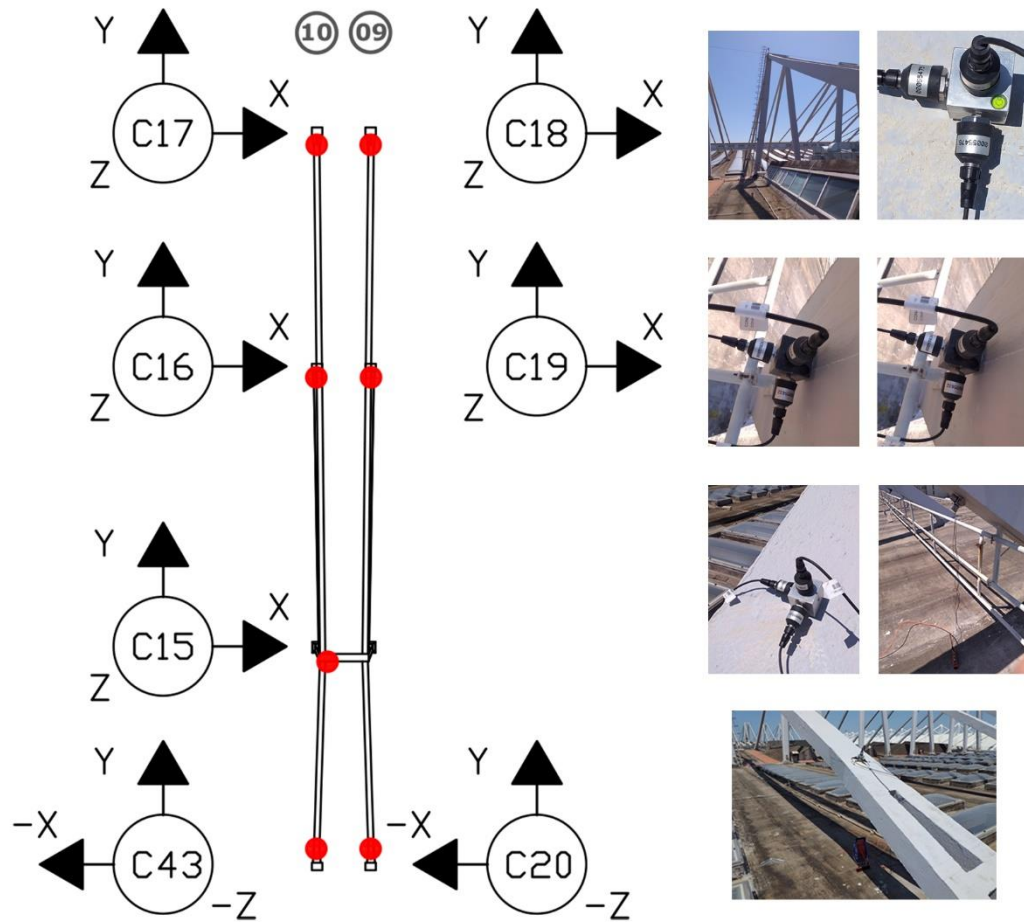


Fig. 4-17 - First sensors layout for 26.06.2020 monitoring

In the second diagram, illustrated in Fig. 4-18, only the portion of the structure connected to the Antenna 10 has been considered, but placing a triad of sensors at the base of this, at an altitude of about 1.00 m.

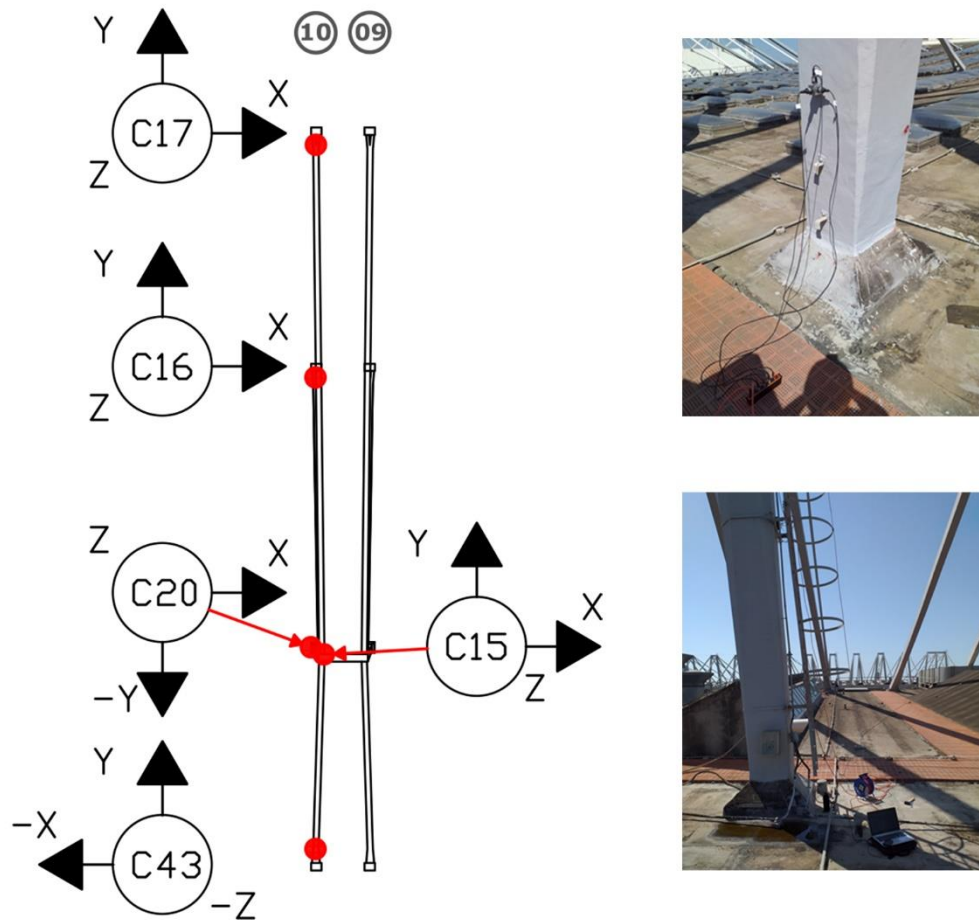


Fig. 4-18 - Second sensors layout for 26.06.2020 monitoring

4.3.2.2 Monitoring campaign on 23.07.2020

The test was carried out by positioning the sensors as indicated in (Fig. 4-19÷Fig. 4-22), and subsequently synchronizing the acquired time histories, so as to maximize the information obtained. In particular, the synchronization is made possible through some sensors always left in the same positions during the various tests.

In the case of the first scheme, shown in Fig. 4-19, **Error. L'origine riferimento non è stata trovata.**, the sensors were positioned at the head of Antenna 28 and at the base of the individual stays, at a variable altitude between 0.85 and 1.30 m.

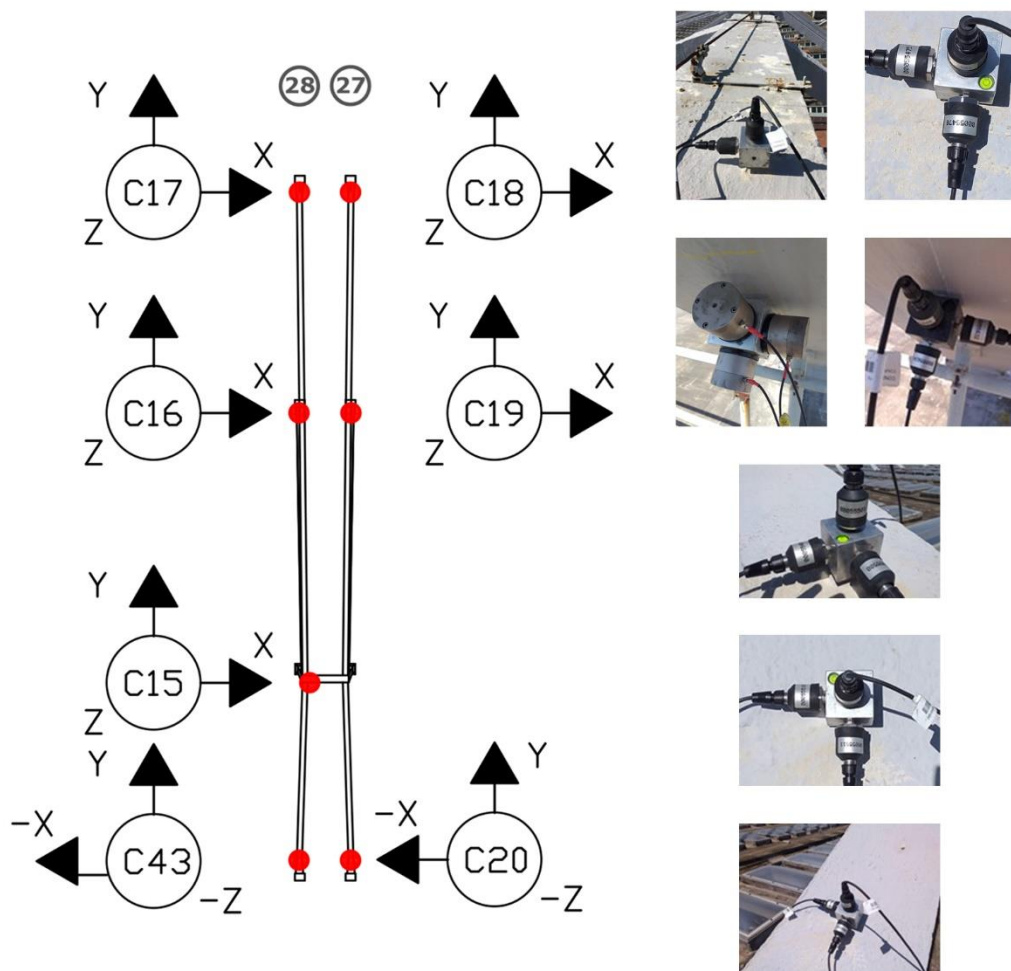


Fig. 4-19 - First Sensors Layout for 23.07.2020 monitoring

In the second diagram, illustrated in Fig. 4-20, the triad of sensors connected to the C43 control unit has been moved near the base of Antenna 27, at an altitude of about 1.00 m, so as to deepen the study of this antenna, and to have more knowledge of its interaction with the Antenna 28, to which it is connected.

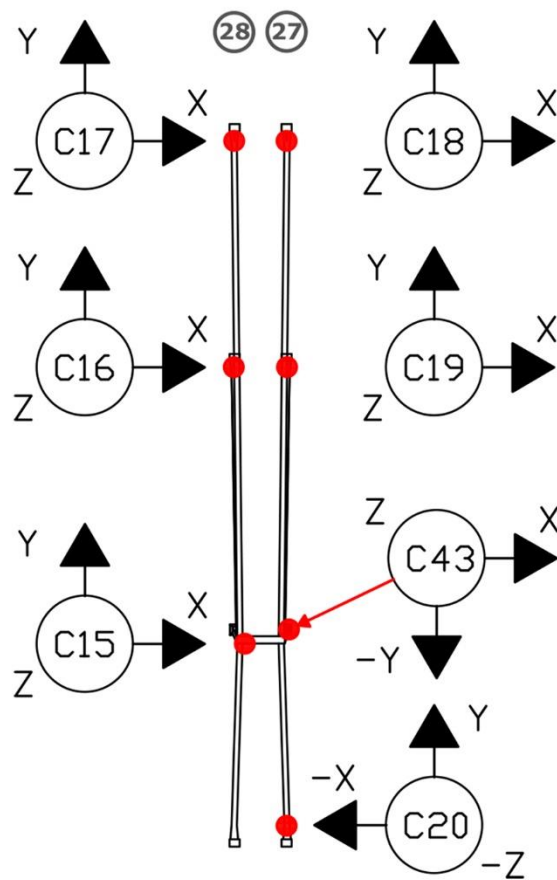


Fig. 4-20 - Second sensors layout for 23.07.2020 monitoring

The third diagram, in Fig. 4-21, provided for the installation of the C43 control unit and the sensors connected to it at the base of the Antenna 28, again at an altitude of about 1.00 m.

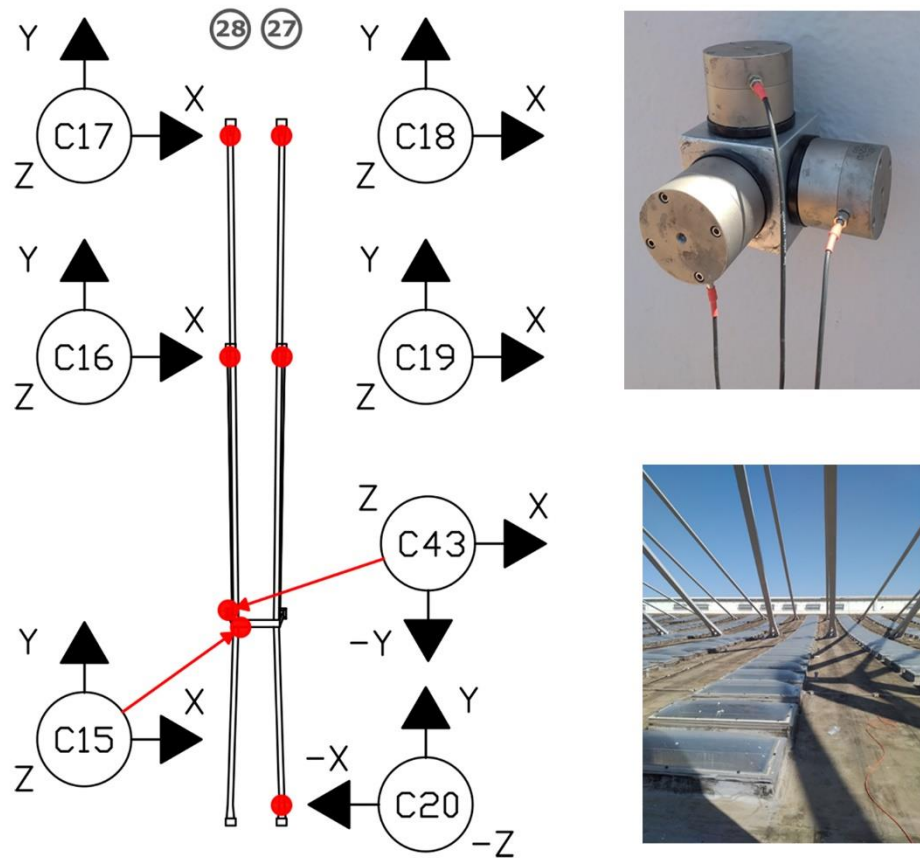


Fig. 4-21 - Third sensors layout for 23.07.2020 monitoring

The last sensor layout, shown in Fig. 4-22, had the purpose of evaluating the behavior in the transverse direction of the Antenna 28 and its interaction with adjacent structures. The triads of accelerometers connected to the control units C17, C18 and C19 were then installed at the feet of Antennas 28, 29 and 30, again at an altitude of about 1.00 m. The other sensors were instead fixed on the stays connected to Antenna 28.

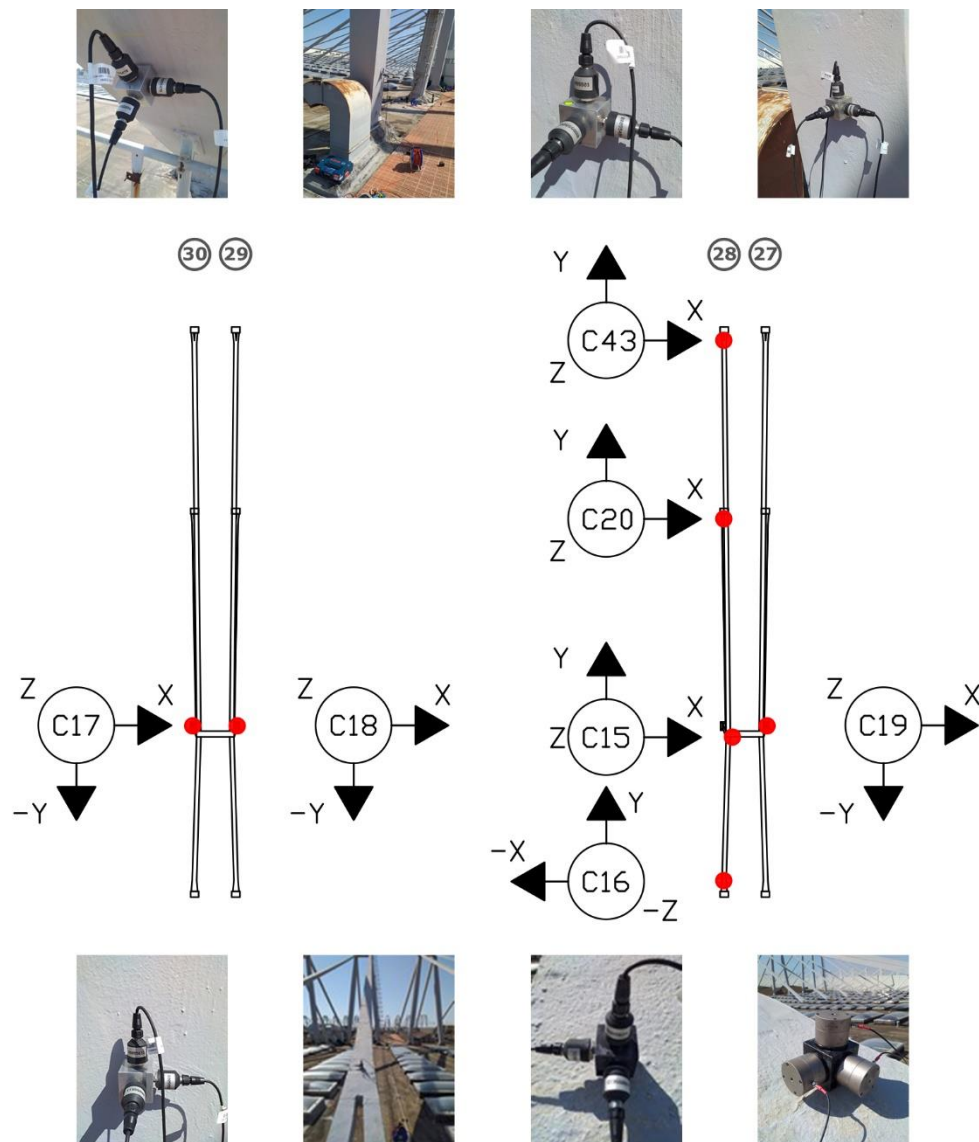


Fig. 4-22 - Fourth sensors layout for 23.07.2020 monitoring

4.3.3 Identification process

4.3.3.1 Preliminary evaluation of the frequency contents of signals acquired on 26.06.2020

The frequency contents of the signals registered during the first day of the monitoring campaign, extrapolated through the FFT algorithm are shown below Fig. 4-23 and Fig. 4-24:

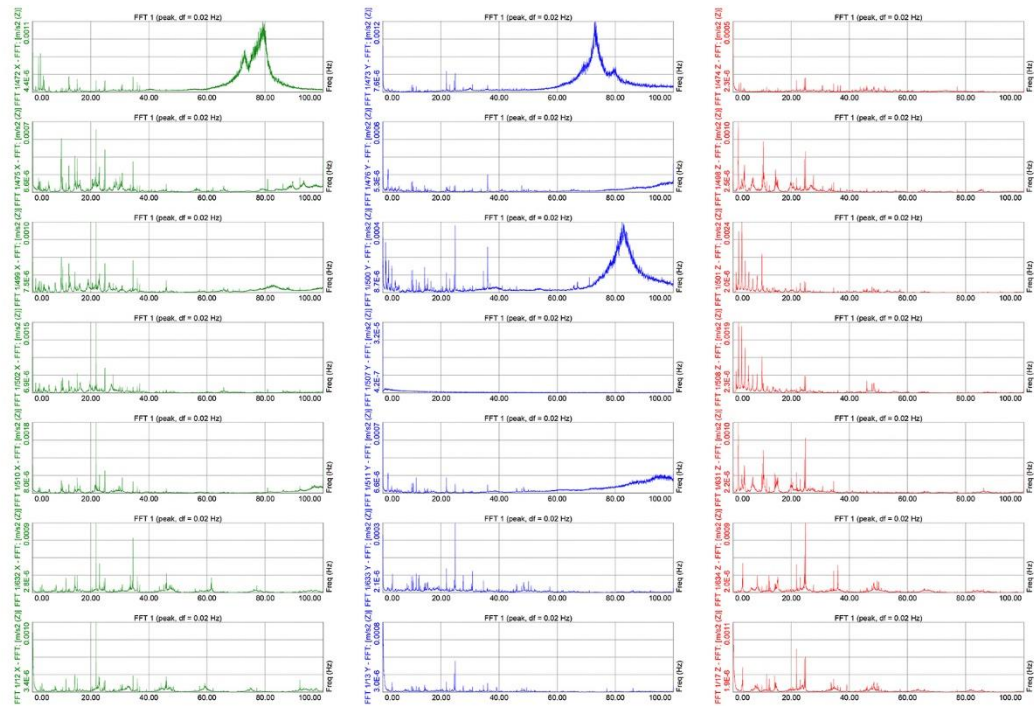


Fig. 4-23 - FFT of the signals of the first acquisition on 26.06.2020

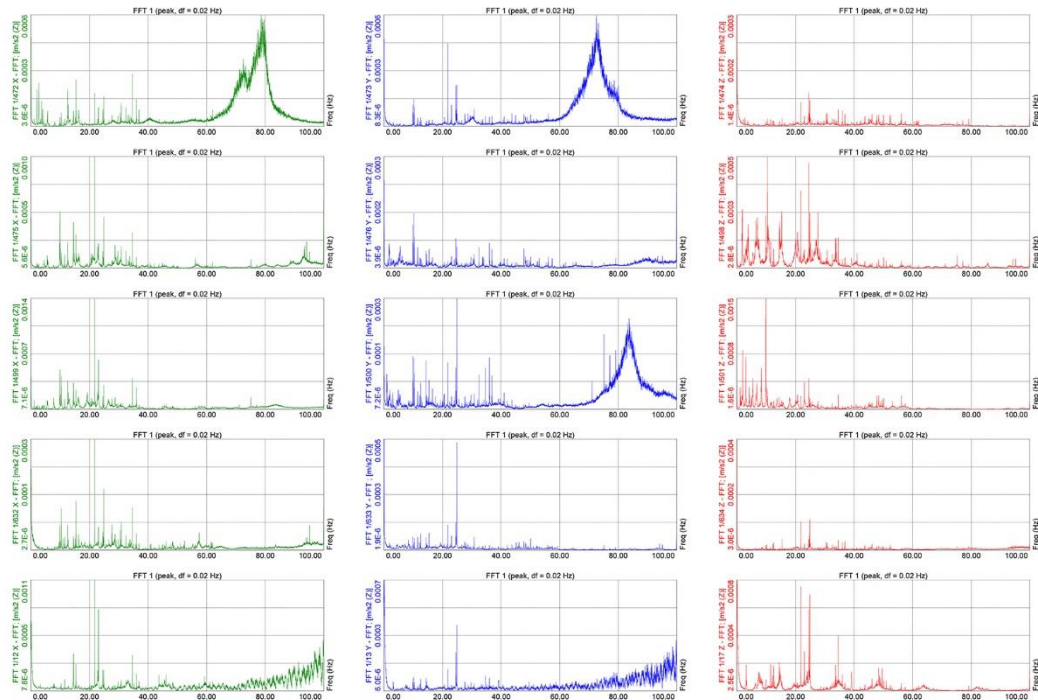


Fig. 4-24 - FFT of the signals of the second acquisition on 26.06.2020

As it possible to see, even in this case, as it is expectable, the frequencies of interest are located in the frequency range between 0 and 20 Hz, which is the one where the investigation have been focused.

4.3.3.2 Preliminary evaluation of the frequency contents of signals acquired on 23.07.2020

The frequency contents of the signals registered during the second day of the monitoring campaign, extrapolated through the FFT algorithm are shown below (Fig. 4-25÷Fig. 4-28):

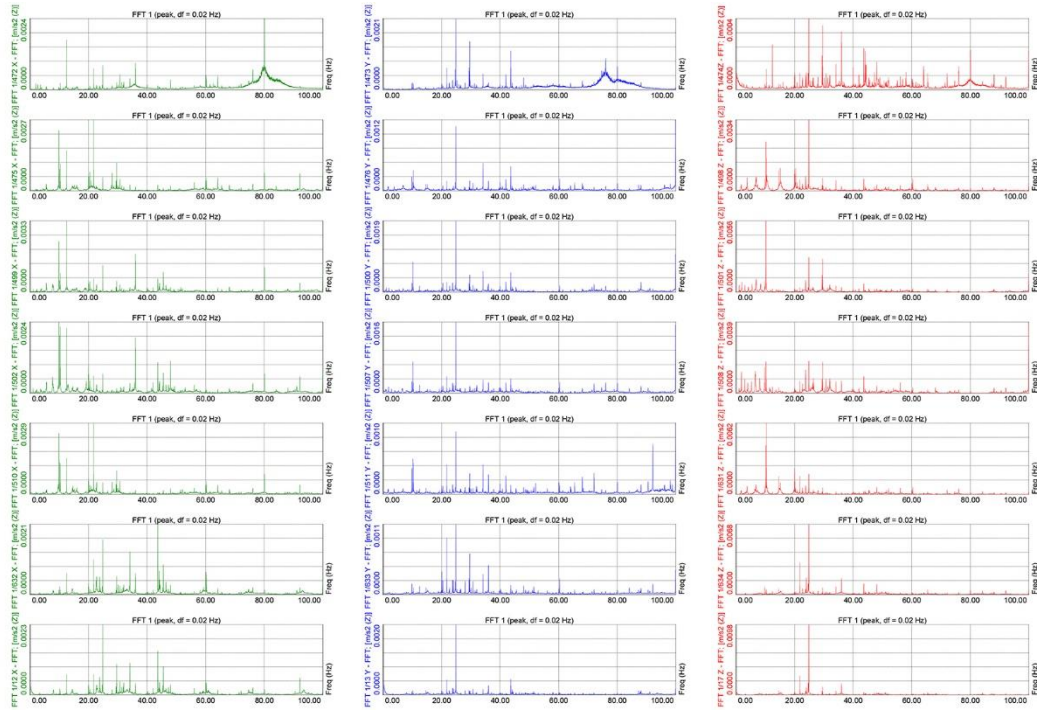


Fig. 4-25 - FFT of the signals of the first acquisition on 23.07.2020

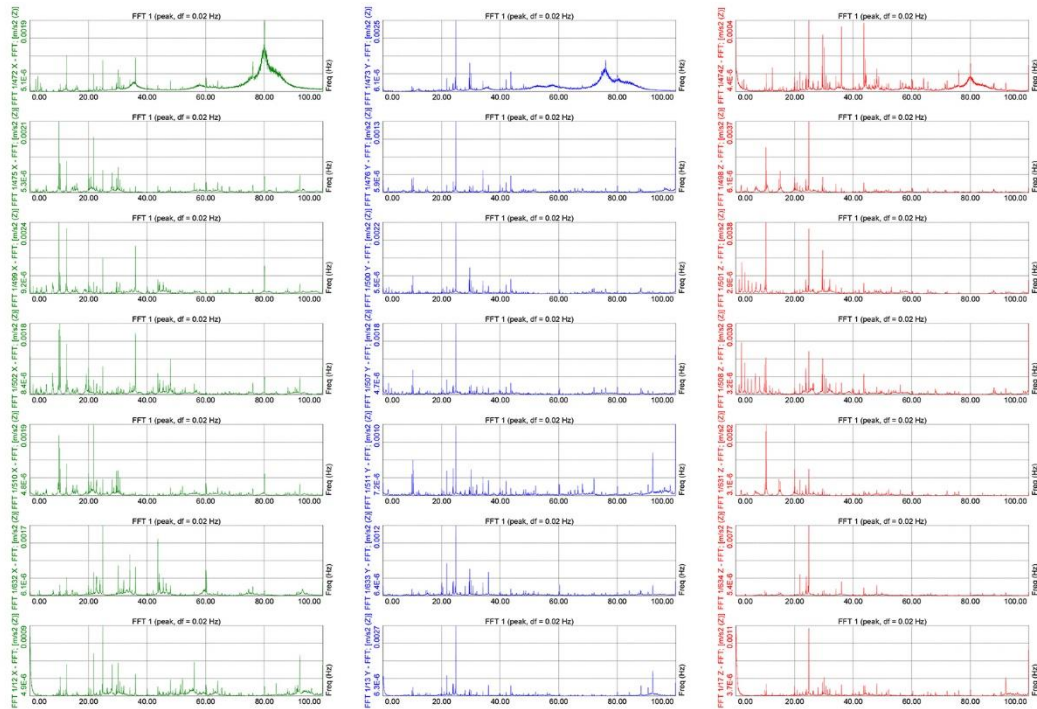


Fig. 4-26 - FFT of the signals of the second acquisition on 23.07.2020

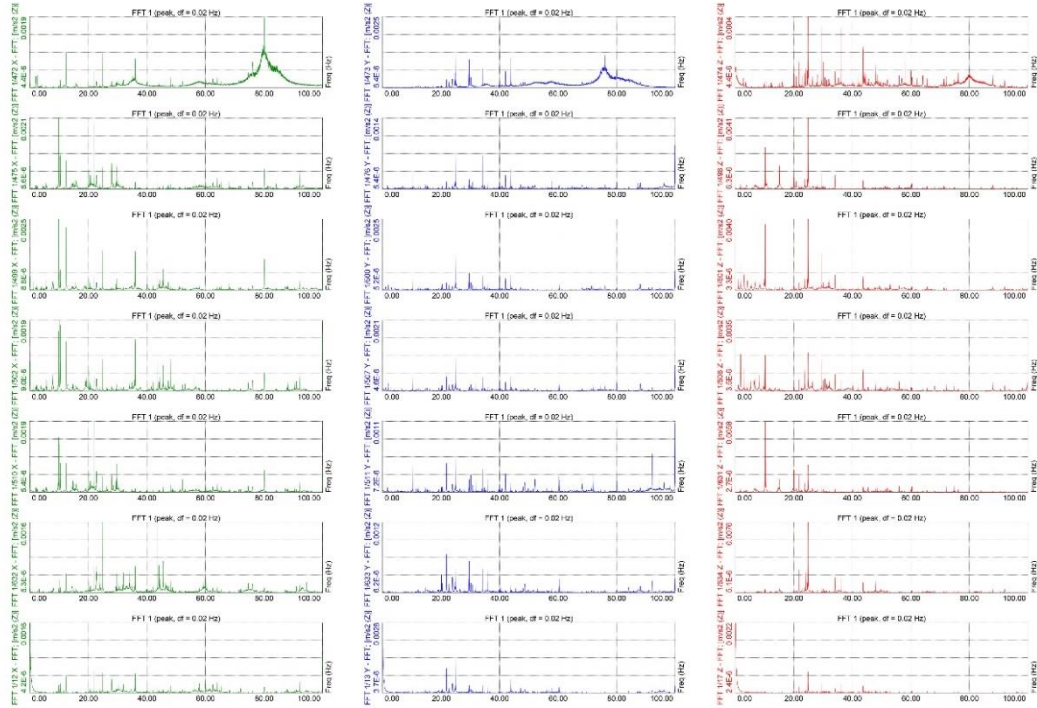


Fig. 4-27 - FFT of the signals of the third acquisition on 23.07.2020

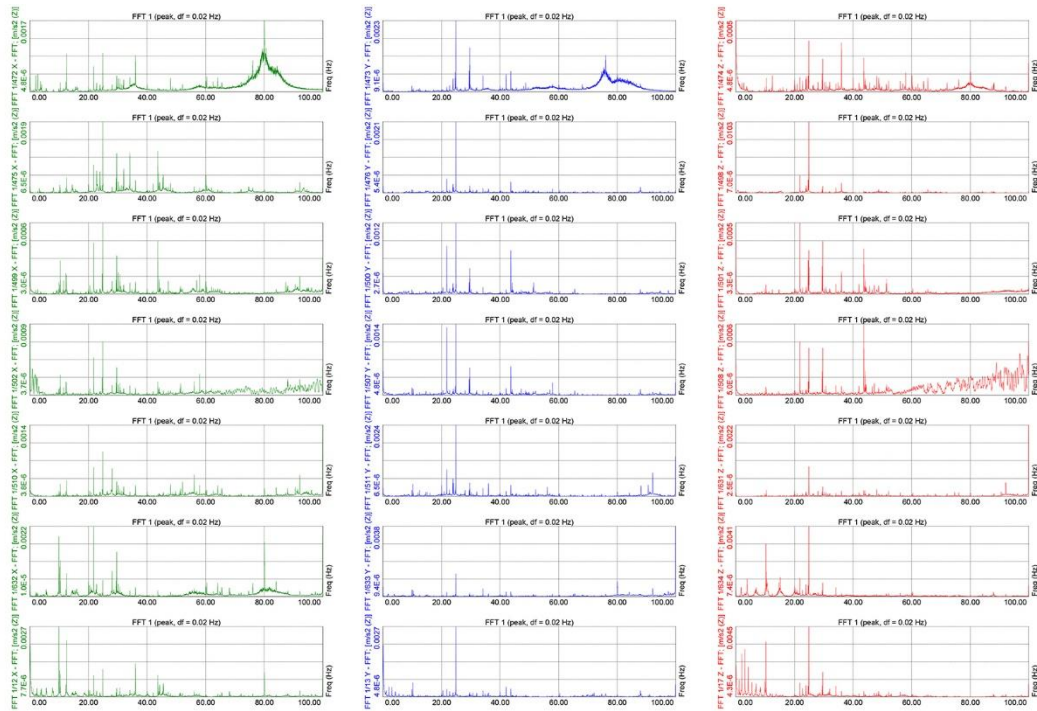


Fig. 4-28 - FFT of the signals of the fourth acquisition on 23.07.2020

Also the antennas numbered from 27 to 30 shows a behavior similar to that found for the structure monitored on the first day. Even in this case the most interesting peaks are concentrated in the range between 0 and 20 Hz.

4.3.4 Identification of Frequencies and Damping ratios through Analysis of Data Acquired on 26.06.2020

By applying the previously described identification algorithm (SSI), the following stabilization diagram is obtained (Fig. 4-29):

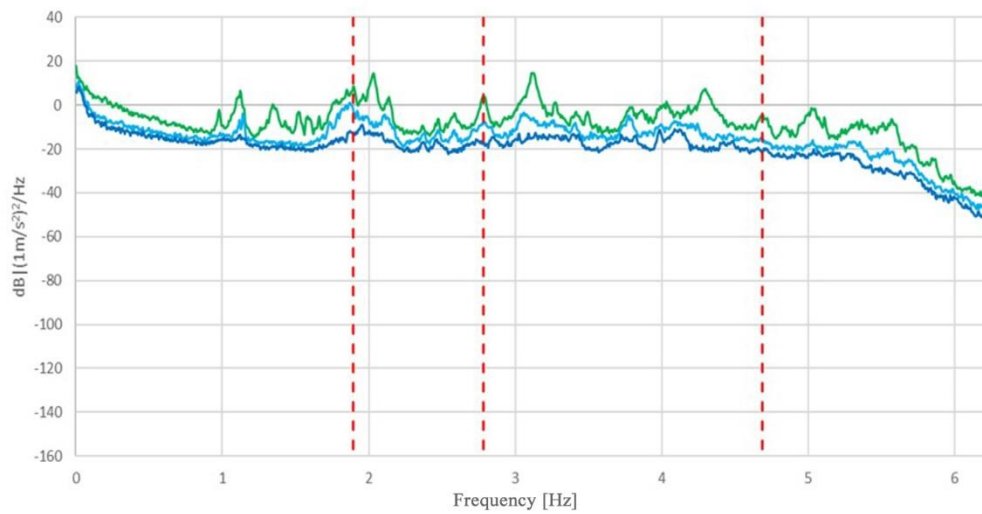


Fig. 4-29 - Stabilization diagram - sample rate 6.25 Hz

Table 4-3 shows the main natural frequencies identified while Fig. 4-30 shows the complexity plot of the estimated frequencies.

Table 4-3 - Main experimental frequencies of Antennas 09 and 10 and related modal dampings

Frequency [Hz]	Damping [%]	Mode Shape
1.894	0.622	Translational X
2.784	0.485	Flexural Z
4.685	0.304	Translational X + Flexural Z

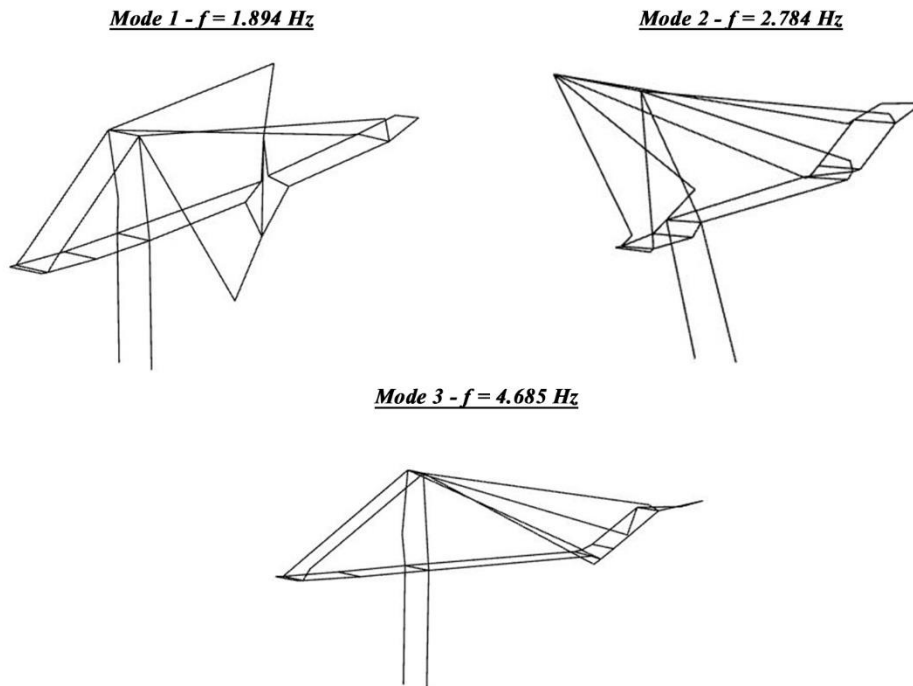


Fig. 4-32 - Mode shapes

The AUTOMAC diagram (Fig. 4-33) correlating the mode shapes with themselves, proves the validity of the extrapolated results.

MAC	1.894 Hz	2.784 Hz	4.685 Hz
1.894 Hz	1	0.0019	0.0004
2.784 Hz	0.0019	1	0.0378
4.685 Hz	0.0004	0.0378	1

Fig. 4-33 - AUTOMAC of the estimated frequencies

4.3.5 Dynamic identification of the stays monitored on 26.06.2020

Table 4-4 shows the frequencies relating to the first proper way of vibrating the stays, obtained through the dynamic identification techniques illustrated in the previous paragraphs. The results of the stays are juxtaposed with each other, so as to highlight the similarity of the results.

Table 4-4 - Frequencies identified for the various stays connected to Antennas 09 and 10

Stay	<u>Antenna 09</u>			<u>Antenna 10</u>		
	Frequency [Hz]	Damping [%]	Complexity [%]	Frequency [Hz]	Damping [%]	Complexity [%]
A	3.208	0.914	0.683	3.306	0.679	0.371
B	1.762	3.03	1.542	1.814	1.089	0.211
C	1.119	3.476	2.47	1.083	1.972	0.042

The mode shapes associated with these frequencies were found to be of the flexural type, while, by passing to the analysis of modes higher than the first, coupling with a transverse component of the motion is observed.

4.3.6 Identification of Frequencies and Damping ratios through Analysis of Data Acquired on 23.07.2020

By applying the previously described identification algorithm (SSI), the following stabilization diagram is obtained (Fig. 4-34) for data acquired over Antennas from Nr. 27 to Nr. 30.

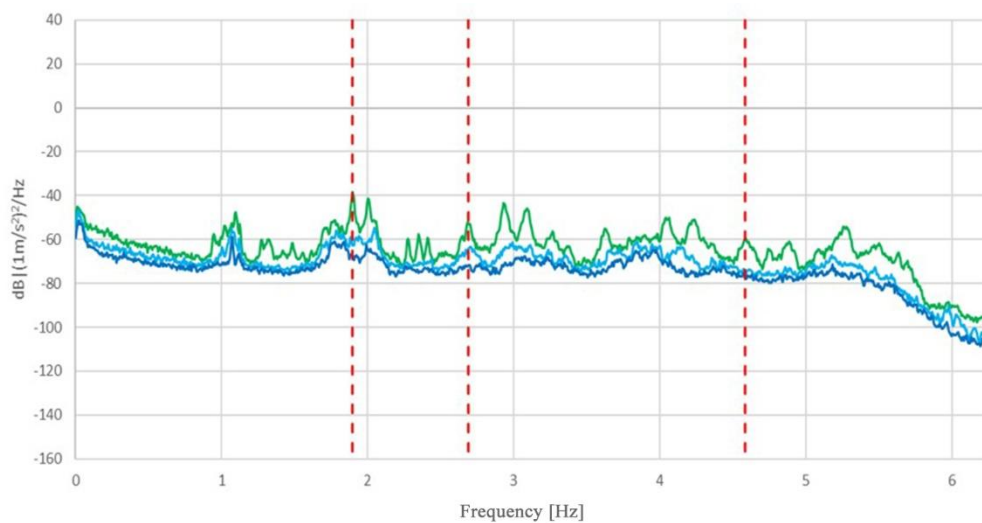


Fig. 4-34 - Stabilization diagram - sample rate 6.25 Hz

Table 4-5 shows the main natural frequencies identified while Fig. 4-35 shows the complexity plot of the estimated frequencies.

Table 4-5 - Main experimental frequencies of the bridge and related modal dampings

Frequency [Hz]	Damping [%]	Mode shape
1.897	0.368	Translational X
2.690	0.580	Flexural Z
4.584	0.399	Translational X + Flexural Z

Looking at the values of extracted modal parameters, and making a comparison with the results of the first part of the monitoring campaign, the similarity of the results is clear, with modal frequencies values, whose variation in respect to those found for Antennas Nr. 09 and Nr. 10, are practically null.

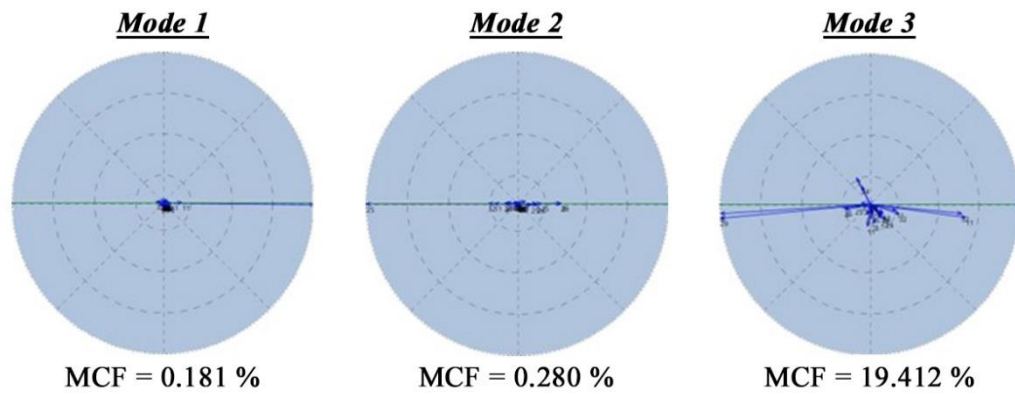


Fig. 4-35 - Complexity plots of the estimated modes

4.3.6.1 Mode shapes representation and validation

Fig. 4-36 illustrates the EM of the structure, where the colored points represents the positions where the sensors have been fixed.

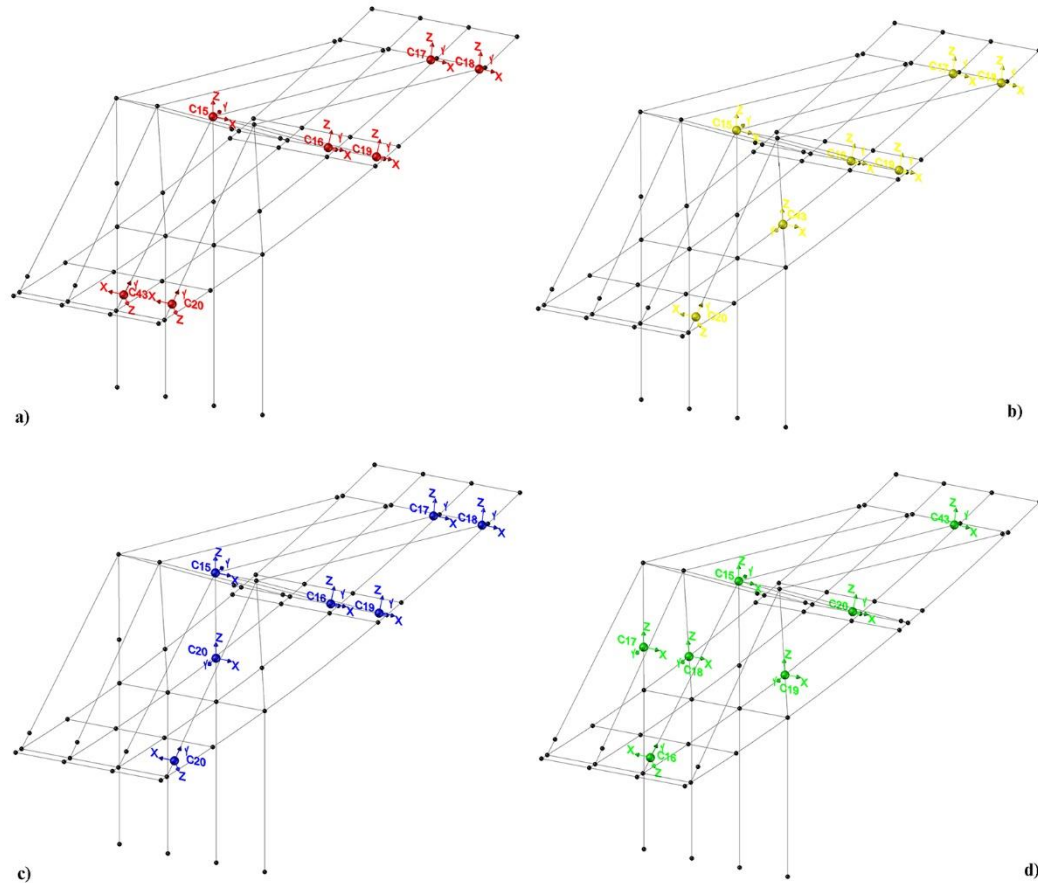


Fig. 4-36 - Experimental model indicating the measurement positions of 23.07.2020: sensor diagram n.1 (a)
sensor diagram n.2 (b) sensor diagram n.3 (c) sensor diagram n.4 (d)

By overlapping the results, obtained by applying the analysis techniques described above to the acquired data, it was possible to identify the following mode shapes (Fig. 4-37) :

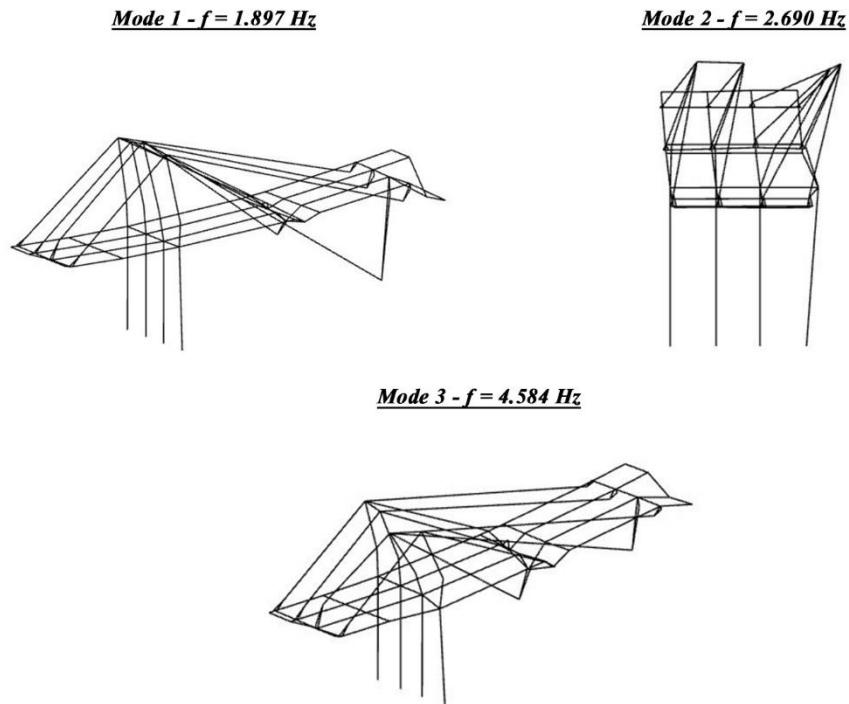


Fig. 4-37 - Mode shapes

Finally, the AUTOMAC diagram is shown (Fig. 4-38), which correlates the modal forms obtained with themselves, assuring the consistency of results.

MAC	1.897 Hz	2.690 Hz	4.584 Hz
1.897 Hz	1	0.0000	0.0150
2.690 Hz	0.0000	1	0.1270
4.584 Hz	0.0150	0.1270	1

Fig. 4-38 - AUTOMAC of the estimated frequencies

Even in this case, a comparison between the dynamic behaviors of the two analyzed systems shows strong similarities, with the principal components of displacements for the first two modes which are practically the same.

4.3.7 Dynamic identification of the stays monitored on 23.07.2020

Table 4-6 shows the frequencies relating to the first proper way of vibrating the stays, obtained through the dynamic identification techniques illustrated in the previous paragraphs. The results of the stays are juxtaposed with each other, so as to highlight the similarity of the results.

Table 4-6 - Frequencies identified for the various stays

<i>Stays</i>	<u><i>Antenna 27</i></u>			<u><i>Antenna 28</i></u>		
	<i>Frequency</i> [Hz]	<i>Damping</i> [%]	<i>Complexity</i> [%]	<i>Frequency</i> [Hz]	<i>Damping</i> [%]	<i>Complexity</i> [%]
A	3.335	1.711	0.141	3.290	0.956	0.485
B	1.798	2.747	0.470	1.779	1.818	0.071
C	1.079	4.609	0.571	1.042	6.647	0.388

Even for the stays of this second system of stays, the mode shapes associated with these frequencies were found to be of the flexural type, with the manifestation, when passing to the analysis of higher modes, of a transversal component of motion.

5 OMA Identification for Model Updating of Finite Elements models of historical buildings

Another field where OMA techniques result particularly effective is that of historical masonry structure, where, thanks to the reduced dimension of the instrumentation, economy and low impact on the artistical heritage, this methodology find always major application. In particular it will be examined one of the most proficient function of this method, which consists in the optimization of Finite Elements models of this building, through a process of calibration of the materials parameters for matching the dynamic characteristics extracted from vibrational data. Thanks to this model updating process it is possible to tune FE models so that the analysis provides more accurate results useful for the preservation of the Cultural Heritage (CH).

Two are the presented case studies: the first one is about the calibration of parameters of four bell towers damaged by earthquake, for whom the model updating was done manually [52]; the second case proposes an innovative procedure of model updating, also applied to a tower, automated through the use of Genetic Algorithm (GA) [53].

5.1 Manual calibration approach: the case study of four bell towers in Ferrara (FE) province, struck by Emilia Earthquake in 2016

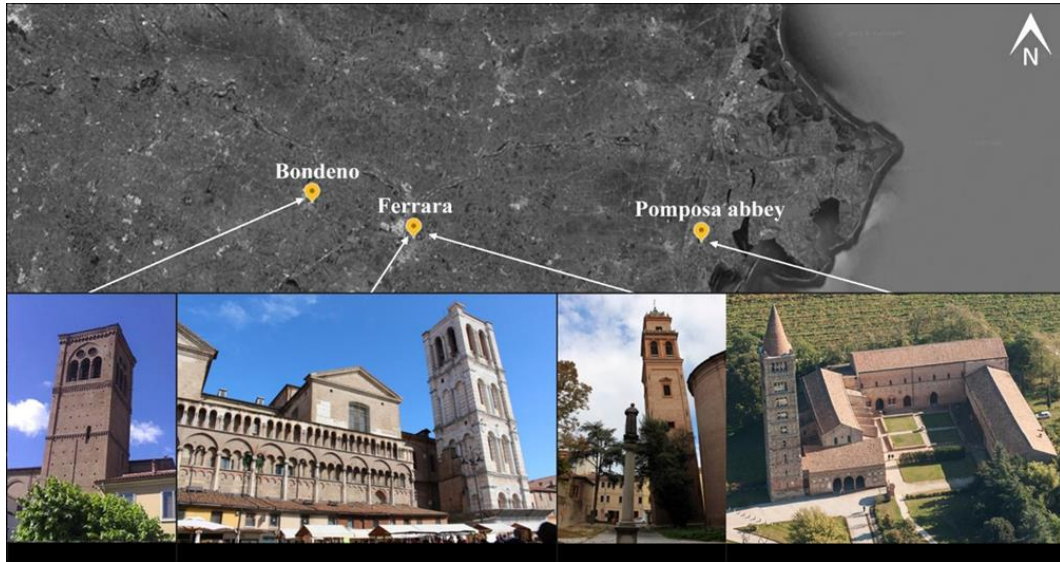


Fig. 5-1 - Towers location - Ferrara Province

The short-time AVT methodology is applied in order to carry out the dynamic identification of four masonry bell towers. To highlight dynamic parameters the acquired time histories were studied both in time and in frequency domains, with the aim to compare the two methodologies. The obtained parameters were then used to update the NMs of each tower. As other authors did [14,54,55], the process of model updating was conducted focusing on the modification of some uncertain materials' parameters, in particular Young's Modulus, in order to have a match of the first natural frequencies and mode shapes between FEMs and OMA. The towers studied are situated in the northern part of Italy in the Emilia-Romagna region, precisely in Ferrara province (Fig. 5-1), and they are:

- San Giorgio Cathedral Belfry in Ferrara;
- San Benedetto Church Belfry in Ferrara;
- Matildea Tower of the Santa Maria church in Bondeno;
- Pomposa Abbey Belfry in Codigoro.

5.1.1 Geometrical and historical description of the case studies

5.1.1.1 *San Giorgio Cathedral Belfry*

The first presented bell tower rises in front of the Trento-Trieste square in the old town of Ferrara, on the south side of the cathedral. The cathedral dates back to the early XII century, while the actual belfry's building process started only in 1412 under the government of Nicolò III d'Este, after that seismic event of 1495 and 1570 damaged the old two little towers that stood on the sides of the presbytery. The structure was erected between 1412 and 1844 but, due to economic matters, the construction was never completed, so it still lacks the initially designed cuspid on the roof. During the years the structure experienced different changes, considering that it was born as isolate tower but in 1703 at the behest of Papa Clemente XI a choir was built beside it and a series of horizontal passages were realized on the vertical walls. However, the bell tower returned to be isolated in 1944, after a bombing during the II Word-war that struck down the choir. The tower has a square plan of 11.70 m sides and a maximum height of 50.78 m. By observing the structure, we can notice four overlapping modules (nuts) whose sides length, constant from the bottom to the top, is approximately 11.7 m. The modules are separated by majestic trabeations, supported by enormous corner columns. The intermediate floors of the two first modules are in wooden, while the others are made by masonry cross vaults, except for the 6th, which has a masonry barrel vault. The cover floor is a not accessible wooden pavilion. The walls are 1.2 m thick, constituted by bricks clamped following the state of the art, with aligned horizontal courses made with good quality mortar. The bricks are covered with rose and white limestone. The thickness remains constant for all the vertical development of the belfry. In all the modules, on the southern side of the tower we can notice arc openings (two for each floor). The arcs are supported by circular columns with diameters varying between 0.75 and 0.9 m. The same architectural order is present on the other sides but without any openings. Only the last module has a different style, with wider arc openings located on every side of the bell cell. On the west side of the tower, there are remains of the old choir of the church (Fig. 5-2). As many of the towers in Ferrara, this one is not in perfect balance since it is inclined of 2° in East-West direction and 0.5° in North-South direction; the inclination is mainly caused by the sandy soil where the city rises up.

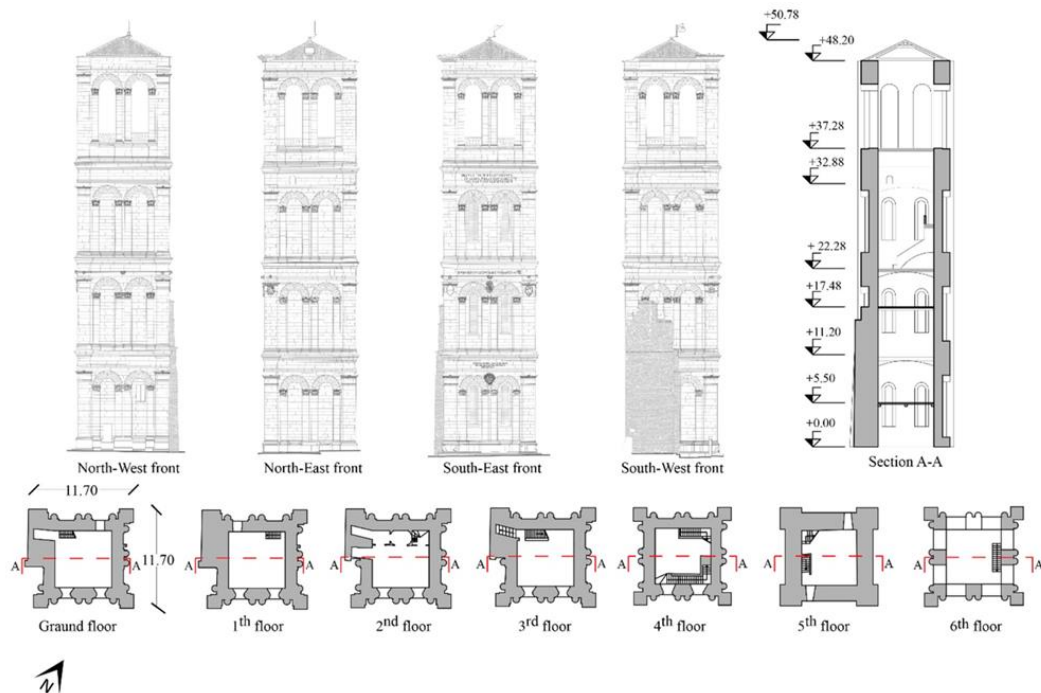


Fig. 5-2 - Geometrical configuration of San Giorgio church belfry in Ferrara

5.1.1.2 San Benedetto Belfry

The isolated belfry of San Benedetto Church arises in the homonymous Square in Ferrara, and it is located on the North-East side of the Church, whose construction started in 1496 thanks to Ercole I d'Este and Andria Bishop after that Benedictine monks abandoned Pomposa Abbey because of a malaria epidemic. The belfry was built starting from 1621, based on the design proposed by Giovanni Battista Aleotti, and was concluded in 1646. During World War II, the church was destroyed but the tower remained unscathed. During the years the bell tower was damaged by a series of storms, the most serious one occurred in 1842 provoking the collapse of the upper part. The structure was also damaged by the seismic events of 2012 that lead to the opening of numerous vertical cracks in both North and South walls.

The tower is 52.45 m tall and presents a squared cross-section plan (7.33 x 7.33 m), which remains constant till the last floor (where the second bell cell is located), where the section decreases to the size of 5.7 x 5.7 m. Even though the outer perimeter remains constant up to the second floor, the walls taper on the inside from 1.40m to 0.88m, while the last floor they consist of 0.45m. There are only two masonry cross vault slabs inside the tower, respectively to 32.37m and 39.7m, connected by a steel stair (Fig. 5-3).

The walls are made of solid and regularly disposed bricks, and with an effective joint offset. Like the one previously described, this tower also has an evident inclination [56], due to the development of foundation' settlement right after the start of the construction works. The building is tilted by 0.5° along North-South direction and 3.07° along East-West direction, which leads to a displacement of the top of the tower of 0.49 m in the North-South direction and 2.82 m in the East-West one. The inclination increased after the 2012 Emilia earthquakes, as reported by the study of [57] that identified an increase of the upper displacement of 18mm. After the 2012 earthquake a series of steel chains were installed at different levels to secure the structure and the foundation was reinforced using micro-piles to prevent a further increase of the inclination.

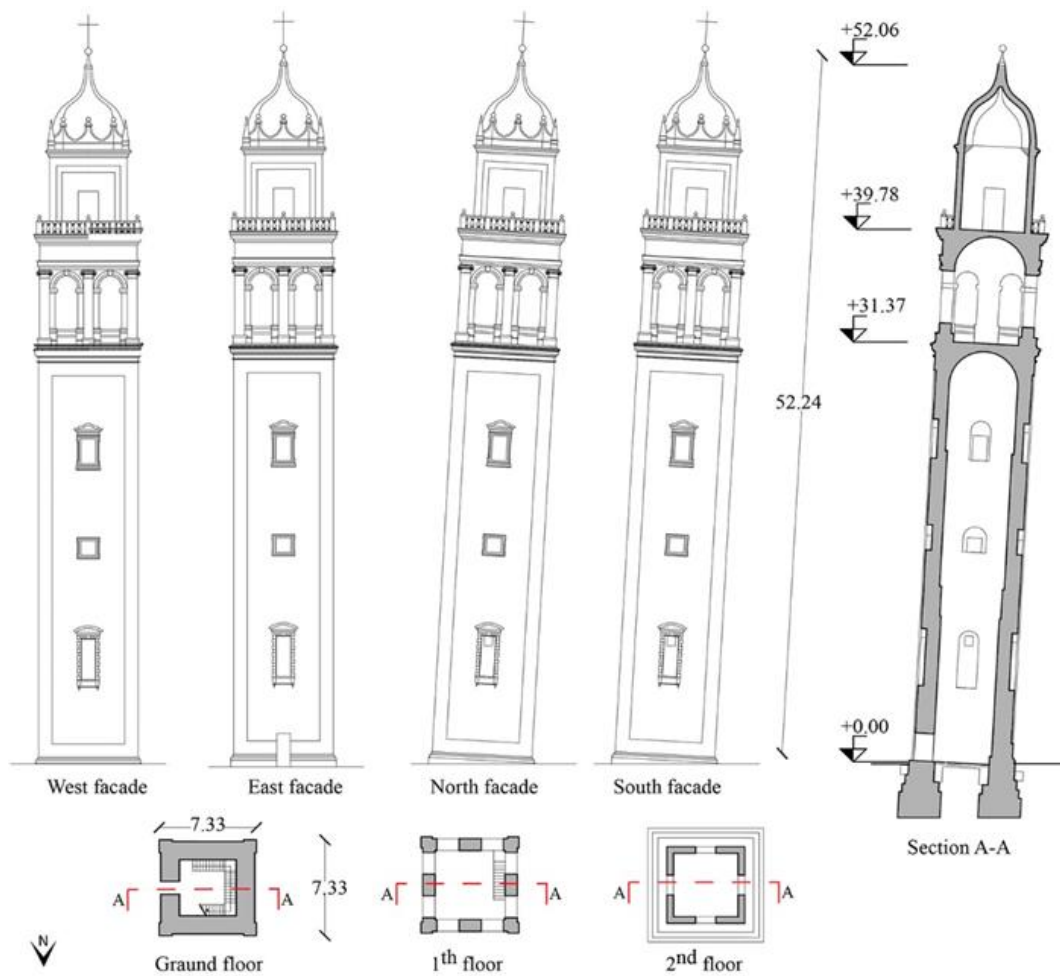


Fig. 5-3 - Geometrical configuration of San Benedetto church tower in Ferrara

5.1.1.3 Matildea Tower

Matildea belfry arises on the side of Maria Vergine Church, which is the main religious building in the city of Bondeno. The church was built in 1114 thanks to a donation made by Matilde of Canossa.

The tower's building process started around the XII century and was concluded at the beginning of the XV century. At the beginning the tower was composed by only two floors (with a height of 12 m) and it was not meant to be a belfry, but it had the aim both to sight and to defend. Two other floors were added later thus the tower reached a height of 30 m becoming a belfry. This development is also testified by the last-gothic style of the bell cell, typical of the latest part of the XIV century. The structure of the tower has a squared cross-section that is constant up to the last floor, with sides of 7.2 m long and a maximum height of 30 m. On the north and east sides, the tower is linked to the church by walls. For what concerns the floors constructive typology, there are cross masonry floors on the first two levels, made with solid bricks, while in the third and the fourth levels the floors are made of wood with orthogonal warping. The cover floor is formed by visible wooden trusses. The walls of the tower are made of solid bricks, with a double case structure that accommodates the stairs in its middle. The external thickness is around 1.05 m for the first three floors, while it decreases to 0.9 m in the remaining three. For the inner part of masonry, the thickness is constant and equal to 0.45 m. The bell cell, that is free of bells, is characterized, on every side, by ogival arcs that encase three-light windows with pointed arches. The ogival arches are supported by little columns, surmounted by oculi (Fig. 5-4).

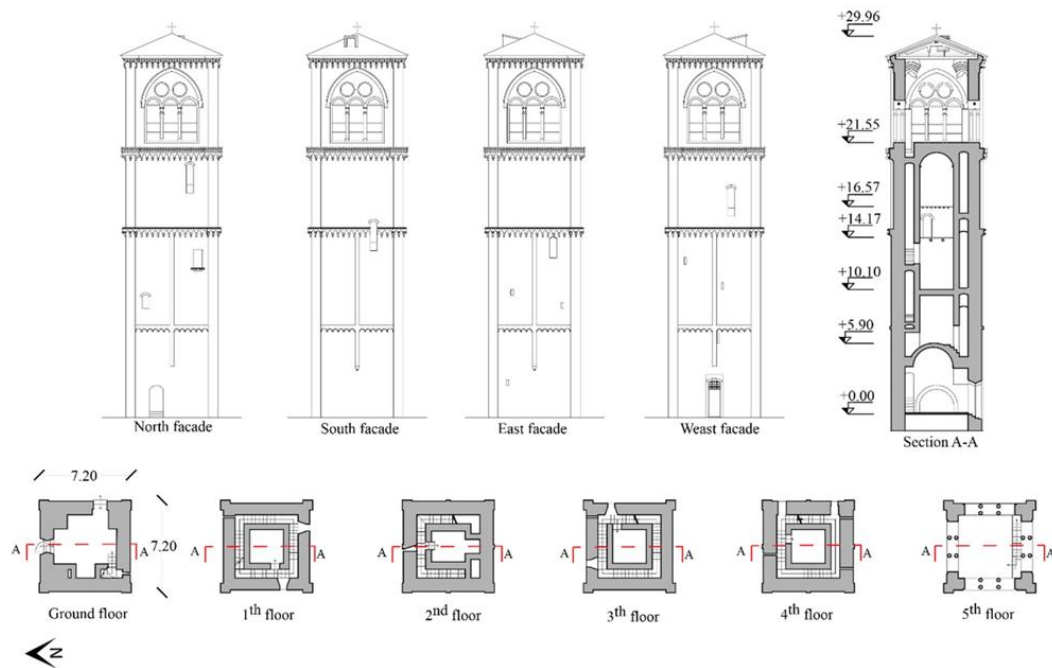


Fig. 5-4 - Geometry configuration of Matildea tower in Bondeno

5.1.1.4 Pomposa Abbey Belfry

This tower is part of the complex of the Benedictine monastery of Pomposa, located in the municipality of Codigoro, and it is a typical example of Romanic architecture. The abbey was built on the remains of a little church of which the construction year is unknown, even though the first traces of its presence date back to IX century, while the bell tower was built-in only 1063 by architect Deusdedit. The belfry did not undergo through many modifications through the years: the first restoration work dates in 1879, when it was necessary to reconstruct the roof cone because of its failing caused by a lightning bolt; in this occasion the walls were also reinforced through the application of steel chains, posed at floors' levels. During the last years a foundation settlement caused the inclination of the building due to the weight of the structure (around 1800 tons).

The belfry is 48 m tall, with a squared cross-section, whose sizes at the base are 7.60 x 7.60 m degressive with the height. The structure is composed by nine modules, surmounted by a conical shape cover of 11.69 m in height and 6.35 m in diameter. The building lands on a truncated pyramid base composed of marmoreal elements. The external walls are made of red and yellow solid bricks, with some fragments of marmoreal parts. Its thickness varies from 1.34 m to 0.59 m. Openings of different shapes are presents on the facades, their size and the number increasing up to the top in order to decrease the weight of the structure. The floors are made of wood with orthogonal warping at all levels, except for the bell cell floor where a concrete ceiling is present. The levels are connected through wooden stairs, and the tower is connected at its base to the monastery by thin walls (Fig. 5-5**Errore. L'origine riferimento non è stata trovata.**).

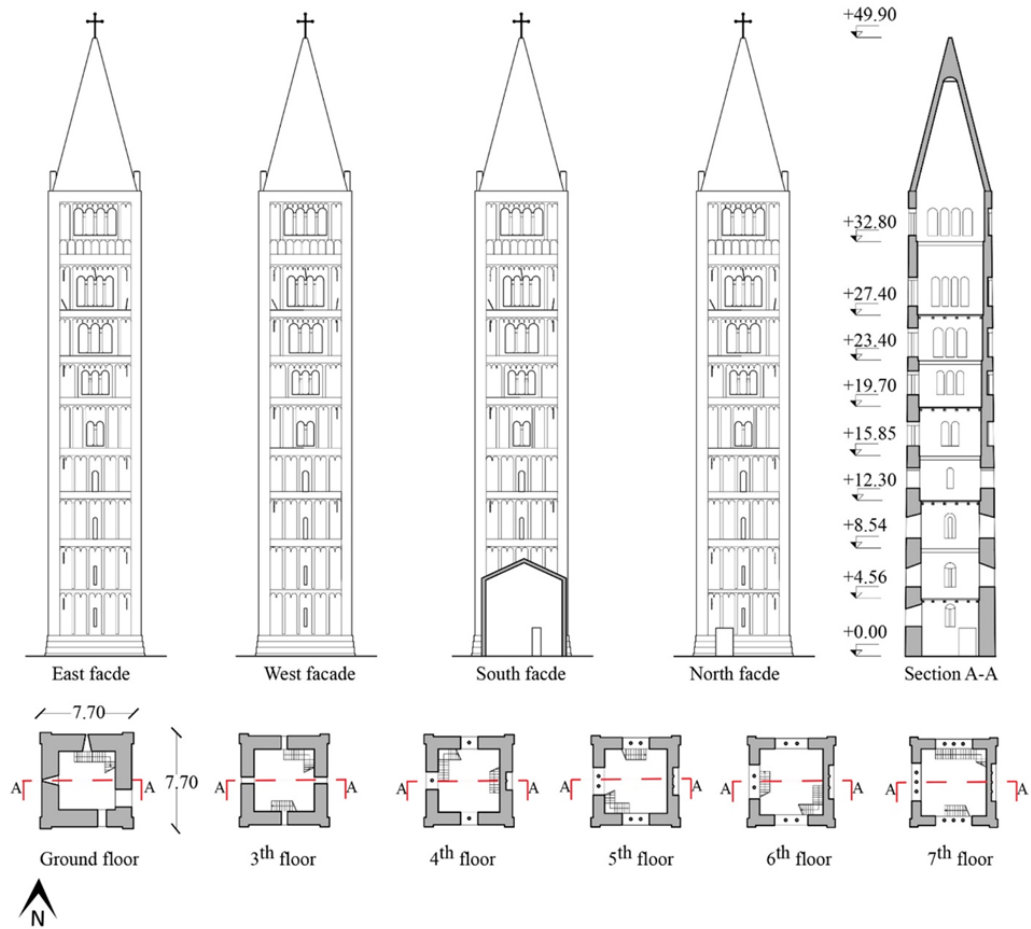


Fig. 5-5 - Geometry configuration of Pomposa abbey tower in Codigoro

5.1.2 Ambient vibration testing

This type of structures, along with all the historical masonry buildings, is usually studied by applying linear and nonlinear analysis on FEMs, since Numerical Models (NMs) give the chance to operate significant simplifications on historical structures due to the impossibility to clearly identify the spandrels and piers for their irregular geometry [11]. In most cases, FEMs seemed to be able to reproduce the real behavior but to be sure on the accuracy of the results all the parameters as the properties of materials and each connection between the elements should be known. During the last few years, the most common technique used to overcome these issues is the AVT, which consists of the monitoring of vibrations of the buildings under ambient noises as wind, traffic etc., in order to identify the real dynamic behavior. The monitoring is performed by using accelerometers placed on the most relevant positions of the structure that are probably most involved by the motion. After recording and filtering the data, the results are processed and then used to produce an Experimental

Model (EM). The EM response is compared with the preliminary response of the NM, which is then refined, by focusing on the unclear parameters, in order to fit the experimental results. In this section each phase is shown starting by the monitoring campaign, passing through the analysis of the data and to finish with the construction and calibration of the NMs.

5.1.2.1 Acceleration sensors layout and data acquisition settings

The sensors network used in the survey campaign was composed of 8 uniaxial accelerometers, with a sensitivity of 1V/g and a measurement range of 8g, connected to two 4-channels modules NI9132 AC/DC with a 24-bit resolution, 102dB dynamic range and anti-aliasing filter related to a multi-channel data acquisition system CompacDAQ-9132.

The configuration was set in the most favorable way to detect the translational and torsional components of displacements of the towers [19]. With this aim, the sensors were positioned to the corners or close to them, depending on the accessibility of the areas. To acquire the largest number of measurements with only a few accelerometers, different acquisitions were carried out by keeping some sensors fixed in the highest reachable position for the towers and modifying the positions of other sensors at each acquisition. The accelerometers were fixed with bi-component resin to make sure they were properly connected to the structure, and to prevent damages on the building. The different sensors layout is shown in Fig. 5-6.

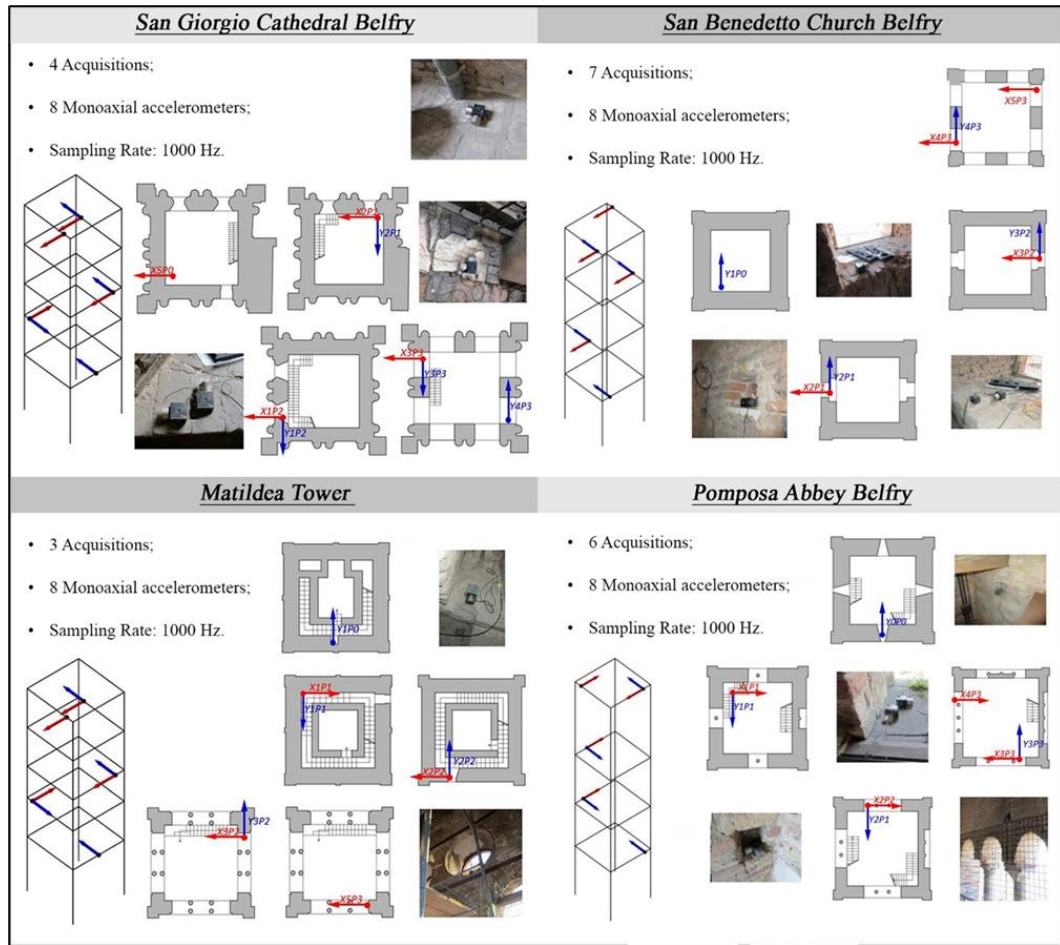


Fig. 5-6 - Wired accelerometric sensors schemes

The registration time for vibrations varied from 20 min to over 1 h, in order to respect Rodriguez condition [58] which imposes an acquisition duration of at least 2000 times the expected period for the structure, so capturing was long enough to eliminate the influence of possible non-stochastic excitations that may occur during the tests. Raw data were originally acquired with a sample rate of 1000 Hz.

5.1.2.2 AVT Data processing

The data were elaborated to obtain the dynamic characteristics. The first operation was to clean the data by all the noise applying a low pass filter. Then, in order to decrease the computational time, raw data were re-sampled through a decimation, before the real signal processing, obtaining the final range of 0 – 6.25 Hz, consistent with the frequencies range of the analyzed structures.

Different algorithms are suitable to process the data; in this work the identification of the frequencies of the four belfries was conducted through two different methods, the Enhanced Frequency Domain

Decomposition (EFDD) and the Stochastic Subspace Identification (SSI), in order to compare the results [59].

In the application of both the methods, we realized that the ideal condition in the definition of a mode is that the eigenvector that describes the mode shape is composed of all real values: satisfying this condition means that for every vibration cycle, being the phase equal to 0° or 180°, the maximum deflection of all the parts of the structure is reached at the same time and so it is possible to adopt a proportional damping model. However, because of the effect of measurement errors and signal noise, the occurrence of aliasing and leakage in the signal post-processing, identification errors, or asymmetries linked to gyroscopic effects or non-linear behavior, is it possible to incur in complex modes [60]. Consequently, the criteria adopted for the selection of the modal frequencies was that the chosen ones should have been those with the lowest level of complexity, which can be measured through the calculation of the so-called Mode Complexity Factor (MCF) [39,61]:

$$MCF_r = 1 - \frac{(S_{xx} - S_{yy})^2 + 4S_{xy}^2}{(S_{xx} + S_{yy})^2} \quad (5.1)$$

where:

- r subscript indicates the considered mode;
- $S_{xx} = Re\{\psi_r\}^T Re\{\psi_r\}$;
- $S_{yy} = Im\{\psi_r\}^T Im\{\psi_r\}$;
- $S_{xy} = Re\{\psi_r\}^T Im\{\psi_r\}$.

5.1.2.3 Enhanced Frequency Domain Decomposition

The EFDD is an improved version of the classical Frequency Domain Decomposition (FDD) technique, which uses a single line from the Fast Fourier Transform (FFT) for the estimation of the natural frequency and does not calculate the modal damping. The EFDD method consists in identifying a Single Degree of Freedom (SDOF) Power Spectral Density (PSD) function in the proximity of a peak of resonance, highlighted through the Peak Picking method (like in FDD), and then transporting it back to the time domain with the Inverse Discrete Fourier Transform.

In EFDD method the measured responses are linked to the unknown input through the relationship expressed by Eq. 5.2:

$$[G_{yy}(\omega)] = [\bar{H}(\omega)][G_{xx}(\omega)][\bar{H}(\omega)]^T \quad (5.2)$$

where:

- G_{xx} is the [r-by-r] PSD matrix of r inputs;

- G_{yy} is the [m-by-m] PSD matrix of m responses;
- $\bar{H}(\omega)$ is the [m-by-r] Frequency Response Function (FRF) matrix, with the overbar indicating its complex conjugate, while the superscript T stands for the transpose.

The G_{yy} matrix is composed by the vectors of the modal shapes associated to the modes concurring at a particular frequency. Through a process known as Singular Value Decomposition (SVD), this form of the matrix is decomposed into a set of eigenvalues and their corresponding eigenvectors, which are an approximation of the mode shapes. This decomposition process leads to the identification of the SDOF models of the problem [62]. Then the natural frequency is calculated on the base of the number of zero-crossing as dependent from time, while the modal damping is evaluated from the logarithmic decrement of the normalized correlation function associated to the SDOF system. Considering also modal damping, EFDD allows a more accurate estimation of both natural frequencies and mode shapes, in comparison with FDD [63].

In Fig. 5-7 the singular values of the PSD matrix of response for every tower are shown and the modal frequencies, and associated damping ratios, are highlighted.

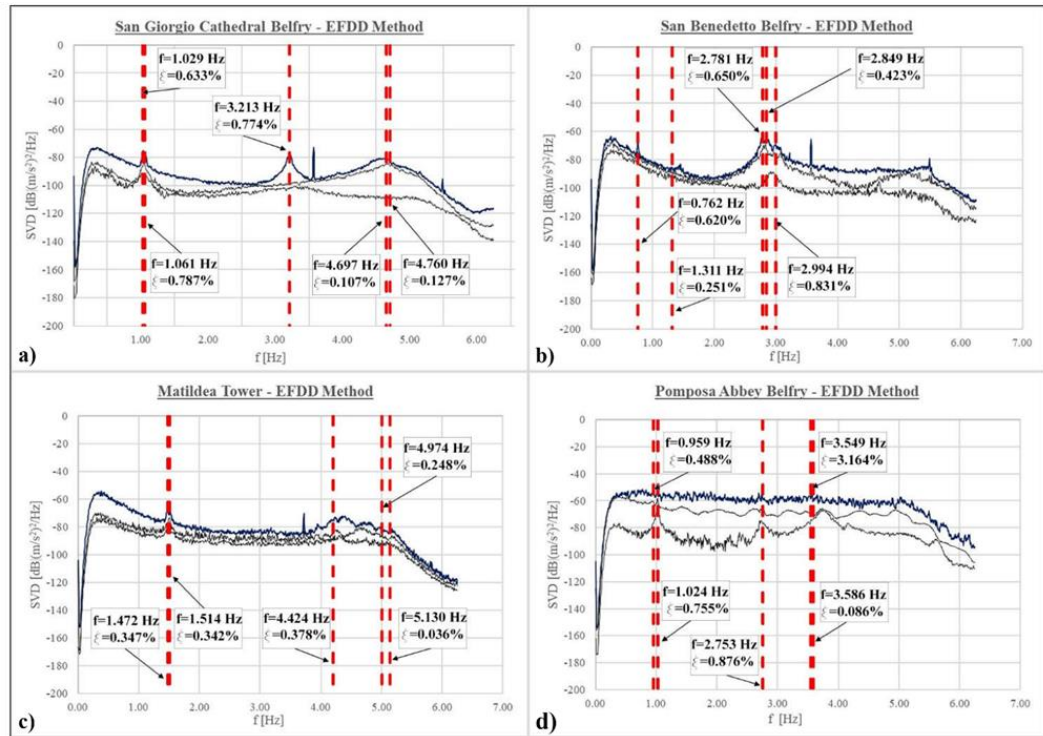


Fig. 5-7 - Graphs for EFDD method

From the EFDD results it is clearly remarkable (Fig. 5-7) that the frequencies are in the range of 1÷5 Hz. As may be expected, the Matildea tower is the most rigid one ($f_1=1.472$ Hz), due to its little height

and its double box structure, whereas San Benedetto appeared to be the most deformable tower ($f_1=0.762$ Hz), since it has only two floors that interrupt the elevation. At a first sight, it is observable that, apart for San Benedetto, all the towers frequencies display the same trend: the first two frequencies are in the range 1÷1.5 Hz (Fig. 5-7), with percentage differences around 3.1-2.9%, for San Giorgio Belfry (Fig. 5-7a) and Matildea Tower (Fig. 5-7c), and 6.8% for Pomposa Abbey Belfry (Fig. 5-7d): the proximity of the first two frequencies is typical of symmetrical structures. The third frequency is in an intermediate position among the first two ones and the 4th and 5th ones, which also result very close to each other (with percentage difference always inferior to the 10%). The differences presented by the tower of San Benedetto are most likely generated by its high inclination, in this case the distance among the first two frequencies is 72% while the third is also close to the 4th and the 5th (Fig. 5-7b).

5.1.2.4 Stochastic Subspace Identification

The SSI method [33], instead, is applied in the time domain. It is the most used identification technique among the OMA methodologies. It mainly consists of the application of a mathematical model which upgrades its parameters in order to match the raw time series data characteristics. It is based on the conversion of the second order problem, expressed by the dynamical equation, into a set of two equations, through the construction of State Space models: the “state equation” (Eq. 5.3) and the “observation equation” (Eq. 5.4), here expressed in their discretized form:

$$\{\hat{x}_{k+1}\} = [A]\{\hat{x}_k\} + [B]\{u_k\} \quad (5.3)$$

$$\{y_k\} = [C]\{\hat{x}_k\} + [D]\{u_k\} \quad (5.4)$$

where:

- $[A]$ is the matrix of input physical information;
- $[B]$ is the matrix of input statistical parameters;
- $[C]$ is the discrete output matrix;
- $[D]$ is the direct output transmission matrix;
- $x_k = x_k(\Delta t)$ is the discrete-time vector containing the sampled displacement and velocities;
- $\{y_k\}, \{u_k\}$ are the vectors of sampled input and output.

Other parameters describing the dynamic system are considered as deterministic and should not be subdued to the variations linked to excitation changes.

The frequencies and damping ratios of the four structures, extracted through the application of the SSI method, are shown in Fig. 5-8, where the Singular Value Decomposition (SVD) graphs are reported.

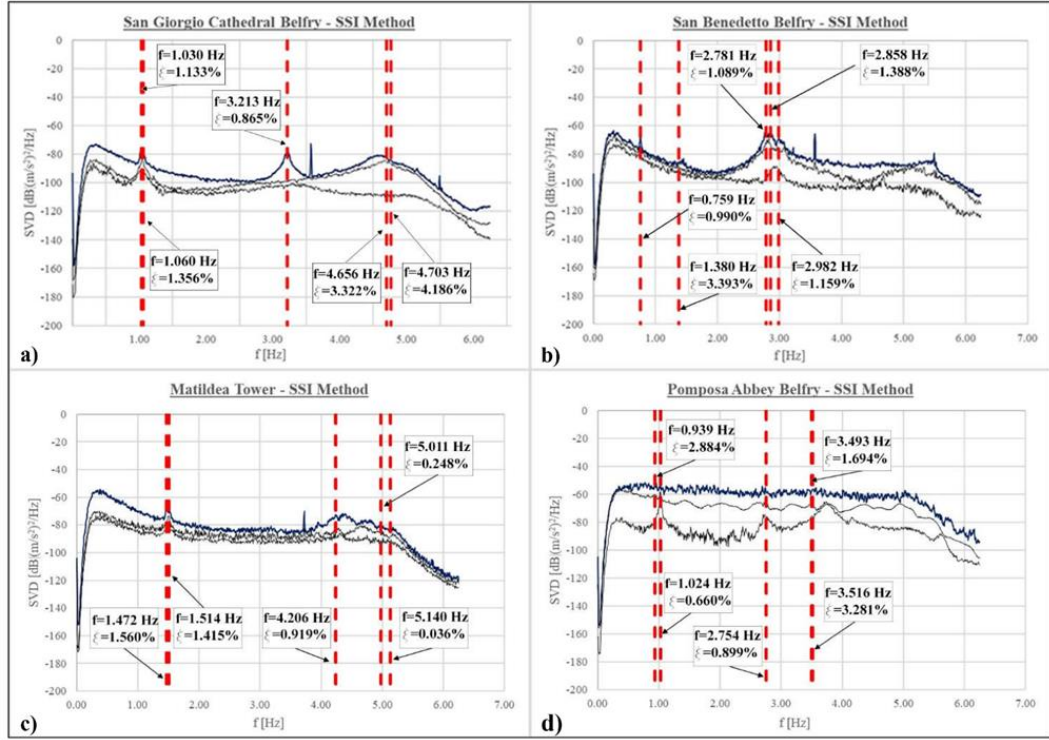


Fig. 5-8 - SVD graphs for SSI method

As seen before for the EFDD, in this case, all the towers frequencies display the same trend, apart for San Benedetto: the first two frequencies are in the range 1÷1.5 Hz (Fig. 5-8), typical of symmetric towers, with percentage differences around 2.7-2.8% for San Giorgio Belfry (Fig. 5-8a) and Matildea Tower (Fig. 5-8c), and 8.3% for Pomposa Abbey Belfry (Fig. 5-8d), the third frequency is located in an intermediate position among the first two ones and the 4th and 5th ones, which also result very near between themselves (with percentage difference always less than 10%).

5.1.2.5 Comparison and validation of the experimental results

A first comparison between the results produced using both methodologies was operated in terms of frequencies, damping ratios and complexity. In particular, the comparison between the frequencies is expressed through the formula [64]:

$$\Delta f_i[\%] = \left| \frac{f_{i,SSI} - f_{i,EFDD}}{f_{i,SSI}} \right| \cdot 100 \quad (5.5)$$

where $f_{i,SSI}$ and $f_{i,EFDD}$ are the natural frequencies for the i -th mode, obtained with the SSI and EFDD methods. In the following parts of the work, in the comparisons among the analytical and experimental frequencies, the subscript SSI will be assigned to the experimental ones, while the EFDD will correspond to the NM ones.

It became clear that both methods provided approximately the same frequencies, in fact the differences are lower than 2% except for the 2nd frequency of the San Benedetto belfry where the difference is of ~5.3% (Fig. 5-10). The results that are more different instead concern the complexity and the damping, as also the study of [65] shows.

It is notable that, even though the maximum difference in terms of frequencies never exceeds the 5%, there is no coincidence between damping ratios extracted from EFDD and SSI, with these last ones that are always more elevate, except for the 2nd and 4th values of Pomposa Belfry. This particular aspect can probably be linked to the low intensity of the measured excitations, that do not allow to obtain reliable measures of the damping ratios [66].

The third comparison was operated on the mode shapes associated to the first five modes analyzed for each tower, which are reported in Fig. 5-9÷Fig. 5-12. As stated in many studies on towers, it has been noted that the first two modes are usually translational while the third appears to be rotational, as we may also notice in these cases, except for San Benedetto in which the third modal shape is not translational but flexural in Y-direction, as seen in the first mode. This difference may be traced back to the inclination of the tower that is just this direction; the last two frequencies instead are flexural for all the models. It is possible to observe a good level of correspondence between SSI and EFDD results.

This feature is also confirmed through a validation process, operated applying MAC [39,61], a tool used in case of complex modes to execute a comparison between the modal vectors describing a modal shape, providing an indication about the consistency of a mode shape. It is calculated as the normalized scalar product of the two sets of vectors $\{\varphi_A\}$, which is the compatible analytical modal vector associated to the r mode, and $\{\varphi_X\}$, which is the test modal vector associated to the q mode:

$$MAC(r, q) = \frac{|\{\varphi_A\}_r^T \{\varphi_X\}_q|^2}{(\{\varphi_A\}_r^T \{\varphi_A\}_r)(\{\varphi_X\}_q^T \{\varphi_X\}_q)} \quad (5.6)$$

The scalar results are arranged in the MAC matrix, whose optimal configuration is that of values near or equal to 1 for the principal diagonal and equal to 0 outside of the diagonal, assuring the perfect independency of the modes.

The MAC was used in this work for the validation process of the modes selected with the EFDD and SSI methods, and to assure the coherence of results through the comparison between the results produced by these different methodologies [59]. This last operation was conducted through a variation of the MAC criterion: the CrossMAC. Like in the classical MAC criterion, every possible combination of analytical and test vector, associated to the *i-th* mode are checked, but the improved version of the consistency correspondence criterion is calculated using as sets of rows and columns of

the MAC matrix, modal shape vectors coming from different sets of modes. This makes the method particularly suitable for evaluate the affinity between test models and FEM models [45]. CrossMAC matrices are reported in Table 5-1÷Table 5-4, as can be seen the data oscillate between 63% and 99.80% a sign that the two methods have identified very similar modes.

Due to the good correspondence of the results between the two methodologies, the identification process was considered satisfactory thus we decided to use only the parameters extracted from the SSI approach as the ones for the definition of the experimental model for the following calibration of the NMs.

Table 5-1 - San Giorgio Belfry - Modal Identification results

<i>San Giorgio Belfry</i>									
Mode	EFDD Method			SSI Method			Comparison		
	f [Hz]	ξ [%]	Complexity [%]	f [Hz]	ξ [%]	Complexity [%]	Δf [%]	$\Delta \xi$ [%]	CrossMAC [%]
$\varphi 1$	1.029	0.633	3.028	1.030	1.133	0.629	0.100	0.500	96.20
$\varphi 2$	1.061	0.787	0.262	1.060	1.356	0.065	0.090	0.569	96.80
$\varphi 3$	3.213	0.774	0.296	3.213	0.865	0.082	0.000	0.091	99.80
$\varphi 4$	4.697	0.107	0.198	4.656	3.322	15.049	0.870	3.215	87.50
$\varphi 5$	4.760	0.127	4.074	4.703	4.186	5.596	1.200	4.059	76.30

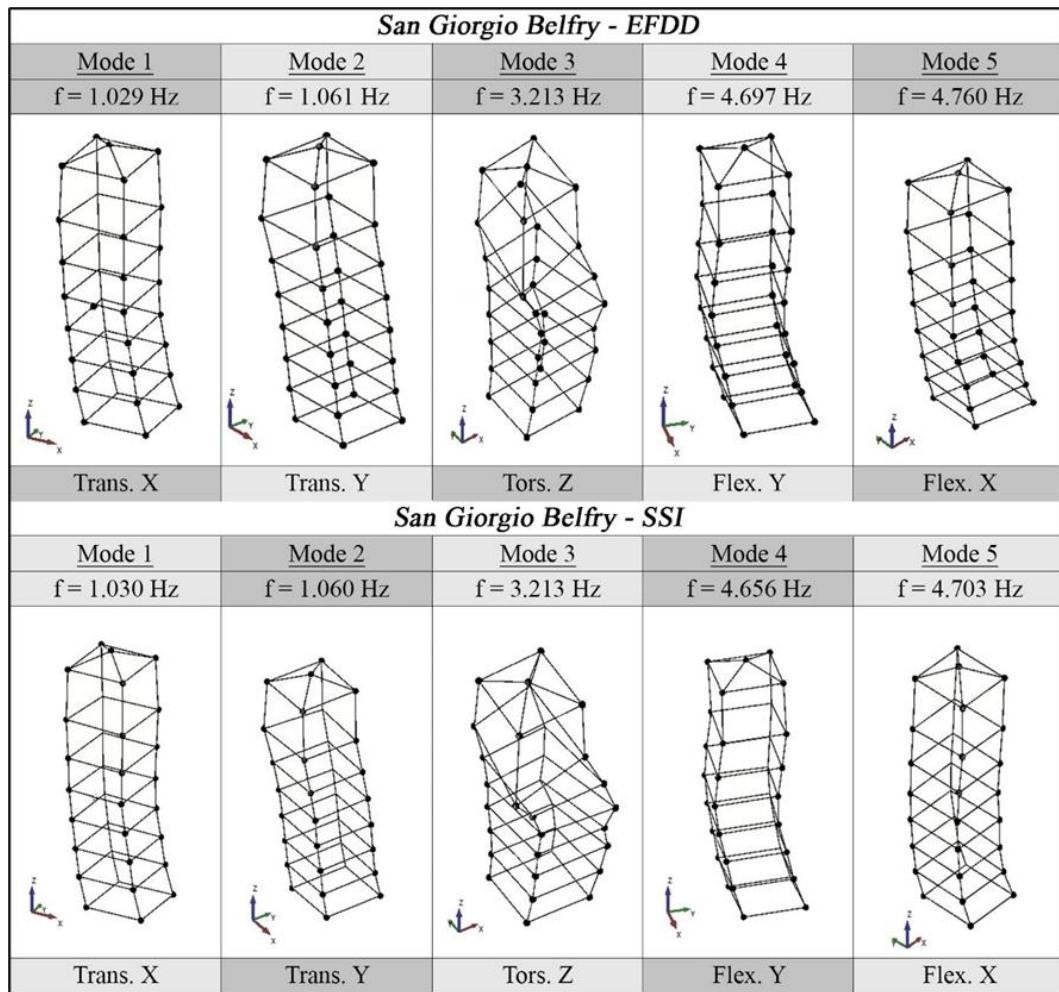


Fig. 5-9 - San Giorgio Belfry - Comparison between EFDD and SSI mode shapes

Table 5-2 - San Benedetto Belfry - Modal Identification results

San Benedetto Belfry									
Mode	EFDD Method			SSI Method			Comparison		
	f [Hz]	ξ [%]	Complexity [%]	f [Hz]	ξ [%]	Complexity [%]	Δf [%]	$\Delta \xi$ [%]	CrossMAC [%]
φ_1	0.762	0.620	4.834	0.759	0.990	0.609	0.390	0.370	96.20
φ_2	1.311	0.251	5.913	1.380	3.393	4.284	5.260	3.142	72.00
φ_3	2.781	0.650	0.774	2.781	1.089	3.498	0.000	0.439	97.70
φ_4	2.849	0.423	11.605	2.858	1.388	3.539	0.320	0.965	92.90
φ_5	2.994	0.831	0.435	2.982	1.159	6.170	0.400	0.328	97.50

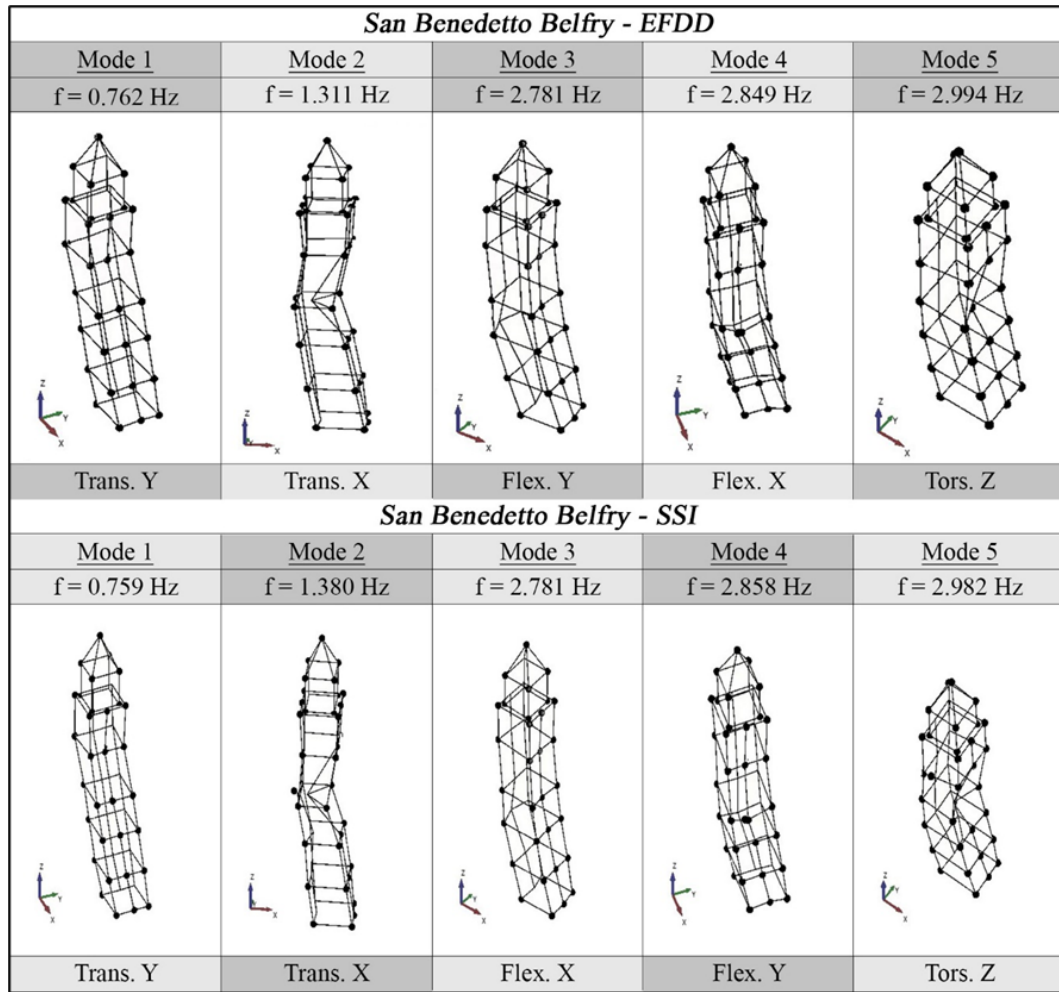


Fig. 5-10 - San Benedetto Belfry - Comparison between EFDD and SSI mode shapes

Table 5-3 - Matildea Tower - Modal Identification results

Matildea Tower									
Mode	EFDD Method			SSI Method			Comparison		
	f [Hz]	ξ [%]	Complexity [%]	f [Hz]	ξ [%]	Complexity [%]	Δf [%]	$\Delta \xi$ [%]	CrossMAC [%]
φ_1	1.472	0.347	1.284	1.478	0.990	0.609	0.410	0.643	94.10
φ_2	1.514	0.342	6.493	1.513	3.393	4.284	0.070	3.051	92.10
φ_3	4.240	0.378	11.001	4.206	1.089	3.498	0.800	0.711	92.90
φ_4	4.978	0.248	4.947	5.011	1.388	3.539	0.660	1.140	83.10
φ_5	5.130	0.036	9.658	5.140	1.159	6.170	0.190	1.123	63.20







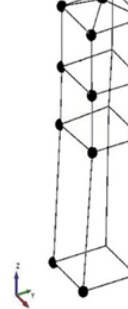



<i>Matildea Tower - EFDD</i>				
Mode 1	Mode 2	Mode 3	Mode 4	Mode 5
f = 1.472 Hz	f = 1.514 Hz	f = 4.240 Hz	f = 4.978 Hz	f = 5.130 Hz
				
Trans. Y	Trans. X	Tors. Z	Flex. Y	Flex. X
<i>Matildea Tower - SSI</i>				
Mode 1	Mode 2	Mode 3	Mode 4	Mode 5
f = 1.478 Hz	f = 1.513 Hz	f = 4.206 Hz	f = 5.011 Hz	f = 5.140 Hz
				
Trans. Y	Trans. X	Tors. Z	Flex. Y	Flex. X

Fig. 5-11 - Matildea Tower - Comparison between EFDD and SSI mode shapes

Table 5-4 - Pomposa Abbey Belfry - Modal Identification results

<i>Pomposa Abbey Belfry</i>									
Mode	EFDD Method			SSI Method			Comparison		
	f [Hz]	ξ [%]	Complexity [%]	f [Hz]	ξ [%]	Complexity [%]	Δf [%]	$\Delta \xi$ [%]	Cross-MAC [%]
φ^1	0.959	0.488	0.041	0.939	2.884	1.089	2.090	2.396	73.50
φ^2	1.024	0.755	0.853	1.024	0.660	0.539	0.000	0.095	96.30
φ^3	2.753	0.876	38.643	2.754	0.899	1.924	0.040	0.023	72.80
φ^4	3.549	3.164	15.282	3.493	1.694	4.607	1.580	1.470	64.00

φ^5 3.586 0.086 3.977 3.516 3.281 5.206 1.950 3.195 65.32

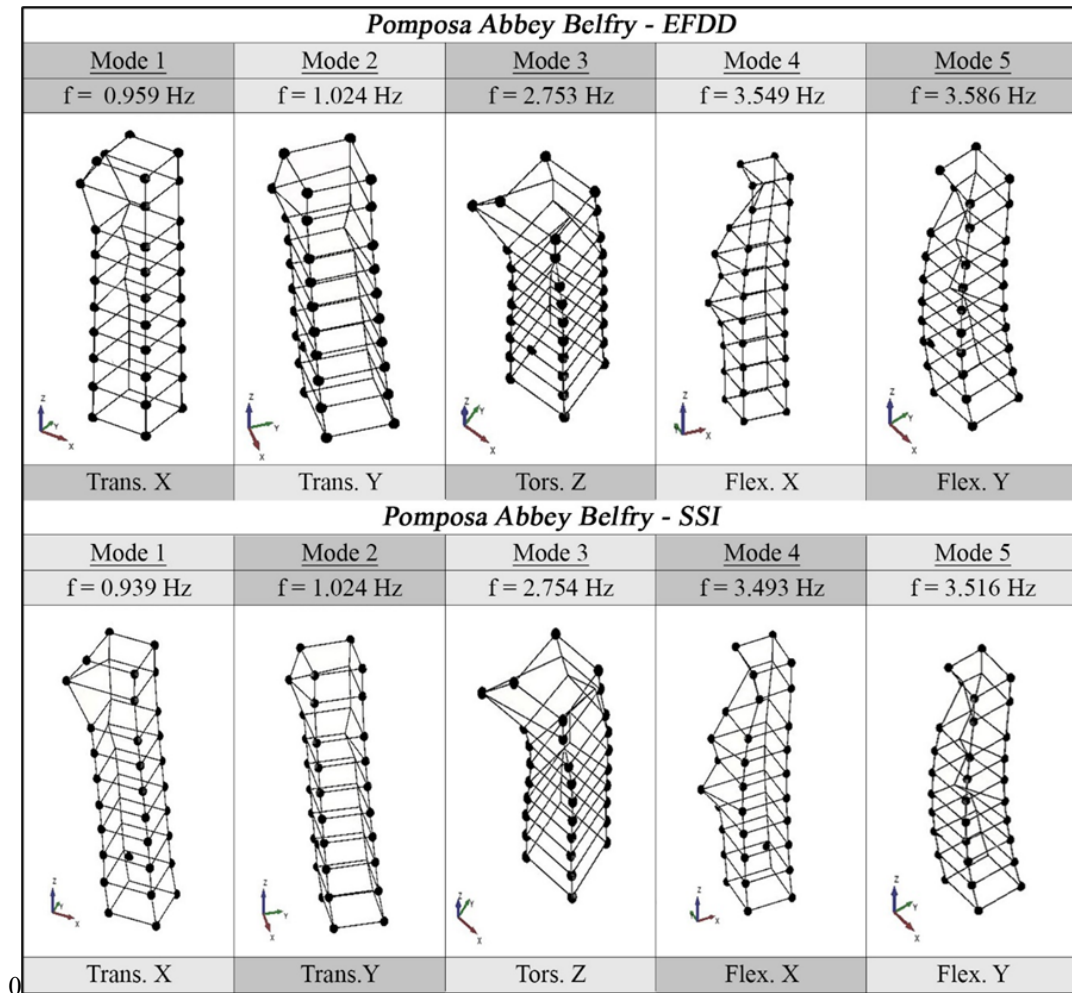


Fig. 5-12 - Pomposa Abbey Belfry - Comparison between EFDD and SSI mode shapes

5.1.3 Model updating process

5.1.3.1 Preliminary FE modeling

After obtaining the real dynamic behavior, the next step is represented by the construction of the NMs. In this study the four bell towers were analyzed using FEM, that were created using the MidasFea© software (Fig. 5-13). The models were carried out starting with the representations of their geometry, paying special attention to all the geometrical characteristics that may affect their dynamic behavior such as the openings, the walls thickness, etc. Afterward, the geometries were discretized using 4-nodes tetrahedral solid elements, to whom were assigned, after a visual inspection and historical

analysis of the typology of masonries, the material parameters reported in the Italian Code [67]. In Table 5-5 are reported the number of elements, the number of nodes and the degrees of freedom for each model.

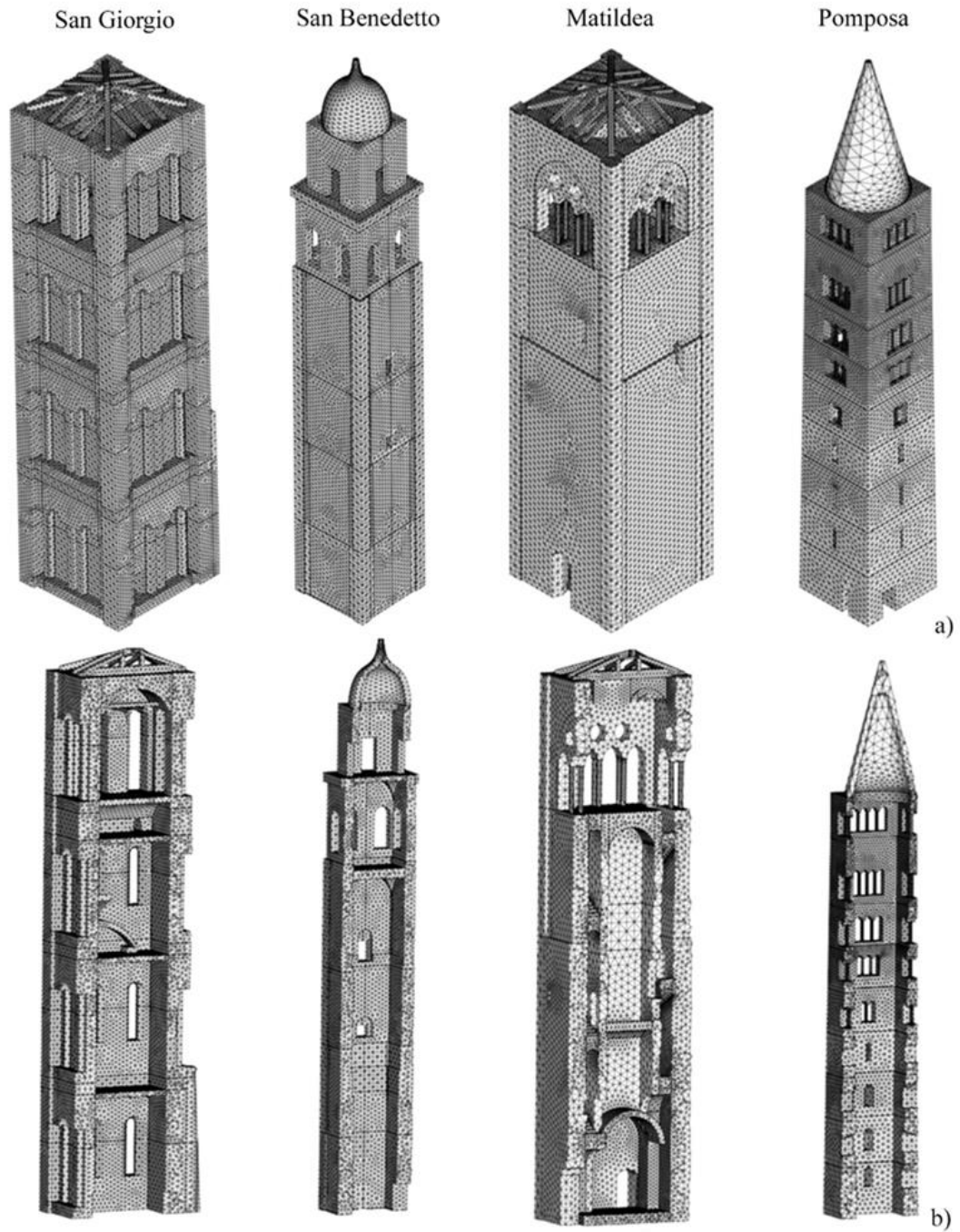


Fig. 5-13 - Towers NMs: a) prospective views; b) section views

Table 5-5 - Key features of the meshed solids

Belfry	Number of elements	Number of nodes	Degrees of freedom
<i>San Giorgio</i>	349750	79284	235512
<i>San Benedetto</i>	141904	32735	97323
<i>Matildea</i>	315743	69491	204996
<i>Pomposa</i>	136017	34337	102450

As may be observed in (Fig. 5-13 **Errore. L'origine riferimento non è stata trovata.**) the masonry cross vaults, the masonry stairs and the wood roofs were modeled, due to their contribution on the stiffness. The other (secondary) structural elements as the wood floors were not modelled but were taken into account by applying their dead loads on the walls. All the belfries were considered fixed at the basis and isolated since the thin walls that connect Pomposa and Matildea Towers with the relative churches are irrelevant. These towers were all built with masonry brick and lime mortar except for the San Giorgio bell tower where the bearing structure of bricks is covered by white and rose calcareous stones.

Table 5-6 reports the elastic parameters assigned to NMs at the early stage of this study; the values were taken following the Italian Code considering the lowest Knowledge Level (KL1). These parameters according to the thickness of the mortar and conservation status were corrected by applying the coefficients of the Table.C8.5.II of [68].

Table 5-6 - Elastic parameters of the preliminary models

KL	E [MPa]	N	γ [kN/m ³]
<i>Solid bricks with lime mortar and square blocks (only for San Giorgio)</i>			
1	2175	0.4	20
<i>Solid bricks and lime mortar</i>			
2	1500	0.3	18

The NMs were tested by modal analysis using the Lanczos method to identify the dynamic behavior. The first five modal shapes and the characteristic of their dynamic motion for each tower are reported in Fig. 5-14 and Table 5-7.

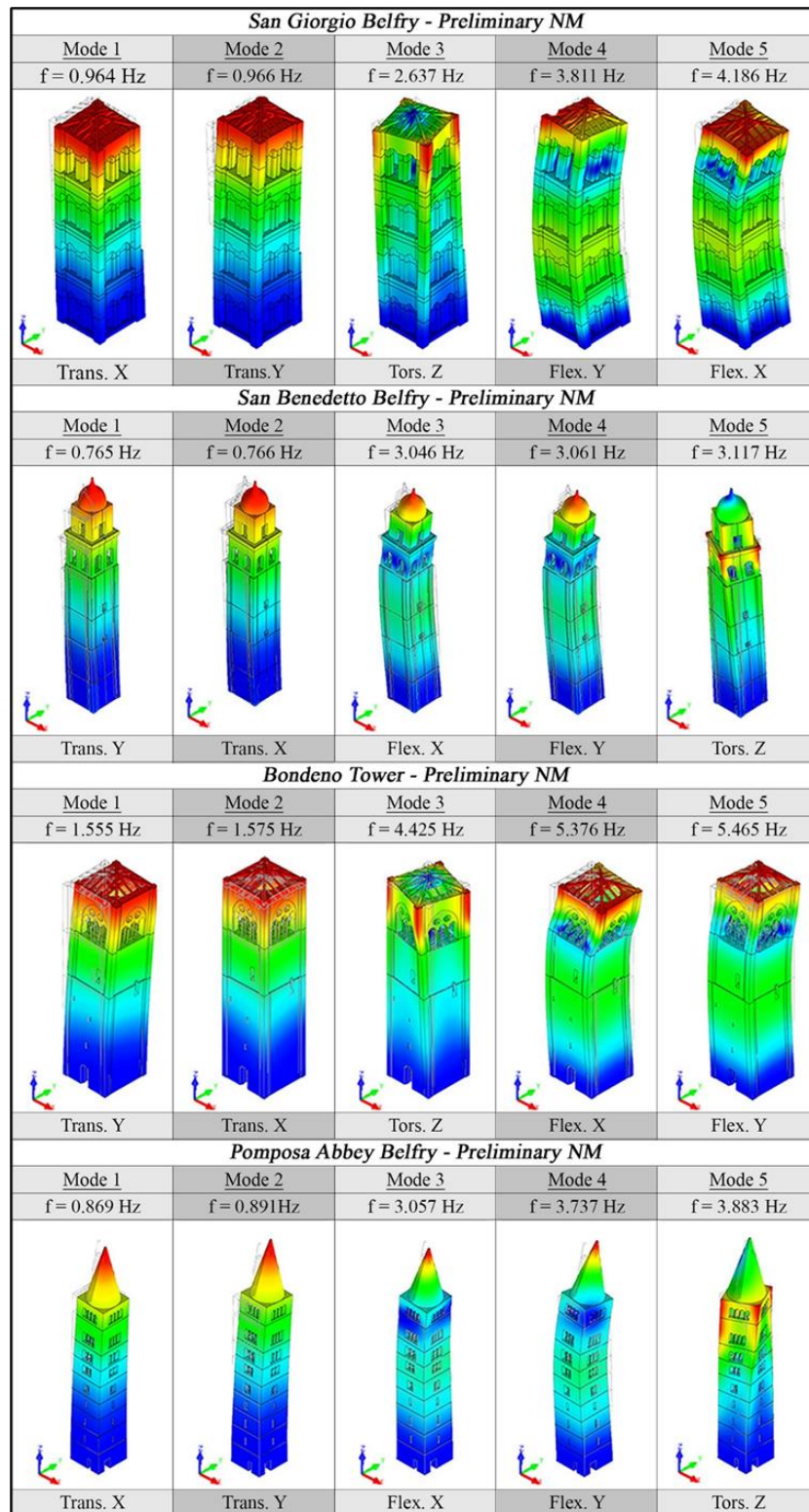


Fig. 5-14 - Mode shapes of towers preliminary model.

Table 5-7 - Modal properties of towers preliminary NMs

<u>San Giorgio Belfry</u>					<u>San Benedetto Belfry</u>				
Mode	Frequency NM [Hz]	Mass Tran-X NM [%]	Mass Tran-Y NM [%]	Mass Rot-Z NM [%]	Mode	Frequency NM [Hz]	Mass Tran-X NM [%]	Mass Tran-Y NM [%]	Mass Rot-Z NM [%]
φ1	0.964	49.57	11.86	0.00	φ1	0.765	0.27	54.02	0.00
φ2	0.966	11.54	50.32	0.00	φ2	0.766	53.73	0.27	0.00
φ3	2.637	0.00	0.00	5.30	φ3	3.046	20.42	0.00	0.00
φ4	3.811	0.00	21.11	0.00	φ4	3.061	0.00	19.52	0.00
φ5	4.186	21.02	0.00	0.00	φ5	3.117	0.00	0.00	0.00

<u>Matildea Tower</u>					<u>Pomposa Belfry</u>				
Mode	Frequency NM [Hz]	Mass Tran-X NM [%]	Mass Tran-Y NM [%]	Mass Rot-Z NM [%]	Mode	Frequency NM [Hz]	Mass Tran-X NM [%]	Mass Tran-Y NM [%]	Mass Rot-Z NM [%]
φ1	1.555	13.51	43.23	0.00	φ1	0.869	44.12	2.95	0.00
φ2	1.575	43.44	13.39	0.00	φ2	0.891	2.84	44.17	0.00
φ3	4.425	0.01	0.04	0.00	φ3	3.057	18.87	4.84	0.00
φ4	5.376	20.40	0.49	0.00	φ4	3.079	5.12	18.81	0.00
φ5	5.465	0.58	20.27	0.00	φ5	3.383	0.00	0.00	0.00

Comparing the numerical with the experimental results, we can notice some differences especially in terms of frequencies; in Table 5-8 we reported the percentage errors between experimental and numerical frequencies. Those results confirm that visual analysis and the use of Code materials parameters are not enough to obtain models that truly represent a building's behavior due to all the uncertainties that there can be.

Table 5-8 - Comparison between experimental and preliminary numerical models' frequencies

	San Giorgio Belfry	S. Benedetto Belfry	Matildea Tower	Pomposa Belfry
Mode	Δf [%]	Δf [%]	Δf [%]	Δf [%]
φ1	6.41	0.39	50.97	9.38

$\varphi 2$	8.87	41.57	48.58	12.99
$\varphi 3$	17.93	9.53	37.72	11.04
$\varphi 4$	18.15	7.44	15.46	13.24
$\varphi 5$	10.99	4.11	16.20	5.66

5.1.3.2 Calibration process

The preliminary results highlight the necessity of a recalibration of the NMs' parameters [54], in order to have correspondence between experimental and numerical models in the modal shapes associated with each vibrational mode. The modal updating procedure was executed in an indirect way, through the modification of the mechanical properties of masonry, varying the values of the (elastic) Young's Modulus E and the density ρ of materials and paying attention to the stiffness of the floors. We opted for an iterative procedure to manually update the parameters, which consists in modifying the stiffness characteristics of the NM in order to make the frequencies coincident from an engineering point of view. The process ran for each tower is illustrated below.

5.1.3.2.1 San Giorgio Cathedral Belfry

The first consideration made in San Giorgio Belfry model updating was to increase the frequencies of all modes in order to have coincidence with the experimental evidence, while the modal shapes seem to be well represented. For this purpose, the first operation related to the increase of the stiffness of the angular columns, that appear to be formed by squared stone blocks connected with a good quality mortar, and the integration of rigid links at the level of the floors for which the stiffness was not certain. As concerns the vaulted ceiling and the arcs, considering the constructive techniques of the time, we assumed an increase of the density to a value equal to 23 kN/m³ and a modulus of 2250 MPa. Those changes produced a raise of the torsional component, associated with the third mode.

Table 5-9 - San Giorgio Belfry - Comparison between experimental and calibrated NMs frequencies

Mode	f_{EXP} [Hz]	f_{NM} [Hz]	Δf [%]	Mass Tran. X	Mass Tran. Y	Mass Rot. Z
				[%]	[%]	[%]
$\varphi 1$	1.030	1.023	0.680	55.86	6.23	0.06
$\varphi 2$	1.060	1.061	0.090	6.16	55.71	0.00
$\varphi 3$	3.213	3.056	4.890	0.00	0.00	5.12
$\varphi 4$	4.656	4.576	1.720	2.50	18.68	0.00
$\varphi 5$	4.703	4.812	2.320	18.33	2.67	0.00

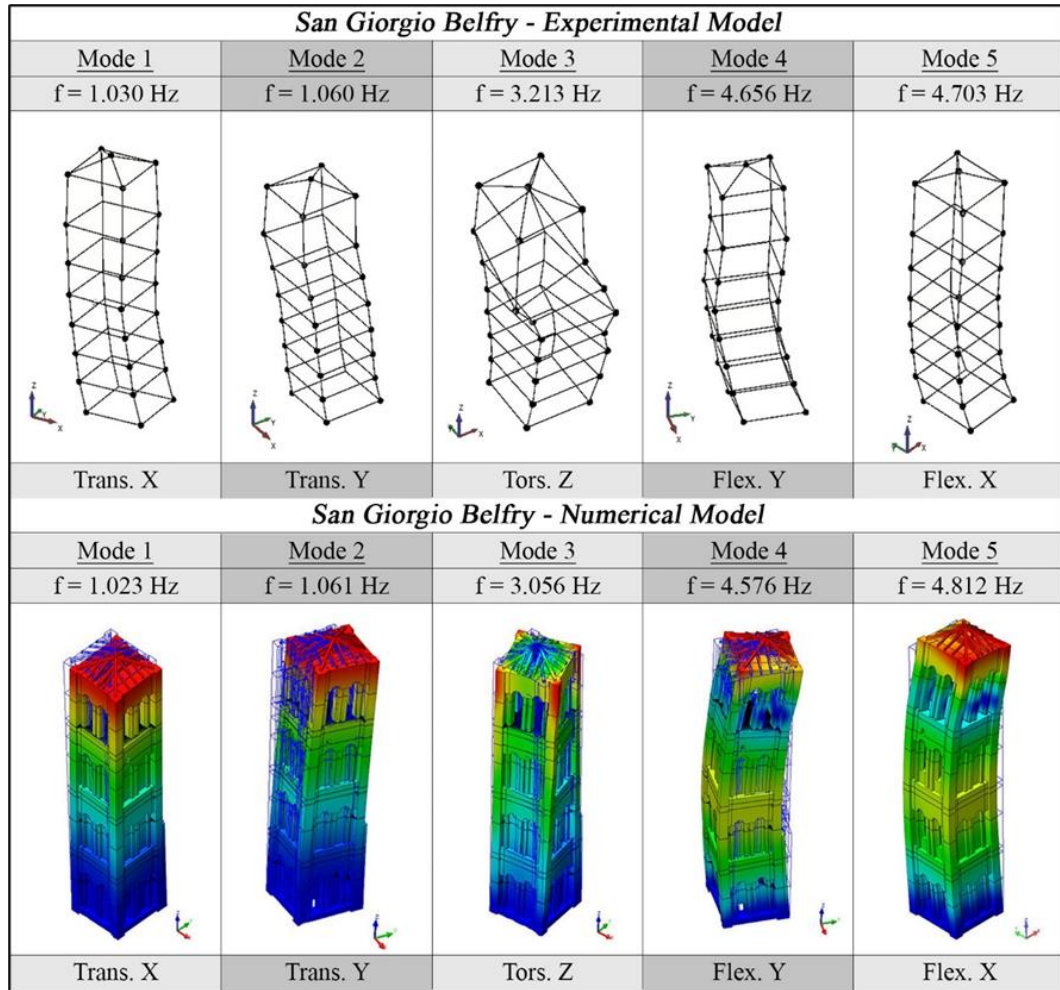


Fig. 5-15 - San Giorgio Belfry - Comparison between experimental and numerical mode shapes after calibration

In the second step, we tried to increase the third mode shape. For this purpose, we augmented the elastic module of the last nut, in order to differentiate it from the inferior part that may be less resistant due to the many changes suffered over the years as seen in the Section 5.1.1.1. This process also leads to obtain a better matching with the bending modal shapes characterizing the 4th and 5th mode. The final results are reported in Table 5-9 and Fig. 5-15.

5.1.3.2.2 *San Benedetto Belfry*

This case clearly shows that in addition to the differences of frequencies there is also a discrepancy of modal shapes between the numerical and experimental models, in the 3rd and 4th modes. In order to correct those, we considered the possible influence of the inclination, through the Elastic Module reduction of half tower in East-direction, since it appears less compressed; this allowed to match the

modal shapes. Subsequently to get closed frequencies, the Young's Modulus was decreased by moving towards the high part of the tower, considering the poor quality of its masonry, related to the lower normal stresses present in this zone. The stiffness of the cell bell was reduced more than in other parts, for its poorer quality provoked by the exposure to weather conditions. The result of the calibration procedure is reported in Table 5-10 and Fig. 5-16.

Table 5-10 - San Benedetto Belfry - Comparison between experimental and calibrated NMs frequencies

Mode	f_{EXP} [Hz]	f_{NM} [Hz]	Δf [%]	Mass Tran. X [%]	Mass Tran. Y [%]	Mass Rot. Z [%]
φ1	0.759	0.737	2.900	0.00	53.33	0.00
φ2	1.380	1.372	0.580	52,75	0.00	0.00
φ3	2.781	2.866	3.060	0.44	19.35	0.03
φ4	2.858	2.868	0.350	19.48	0.45	0.00
φ5	2.982	2.994	0.400	0.02	0.04	0.00

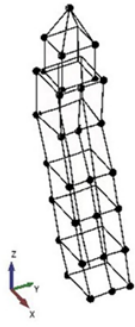

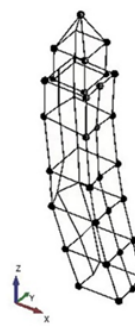
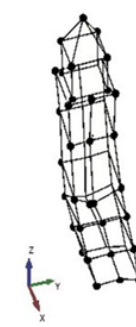

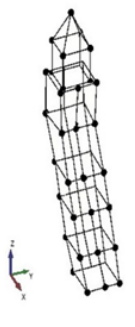


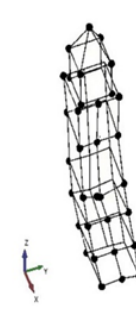
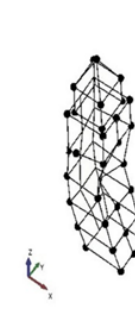
<i>San Benedetto Belfry - EFDD</i>				
Mode 1	Mode 2	Mode 3	Mode 4	Mode 5
$f = 0.762$ Hz	$f = 1.311$ Hz	$f = 2.781$ Hz	$f = 2.849$ Hz	$f = 2.994$ Hz
				
Trans. Y	Trans. X	Flex. Y	Flex. X	Tors. Z
<i>San Benedetto Belfry - SSI</i>				
Mode 1	Mode 2	Mode 3	Mode 4	Mode 5
$f = 0.759$ Hz	$f = 1.380$ Hz	$f = 2.781$ Hz	$f = 2.858$ Hz	$f = 2.982$ Hz
				
Trans. Y	Trans. X	Flex. X	Flex. Y	Tors. Z

Fig. 5-16 - San Benedetto Belfry - Comparison between experimental and numerical mode shapes after calibration

5.1.3.2.3 *Matildea Tower*

The first step of the recalibration process was to decrease the numerical frequencies which results slightly higher than the experimental ones. The strategy adopted implicate a reduction of the Young's Modulus assigned to the masonry constituting the higher block of the tower.

In the second step, in order to represent in a realistic way, the deterioration of the mechanical properties of the structure [69], we adopted for the bell cell an elastic Young's Modulus equal to 1000 MPa, which highlights the severity of the damage suffered by the structure due to the seismic event of 2012. In Table 5-11 and Fig. 5-17 differences between the numerical model and the experimental data are shown.

Table 5-11 - Matildea Tower - Comparison between experimental and calibrated NMs frequencies

Mode	f_{EXP} [Hz]	f_{NM} [Hz]	Δf [%]	Mass Tran. X [%]	Mass Tran. Y [%]	Mass Rot. Z [%]
φ_1	1.478	1.478	0.000	8.52	45.17	0.00
φ_2	1.513	1.511	0.130	44.23	8.21	0.00
φ_3	4.206	3.917	6.870	0.09	0.02	0.12
φ_4	5.011	4.767	4.870	3.37	15.86	0.00
φ_5	5.140	5.169	0.560	15.46	3.32	0.00

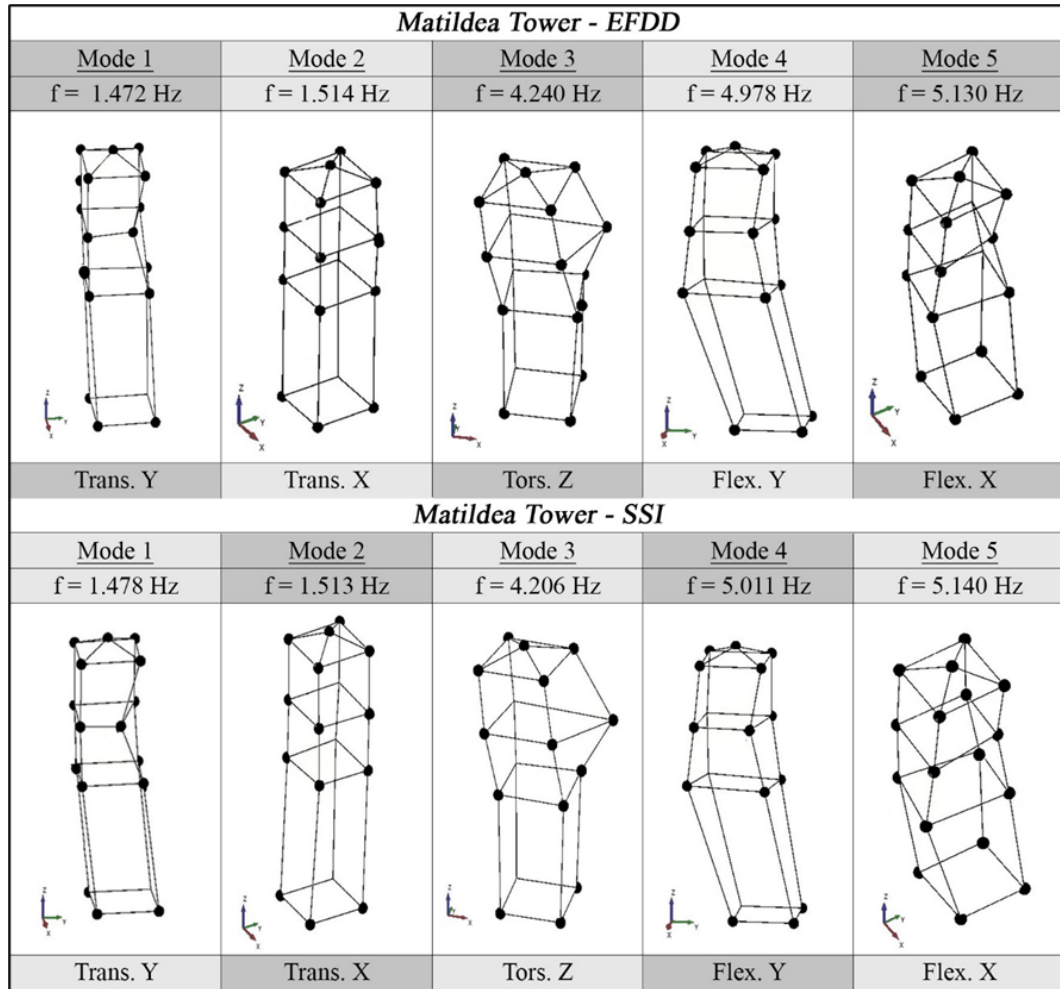


Fig. 5-17 - Matildea Tower - Comparison between experimental and numerical mode shapes after calibration

5.1.3.2.4 *Pomposa Abbey Belfry*

At a first glance, the exam of the results in terms of frequencies displayed how difficult it is to differentiate the frequencies associated with the first two modes, and the necessity to reduce the third one.

The first step of the calibration [70] consisted in removing the conical cover of the tower. During the AVT, that part of the tower was not instrumented due to access difficulties, thus it was considered a dead load in order to eliminate its influence on the first modes. This expedient permitted a better identification of the first two translational modes, and a significant increment of the frequency associated with the fourth one.

The following step of the calibration aimed to increase the gap between the first two frequencies and to reduce the third one. In order to achieve this goal, the first step consisted in the increment of the stiffness of the lower part of the tower, that resulted less damaged during the preliminary visual inspection. The following operation has been the assignment of different properties to the materials in the X and Y direction with the aim of better simulating the bigger degradation endured by the East - West facade due to the seismic events and atmospheric agents. At last, the Elastic Young Modulus of the top level of the tower has been reduces, because of the worse quality of masonry and the negative effect of lower normal stresses in this part of the tower.

The modal shapes and the difference between the numerical and experimental data, obtained at the end of the last step, are reported in Table 5-12 and Fig. 5-18.

Table 5-12 - Pomposa Abbey Belfry - Comparison between experimental and calibrated NMs frequencies

Mode	f_{EXP} [Hz]	f_{NM} [Hz]	Δf [%]	Mass Tran. X [%]	Mass Tran. Y [%]	Mass Rot. Z [%]
φ1	0.939	0.934	0.530	45.67	0.06	0.00
φ2	1.024	1.018	0.590	0.05	45.57	0.00
φ3	2.754	2.818	2.320	0.02	1.31	0.04
φ4	3.493	3.433	1.720	23.62	0.02	0.00
φ5	3.516	3.487	0.820	0.03	24.11	0.00

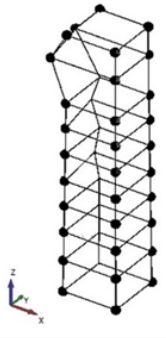
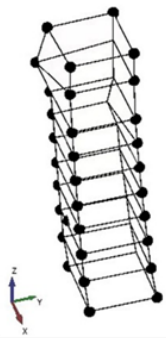
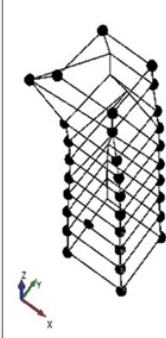
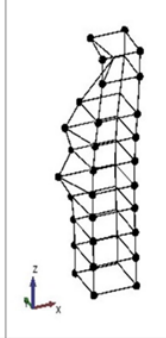
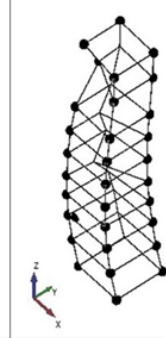
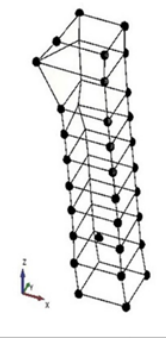
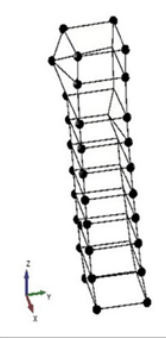
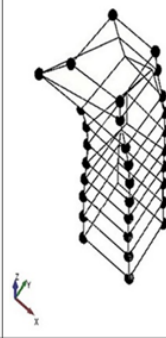
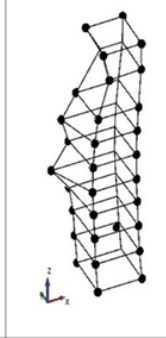
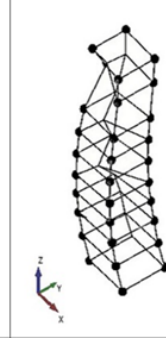
<i>Pomposa Abbey Belfry - EFDD</i>				
Mode 1	Mode 2	Mode 3	Mode 4	Mode 5
$f = 0.959 \text{ Hz}$	$f = 1.024 \text{ Hz}$	$f = 2.753 \text{ Hz}$	$f = 3.549 \text{ Hz}$	$f = 3.586 \text{ Hz}$
				
Trans. X	Trans. Y	Tors. Z	Flex. X	Flex. Y
<i>Pomposa Abbey Belfry - SSI</i>				
Mode 1	Mode 2	Mode 3	Mode 4	Mode 5
$f = 0.939 \text{ Hz}$	$f = 1.024 \text{ Hz}$	$f = 2.754 \text{ Hz}$	$f = 3.493 \text{ Hz}$	$f = 3.516 \text{ Hz}$
				
Trans. X	Trans. Y	Tors. Z	Flex. X	Flex. Y

Fig. 5-18 - Pomposa Abbey Belfry - Comparison between experimental and numerical mode shapes after calibration

5.1.3.3 Validation of mode shape through CrossMAC matrix

The model updating process seemed to produce a good match between the experiment and NM, both in terms of frequencies [71] and modal shapes [72,73]. To be sure of the outcome's reliability, the mode shapes produced by the NMs were compared with the corresponding ones deriving from the modal identification executed through the SSI estimation methodology, using the Cross MAC explained in §5.1.2.5. The results for each tower are presented in Table 5-13.

Even though the results are not satisfying, in particular from the fourth mode where the values are in the ranges of $0.01 \div 0.3$, we obtained an improvement of the results during the iterative step by step process, which proofs that the adopted procedure is correct.

Table 5-13 - Cross-MAC between experimental and numerical mode shapes after calibration

<u>San Giorgio Belfry</u>					<u>San Benedetto Belfry</u>				
Mode	f_{EXP} [Hz]	f_{NM} [Hz]	Δf [%]	CrossMAC [%]	Mode	f_{EXP} [Hz]	f_{NM} [Hz]	Δf [%]	CrossMAC [%]
φ1	1.030	1.023	0.68	89.70	φ1	0.759	0.737	2.90	99.20
φ2	1.060	1.061	0.09	86.30	φ2	1.38	1.372	0.58	63.80
φ3	3.213	3.056	4.89	100.00	φ3	2.781	2.866	3.06	4.80
φ4	4.656	4.576	1.72	68.30	φ4	2.858	2.868	0.35	9.60
φ5	4.703	4.812	-2.32	66.70	φ5	2.982	2.994	-0.40	14.90

<u>Matildea Tower Belfry</u>					<u>Pomposa Abbey Belfry</u>				
Mode	f_{EXP} [Hz]	f_{NM} [Hz]	Δf [%]	CrossMAC [%]	Mode	f_{EXP} [Hz]	f_{NM} [Hz]	Δf [%]	CrossMAC [%]
φ1	1.478	1.478	0.00	84.70	φ1	0.939	0.934	0.53	73.50
φ2	1.513	1.511	0.13	97.20	φ2	1.024	1.018	0.59	96.30
φ3	4.206	3.917	6.87	38.40	φ3	2.754	2.818	2.32	72.80
φ4	5.011	4.767	4.87	0.50	φ4	3.493	3.433	1.72	5.40
φ5	5.14	5.169	0.56	35.20	φ5	3.516	3.487	0.82	1.50

The discrepancy of the results is probably related to an inhomogeneity of the material' properties, due to cracks, followed to the seismic events occurred in recent years, and to localized deterioration of the connections among the bricks, forming the masonry wall, whose effects would be probably better represented through the usage of anisotropic material [71], taking into account the influence of shear modulus (G) and the variations of the elastic modulus in the three spatial direction. This will be the subject of future works.

5.2 Automatic calibration approach via Genetic

Algorithms: the case study of Ostra Civic Tower

Within this framework, the present work aims to provide a contribution to the field of structural assessment and damage identification of historic masonry structures by proposing an iterative updating procedure based on Genetic Algorithms (GA) to build a reliable reference model of a heritage tower located in Central Italy for future comparative analyses and health monitoring [59,74].

For the purpose of this work, the genetic algorithm provided by the open-source finite element solver Code_Aster© is employed to automatically find the optimal values for the unknown material properties of the investigated tower, starting from the model calibrated against 2018 experimental results and then updated to match the behaviour identified with 2019 measurements [75–80]. To better assess the efficiency, accuracy and reliability of the proposed approach, the dimensionality of the problem is upscaled by increasing the number of updating variables to be determined, thereby allowing to take into account also the uncertainties associated with the modelling of masonry as an isotropic or orthotropic material. Without artificial intelligence, such a detailed study would not be possible.

In addition to this introductory section, the remaining of the work is organized as follows. Section 5.2.1 describes the tower history and the outcome of the geometric and material surveys; Section 5.2.2 focuses on the identification of the modal parameters of the structure through OMA techniques; Section 5.2.3. presents and discusses in detail the model updating process using GAs. Finally, Section 5.2.4. summarizes the main conclusions that can be drawn from the work.

5.2.1 Ostra Civic Tower: description of the case study

5.2.1.1 *Historical survey*

Located about 40 km away from Ancona, Ostra is one of the typical villages of the Marche region, in Central Italy. Lying on a hill, overlooking the river Misa Valley, it is said that Ostra was founded by the exiles of the Roman Empire and its original name, till 1881, was Montalboddo. Destroyed during Goths invasion, the village was rebuilt, and during the Middle Age, it was surrounded by a protective wall, 1200 meters long, interspersed with square section towers, nine of those still existing today.

Nowadays, the centre of the city life is represented by the central Piazza dei Martiri, located in the upper part of the historic centre, where the most important buildings, such as Palazzo Comunale, San Francesco Church, La Vittoria Theatre, are found. Among them, the most emblematic building of the city – case study of this work – stands: Ostra Civic Tower (Fig. 5-19). Built in the XVI century, this

tower is also known as “Clock Tower” because of the ancient clock gears still present today, even if no longer in operation.



Fig. 5-19 - Ostra Civic Tower localization.

According to historical sources [81,82], the belfry tower was originally connected to San Giovanni Church (Fig. 5-20a). The two buildings had autonomous origins: the church was mentioned for the first time in archival documents in 1454, while the tower was built in 1552 at the behest of the magistracy. The bell, hosted today by the third order of floors, dates to 1631.



Fig. 5-20 - San Francesco Church and the Tower before bombardments (a) and a view of the central square to the present days (b).

With its architecture and double staircase, the church closed the fourth side of the square, making it an elegant “living room”. The interior of the structure treasured various artworks, including many altarpieces such as that of Andrea Sacchi (1599/1661) depicting San Bonaventura da Bagnoregio and San Tommaso d'Aquino (today stored at the Superintendence of Urbino). Though, following the aerial bombardments occurred in 1944 during the II World War, only the church façade and the civic tower survived.

Because of the precarious conditions of the structures, it was decided to intervene by demolishing the rests of the façade and strengthening the tower. Façade demolition led to the uncovering of the foundations of the tower walls and of the external staircase of the building, making them prone to degradation phenomena due to atmospheric agents and pollutants. Therefore, foundation works were promptly carried out along with the recovery of the base walls. Parts of the external walls and battlements damaged by the bursts of artillery bullets were also restored.

After the works, a new architectural arrangement of the square became indispensable. Some projects envisaged creating a decent background, in harmony with the palaces that frame the town square and erecting a building that could replace the beautiful (demolished) façade and which could form, together with the civic tower, a single majestic and harmonious architectural complex (Fig. 5-20b).

5.2.1.2 Geometrical and material survey

With an overall height of 30 meters (before the interventions executed in 1950, when the foundations were partially uncovered and the top part was added, the original height was 25 meters), the Civic Tower of Ostra is a historical masonry structure featuring four main parts: the basement, the central body, the bell cell and the top roof (Fig. 5-21). In what concerns the parts belonging to the original

tower, the bell cell is unchanged, while the central body is partially reconstructed, as the changes of the masonry texture reveal.

The basement consists of a truncated pyramid, whose lower base measures approximately 7.30 x 7.50 m², while the upper base is about 5.30 x 5.60 m². This part develops up to a height of 9.55 meters, culminating in an embattled balcony. Hereon, the parallelepipedal central body starts, keeping the same shape for additional 9.50 meters. Then, the cross section of the tower slightly reduces at the level of the bell cell and remains unchanged till the embattled enlargement of the upper part.

The tower results composed of five floors: the first three are connected through spiral staircases starting from the ground level, while the last two orders of floors are reachable using an iron ladder. The clock mechanism is located on the second floor, whereas the bell cell occupies the third level, whose perimetral walls are pierced by single-light arched windows, one per side. The entrance is located on the main façade (north-east oriented), which overlooks Piazza dei Martiri.

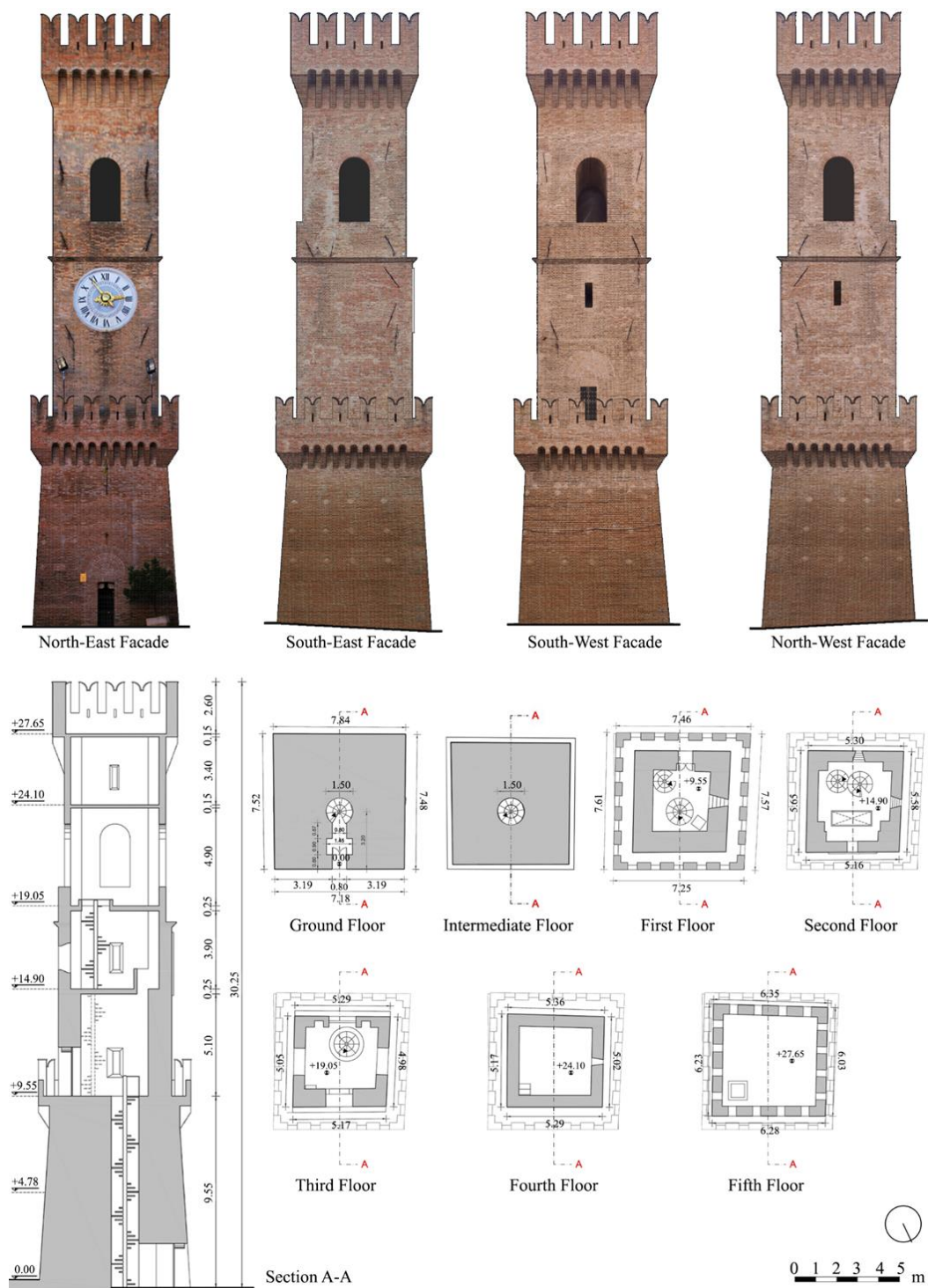


Fig. 5-21 - Geometrical survey of the investigated tower: front views (top) and CAD sections (bottom).

The survey allowed to distinguish different construction features and materials across the tower (Fig. 5-22). Particularly, the bearing walls, whose thickness ranges from 1.1 meters in the lower part (first

floor) to 0.6 meters in the upper part (last floor), resulted built with solid brick masonry and thin mortar joints. As for the basement walls, their remarkable thickness let infer the presence of an inner rubble core between brick outer layers, though no investigation could be performed to confirm the hypotheses about their internal morphology. The structural interventions undergone by the tower include the reinforced concrete slabs constituting the floors, whose thickness varies from 0.11 meters to 0.27 meters, the concrete columns built to reinforce the corners at the third level, and the iron tie-rods installed after the 1997 seismic events of Umbria-Marche region aimed at restraining possible out-of-plane mechanisms. No worrying cracks nor other structural damages were detected during the visual inspection.



Fig. 5-22 - Excerpts from the photographic survey of the tower: (1) trapdoor accessing the upper level and connecting iron ladder; (2) close-up of the 4th level brickwork; (3) concrete slab of the 3rd floor with ladder opening; (4) particular of the reinforcement intervention with tie rods; (5) close-up of the 2nd level internal brickwork; (6) external brickwork of the 1st level; (7) basement brickwork; (8) spiral staircase at the entrance level.

5.2.2 Ambient vibration testing

Given its non-destructive nature, Ambient Vibration Testing (AVT) has become a common in situ investigation technique for the estimation of dynamic parameters associated with the global behavior of historical structures. This tool results extremely useful to collect reliable experimental data and

increase the level of knowledge of the structure whenever its historical value may pose limitations to the application of other diagnostic techniques for the system's characterization. By deploying a set of sensors at selected locations and capturing the vibration response of the structure to random ambient excitations (traffic, wind, human walking, micro-tremors), the dynamic features of the system, namely natural frequencies (f), damping ratios (ξ) and mode shapes (ϕ), can be extracted and used to better interpret the actual behaviour of age-old constructions, which are often highly complex and mechanically diverse.

In the last years, numerous works showed the potentiality of vibration monitoring through accelerometric sensors in the study of the dynamic behavior of historical buildings, both for short-term [71,72] and long-term applications [83]. Indeed, besides the economic benefits associated with the possibility of using freely available environmental excitations, AVT allows to perform rapid screenings of the structural fitness under real operational and boundary conditions. Moreover, the processing of the acquired vibration data enables the construction of an Experimental Model (EM) of the structure, which provides the dynamic parameters that the Numerical Model (NM) has to match to realistically reproduce the structural response [73].

5.2.2.1 Field testing procedure

In order to characterize the dynamic behaviour of the Civic Tower of Ostra, two field dynamic testing campaigns in operational conditions were conducted in June 2018 and in February 2019. The sensor network was composed of four triaxial piezoelectric accelerometers, with an integrated MEMS tilt-meter system for correction of errors due to inclination, characterized by a maximum measurement range of 8 g, a sensitivity of 1000 mV/g and a bandwidth range from 0.8 to 100 Hz. The digitization process was automated through an A/D converter with 24 bits of resolution, 120 dB of dynamic range and provided with anti-aliasing filter. The synchronization between sensors was ensured by a 4-channel Sync Hub connecting the accelerometers to the PC for data storage.



Fig. 5-23 - Instrumentation used for the ambient vibration tests.

In both campaigns, three setups were used to measure the response of the tower in 8 selected points evenly deployed on the opposite corners of four levels (Fig. 5-24). Each setup consisted of four accelerometers: two were fixed on the top floor and kept as reference sensors, while the remaining two were moved downward in each acquisition so as to record the vibration processes of the tower along the three directions of the 8 identified points, allowing to catch all the meaningful modal displacements of the structure, including torsional components. It is noted that the sensor layouts for the signal acquisition were established in accordance with the results of a preliminary numerical modal analysis coupled with an Optimal Sensor Placement (OPT) procedure [19,84], with the intent of identifying the best position for the accelerometers to maximize the quality of the AVT information despite the limited number of available sensors.

To comply with Rodriguez's indications [58], the total duration of the acquisition was set longer than 2000 times the estimated fundamental period of the structure: indeed, every registration lasted around 40 minutes, thereby assuring the elimination of the possible influence of non-stochastic excitations. Moreover, to guarantee a high frequency resolution for the spectral density estimation, a sampling frequency of 1024 Hz was adopted, resulting in 2,457,600 datapoints per time series.

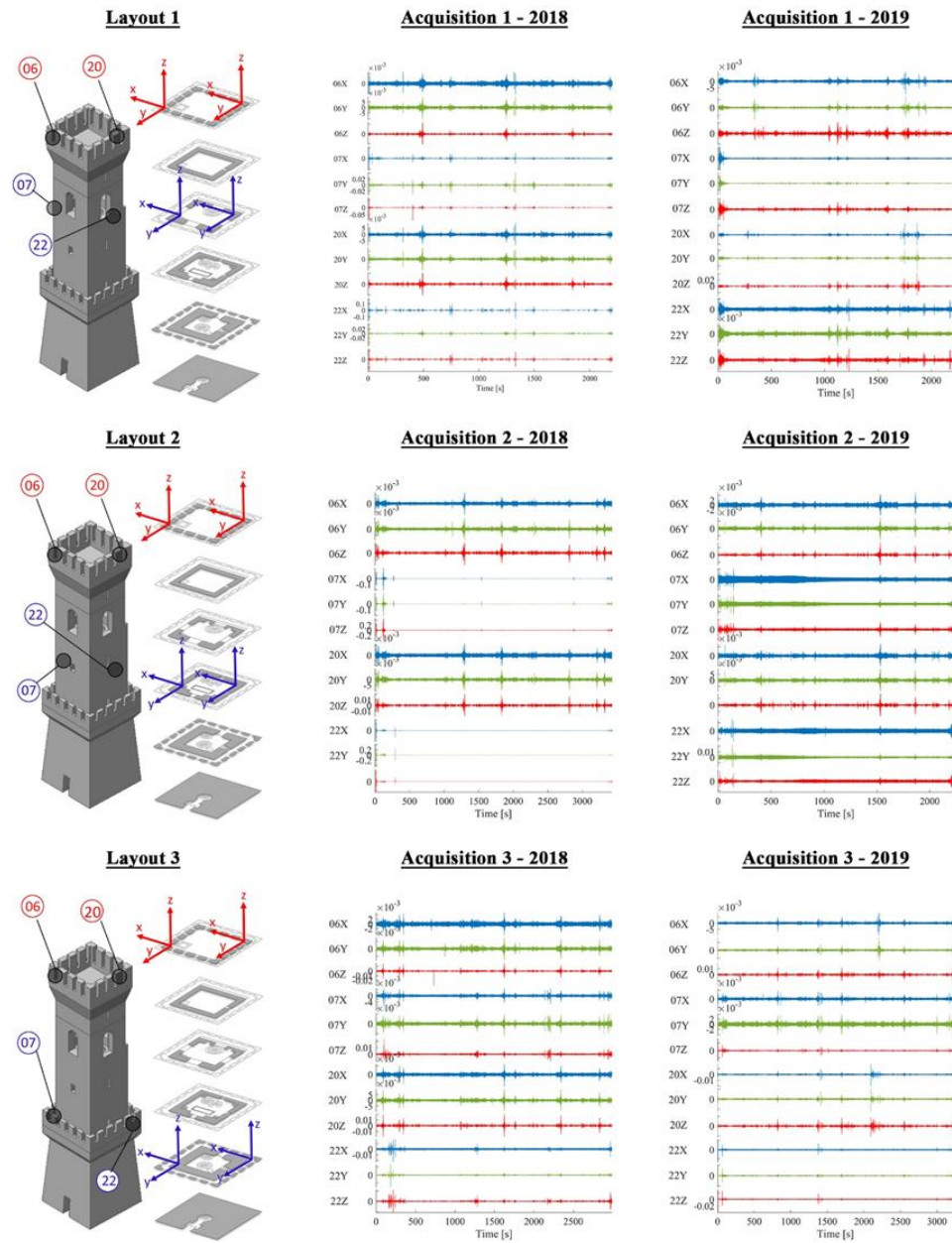


Fig. 5-24 - Sensor layouts and corresponding acceleration time series for 2018 and 2019 dynamic testing campaigns (blue, green and red colours indicate signals in x, y and z direction, respectively).

5.2.2.2 Operational modal analysis

5.2.2.2.1 Data processing

The extraction of the dynamic features of the tower (i.e., natural frequencies f , damping ratios ξ and mode shapes ϕ) was performed through the application of Operational Modal Analysis (OMA) techniques, using the acceleration time series acquired in operating conditions through the aforementioned contact sensor network. Many are the output-only dynamic identification approaches available in the literature that can be adopted for this purpose, both in the time and in the frequency domain [13,52,59,85]. Yet, regardless of the strategy, a pre-processing stage is needed before further data elaboration in order to remove residual noise and possible trends from the vibration signals, filter undesired frequency components, minimize leakage errors and eventually down-sample the time series to reduce the subsequent data processing time.

As for the present work, the pre-processing operation was executed through a Matlab© script, applying a 10th order Butterworth low-pass filter to the raw signals. Then, the cleaned data were down-sampled, passing from a spectral resolution of 1024 Hz to 100 Hz. As observed in analogous structures, the frequency content of interest for the tower fell in the range 0-10 Hz, thus data were further decimated with a factor of 8, reducing the analyzed range to 0-12.5 Hz. Finally, the pre-processed signals were analyzed through the Stochastic Subspace Identification (SSI) method available in the commercial software ARTeMIS [49].

5.2.2.2.2 Theoretical background on SSI-based methods

The SSI method can be considered as one of the principal approaches for the extraction of modal parameters from output-only vibration data. The large attention lately received by SSI methods is likely due to the fact that these techniques are apt to accurately identify closely spaced modes and especially suited to be automated [13]. For the sake of completeness, only a brief description of this modal identification procedure is provided hereafter; for further details the reader is referred to [33].

SSI can be implemented in two classic forms: covariance driven (SSI-cov) and data driven (SSI-data). Working in the time domain, the SSI method starts from the construction of a State Space model, where the second order equation of motion is converted into a system composed of two linear equations, called respectively “state equation” Eq. 5.7 and “observation equation” Eq. 5.8, which in the case of ambient vibration testing (unknown input) read:

$$\mathbf{x}_{k+1} = \mathbf{A}\mathbf{x}_k + \mathbf{w}_k \quad (5.7)$$

$$\mathbf{y}_k = \mathbf{C}\mathbf{x}_k + \mathbf{v}_k \quad (5.8)$$

where:

- k is the generic time instant;
- $\mathbf{x} \in \mathcal{R}^{nx1}$ is the discrete-time state vector;
- $\mathbf{y} \in \mathcal{R}^{lx1}$ is the vector containing the l output measurements;
- $\mathbf{A} \in \mathcal{R}^{nxn}$ is the system matrix that describes all the dynamic information of the system;
- $\mathbf{C} \in \mathcal{R}^{lxn}$ is the corresponding output matrix;
- $\mathbf{w} \in \mathcal{R}^{nx1}$ is a white noise vector process representing disturbances and modelling inaccuracies;
- $\mathbf{v} \in \mathcal{R}^{lx1}$ is another white noise vector process representing the measurement noise due to sensor inaccuracy.

These equations represent the discrete-time state space form of the dynamics of a linear-time-invariant system under unknown excitation. Particularly, Eq. 5.7 models the dynamic behavior of the physical system, whereas Eq. 5.8 controls which part of the dynamic system can be observed in the output of the model. The core of the process aims at identifying the system dynamic matrix \mathbf{A} by fitting the state-space model to the experimental data. In case of SSI-Cov method, the modal estimates are obtained from the Singular Value Decomposition (SVD) of the block Toeplitz matrix, a matrix gathering the covariances of the measured output time series; while in case of SSI-data, the modal identification is performed starting from the SVD of the block Hankel matrix, a matrix containing past and future output measurements.

Like all parametric system identification techniques, a user-defined integer is required to process the data, i.e. the maximum model order. In principle, the model order must be twice the number of the modes that are needed to describe the dynamic response of the system. Notwithstanding, to identify weakly excited modes, it is often necessary to consider larger model orders which can lead in turn to the appearance of many spurious modes associated to the noise content of the measurements. To overcome this issue, different SSI analyses with a range of candidate model orders can be carried out trying to identify the model order that better fits the experimental data and leads to the best stabilization diagram. The latter is an order-frequency plot in which the estimated physical (structural) and computational (spurious) modes are represented as poles and discriminated based on the fulfilment of user-specified requirements (e.g. maximum allowed deviation between successive models in terms of modal frequencies, damping ratios and MAC values). If the model order is high enough, a repeated trend of stable poles will appear in the SSI output diagram, allowing the estimation of the structural modes characterizing the system.

5.2.2.2.3 *Modal results*

In both dynamic testing campaigns, five vibration modes were identified in the frequency range 0-10 Hz: two close-spaced translational modes (φ_1) and (φ_2) in x and y directions, respectively, featuring in-phase modal components; one torsion mode (φ_3); and two dominant double bending modes (φ_4), (φ_5) in the xz and yz planes, respectively. As expected, the first two vibration modes exhibit relatively high frequency values compared to those featured by typical historical masonry towers. This outcome is imputable to the low aspect ratio ($\lambda = 4$) characterizing the tower object of study as well as to the increased stiffness resulted from the past restoration works.

The estimated natural frequencies and damping ratios, used for the following calibration process, are reported in Table 5-14 for both campaigns, together with the Mode Complexity Factor (MCF) associated to each mode. This value is a scalar that lies in the range 0%-100% and quantifies the degree of complexity of a mode shape, namely how much the modal vector differs from a real-valued one [39,60,86]. Real-valued mode shapes feature complexities close to 0 (MCF = 0%), while mode shapes with predominant imaginary components exhibit complexity values close to 1 (MCF = 100%). The dispersion of the real and imaginary parts of each mode is further analysed by plotting their components in a two-dimensional polar coordinate system, namely through the complexity plots, as illustrated in Fig. 5-25. It is observed that in the first dynamic testing campaign, the first three mode shapes, as well as the last one, are close to monophasic vectors (components are aligned along the horizontal direction) and only the fourth mode has a higher complexity, whereas in the second dynamic testing campaign the modal components of both the third and fourth modal vectors present greater complexities. This slight difference between the MCF values of the two campaigns is probably associated to the different level of ambient excitations present during the AVTs which might have affected the signal-to-noise ratio introducing some inaccuracy in the modal estimates. However, it is worth mentioning that the actual mode shapes of a physical system are never exactly monophasic vectors, thus some degree of complexity is always expected in the experimental modes.

Table 5-14 - Global modal parameters identified for EM 2018 and EM 2019.

Mode	<u>2018</u>			<u>2019</u>		
	f [Hz]	ξ [%]	MCF [%]	f [Hz]	ξ [%]	MCF [%]
φ_1	2.082	0.817	3.929	2.092	0.762	3.320
φ_2	2.156	0.893	0.178	2.165	0.787	0.370
φ_3	6.293	0.578	2.765	6.302	0.666	11.241
φ_4	6.442	2.423	12.471	6.449	3.397	19.642

φ_5	6.941	2.463	2.053	6.872	2.739	4.851
-------------	-------	-------	-------	-------	-------	-------

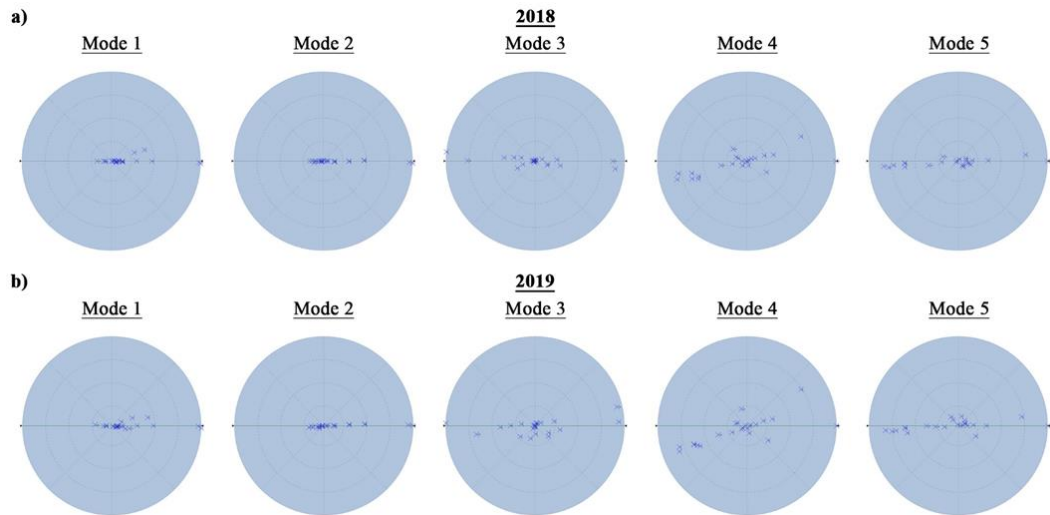


Fig. 5-25 - Complexity plots of the identified experimental modes for EM 2018 (a) and EM 2019 (b).

To drive the accurate selection of the structural modes, a cross-validation was performed by comparing the modes identified with the SSI modal estimator against the ones extracted through another OMA technique operating in the frequency domain, namely the Enhanced Frequency Domain Decomposition (EFDD) [55,56]. The close pairwise correspondence of the five vibration modes estimated in each campaign is visually highlighted in Fig. 5-26, where the mode shapes from the two modal estimators are superimposed, and also confirmed by the values of the Modal Assurance Criterion (MAC) reported both in Fig. 5-26 and in Table 5-15. As well-known in the literature, the MAC is a statistical indicator used to measure the degree of similarity between mode shape vectors [45]: the closer the values are to 1 (MAC = 100%), the higher the correlation between modes and vice versa.

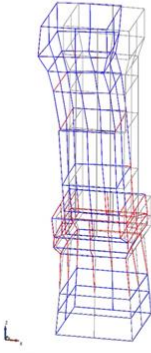
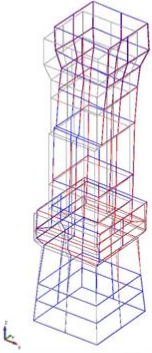
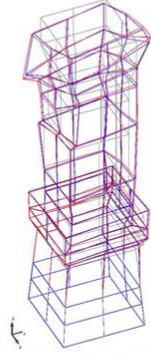
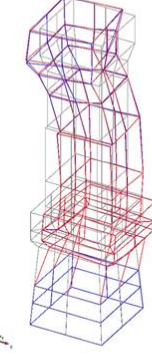

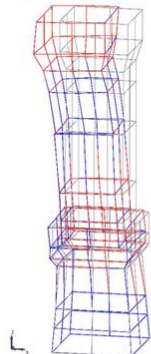
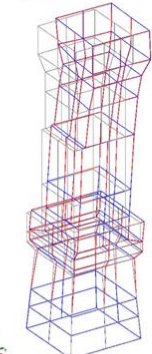
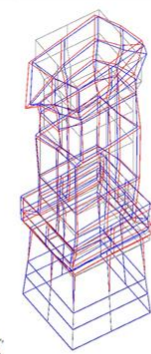
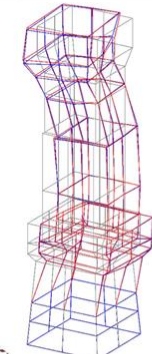
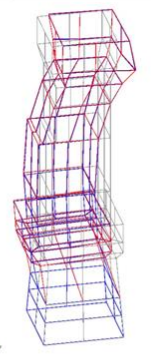
2018				
Mode 1 $f_{SSI} = 2.082$ Hz $f_{EFDD} = 2.082$ Hz	Mode 2 $f_{SSI} = 2.156$ Hz $f_{EFDD} = 2.155$ Hz	Mode 3 $f_{SSI} = 6.293$ Hz $f_{EFDD} = 6.305$ Hz	Mode 4 $f_{SSI} = 6.442$ Hz $f_{EFDD} = 6.459$ Hz	Mode 5 $f_{SSI} = 6.941$ Hz $f_{EFDD} = 6.950$ Hz
				
Translational X	Translational Y	Torsional	Bending X	Bending Y
MAC _{SSI-EFDD} = 100%	MAC _{SSI-EFDD} = 99.8%	MAC _{SSI-EFDD} = 86.7%	MAC _{SSI-EFDD} = 92.4%	MAC _{SSI-EFDD} = 98.0%
2019				
Mode 1 $f_{SSI} = 2.092$ Hz $f_{EFDD} = 2.090$ Hz	Mode 2 $f_{SSI} = 2.165$ Hz $f_{EFDD} = 2.165$ Hz	Mode 3 $f_{SSI} = 6.302$ Hz $f_{EFDD} = 6.301$ Hz	Mode 4 $f_{SSI} = 6.449$ Hz $f_{EFDD} = 6.443$ Hz	Mode 5 $f_{SSI} = 6.872$ Hz $f_{EFDD} = 6.893$ Hz
				
Translational X	Translational Y	Torsional	Bending X	Bending Y
MAC _{SSI-EFDD} = 99.9%	MAC _{SSI-EFDD} = 99.7%	MAC _{SSI-EFDD} = 81.2%	MAC _{SSI-EFDD} = 89.1%	MAC _{SSI-EFDD} = 94.3%

Fig. 5-26 - Mode shapes of 2018 and 2019 EMs identified with SSI method (in blue) and cross-comparison with the respective mode shapes identified with EFDD method (in red).

Table 5-15 - MAC between mode shapes identified with SSI and EFDD methods: (a) EM 2018 and (b) EM 2019.

a)						
CrossMAC 2018		SSI				
		2.082 Hz	2.156 Hz	6.293 Hz	6.442 Hz	6.941 Hz
EFDD	2.082 Hz	1.000	0.000	0.000	0.032	0.002
	2.155 Hz	0.002	0.998	0.001	0.000	0.024
	6.305 Hz	0.003	0.002	0.867	0.028	0.001
b)						
CrossMAC 2019		SSI				
		2.092 Hz	2.165 Hz	6.302 Hz	6.449 Hz	6.872 Hz
EFDD	2.090 Hz	0.999	0.001	0.001	0.034	0.003
	2.165 Hz	0.003	0.997	0.002	0.000	0.027
	6.301 Hz	0.004	0.002	0.812	0.006	0.003

	6.459 Hz	0.036	0.000	0.039	0.924	0.021			6.443 Hz	0.034	0.001	0.061	0.891	0.020
	6.950 Hz	0.001	0.026	0.002	0.010	0.980			6.893 Hz	0.002	0.028	0.002	0.008	0.943

Analysing in depth the global modal parameters estimated in 2018 and 2019, no significant change is found in terms of frequency values (f) as the percentage variations recorded between corresponding modes are less than or equal to 1.0% (Table 5-16), meaning that the global dynamic behaviour of the tower remained unchanged in the period elapsed between the two campaigns. As concerns modal damping (ξ), relatively high percentage variations are found when comparing the damping ratios of corresponding modes between 2018 and 2019, with a maximum difference greater than 20% for the 4th mode (Table 5-16). Unlike frequencies, damping values are much more prone to be affected by measurement uncertainties and random error sources. Still, all the estimated values are consistently under 5% in each campaign, allowing to infer that, in the present case, the observed scatter is not associated with incipient damage mechanisms, but it is related to the intrinsic complex nature of this modal parameter.

Table 5-16 - Percentage variation between modal frequencies and damping ratios of EM2018 and EM2019.

Mode	f_{EM18} [Hz]	ξ_{EM18} [%]	f_{EM19} [Hz]	ξ_{EM19} [%]	Δf [%]	$\Delta \xi$ [%]
φ_1	2.082	0.817	2.092	0.762	0.478	-7.218
φ_2	2.156	0.893	2.165	0.787	0.416	-13.469
φ_3	6.293	0.578	6.302	0.666	0.143	13.213
φ_4	6.442	2.423	6.449	3.397	0.109	28.672
φ_5	6.941	2.463	6.872	2.739	-1.004	10.077

In what concerns the experimental mode shapes estimated from 2018 and 2019 AVT data (Fig. 5-27), their configuration is consistent over time and clearly points out the typical behavior of a monolithic cantilever beam with rigid constraint at the base. The principal components of displacement result well-defined for each mode and a nearly perfect correlation is found between corresponding mode pairs. The cross-validation process operated through the MAC matrix (Table 5-17) also proves the modes to be consistent, well-decoupled and accurately identified from both field campaigns.

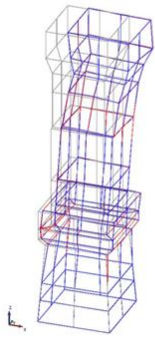
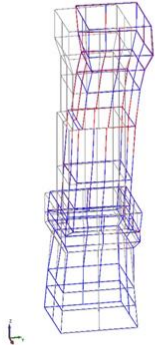
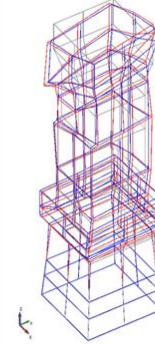
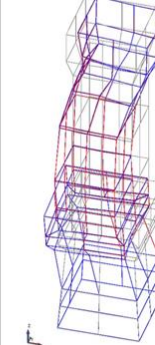
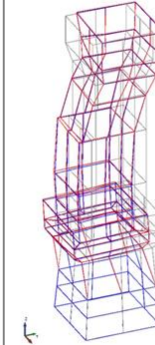
Mode 1 $f_{SSI2018} = 2.082$ Hz $f_{SSI2019} = 2.092$ Hz	Mode 2 $f_{SSI2018} = 2.156$ Hz $f_{SSI2019} = 2.165$ Hz	Mode 3 $f_{SSI2018} = 6.293$ Hz $f_{SSI2019} = 6.302$ Hz	Mode 4 $f_{SSI2018} = 6.442$ Hz $f_{SSI2019} = 6.449$ Hz	Mode 5 $f_{SSI2018} = 6.941$ Hz $f_{SSI2019} = 6.872$ Hz
				
Translational X MAC = 99.2%	Translational Y MAC = 99.5%	Torsional MAC = 98.1%	Bending X MAC = 99.0%	Bending Y MAC = 97.1%

Fig. 5-27 - Comparison between mode shapes of EM 2018 (in blue) and the corresponding ones of EM 2019 (in red).

Table 5-17 - MAC between EMs mode shapes identified with SSI method.

CrossMAC 2018-2019		EM19				
		2.092 Hz	2.165 Hz	6.302 Hz	6.449 Hz	6.872 Hz
EM18	2.082 Hz	0.992	0.000	0.001	0.037	0.001
	2.156 Hz	0.003	0.995	0.004	0.001	0.026
	6.293 Hz	0.002	0.000	0.981	0.077	0.018
	6.442 Hz	0.030	0.000	0.110	0.990	0.010
	6.941 Hz	0.005	0.025	0.009	0.002	0.971

5.2.3 Numerical modelling and updating via Genetic Algorithm

The uniqueness and complexity of heritage structures make the understanding of their actual behaviour a true challenge. By updating FE models with OMA information, one can reproduce as closely as possible the measured response of the structure and carry out a reliable condition assessment. The process consists in updating the system matrices of the FE model (mass, stiffness and possibly damping matrices) till the difference between experimental and numerical modal data is

minimized. If the FE model is not adequately representative of the reality, structural assessment cannot be performed.

Despite the degree of maturity of existing modal-based updating techniques for the calibration of realistic numerical models, experience has shown that the updating process is not trivial especially when trying to upgrade these procedures for damage localization purposes [65,87]. First and foremost, the FE model for updating requires a level of detail sufficient enough to represent both geometric and structural forms. Moreover, the number of parameters to update should be selected in order to guarantee a well-conditioned problem, independent of the contingent state of the structure and easily replicable in nearly real-time to evaluate possible global and local changes with respect to the reference modal data. The determination of reasonable initial values for the updating parameters, together with the definition of their lower and upper bounds, also plays an important role to guarantee the convergence of the iterative process and the physical significance of the final updated parameters.

Rooted in these considerations, a modal-based updating procedure relying on Genetic Algorithms (GA) is hereafter presented and employed to calibrate a realistic FE model of the masonry tower under investigation and establish baseline information for future comparative analyses at global and local level.

5.2.3.1 Preliminary FE model

An initial 3D FE model (NM0) of the tower was built using MidasFea© in order to preliminary assess the meaningful dynamic characteristics of the structure. The peculiar geometry of the tower, which is one of the parameters that mostly affects its global dynamic response, required a very high degree of detail in the modelling process of the different elements and construction features like openings, wall thickness, geometrical irregularities, etc. Particular attention was given to the reproduction of the rubble-filled masonry of the basement of the tower as well as to the concrete floors of the higher levels which were considered as rigid diaphragms in their plane. As concerns secondary elements, like stairs, deformable wooden floors, clock mechanism and bells, they were not explicitly modelled, but their influence was accounted for as added masses.

Once the geometry of the tower was defined (Fig. 5-28), all the solids composing the model were discretized as 4-node tetrahedral elements, whose mesh size was set equal to 0.3 m, resulting into a model with 21,726 nodes, 78,926 volume elements and 67806 DOFs. Considering the tower as a cantilever beam, rigid constraints were applied at the base.

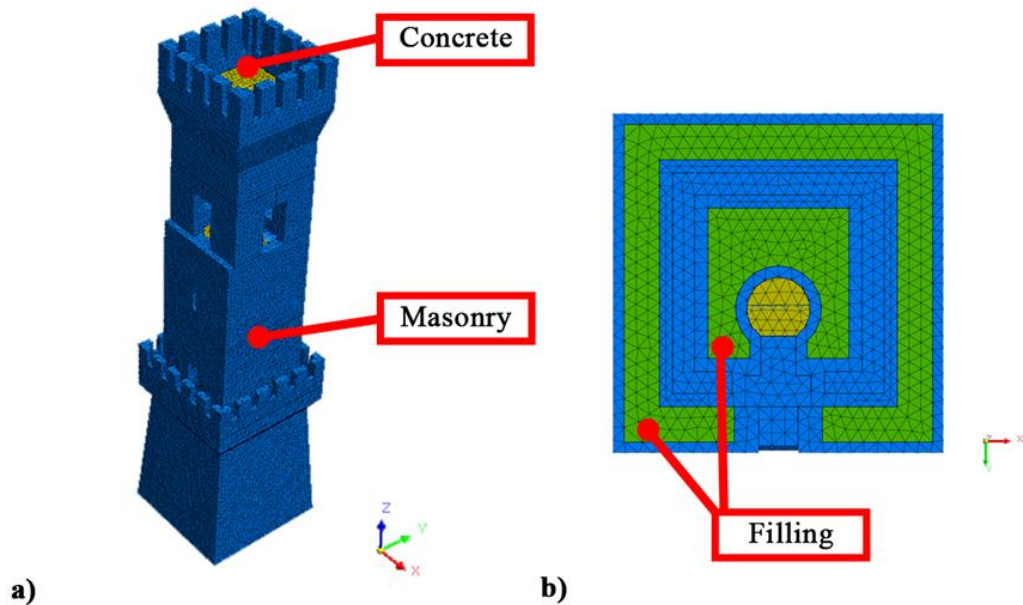


Fig. 5-28 - FE modelling of the Civic Tower of Ostra: (a) Assonometric view, (b) Bottom view at foundation level

At first, a three-group material discretization was applied, modelling each material as homogeneous and isotropic, with Young's modulus (E), Poisson's ratio (ν) and mass density (γ) chosen according to the Italian Technical Standards for Structures [67]. The initial values assumed for the afore-mentioned elastic parameters are reported in Table 5-18. It is noticed that in the definition of the elastic modulus of the concrete, a 30% reduction was considered, because of the uncertainties linked to aging effects, while for the rubble masonry properties the values suggested in the Italian code [67] for irregular masonry were assigned.

Table 5-18 - Elastic properties of the initial FE model.

Material	E [MPa]	ν [-]	γ [kN/m ³]
Masonry	1800	0.20	18
Concrete	18000	0.20	25
Filling	1100	0.20	18

A preliminary modal analysis, implemented through the Lanczos method [88–91], was carried out on the initial FE model to evaluate the dynamic properties of the tower and quantify the residuals between numerical and experimental modal parameters. The results from this first step are reported in Table 5-19, where the remarkable differences between actual experimental frequencies (EM) and calculated numerical frequencies (NM0) of the not yet calibrated model are highlighted.

Table 5-19 - Preliminary numerical results (NM0) and differences with the experimental frequency values (EM).

Mode	f_{NM0} [Hz]	T_{NM0} [s]	Eff. Mass Direction X [%]	Eff. Mass Direction Y [%]	f_{EM18} [Hz]	f_{EM19} [Hz]	$ \Delta f_{EM18-NM0} $ [%]	$ \Delta f_{EM19-NM0} $ [%]
φ_1	1.509	0.663	35.80	0.00	2.082	2.092	27.52	27.87
φ_2	1.536	0.651	0.00	35.72	2.156	2.165	28.76	29.05
φ_3	5.012	0.200	0.02	0.00	6.293	6.302	20.36	20.47
φ_4	5.821	0.172	21.21	0.00	6.442	6.449	9.64	9.74
φ_5	5.883	0.170	0.00	29.38	6.941	6.872	15.24	14.39

With respect to the mode shapes (Fig. 5-29), their main displacement components present a good visual correlation with their experimental counterpart, being the first two modes translational in the x and y direction, respectively, the third mode a torsional one, and the last two being dominant bending modes in the xz and yz planes.

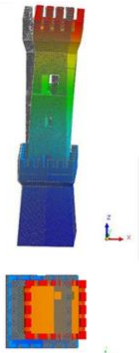
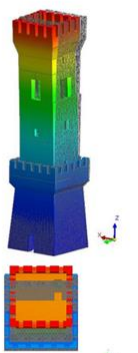
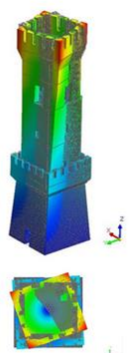
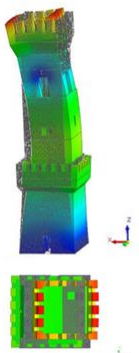
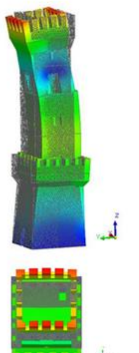
Mode 1 $f = 1.509$ Hz	Mode 2 $f = 1.536$ Hz	Mode 3 $f = 5.012$ Hz	Mode 4 $f = 5.821$ Hz	Mode 5 $f = 5.883$ Hz
				
Translational X	Translational Y	Torsional	Bending X	Bending Y
MAC _{NM0-EM18} = 77.6% MAC _{NM0-EM19} = 82.5%	MAC _{NM0-EM18} = 81.5% MAC _{NM0-EM19} = 67.2%	MAC _{NM0-EM18} = 22.1% MAC _{NM0-EM19} = 2.6%	MAC _{NM0-EM18} = 52.2% MAC _{NM0-EM19} = 47.6%	MAC _{NM0-EM18} = 1.1% MAC _{NM0-EM19} = 44.7%

Fig. 5-29 - Frequencies values and mode shapes resulting from modal analysis operated on the preliminary FE model.

On the other hand, the comparison of the degree of consistency between numerical and experimental modal vectors in terms of MAC values (Table 5-20) shows a fair correlation only for the first two fundamental modes of the tower, while higher modes feature quite a poor (4th and 5th modes) or no (3rd mode) correlation either using 2018 or 2019 modal data as comparative metric.

Table 5-20 - MAC between numerical and experimental mode shapes: (a) NM0-EM 2018 and (b) NM0-EM 2019. NM0 stands for preliminary numerical model.

a)

CrossMAC		EM18				
		2.082 Hz	2.156 Hz	6.293 Hz	6.442 Hz	6.941 Hz
NM0	1.509 Hz	0.776	0.023	0.016	0.038	0.003
	1.536 Hz	0.002	0.815	0.002	0.002	0.040
	5.012 Hz	0.004	0.006	0.221	0.000	0.003
	5.821 Hz	0.010	0.000	0.054	0.522	0.011
	5.883 Hz	0.042	0.007	0.091	0.019	0.650

b)

CrossMAC		EM19				
		2.092 Hz	2.165 Hz	6.302 Hz	6.449 Hz	6.872 Hz
NM0	1.509 Hz	0.825	0.025	0.000	0.066	0.005
	1.536 Hz	0.001	0.672	0.007	0.003	0.026
	5.012 Hz	0.050	0.038	0.026	0.029	0.029
	5.821 Hz	0.005	0.003	0.031	0.476	0.020
	5.883 Hz	0.005	0.025	0.124	0.000	0.447

5.2.3.2 GA-based model updating

As mentioned in the Introduction, iterative model updating procedures aim at calibrating an FE model through the solution of an inverse problem based on modal analysis, where corrections are applied to local physical and/or mechanical parameters of the FE model by setting an objective function and searching for the optimum solution till the difference between experimental and numerical modal data is minimized. To overcome the limitations inherently associated to manual or approximate updating processes, a genetic algorithm (GA) implemented in Code_Aster© software environment [92] was used in this work to calibrate the FE model of Ostra Civic Tower.

The genetic algorithms are inspired by Darwin's theory and are based on the process of natural selection. These algorithms are considered robust tools for solving optimization problems and explore diverse regions of interest by running the same problem on different conditions and allowing to locate with high probability the global optimum without getting trapped into local minima [74,88,93,94]. They are part of a stochastic method that "mimics" the evolution through combinations of random mutations and natural selection in order to find optimal numerical values of functions. A better understanding of the methodology can be achieved through the description of the updating process scheme as it was implemented.

NM and EM were initially imported and read by Code_Aster©, where a condensed experimental model (CEM) containing the frequency and mode shape data belonging to the five estimated modes was created. Then, CEM data were projected onto the NM (Fig. 5-30) in order to upscale the EM

DOFs. This operation enabled the possibility to visualize and interact with the data onto a 3D model while also creating the dependencies for the displacement calculations between the existing nodes of the NM with respect to the data of the EM.

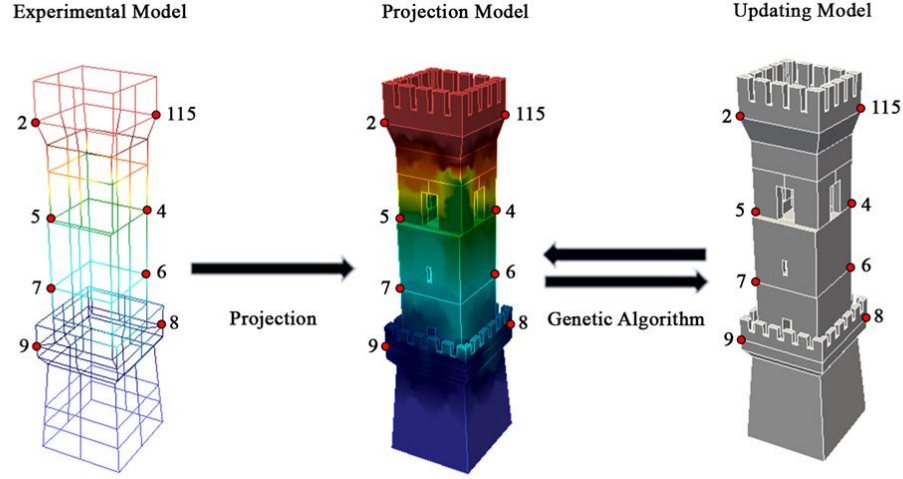


Fig. 5-30 - Workflow for the projection of the experimental data onto the NM for the genetic algorithm updating, with measured nodes highlighted.

Once the projection was done, a preliminary modal analysis was performed, generating the initial population for the values of the unknown material properties to be considered in the calibration process. Upper and lower bounds of physical significance were also set for each updating parameter based on values retrieved from the literature and belonging to analogous structures. Any value within the bounds was a candidate solution.

For each iteration, the fulfilment of convergence criteria established beforehand was progressively checked using a very strict two-term objective function that accounted for both frequencies and mode shapes residuals between EM and NM models, as reported below:

$$\Delta f + \Delta_{crossMAC} = \sqrt{\sum_{i=1}^n \left(\frac{f_{exp}^i - f_{num}^i}{f_{exp}^i} \right)^2} + \sqrt{\sum_{i=1}^n (1 - MAC^i)^2} \leq 0.05 \quad (5.9)$$

The model updating process was set to stop either when the residual tolerance of two consecutive steps reached $1e^{-4}$ or after 2000 evaluations (Fig. 5-31), hence ensuring the stability of the iterative solution.

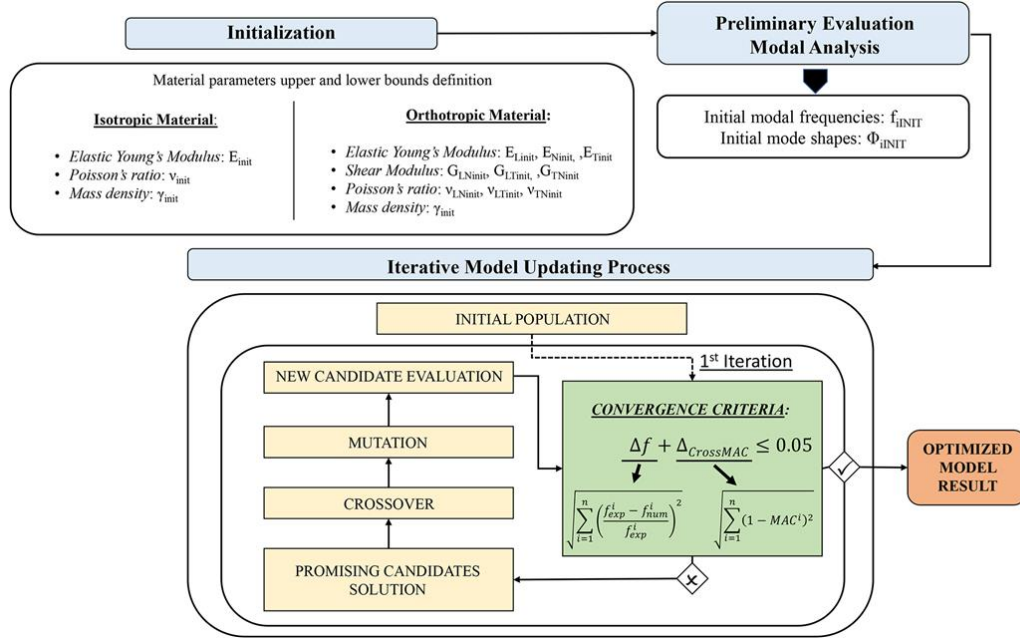


Fig. 5-31 - GA-based model updating flowchart.

5.2.3.3 Calibration process

5.2.3.3.1 Twelve-group discretization approach

To account for the visible variability of the masonry properties across the tower and better tune the model dynamic response, the number of updating parameters was increased by further discretizing the preliminary FE model into twelve parts, or solid groups (Fig. 5-32). The GA-based updating process was then repeated by employing as reference modal data the frequencies and MAC values of the five vibration modes estimated from both the 2018 and 2019 AVT measurements, and iteratively varying the elastic parameters assigned to each of the twelve parts till the residuals between numerical and experimental modal data were minimized. The final number of updating parameters thus greatly exceeded the initial number considered in the preliminary assessment.

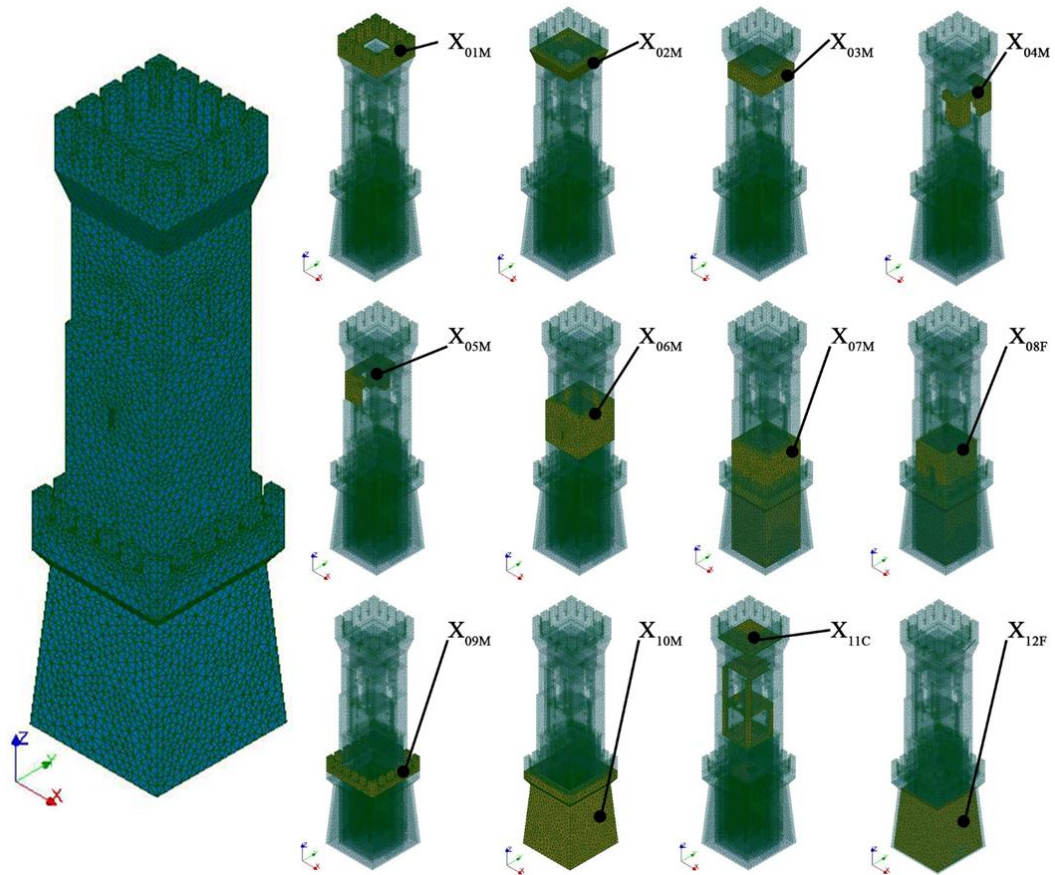


Fig. 5-32 - Updating variables for the twelve-group discretization of the FE model. Each material group is named as “X” followed by a subscript composed by a number (from 00 to 12) which stands for the group and a letter (“M” is masonry, “C” is concrete and “F” is the filling material).

The elastic properties of the twelve parts were attributed considering two different behavioural models for the materials: in the first stage all materials were modelled as homogeneous and isotropic, requesting the solution of a thirty-six parameters convergence problem ($3 \times 12 = 36$), whereas in the second stage the masonry material was modelled as orthotropic due to its complex and non-homogeneous internal structure, leading to the calibration of one hundred-thirteen updating parameters (masonry: $10 \times 11 = 110$; concrete: $3 \times 1 = 3$). It is remarked how the complexity and high dimensionality of the optimization problem could not be tackled via a manual updating procedure but required a sophisticated algorithm capable of dealing with large and multi-dimensional problems.

Reasonable variation ranges for the material parameters were assigned to each part in accordance with the values provided by the Italian Technical Standards for Structures [67] as well as with the values retrieved from the literature for analogous materials and in light of the outcome of the condition survey. The established upper and lower bounds [95–97] are summarized in Table 5-21 and Table

5-22 for the isotropic and orthotropic cases, respectively. The initial population of updating variables used in the GA-based updating process was randomly selected within these bounds.

Table 5-21 - Lower and upper bounds for isotropic elastic properties (*E* is the Elastic Young's Modulus, *v* is the Poisson's ratio and γ is the mass density).

Material	E	v	γ
	[MPa]	[-]	[kN/m ³]
	<i>Min - Max</i>	<i>Min - Max</i>	<i>Min - Max</i>
Masonry	600 - 3300	0.01 – 0.45	15 - 20
Filling	600 - 2400	0.01 - 0.45	15 - 20
Concrete	27000 - 32000	0.01 – 0.45	23 - 26

Table 5-22 - Lower and upper bounds for orthotropic elastic properties (*G* is the shear Modulus, while the subscripts *L*, *N* and *T* indicate Longitudinal, Normal and Tangential components respectively). (*) Concrete stayed as isotropic material.

Material	E_L	E_N	E_T	G_{LN}	G_{LT}	G_{TN}	v_{LN}	v_{LT}	v_{TN}	γ
	[MPa]	[MPa]	[MPa]	[MPa]	[MPa]	[MPa]	[-]	[-]	[-]	[kN/m ³]
	<i>Min-Max</i>	<i>Min-Max</i>	<i>Min-Max</i>	<i>Min-Max</i>	<i>Min-Max</i>	<i>Min-Max</i>	<i>Min-Max</i>	<i>Min-Max</i>	<i>Min-Max</i>	<i>Min-Max</i>
Masonry	600-	600-	600-	230-	230-	230-	0.01-	0.01-	0.01-	15-20
	3300	3300	3300	1400	1400	1400	0.45	0.45	0.45	
Filling	600-	600-	600-	230-	230-	230-	0.01-	0.01-	0.01-	15-20
	2400	2400	2400	1400	1400	1400	0.45	0.45	0.45	
Concrete	27000-32000		(automatically calculated)					0.01-0.45		23-26

The main scope of this GA-based model updating procedure, run first considering 36 variables (isotropic material) and then accounting for 113 unknowns (orthotropic material), was to produce a refined baseline model closely representative of the initial experimental target and that could be speedily updated with new data to serve as a future digital twin of the physical structure for predicting its performance against different scenarios. Hence the need of collecting data from two distinct AVT campaigns. In the second updating phase against 2019 experimental data, an in-depth sensitivity analysis [98,99], was also conducted to evaluate the influence of every single material parameter on the outcome of the updating process. In light of the results, although reducing the number of

unknowns is common practice in the literature [77], it was decided to continue calibrating the model through the proposed GA-based procedure and keep all the afore-mentioned parameters as updating variables, given the greater computational efficiency of the proposed method and considering this the only solution for a future extent of this study to the damage localization field.

5.2.3.3.2 *Model updating results*

The optimal mechanical parameters obtained downstream the GA-based updating process of the isotropic FE model of Ostra Civic Tower are reported in Table 5-23. It is interesting to notice that the final values of the material properties are consistent with the expected ranges and clearly reflect the visible masonry changes resulting from past interventions and restoration works. Particularly, the Young's moduli of the masonry tend to decrease from the basement (reinforced during the 1950s restoration works) to the central body (which was only partially reconstructed) and increase again towards the upper part of the tower (added later), reading values consistent with those reported in the Italian code [67].

Table 5-23 - Optimal values for the material parameters of the isotropic FE models after calibration and successive updating.

Updating parameter	<u>2018 NM</u>			<u>2019 NM</u>		
	E [MPa]	ν [-]	γ [kN/m ³]	E [MPa]	ν [-]	γ [kN/m ³]
X _{01M}	2036	0.18	15	2092	0.17	15
X _{02M}	2112	0.22	15	1960	0.24	15
X _{03M}	1278	0.21	15	1074	0.22	15
X _{04M}	1325	0.20	16	1220	0.20	16
X _{05M}	1267	0.23	15	1113	0.28	15
X _{06M}	2471	0.18	20	3133	0.17	20
X _{07M}	3289	0.19	20	3288	0.19	20
X _{08F}	2396	0.18	20	2399	0.18	20
X _{09M}	2667	0.19	20	2521	0.17	20
X _{10M}	3052	0.20	20	3282	0.21	20
X _{11C}	27615	0.26	24	27037	0.25	23
X _{12F}	1681	0.21	20	1470	0.21	20

Analogous observations can be drawn for the updating parameters calibrated through the GA-based updating process of the orthotropic FE model of the tower, whose results are reported in Table 5-24

and Table 5-25. The optimal values obtained for the elastic moduli of the masonry material feature a similar trend of variation as compared to the isotropic FE model, being consistent with the range of values expected from the visual assessment of the masonry quality. Meaningful values are found as far as the material density is concerned, whereas consistent but slightly larger variations are obtained for the Poisson's ratios.

Table 5-24 - Optimal values for the material parameters of the orthotropic FE model after calibration against 2018 EM modal data. () Concrete stayed as isotropic material.*

Updating parameter	E _L [MPa]	E _N [MPa]	E _T [MPa]	G _{LN} [MPa]	G _{LT} [MPa]	G _{TN} [MPa]	ν _{LN} [-]	ν _{LT} [-]	ν _{TN} [-]	γ [kN/m ³]
X _{01M}	2148	2007	1784	1005	894	970	0.20	0.19	0.19	15
X _{02M}	2188	2238	2125	679	911	981	0.18	0.20	0.20	15
X _{03M}	2449	1877	1726	552	784	663	0.20	0.28	0.19	15
X _{04M}	1800	1033	1941	625	939	999	0.21	0.19	0.18	15
X _{05M}	1822	1343	2103	627	825	415	0.18	0.18	0.17	15
X _{06M}	1607	2091	2439	1258	1168	1077	0.17	0.19	0.16	19
X _{07M}	2300	3248	2410	1357	988	1392	0.19	0.19	0.20	20
X _{08F}	1974	2387	2283	515	511	712	0.20	0.20	0.18	20
X _{09M}	2079	1898	2074	1034	1116	870	0.19	0.17	0.20	20
X _{10M}	1700	2978	2322	972	991	991	0.22	0.16	0.21	20
*X _{11C}		27345		(automatically calculated)				0.31		24
X _{12F}	2007	2212	2118	345	558	748	0.17	0.19	0.20	20

Table 5-25 - Optimal values for the material parameters of the orthotropic FE model after updating with 2019 EM modal data. () Concrete stayed as isotropic material.*

Updating parameter	E _L [MPa]	E _N [MPa]	E _T [MPa]	G _{LN} [MPa]	G _{LT} [MPa]	G _{TN} [MPa]	ν _{LN} [-]	ν _{LT} [-]	ν _{TN} [-]	γ [kN/m ³]
X _{01M}	2145	2031	1908	946	916	1022	0.21	0.20	0.20	15
X _{02M}	2121	2397	1882	636	950	996	0.18	0.20	0.21	15
X _{03M}	2294	1909	1761	460	725	614	0.18	0.27	0.19	15
X _{04M}	1682	967	1946	564	924	1036	0.22	0.19	0.17	15

X _{05M}	1694	1301	2133	528	770	338	0.18	0.17	0.16	15
X _{06M}	1615	2092	2230	1374	1122	1221	0.17	0.18	0.16	20
X _{07M}	2327	3297	2508	1400	1092	1391	0.19	0.19	0.20	20
X _{08F}	1711	2397	2351	563	516	772	0.20	0.21	0.18	20
X _{09M}	2048	1956	2143	1038	1116	899	0.20	0.18	0.21	20
X _{10M}	1743	3016	2507	1126	1054	1054	0.19	0.16	0.20	20
*X _{11C}			27106		(automatically calculated)				0.33	25
X _{12F}	2035	2201	2060	330	542	795	0.17	0.20	0.20	20

The frequency results obtained from the modal-based FE model updating of Ostra Civic Tower through GA are exposed in Table 5-26 and Table 5-27. For both material modelling approaches, the comparison between EM and NM frequency values is more than satisfactory, being the absolute value of their relative errors always under 4%, with the largest percentage error in correspondence of the 4th mode, error that consistently reduces if an orthotropic material is considered for masonry. In general, the orthotropic model allows to better tune the frequencies of the fundamental global modes of the tower and to closely reproduce the frequencies of higher modes, which are notably more sensitive to localized damage.

Table 5-26 - Comparison between 2018 experimental (EM) and numerical (NM) frequencies for different material modelling approaches and different updating parameters.

Mode	f _{EM18} [Hz]	f _{NM18} [Hz]	f _{NM} [Hz] 113 variables (Orthotropic)	Eff. Mass Direction X [%]	Eff. Mass Direction Y [%]	Δf _{EM18-NM18}	Δf _{EM18-NM18}
		36 variables (Isotropic)				[%] (Isotropic)	[%] (Orthotropic)
φ ₁	2.082	2.070	2.084	34.14	0.01	0.58	0.10
φ ₂	2.156	2.111	2.137	0.01	33.53	2.09	0.88
φ ₃	6.293	6.245	6.284	0.26	0.00	0.76	0.14
φ ₄	6.442	6.693	6.516	29.89	0.11	3.90	1.15
φ ₅	6.941	6.839	6.907	0.12	29.25	1.47	0.49

Table 5-27 - Comparison between 2019 experimental (EM) and numerical (NM) frequencies for different material modelling approaches and different updating parameters.

Mode	f_{EM19} [Hz]	f_{NM19} [Hz] 36 variables (Isotropic)	f_{NM19} [Hz] 113 variables (Orthotropic)	Eff. Mass Direction X [%]	Eff. Mass Direction Y [%]	$ \Delta f_{EM19-NM19} $ [%] (Isotropic)	$ \Delta f_{EM19-NM19} $ [%] (Orthotropic)
φ_1	2.092	2.079	2.091	33.94	0.00	0.62	0.05
φ_2	2.165	2.123	2.143	0.00	33.41	1.94	1.02
φ_3	6.302	6.277	6.229	0.41	0.06	0.40	1.16
φ_4	6.449	6.645	6.510	29.22	0.03	3.04	0.95

The numerical mode shapes corresponding to the FE model calibrated with the optimal values of the material parameters are displayed in Fig. 5-33 and Fig. 5-34. Similar considerations can be drawn in this case. Indeed, a very good agreement is visually observed between experimental and numerical mode shape configurations: the 1st and 2nd mode are in-phase translational modes in x and y directions, respectively, the 3rd mode is torsional, while the 4th and 5th modes result dominant bending modes in the xz and yz planes.

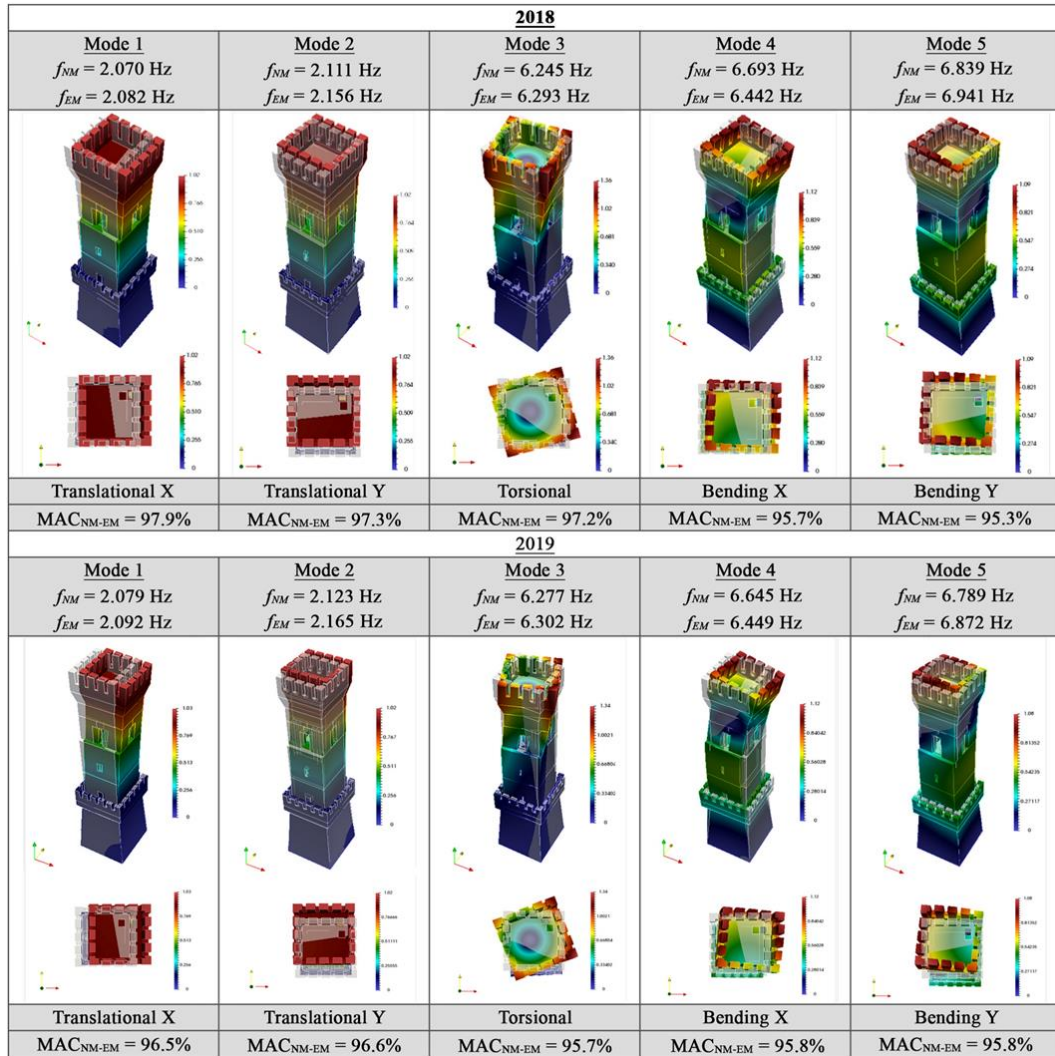


Fig. 5-33 - Numerical mode shapes after calibration using isotropic material modelling.

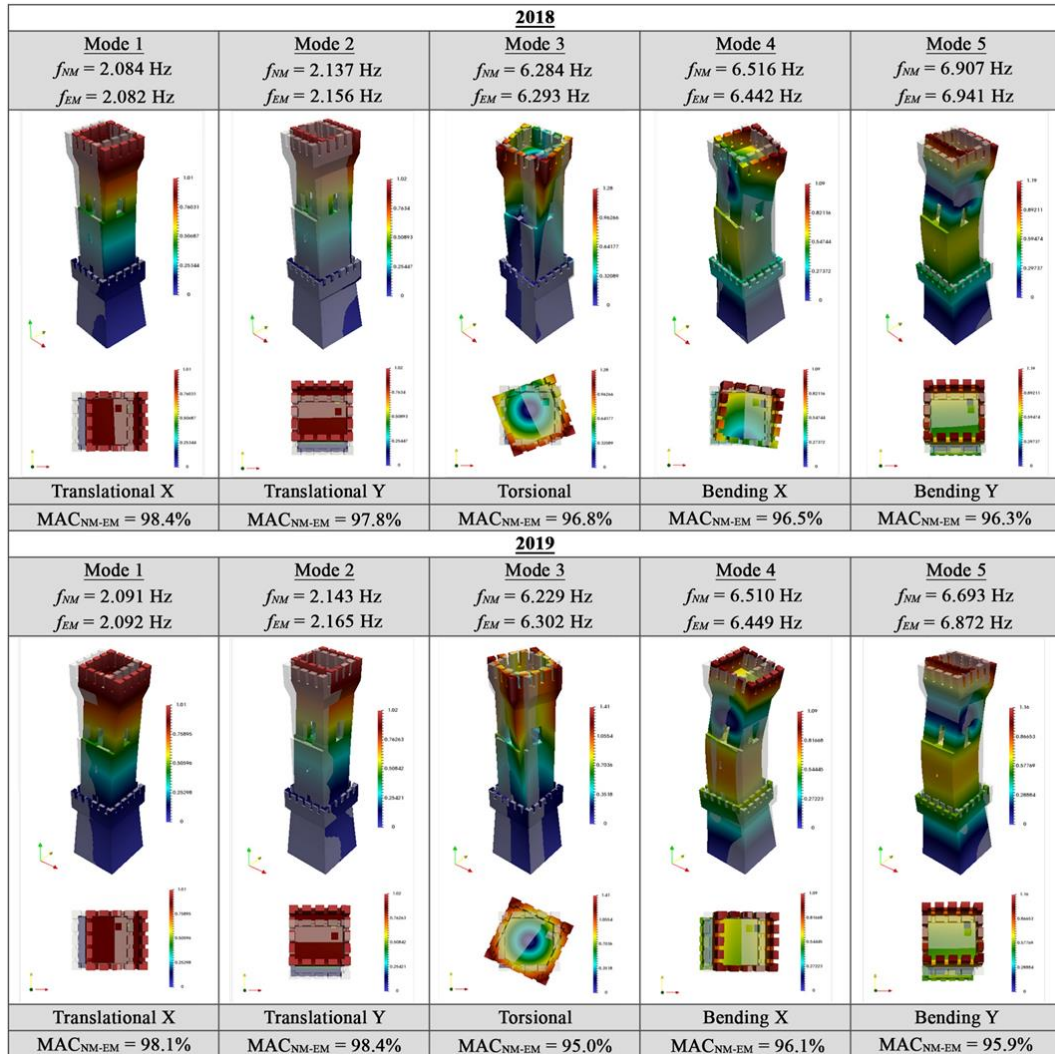


Fig. 5-34 - Numerical mode shapes after calibration using orthotropic material modelling.

The direct cross-validation between EM and NM mode shapes through the MAC further proves the good agreement between experimental and numerical counterparts, being all five modes very well correlated ($MAC > 95\%$) and decoupled, as demonstrated by the low values of the out-of-diagonal elements of the Cross-MAC matrix (Table 5-28). It is worth highlighting the relevance of the achieved results: in fact, the majority of FE model updating techniques applied in the literature typically result into much higher relative errors between experimental and numerical frequencies and, in the rare instances in which a two-term objective function is adopted, into MAC values sensibly lower than 80% for higher order modes.

Table 5-28 - CrossMAC between EMs and calibrated NMs considering isotropic and orthotropic materials:
(a) NM 2018 with isotropic material, (b) NM 2019 with isotropic material, (c) NM 2018 with orthotropic material, (d) NM 2019 with orthotropic material.

a)

CrossMAC		EM18				
		2.082 Hz	2.156 Hz	6.293 Hz	6.442 Hz	6.941 Hz
NM18_iso	2.070 Hz	0.976	0.011	0.001	0.018	0.002
	2.111 Hz	0.021	0.969	0.000	0.000	0.026
	6.245 Hz	0.000	0.000	0.972	0.015	0.015
	6.693 Hz	0.035	0.002	0.011	0.965	0.001
	6.839 Hz	0.003	0.015	0.005	0.010	0.960

b)

CrossMAC		EM19				
		2.092 Hz	2.165 Hz	6.302 Hz	6.449 Hz	6.872 Hz
NM19_iso	2.079 Hz	0.962	0.016	0.000	0.019	0.000
	2.123 Hz	0.040	0.963	0.002	0.002	0.027
	6.277 Hz	0.001	0.000	0.958	0.010	0.024
	6.645 Hz	0.033	0.001	0.011	0.966	0.002
	6.789 Hz	0.006	0.017	0.006	0.024	0.960

c)

CrossMAC		EM18				
		2.082 Hz	2.156 Hz	6.293 Hz	6.442 Hz	6.941 Hz
NM18_Ortho	2.084 Hz	0.981	0.005	0.001	0.018	0.002
	2.137 Hz	0.013	0.977	0.000	0.000	0.027
	6.284 Hz	0.000	0.000	0.959	0.014	0.006
	6.516 Hz	0.033	0.002	0.013	0.957	0.005
	6.907 Hz	0.002	0.010	0.001	0.002	0.965

d)

CrossMAC		EM19				
		2.092 Hz	2.165 Hz	6.302 Hz	6.449 Hz	6.872 Hz
NM19_Ortho	2.091 Hz	0.979	0.004	0.000	0.021	0.001
	2.143 Hz	0.019	0.981	0.003	0.001	0.028
	6.229 Hz	0.001	0.000	0.963	0.011	0.013
	6.510 Hz	0.031	0.001	0.009	0.971	0.020
	6.693 Hz	0.003	0.011	0.001	0.002	0.968

aspects of this work, namely the exploitation of an automatic procedure capable of handling a very large number of unknowns, which enabled to consider as variables all the meaningful parameters describing the orthotropic behaviour of the masonry material and to compare the goodness of the simulated modal response against the one obtained from the isotropic model. Overall, although the orthotropic approach produced slightly better results in terms of final modal residuals, the improvement was not as marked as it could be expected. Due to the complexity of orthotropic modelling when dealing with unconventional historical structures in both linear and non-linear fields, resorting to the isotropic assumption can allow to greatly reduce the computational effort inherent to the calibration process and subsequent analyses, without compromising the accuracy and reliability of the results. Finally, it is worth stressing that, unlike most of current FE model updating techniques, the method herein proposed does not run into difficulties when tackling a great number of parameters and has been demonstrated feasible even when the number of subproblems to solve grows exponentially, confirming its suitability to be employed as preferred tool to optimize the control of the structural integrity at global and local level.

6 Automatic OMA identification process for long-time monitoring

6.1 The case study: Camerino Dome twin bell towers

In the previous chapters, different applications of OMA identification techniques have been showed, confirming the potentiality of this method in the assessment of the health state of structures (as demonstrated for the identification of Morandi Hangar cover and damaged stays of Garigliano River bridge) and also the possibility to improve the knowledge about mechanical properties of structures, and in particular historical ones, towards model updating processes conducted manually at first, and through automatic process as in the case of Ostra Civic Towers.

Now, in this section, on the basis of the previous experiences, the main core of this thesis is presented, consisting of the definition of an automatic procedure for continuous analysis of dynamic monitoring data, to be coupled to all the previous mentioned application, in order to know have the conditions of a monitored structure always under check, through a modal tracking of the main structural modes, which also considers the effects of environmental agents.

A particular application of this technique is the system, composed of four MEMS accelerometers, installed on the 4th of February 2020 in the bell towers of the Cathedral of Santissima Maria Annunziata of Camerino. This monument suffered severe damage during the seismic sequence of 2016 that stroked Central Italy, leading to reinforcement interventions that made the church an iconic case study for the development of a continuous monitoring system.

The automatic procedure for modal parameters tracking is implemented in Matlab©, using the toolboxes available in this programming environment, and the results of over one year acquisition and data analysis are presented in the following sections.

6.1.1 Localization and History



Fig. 6-1 - Localization of the city of Camerino (a) and a view of Santissima Maria Annunziata Cathedral (b)

The city of Camerino (Fig. 6-1a) arises on a hill (661 m a.m.s.l.) of the Macerata Province, in the Marche region (Italy). In the main square is located the Cathedral (Fig. 6-1b) nowadays known as Santissima Annunziata of Camerino, originally built during the V century d.C. as a Roman basilica dedicated to San Giuseppe. Starting from XIII century, according to the historical documentation, the structure is subject to great alterations because of the Swabian devastations and the evolution of the economy and demography of the city. The renovation culminated with the restoration works following the complete collapse of the bell tower caused by an earthquake in 1279. New restyling operations started between 1748-1749, when the XIII century façade was completely rebuilt with baroque canons.

Due to the 1799 seismic events, the building was destroyed, thus re-building works started under the direction of Andrea Vici. This project contemplated the complete reconstruction of the church with a Latin-cross planimetry and the expansion of the square in the front.

After a stop, due to the French occupation in 1807, the restoration works were resumed 10-20 years later and the Cathedral assumed the shape we observe nowadays, with the two robust symmetrical belfries and the front gallery. The works finished in 1832, when the church was consecrated to Santissima Annunziata.

Other earthquakes occurred in the following years (i.e., 1873, 1897, 1979) and only after the seismic events of 1997 steel curbs were installed in the roof.

6.1.2 Geometrical and Material Survey

The geometrical and material surveys of the Church were operated through laser scanning technology, which allowed to extract the planimetry, the lateral views and the sections of the building. From the right aisle, it is possible to access the relative tower, otherwise the left tower (Fig. 6-1b) is accessible through a door from the outside.

The towers are symmetrical, with a peak height of 40.8 meters above the countryside level, with an irregular octagonal cross-section and a planimetric footprint of around $7.40 \times 6.92 \text{ m}^2$. The belfries floors stand at around 25 m of altitude and present four vast arch opening on the sides (Fig. 6-1b).

Several types of masonry texture, the presence of opening and different heights of the foundations constitutes vulnerability elements which contributed to reach the level of damage which is observable in Fig. 6-2.



Fig. 6-2 - Crack patterns and material surveys

6.2 Preliminary Finite Elements Model

All the information obtained from geometrical and material survey of the structure have been used to create a preliminary, not calibrated, FE model of the church complex, realized into Midas FEA© software. This model, as it is common practice in SHM field [52,101,102], is used to conduct a first modal analysis aimed to restrict the frequency range to be considered during the identification process, and to make a preliminary evaluation of the most sensitive point where the sensors of the monitoring system should be positioned.

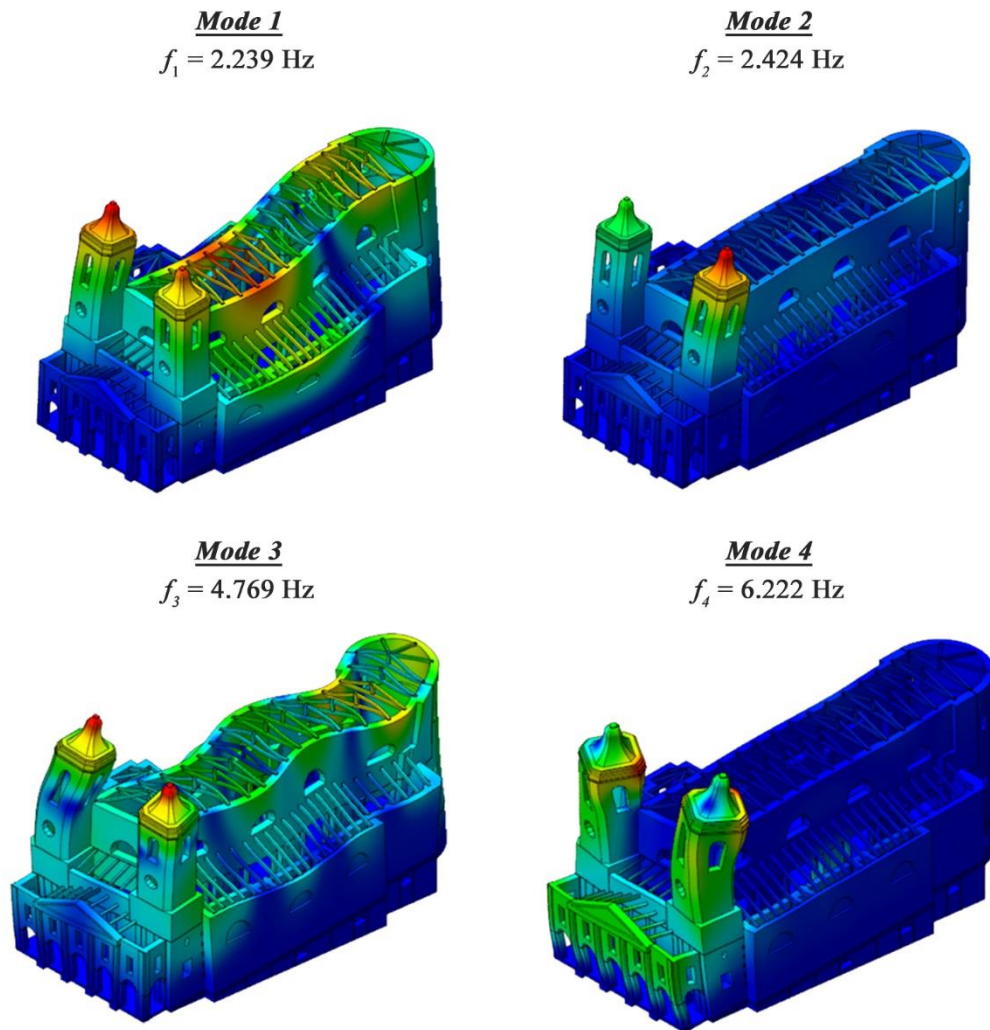


Fig. 6-3 - Mode shapes resulting from modal analysis over non calibrated FE model

As it is possible to see from the results illustrated in Fig. 6-3, four modes are expected in the frequency range 0 - 10 Hz, all of them involving the two towers, with the zones near the peaks being

the ones subdued to the largest displacements, as it was easily expectable. Modes 1 and 3 involve the structure in its integrity.

Focusing on the bell towers, the first two modes show a marked translational component of displacement, which tend to be coupled by a rotational movement for higher modes. It is peculiar to observe how the mode shapes of the two towers seem to be antiphase. From this consideration and because of the duality of the investigated structure, in order to have a better comprehension of the dynamic behavior of both the towers (indicated, in Fig. 6-4, respectively with subscript “Sx” for the left one and “Dx” for the right one), after pre-processing operations, the script extracts the modal parameters about the two towers separately.

6.3 Ambient Vibration Testing - Instrumentation and sensors layouts

The start of the continuous monitoring process has been preceded from a short-time acquisition, necessary to assess the actual health status of the two towers and fix the initial conditions in terms of modal characteristics. This operation has been executed using 18 monoaxial piezoelectric accelerometers, of the PCB 393B12 series, characterized by a sensitivity of 10 V/g, connected to Dewesoft© Krypton 4-ch A/D converters. The accelerometers have been fixed through mounting supports in groups of three orthogonal sensors, each one monitoring a spatial direction (X, Y, Z). For each of the towers, three adjacent corners, at height of around 4m above the bell cell floor, were chosen as location, two of the three points in proximity of the positions of MEMS sensors (Fig. 6-4). This acquisition lasted 40 minutes with a sampling frequency of 100 Hz.

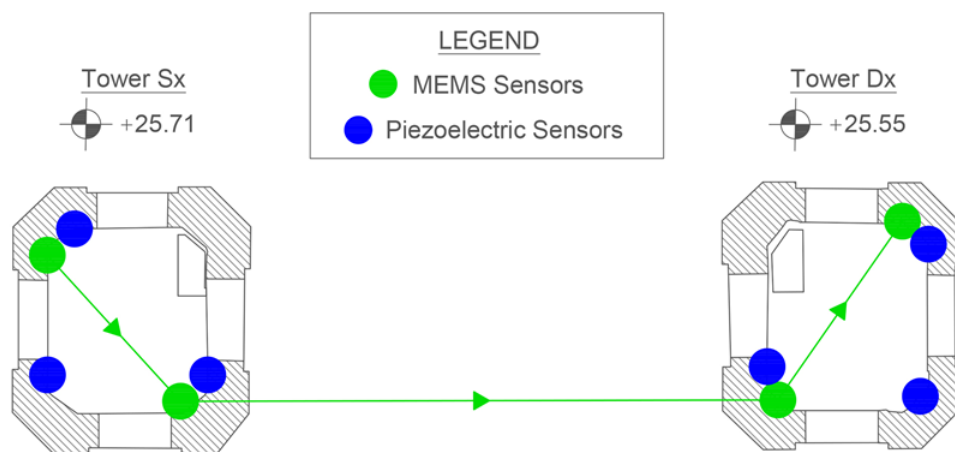


Fig. 6-4 - Sensors layouts: respectively the continuous monitoring system (in green) and the short-time monitoring system (in blue).

The continuous monitoring system is composed of four triaxial MEMS accelerometers (of the MonoDAQ-E-gMeter), installed in pairs on two opposite corners of the towers (Fig. 6-4). All the sensors are connected in chain, assuring the synchronization of the measures. The system is set to acquire a time history with a duration of 20 minutes every hour, with a sampling frequency of 100 Hz. When the continuous acquisition process stops, acquisition on trigger activates (Fig. 6-5) and, in case of events, registrations start with sampling frequency of 1000 Hz and duration of 90 seconds of pre- and 90 seconds of post-triggering.

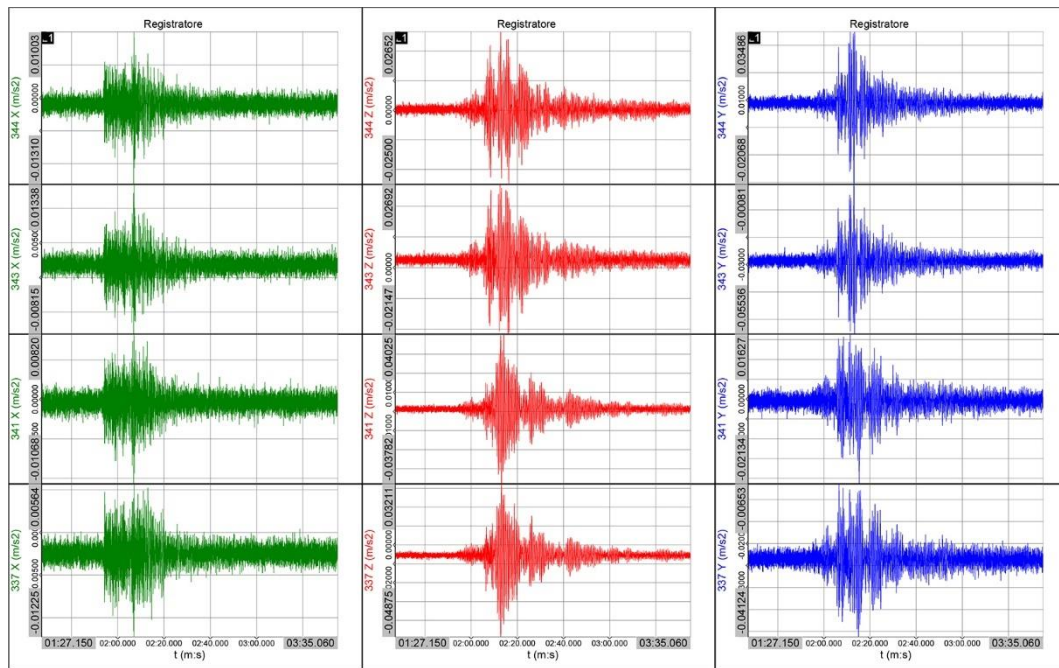


Fig. 6-5 - Example of acquisition in trigger modality: Cartoceto (PU) seismic event on 29.10.21 at 12:53:10 - Magnitude 4.1

Data are stored in a physical unit located on site and also charged online for the analysis process.

Environmental data, concerning external temperature, external humidity, and wind speed, are collected through a weather station positioned in the proximity of the structure, available for consultation on the site <http://app.protezionecivile.marche.it/sol/info.sol?lang=it>.

6.4 The automatic identification procedure

6.4.1 Flow-chart of the method

Matlab© environment provides a series of modules and toolboxes specifically designed for treatment, analysis of signals and identification of systems. Thanks to these powerful tools it is possible to

implement a program able to manage a large series of accelerations time histories and extract from them the principal modal characteristics of the investigated structure: modal frequencies (f), damping ratios (ξ) and mode shapes (φ).

Stored data are saved in a dedicated file format, so when they are loaded in Matlab© environment they are at first converted to text file and a script provide to the organization of data channels, ordering the columns of the file and eventually reorganizing the orientation of axis.

Another file containing all the geometrical information of the structure (nodes positions, connections and boundary conditions) useful for the creation of the experimental model and the successive visualization of mode shapes is also imported and a simplified scheme of the building, also showing the reference nodes, is generated (Fig. 6-6).

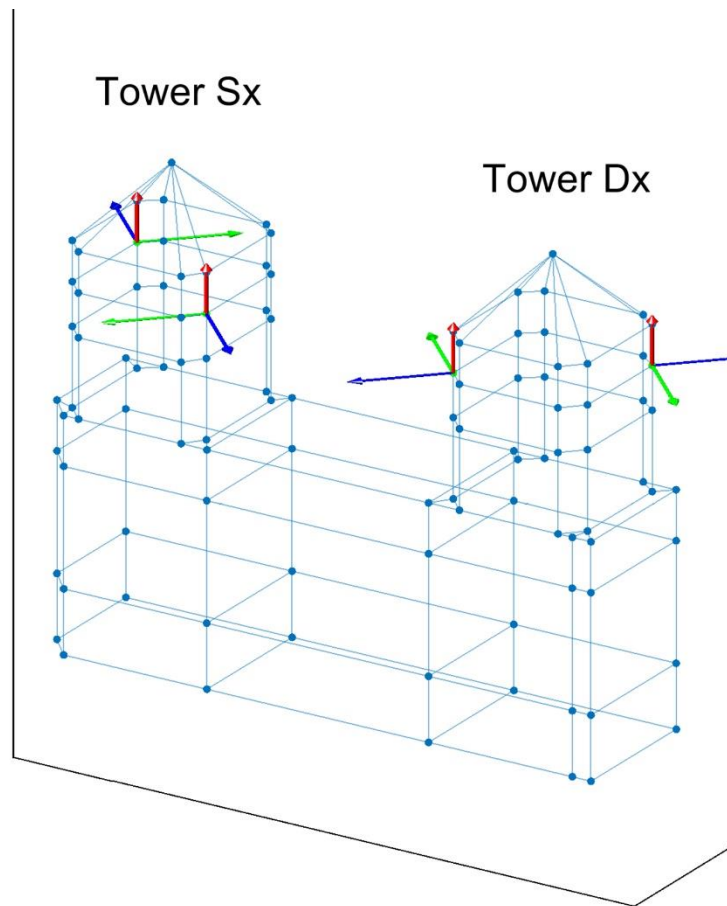


Fig. 6-6 - Geometrical model with highlighted reference nodes.

Then, after the setting of the analysis parameters, the program starts to process each of the acquisitions files, following the procedure summarized in Fig. 6-7.

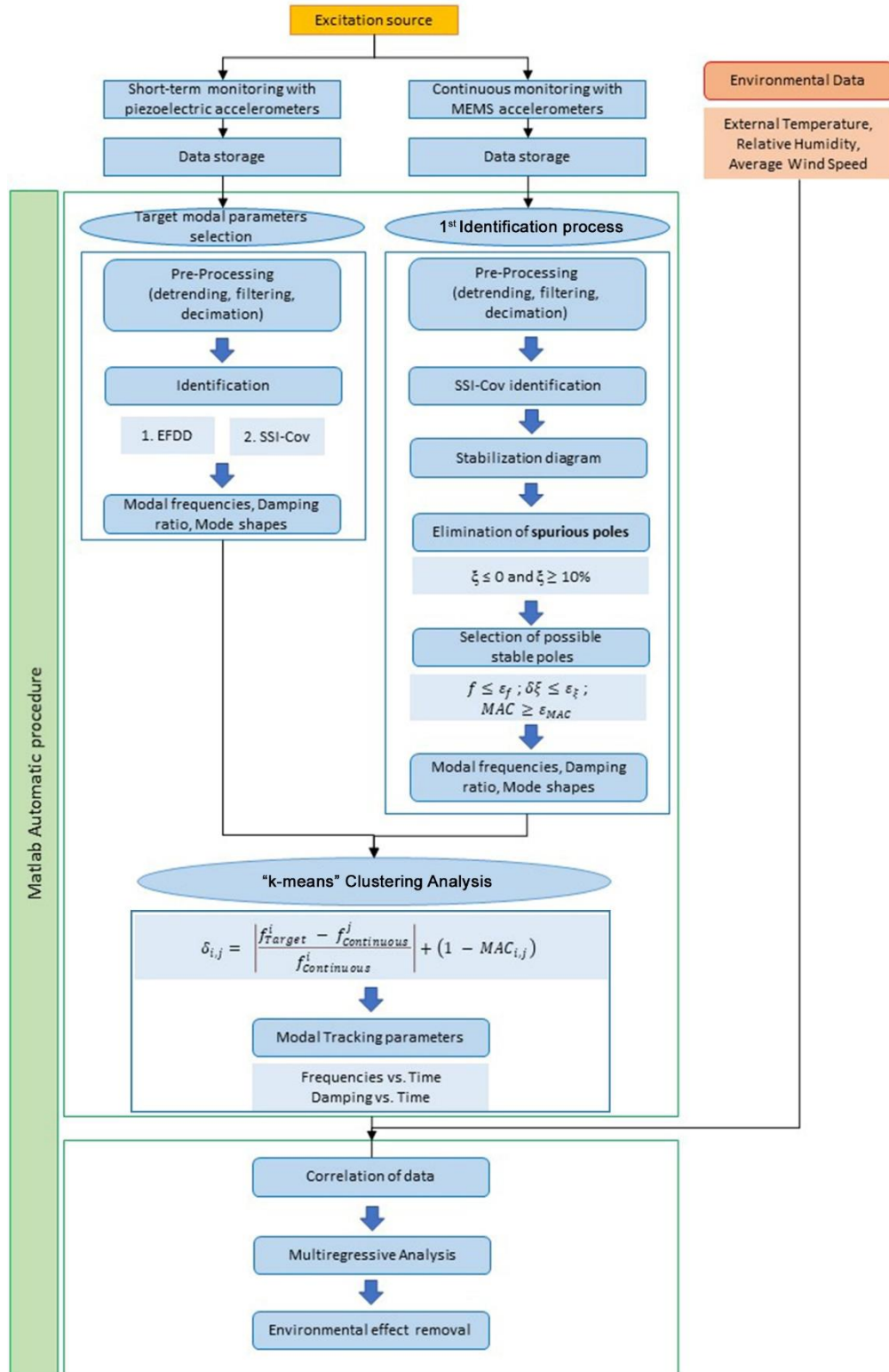


Fig. 6-7 - Flowchart of the proposed methodology

The process is inspired to the ones described in [103], and consists of two consecutive step of analysis:

1. a first step where, SSI-cov method is applied to each data file, after the execution of pre-processing operations, and modal parameters are calculated for different model orders. Always in this first block, *spurious poles* elimination is conducted, applying two different sets of *validation criteria*;
2. second step where the previous formed sets are subjected to *k-means clustering analysis* to choose the modes which result more similar to the one automatically identified from preliminary monitoring data.

Then modal characteristics are correlated with environmental data (external temperature, relative humidity and average wind speed) and their effect is removed applying linear regressive methods.

In the following paragraphs the steps of the proposed methodology are discussed with more detail.

6.4.2 Preliminary modal identification

Data acquired in the preliminary monitoring activity, executed through the piezoelectric sensors, are also imported in the program at its start. After a brief pre-process, consisting in detrending, filtering and decimation of the signal to the 0-12.5 Hz frequency range, the data are subjected to two consecutive identification processes:

1. the first process is executed in frequency domain, applying an automatic EFDD identification, which highlight the most significant modes;
2. the second step is operated in time domain, recurring to SSI-Cov method implemented with the automatic algorithm used for modal tracking process of the continuous monitoring data, which will be exposed in the following paragraphs.

The modal parameters, that will become the *targets* of the *k-means clustering analysis*, operated in “post-processing step”, are chosen through and iterative procedure of comparison of each *j-th* modal frequencies and mode shape found in time domain with the *i-th* parameter found in frequency domain, until the minimization of the objective function expressed in Eq. 6.1 [53,103]:

$$\delta_{i,j} = \left| \frac{f_{EFDD}^i - f_{SSI}^j}{f_{EFDD}^i} \right| + (1 - MAC_{i,j}) \quad (6.1)$$

In Table 6-1 are reported the identified frequencies for the first four modes. The comparison is calculated as follows:

Table 6-1 - Comparison of the modal frequencies of the towers identified from preliminary monitoring data.

Mode	f_{sx} [Hz]	f_{dx} [Hz]	Δf [%]
φ_1	1.805	1.719	4.76
φ_2	2.318	2.218	4.31
φ_3	4.218	4.198	0.47
φ_4	5.906	5.848	0.98

The corresponding mode shapes are shown in Fig. 6-8. From these preliminary results is immediately obvious how the two towers, even if symmetric, have two dynamic behaviors quite different, with the right tower characterized from frequencies values lower in respect to the left and more evident torsional component already from the lower modes. This feature also confirms the goodness of the initial assumption of applying the OMA identification on the data of the two structures separately.

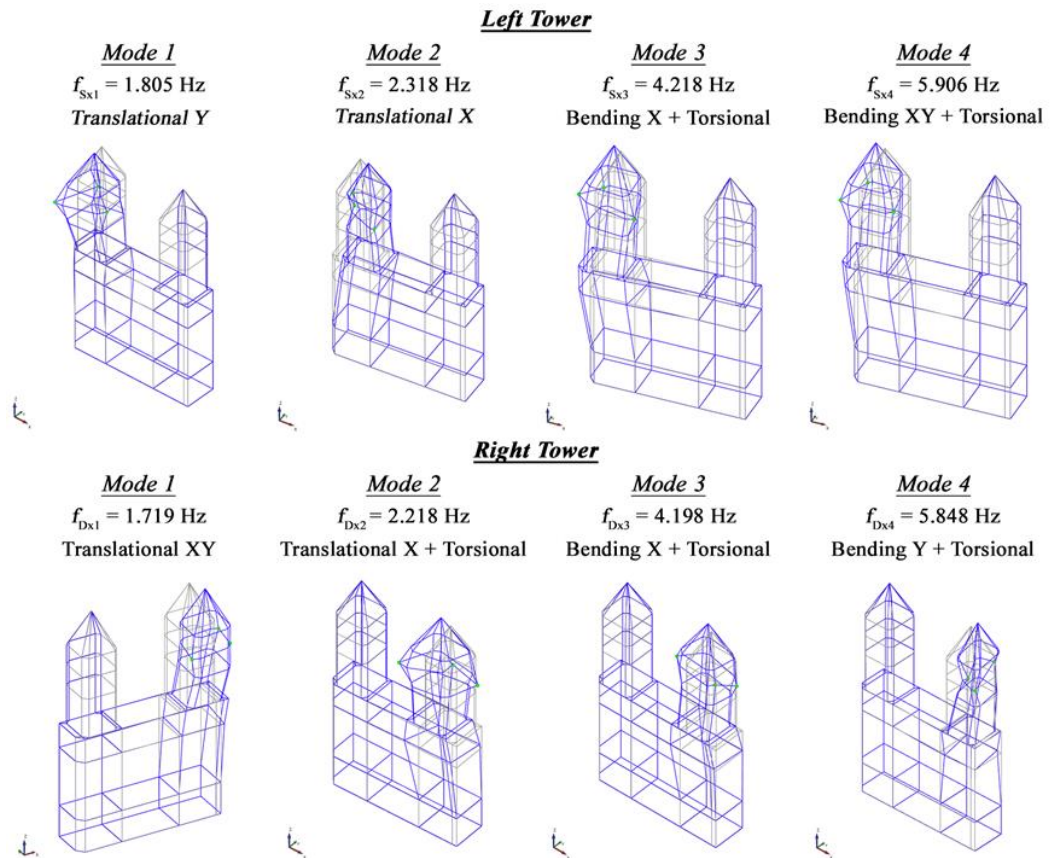


Fig. 6-8 - Target frequencies and mode shapes obtained from short-time monitoring data analysis

6.4.3 Pre-Processing of long-term monitoring data

Once the continuous monitoring acquisition are imported and the columns of the files are organized, a dedicated subroutine takes care of the pre-processing operations, which consists of:

1. *Detrending*: acquired signals can sometimes show polynomial trends, not intrinsic to the data, which can eventually interfere with data analysis. Such patterns are removed applying a *linear detrending* to the vectors of data (Fig. 6-9);

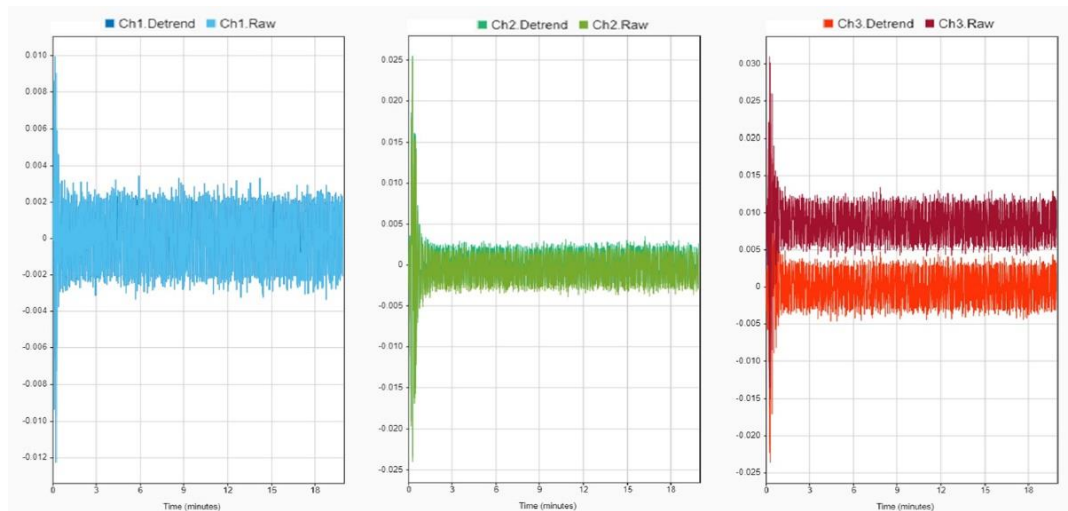


Fig. 6-9 - Example of detrending of data acquired with one triaxial sensor

2. *Filtering*: using “designfilt” function two digital filters are created, a high-pass filter to remove disturbance factors for frequencies comprised between 0 and 0.5 Hz, and a low-pass finite input response (FIR) filter based on “Kaiser” window (Fig. 6-10) to remove all the undesired frequency components from the signal in the range of interest.

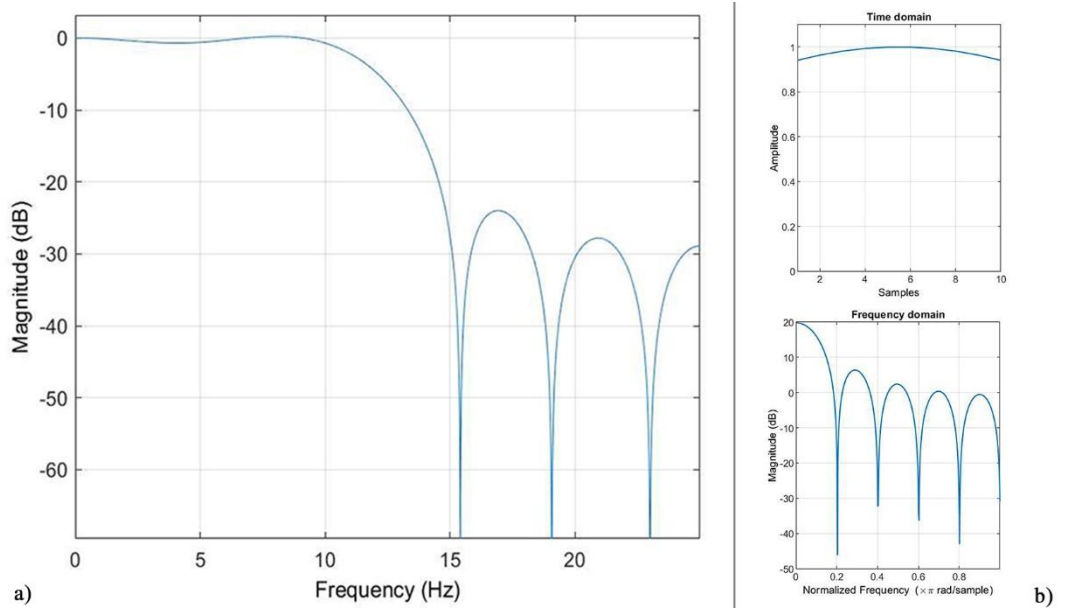


Fig. 6-10 - Low-pass filter with cut-off frequency at 12.5 Hz (a); Kaiser Window (b)

3. *Decimation*: being the range of interest for the lower modes comprised between 0 and 12.5 Hz, a *decimation factor* of 8 is applied and data are *resampled* in the new range. A new filtering process is executed in order to remove eventual disturbance given from the resampling operation.

6.4.4 Automatic modal parameters identification process

6.4.4.1 Stable poles identification

6.4.4.1.1 SSI-cov method and stabilization diagram

Pre-processed data are passed, one-by-one, to a sub-routine implementing SSI-cov method [33] able to build a State Space model for the system. Into this space, the second order equation of motion is converted into a system composed by the so-called *state equation* (Eq. 6.2) and *observation equation* (Eq. 6.3), which result linear:

$$\mathbf{x}_{k+1} = \mathbf{A}\mathbf{x}_k + \mathbf{w}_k \quad (6.2)$$

$$\mathbf{y}_k = \mathbf{C}\mathbf{x}_k + \mathbf{v}_k \quad (6.3)$$

where:

- k is the generic time instant;
- $\mathbf{x} \in \mathcal{R}^{n \times 1}$ is the discrete-time state vector;
- $\mathbf{y} \in \mathcal{R}^{l \times 1}$ is the vector containing the l output measurements;

- $A \in \mathcal{R}^{n \times n}$ is the system matrix that describes all the dynamic information of the system;
- $C \in \mathcal{R}^{l \times n}$ is the corresponding output matrix;
- $w \in \mathcal{R}^{n \times 1}$ is a white noise vector process representing disturbances and modelling inaccuracies;
- $v \in \mathcal{R}^{l \times 1}$ is another white noise vector process representing the measurement noise due to sensor inaccuracy.

From this system it is easy to extract the modal parameters, being them contained into the matrix A and C: the eigenvalues of A (μ_k) are the poles of the discrete-time state-space model, related to the ones of the continuous-time model (λ_k); among these poles, those with positive imaginary components are used to get the natural frequencies (f_k) and the modal damping ratios (ξ_k), through Eq. 6.4:

$$\lambda_k = \frac{|\mu_k|}{\Delta t} \Rightarrow f_k = \frac{|\lambda_k|}{2\pi} ; \xi_k = -\frac{Re(\lambda_k)}{|\lambda_k|} \quad (6.4)$$

As already stated in Chapter 3, in practical applications it is not possible to know from the start what is the order value that better fit the description of the dynamic behavior of the monitored structure. So, the easiest way to overcome this issue is that of overestimating the modal order, imposing a maximum value at least two times greater than the number of expected physical modes, and calculate all the responses for each of the steps if incrementation of the model order (starting from the minimum level imposed till the max). In particular, in order to reduce the computational cost of calculating modal parameters for every model orders, as it is a diffused practice [103], solutions were calculated between minimum and maximum model order with a step of five orders.

Due to the use of high model orders, it is very common to introduce among solutions those related to only numerical modes (also called *spurious poles* or *noise modes*), having no physical meaning, and caused by excessive noise content or inaccuracies in the modelling operations. To discern between the physical and noise modes, as already stated in §3.2.1.3, the most adopted method is that of creating and interpreting *stabilization diagrams*, which consists of charts designed with frequencies on the abscissa axis and model orders on the ordinate axis, where all of the solutions for the increasing order are reported (Fig. 6-11).

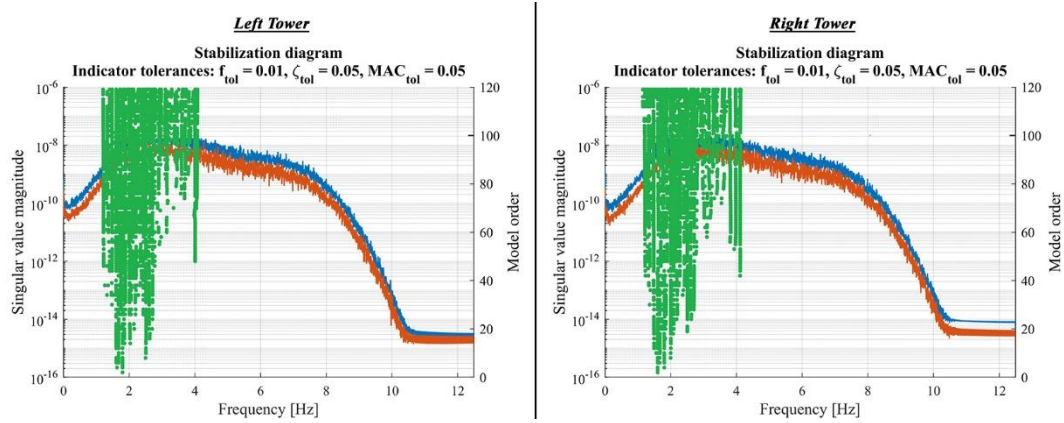


Fig. 6-11 - Stabilization diagrams

The interpretation of the stabilization diagram is suitable to be handled through clustering procedures as already demonstrated from various works present in literature [104,105]. These procedures are mainly devoted to recognizing *stables poles* on the stabilization diagram that maintain consistency in terms of natural frequency, mode shape and modal damping. These poles are those which more frequently appears for the various orders, and usually, due to the similarities of the modal features they are associated, they manifest a vertical alignment. On the contrary, *spurious poles* tend to be scattered throughout the diagram [26].

6.4.4.1.2 Elimination of spurious poles

Various aspects, linked to the instrumentation (low level of signal-to-noise ratio (SNR), low number of sensors) and to the overestimation of the model order, can negatively influence the quality of the stabilization diagram, where a high number of spurious poles can appear. It becomes necessary to remove these spurious poles, in order to have more accurate results, with identification of physical modes.

The first discrimination that can be done is based on some considerations regarding damping ratios:

- in normal operating conditions the behavior of the structure is strictly stable, and the structure is lightly damped, which implies that the damping ratio corresponding to a structural mode should be positive [106];
- highly damped modes (for instance, with a damping ratio larger than 10%) are not realistic quite for sure caused by noise content of the signal [105,107].

Therefore, a first way to eliminate unstable poles is that of fixing a damping ratio threshold, so that poles associated to negative damping ratio or high damping (i.e., damping exceeding a 10% threshold,

which seem a conservative value for Civil Engineering structures under ambient and/or operational excitations) are discarded (Fig. 6-12).

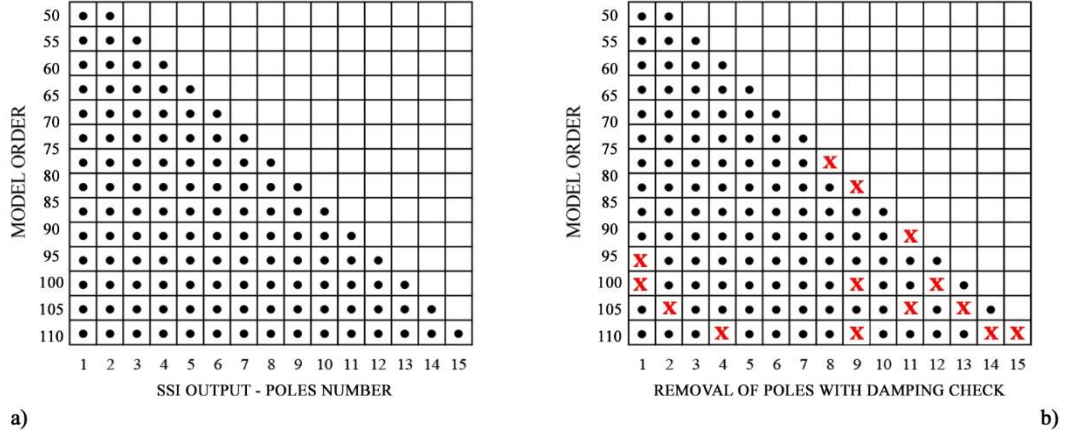


Fig. 6-12 - Damping check for removal of spurious poles (b) from the ones identified (a).

6.4.4.1.3 Validation criteria

Once most of all spurious poles are removed from stabilization diagram, the subsequent step is aimed at detecting the set of modal estimates related with the same model. To do so, the clustering approach have been implemented using tolerance values checking the variability of the modal parameters for increasing model order of the state-space model (Eq. 6.5).

The check is generally performed on the variation of the natural frequencies, damping ratios and mode shapes (using MAC index and comparing mode shapes estimates obtained for consecutive model order). This approach is quite effective, and it is also implemented in well-known commercial software used for dynamic tests and OMA analysis. The main disadvantage of this approach is related to the number of the tolerance values that need to be tuned requiring a strong human interaction during the analysis.

$$\delta f = \left| \frac{f_{i,n} - f_{j,n+\Delta n}}{f_{i,n}} \right| \cdot 100 \leq \varepsilon_f$$

$$\delta \xi = \left| \frac{\xi_{i,n} - \xi_{j,n+\Delta n}}{\xi_{i,n}} \right| \cdot 100 \leq \varepsilon_\xi \quad (6.5)$$

$$MAC(\varphi_{i,n}, \varphi_{j,n+\Delta n}) = \frac{|\varphi_{i,n} * \varphi_{j,n+\Delta n}|^2}{\|\varphi_{i,n}\|_2^2 \|\varphi_{j,n+\Delta n}\|_2^2} \geq \varepsilon_{MAC}$$

Once also validation criteria are applied (Fig. 6-13), matrices containing all the candidate modal parameters, for each model order, are subdued to a second process of clustering, described in the next section.

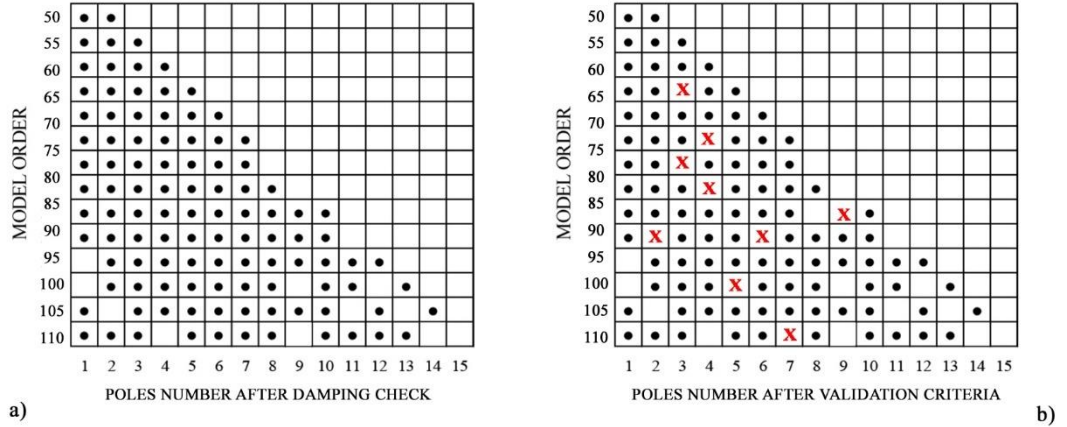


Fig. 6-13 - Reduction of poles after application of validation criteria (b) after removal of spurious poles with damping check (a)

6.4.4.2 “k-means” clustering analysis

The clustering process herein adopted is based on the definition and on the use of *k-means clustering analysis* [108,109]. It is a partitioning method, available in Matlab© environment, where a function “*kmeans*” groups data into *k* mutually exclusive clusters giving back a value identifying the cluster for each observation, where the observation and corresponding data are treated as an object occupying a space. Function “*kmeans*” tries to organize the different partitions in order to maximize the distances between different clusters and minimize those between the elements of the same one. The requirements are a *distance* metric, adaptable to the data type, and the definition of a number of clusters to be built. Unlike *hierarchical clustering*, which operates on the differences between the pairs observation in the data, *k-means clustering* operates on actual observations, creating only a single level of clusters, rather than a multilevel hierarchy of clusters.

Each cluster in a k-means partition consists of member objects and a *centroid* or *center* (Fig. 6-14).

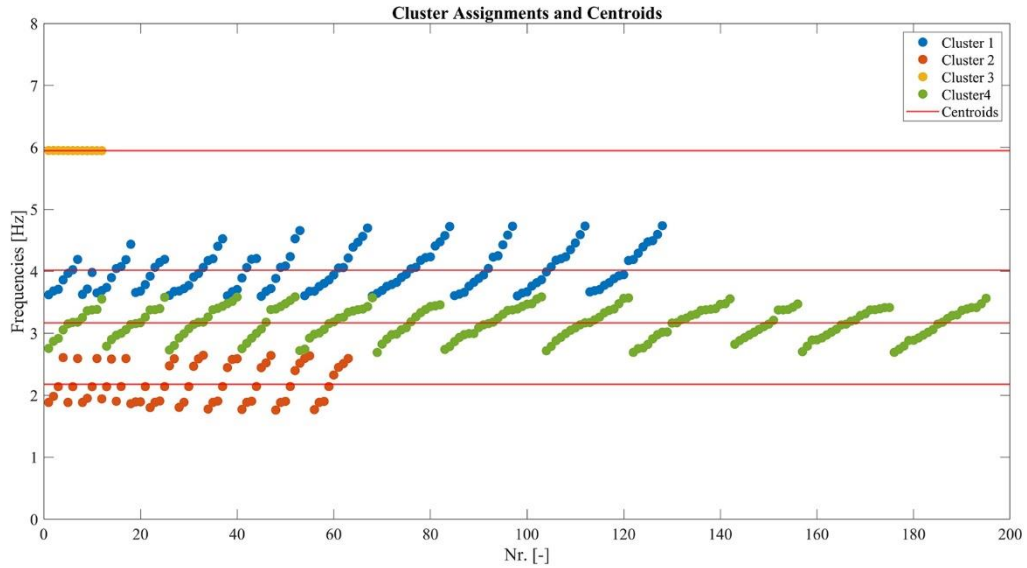


Fig. 6-14 - *k-mean cluster and centroids*

All of the modal characteristics associated to the stable poles extracted for the different model orders, through the procedures described in the previous sections, are grouped into a matrix, which is subduced to the *k-means* clustering. The number of the *k* partitions is selected pair to the number of the *target parameters*, in order to separate the different parameters. Distances from the *centroids* are calculated automatically through *Euclidean Distance metric* and, once the groups are formed the four partitions having the higher number of elements are chosen. The frequencies here contained become the candidate parameters to be tracked. At least, these characteristics, and the relative mode shapes vectors (calculated and stored during the previous identification process) are compared with the *target parameters*, starting from the one which is the nearest to the *centroid* of the partition, using a two terms iterative functions, very similar to the one proposed for the GA process for calibrating Ostra Civic Tower, accounting both for frequencies variation both for mode shapes (Eq. 6.6) [103,104] :

$$\delta_{i,j} = \left| \frac{f_{Target}^i - f_{Continuous}^j}{f_{Continuous}^i} \right| + (1 - MAC_{i,j}) \quad (6.6)$$

6.4.4.3 Preliminary modal tracking results

At the conclusion of this first section of the script modal tracking of modal frequencies relative to the first four modes for both the tower are printed (Fig. 6-15 **Errore. L'origine riferimento non è stata trovata.**). Because of interruption of the service due to malfunctioning of the alimentation system, some gap are evident in the images. Moreover, being the structure located into a non-accessible zone of

the city, due to the life risk of accessing the area after the seismic event, the excitation level is often too low to permit a satisfactory analysis of data.

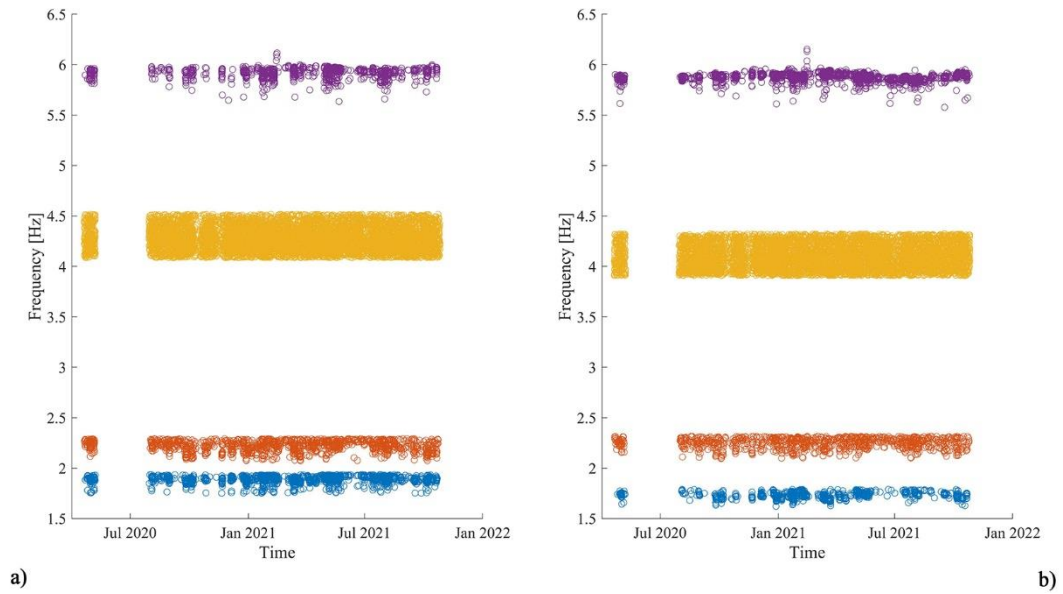


Fig. 6-15 - Modal tracking of the frequencies associated to the first four modes: left tower (a), right tower (b)

From Table 6-2, where the mean values for frequencies and damping ratios are reported, it is possible to observe a good correspondence between the identified parameters and the target ones. Moreover, the differences in the dynamic behaviors of the two towers is pretty evident, especially for the first and third modes, where the gaps are respectively equal to 8.31% and 4.19%. Damping ratios are also quite different between themselves, but they result consistent being the values decremental for higher modes.

Table 6-2 - Modal parameters identified for the bell towers and comparison

Mode	<i>Left Tower</i>		<i>Right Tower</i>		Comparison	
	f_{mean} [Hz]	ξ_{mean} [%]	f_{mean} [Hz]	ξ_{mean} [%]	$ \Delta f $ [%]	$ \Delta \xi $ [%]
φ_1	1.890	1.240	1.733	1.700	8.31	37.10
φ_2	2.226	0.990	2.258	0.860	1.44	13.13
φ_3	4.275	0.450	4.096	0.460	4.19	2.22
φ_4	5.927	0.590	5.877	0.430	0.84	27.12

An interesting phenomenon, highlighted plotting the modal tracked frequencies, is that of the so called “freezing condition” (Fig. 6-16), observable on 15.02.2021, day in which the minima temperatures of

the period were registered, for both towers. This event consists in a sudden increment of the frequencies values due to the increment of stiffness due to the freezing of water particles contained in the micro-pores of masonry. As expected, the phenomenon stopped as soon as the temperatures started going up and frequencies assumed their trends once again [19,20].

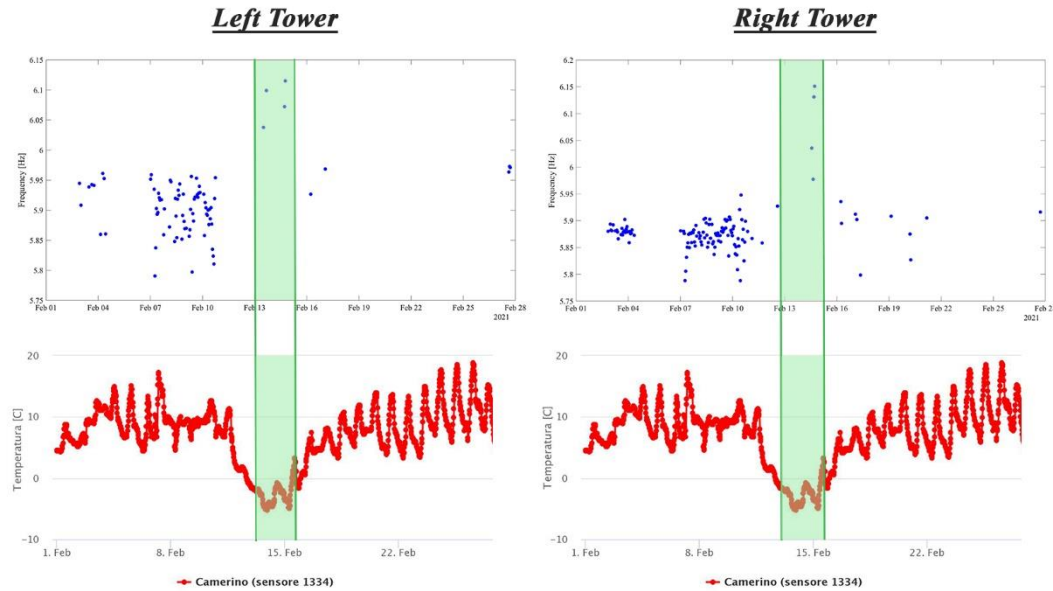


Fig. 6-16 - Freezing condition in correspondence of the minimum temperature value on 15.02.2021

6.5 Environmental effects on modal parameters

In order to develop a successful damage detection process, it is fundamental to detect modal characteristics which are strictly linked only to structure. In operative conditions it is evident that this is not possible, due to the presence of external factors, mainly constituted by environmental agents, such as temperature, humidity and wind, which obviously affects the identified parameters, often causing significant variations. Many works report practical examples describing the effects of external factor on modal parameters: daily fluctuations of the first natural frequency due to temperature variations were observed in many monitoring activities [110], with range of variations of the eigenfrequencies also around 5% of the nominal values [18,87,111–113].

So, it is clear that a correct process of modal tracking should be depurated of these effects. This requires a deep knowledge of the factors influencing the structure and more importantly how they are linked and in what measure to the modal parameters [112]. The correlation between modal properties and environmental effects is usually carried out through a class of algorithms called *input-output* models [113–117].

Input-output models are applied in order to establish a relation, usually through linear regression, between various sets of *external factors*, usually constituted by the continuously monitored environmental and operational agents exciting the structure, and the *extrapolated parameters*, in particular modal frequencies and damping ratios. Different datasets are needed in order to truly understand how and how much each *output* parameter is influenced by the variation of the *input* ones, so that the model is trained to predict the future outcome of a response parameter starting from known inputs (like in the so called “static method”), or to evaluate the output for a previous time step (like in “dynamic method”).

This procedure, once perfected, allows to recognize the occurrence of variation in the structural behavior (in particular of damage) through the comparison between the *predicted* data (or “*expected*”) and the ones coming from elaboration of real *measured* data.

6.5.1 Multiple Regression Analysis

As already mentioned in the previous section, Multiple Regression Analysis (MRA) is the most common statistical tool adopted for elaboration of *input-output* models. MRA is a technique which allows to evaluate the dependency between a *variable* and one or more independent factors, usually known as *predictors*. For applications in the context of SHM linked to civil engineering, modal parameters (frequencies and damping) are considered as *variable* and their dependence from environmental agents (the *predictors*) is investigated. The correlation between these factors, once established, make possible to predict the outcome of the *variable* in response to the values assumed by the *predictors*. Also, because of the difference in the percentage of contribution each *predictor* has on the evolution of the *output variable*, *weight coefficients* are applied to the *independent variables* in the prediction formulation.

Given a variable y , dependent only by a single predictor, denoted as x , the regression relationship which can be instituted between these two factors is defined as “*simple regression*”, expressed under the formulation of Eq. 6.7:

$$y = \theta_0 + \theta_1 x + \varepsilon \quad (6.7)$$

Where:

- θ_0 is a the regression parameter known as “*intercept*”;
- θ_1 is the so-called “*regression coefficient*”;
- ε is called “*prediction error*” or “*residual*” and calculates the difference between actual and predicted values of y .

Due to the polynomial formulation, Eq. 6.7 can be modified through the addition of non-linear terms, which is quite an advantage in those cases where the modelling of curvilinear effects becomes necessary to correctly estimates the *independent variable* behavior. The “simple regression” is then expressed as shown in Eq. 6.8:

$$y = \theta_0 + \theta_1 x + \theta_2 x^2 + \varepsilon \quad (6.8)$$

When more then one *predictor* are used for the correlation problem, the process is known as “*multiple regression*” (Eq. 6.9):

$$y = \theta_0 + \theta_1 x_1 + \theta_2 x_2 + \dots + \theta_n x_n + \varepsilon \quad (6.9)$$

Eq. 6.7 and Eq. 6.9, valid for expressing the relationship between a certain number of *predictors* and one *dependent variable*, can also be adapted to the case of more *dependent variables*, through the use of *multivariate polynomials*, for whose definition the following form can be used:

$$y = X\theta + \varepsilon \quad (6.10)$$

Where:

- y is a $[n\text{-by-}1]$ column vector containing the n measures (y_k) of the *dependent variable* (y);
- X is a $[n\text{-by-}p]$ matrix that connects n dependent values of the corresponding p selected *predictors*;
- θ is a $[p\text{-by-}1]$ column vector formed by the p parameters weighting the contribution of each independent variable;
- ε is the $[n\text{-by-}1]$ column vector of the *prediction errors* (ε_k) that account for measurement errors of the element of y and for the effects of other variables not explicitly considered in the model.

Regarding the term accounting for *prediction of errors*, ε , two properties are attributed to this parameter, expressed in Eq. 6.11:

$$\begin{aligned} E[\varepsilon] &= 0 \\ Cov[\varepsilon] &= [\varepsilon \cdot \varepsilon^T] = \sigma_\varepsilon^2 \cdot I \end{aligned} \quad (6.11)$$

Where:

- $E[\bullet]$ is the expected value operator;
- $[\bullet]^T$ means *transpose*;
- I represent the Identity matrix $[n\text{-by-}n]$.

This implies that the mean value for ε is zero and that the errors are independent (also their variance is constant).

The selection of the most prominent parameters for the development of a model that correctly reproduce the evolution of the *dependent variables* becomes fundamental, and so the best estimation of the θ_k parameters is required. Generally, the problem is solved recurring to the well known Least Squares (LS) method, where the model parameters $\hat{\theta}$ are estimated through the minimization of the sum of the squared errors (Eq. 6.12):

$$\hat{\theta} = (X^T X)^{-1} X^T y \quad (6.12)$$

During the operations, a common practice consists in the normalization of input and output data, which usually is done removing the mean values from each measurements and dividing for the variables standard deviation as in Eq. 6.13:

$$\tilde{x}_k = \frac{x_k - \bar{x}}{\sigma_x} ; \tilde{y}_k = \frac{y_k - \bar{y}}{\sigma_y} \quad (6.13)$$

In this way, the origin of the x and y axes corresponds to the “center of gravity” of the data and the regression line slope represents the correlation coefficient [118].

As the LS method minimizes the sum of the squares of the equation errors, a first quality criterion is the value of the Loss Function (LF):

$$LF = \frac{1}{N} \sum_{k=1}^N \varepsilon_k^2 \quad (6.14)$$

where N is the total number of samples, and the prediction errors are obtained as the difference between experimental and estimated values of the output variable.

Alternatively, in Eq. 6.15, the *coefficient of determination* R^2 , expressed as the ratio between two variances [119], is proposed as criterium for the evaluation of the quality of the regression model:

$$R^2 = 1 - \frac{\sum_{k=1}^N \hat{\varepsilon}_k^2}{\sum_{k=1}^N (y_k - \bar{y})^2} = \frac{\sum_{k=1}^N (\hat{y}_k - \bar{y})^2}{\sum_{k=1}^N (y_k - \bar{y})^2} \quad (6.15)$$

This coefficient assess the percentage of variation a single *predictor* has over the total variation of one of the considered *dependent variables*: if the tendency is towards zero, the *output variable* and the considered *predictor* are quite independent, while a value tendent to one, means that the *predictor* is the only factor accountable for the *dependent variable* modification.

In this kind of applications, where the acquisition of dynamic data and environmental ones is not executed simultaneously, the use of the so-called *dynamic regression models*, accounting for the

influence of inputs measured at previous time instants, results the most convenient strategy. So, a *dynamic regression* relationship (formulated as in Eq. 6.16) is established between the dependent variable at time k and values of a single predictor at current time k as well as at $(p - 1)$ previous time instants:

$$y_k = \theta_0 + \theta_1 x_k + \theta_2 x_{k-1} + \dots + \theta_p x_{k-(p-1)} + \varepsilon_k \quad (6.16)$$

Where:

$$X = \begin{bmatrix} x_1 & \cdots & x_{1-(p-1)} \\ x_2 & \cdots & x_{2-(p-1)} \\ \vdots & \ddots & \vdots \\ x_n & \cdots & x_{n-(p-1)} \end{bmatrix} \quad (6.17)$$

As concerns the environmental parameters selected as *predictors*, into this work, as it is usual practice in literature temperature (external) [°C], relative humidity [%] and average wind speed [m/s] are selected, and their influence over frequencies and damping (assumed as *dependent variables*) is studied. During the correlation process, whose results for frequencies are reported in Fig. 6-17, in the establishment of the relationship describing the variation of damping ratios (Fig. 6-18), also the dependence by frequency has been taken into account, so the regression has been operated using four parameters as *predictors*.

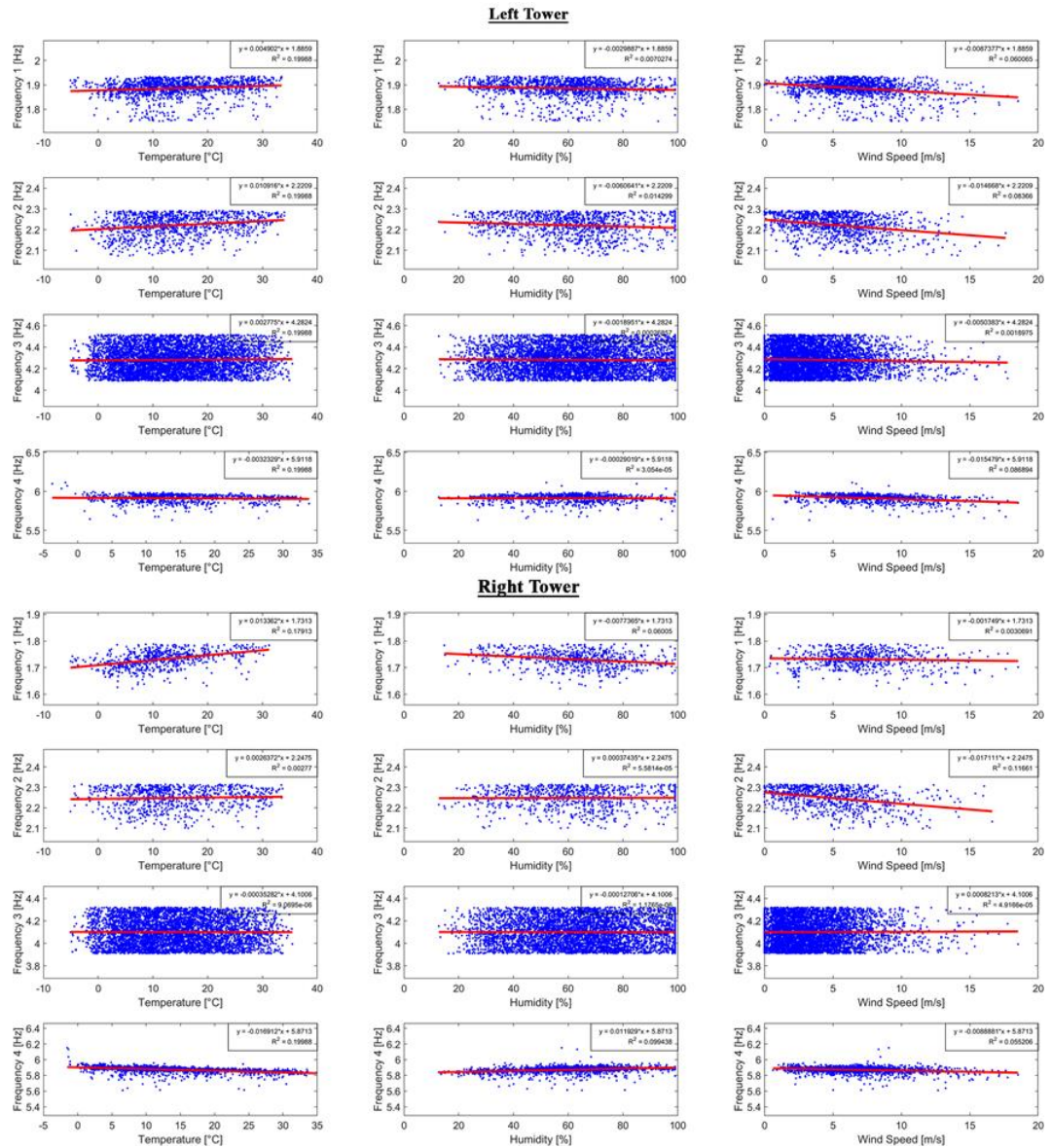


Fig. 6-17 - Correlation of frequencies with environmental data

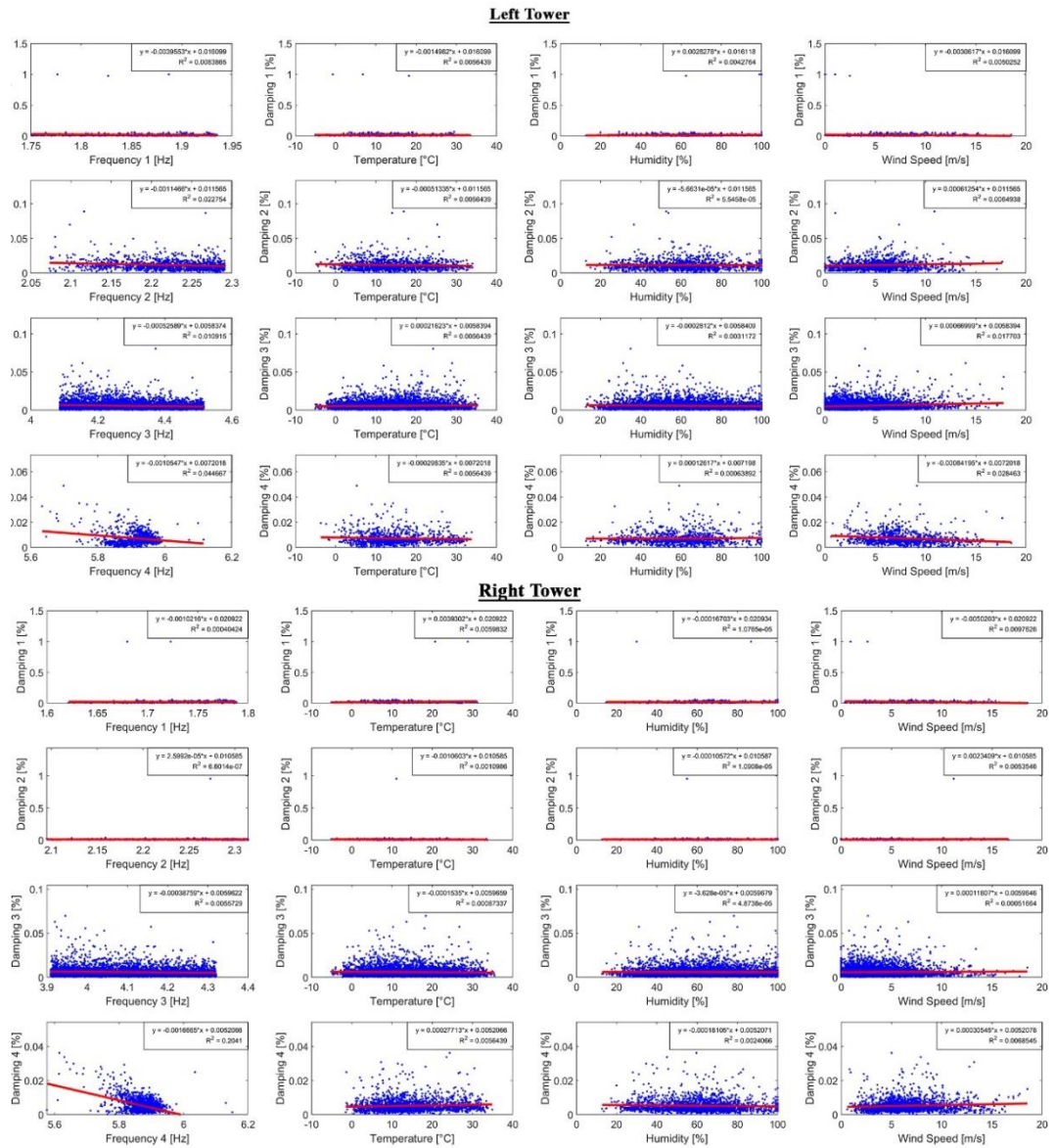


Fig. 6-18 - Correlation of damping with frequencies and environmental data

It is possible to observe a linear increment of frequencies values with the increment of temperature, while the relationship with relative humidity is the opposite. As it is remarkable in the first two modes, frequencies tend to decrement when wind speeds grow, and this trend is reversed for the last two identified modes. It is also evident the high level of uncertainty which characterizes the third mode correlation. This occurrence is more likely linked to the low level of Signal to Noise Ratio (SNR), being the Cathedral located in a not accessible area of the city which reflects in a lack of external sources of excitation.

6.6 Monitoring activity results

At last, the autoregressive model is applied to the data. The training operation, having the objective to establish the dependencies necessary to make a prevision of the modal parameters output from the environmental conditions, is operated over the 80% of data, collected between the first day of monitoring till the end of April 2021. The prevision is then elaborated over the remaining data. The results for frequencies modal tracking, for both towers, is illustrated in Fig. 6-19, where the provisional data (in black) are superimposed over the original identified frequencies.

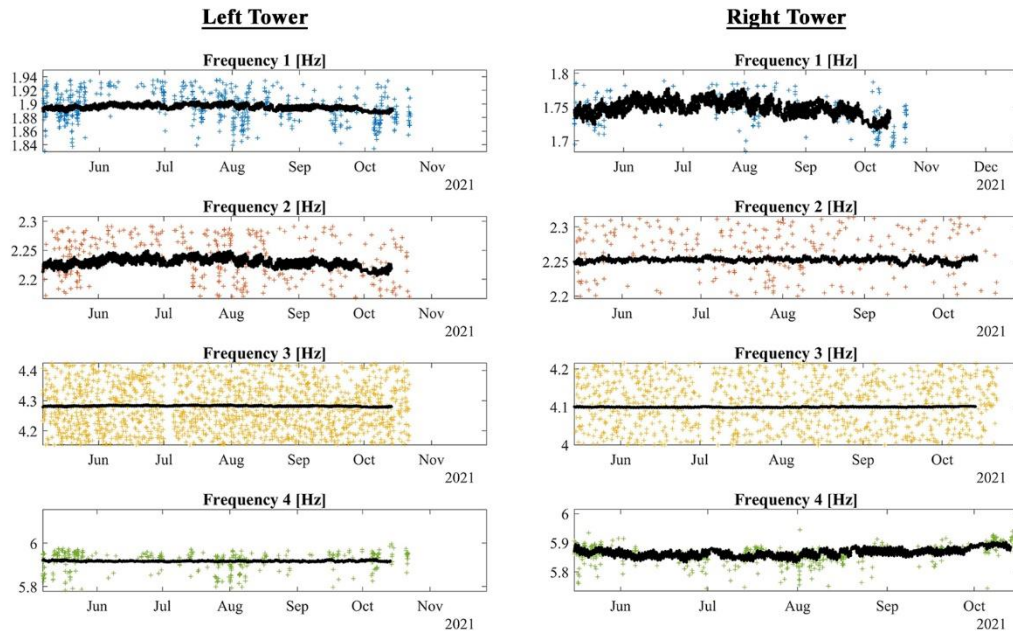


Fig. 6-19 - Modal tracking of frequencies after removal of environmental effects (in black)

In Table 6-3 are reported the average values for the tracked provisional frequencies. Their comparison shows the same trend of §6.3.4.3, confirming the consistency of results of the automatic procedure.

Table 6-3 - Comparison of the twin towers modal parameters after removal of environmental effects

Mode	Left Tower		Right Tower		Comparison	
	$f_{pred,mean}$ [Hz]	$\xi_{pred,mean}$ [%]	$f_{pred,mean}$ [Hz]	$\xi_{pred,mean}$ [%]	$ \Delta f $ [%]	$ \Delta \xi $ [%]
φ_1	1.892	1.270	1.737	1.690	8.19	33.07
φ_2	2.222	1.030	2.251	0.880	1.31	14.56
φ_3	4.281	0.470	4.100	0.480	4.23	2.13
φ_4	5.919	0.610	5.878	0.450	0.69	26.23

Conclusions

The thesis is focused on the application OMA in the context of vibration-based SHM in order to assess the health conditions of different kinds of structures, from infrastructures to cultural heritage buildings.

Starting from an overview of the most common OMA algorithms, the main methodologies for application of identification process are illustrated: Peak Picking and FDD methods, developed in the frequency domain, and the SSI-Cov and the SSI-Data methods, implemented in the time domain.

Then practical examples of applications of these methods are presented in Chapter 4 and Chapter 5. The analysis of the health status of a bridge and an airport hangar cover are showed, at first. Then another possible use of the technique, more suited for historical buildings analysis, is presented and a possible new automated approach for model updating of FE model is proposed. All these examples are meant to furnish a clear understand of the methodology that converged in the elaboration of the main theme of the research: the implementation of an automatic algorithm able to manage the data coming from the continuous dynamic monitoring of the bell towers of the Dome of Camerino, a monument strongly affected by the seismic events of Central Italy. In this context an element of innovation is constituted by the type of sensor adopted for the monitoring activity, which are MEMS based accelerometers, a pretty new type of sensors which are starting to be used in civil engineering applications, due to their advantages in terms of economy and easy installation.

The proposed algorithm, developed in Matlab© environment, is able to identify the main modes of the structure, through the application of SSI-Cov method. A particular clustering analysis is adopted in order to extract the physical modes of the structure, based on k-means clustering analysis, having as target parameters those coming from the automatic analysis of data acquired on the date of installation of the continuous monitoring system through the classical methodology.

For each of the tower the first four modes are successfully identified. Then data are correlated with environmental parameters for the removal of the effects linked to these agents.

The success of the automatic process also confirms the validity of MEMS sensors for long-term applications.

At last, due to the potentiality of the proposed methodology possible future development could be the implementation of another module for damage detection, able to provide possible damage scenarios, useful for preservation of structures and designing of interventions. Moreover, the coupling of this

algorithm with genetic algorithm model updating procedures could provide finite elements models always updated which can produce important information on the health status of monitored structures.

References

- [1] M. Acito, M. Bocciarelli, C. Chesi, G. Milani, Collapse of the clock tower in Finale Emilia after the May 2012 Emilia Romagna earthquake sequence: Numerical insight, *Eng. Struct.* 72 (2014) 70–91. <https://doi.org/10.1016/j.engstruct.2014.04.026>.
- [2] M. Betti, A. Vignoli, Numerical assessment of the static and seismic behaviour of the basilica of Santa Maria all'Impruneta (Italy), *Constr. Build. Mater.* 25 (2011) 4308–4324. <https://doi.org/10.1016/j.conbuildmat.2010.12.028>.
- [3] G. Brandonisio, G. Lucibello, E. Mele, A. De Luca, Damage and performance evaluation of masonry churches in the 2009 L'Aquila earthquake, *Eng. Fail. Anal.* 34 (2013) 693–714. <https://doi.org/10.1016/j.engfailanal.2013.01.021>.
- [4] F. Clementi, A. Ferrante, E. Giordano, F. Dubois, S. Lenci, Damage assessment of ancient masonry churches stroked by the Central Italy earthquakes of 2016 by the non-smooth contact dynamics method, *Bull. Earthq. Eng.* (2019). <https://doi.org/10.1007/s10518-019-00613-4>.
- [5] S. Lagomarsino, S. Podestà, Damage and Vulnerability Assessment of Churches after the 2002 Molise, Italy, Earthquake, *Earthq. Spectra.* 20 (2004) 271–283. <https://doi.org/10.1193/1.1767161>.
- [6] G. Bartoli, M. Betti, L. Galano, G. Zini, Numerical insights on the seismic risk of confined masonry towers, *Eng. Struct.* 180 (2019) 713–727. <https://doi.org/10.1016/j.engstruct.2018.10.001>.
- [7] A. Cabboi, C. Gentile, A. Saisi, From continuous vibration monitoring to FEM-based damage assessment: Application on a stone-masonry tower, *Constr. Build. Mater.* 156 (2017) 252–265. <https://doi.org/10.1016/j.conbuildmat.2017.08.160>.
- [8] G. Castellazzi, A.M. D'Altri, S. de Miranda, A. Chiozzi, A. Tralli, Numerical insights on the seismic behavior of a non-isolated historical masonry tower, *Bull. Earthq. Eng.* 16 (2018) 933–961. <https://doi.org/10.1007/s10518-017-0231-6>.
- [9] A. Saisi, C. Gentile, M. Guidobaldi, Post-earthquake continuous dynamic monitoring of the Gabbia Tower in Mantua, Italy, *Constr. Build. Mater.* 81 (2015) 101–112. <https://doi.org/10.1016/j.conbuildmat.2015.02.010>.
- [10] C. Gentile, M. Guidobaldi, A. Saisi, One-year dynamic monitoring of a historic tower:

- damage detection under changing environment, *Meccanica*. 51 (2016) 2873–2889.
<https://doi.org/10.1007/s11012-016-0482-3>.
- [11] E. Quagliarini, G. Maracchini, F. Clementi, Uses and limits of the Equivalent Frame Model on existing unreinforced masonry buildings for assessing their seismic risk: A review, *J. Build. Eng.* 10 (2017) 166–182. <https://doi.org/10.1016/j.jobbe.2017.03.004>.
 - [12] V. Nicoletti, D. Arezzo, S. Carbonari, F. Gara, Expedient methodology for the estimation of infill masonry wall stiffness through in-situ dynamic tests, *Constr. Build. Mater.* 262 (2020) 120807. <https://doi.org/10.1016/j.conbuildmat.2020.120807>.
 - [13] F. Ubertini, C. Gentile, A.L. Materazzi, Automated modal identification in operational conditions and its application to bridges, *Eng. Struct.* 46 (2013) 264–278.
<https://doi.org/10.1016/j.engstruct.2012.07.031>.
 - [14] C. Gentile, A. Saisi, Ambient vibration testing of historic masonry towers for structural identification and damage assessment, *Constr. Build. Mater.* 21 (2007) 1311–1321.
<https://doi.org/10.1016/j.conbuildmat.2006.01.007>.
 - [15] M.-G. Masciotta, J.C.A. Roque, L.F. Ramos, P.B. Lourenço, A multidisciplinary approach to assess the health state of heritage structures: The case study of the Church of Monastery of Jerónimos in Lisbon, *Constr. Build. Mater.* 116 (2016) 169–187.
<https://doi.org/10.1016/j.conbuildmat.2016.04.146>.
 - [16] R. Brincker, L. Zhang, Frequency domain decomposition revisited, in: *Starrylink Editrice (Ed.), Proc. 3rd Int. Oper. Modal Anal. Conf. - IOMAC 2009*, 2009: pp. 615–626.
 - [17] B. Peeters, G. De Roeck, Reference-Based Stochastic Subspace Identification for Output-Only Modal Analysis, *Mech. Syst. Signal Process.* 13 (1999) 855–878.
<https://doi.org/10.1006/mssp.1999.1249>.
 - [18] F. Magalhães, A. Cunha, E. Caetano, Vibration based structural health monitoring of an arch bridge: From automated OMA to damage detection, *Mech. Syst. Signal Process.* 28 (2012) 212–228. <https://doi.org/10.1016/j.ymssp.2011.06.011>.
 - [19] F. Ubertini, G. Comanducci, N. Cavalagli, A. Laura Pisello, A. Luigi Materazzi, F. Cotana, Environmental effects on natural frequencies of the San Pietro bell tower in Perugia, Italy, and their removal for structural performance assessment, *Mech. Syst. Signal Process.* 82 (2017) 307–322. <https://doi.org/10.1016/j.ymssp.2016.05.025>.
 - [20] E. García-Macías, F. Ubertini, MOVA/MOSS: Two integrated software solutions for

- comprehensive Structural Health Monitoring of structures, *Mech. Syst. Signal Process.* 143 (2020) 106830. <https://doi.org/10.1016/j.ymssp.2020.106830>.
- [21] K. Guru Manikandan, K. Pannirselvam, J.J. Kenned, C. Suresh Kumar, Investigations on suitability of MEMS based accelerometer for vibration measurements, *Mater. Today Proc.* 45 (2021) 6183–6192. <https://doi.org/10.1016/j.matpr.2020.10.506>.
 - [22] M. Preeti, Koushik Guha, K.L. Baishnab, K. Dusalapudi, K. Narasimha Raju, Low frequency MEMS accelerometers in health monitoring – A review based on material and design aspects, *Mater. Today Proc.* 18 (2019) 2152–2157. <https://doi.org/10.1016/j.matpr.2019.06.658>.
 - [23] F. Moschas, S. Stiros, Experimental evaluation of the performance of arrays of MEMS accelerometers, *Mech. Syst. Signal Process.* 116 (2019) 933–942. <https://doi.org/10.1016/j.ymssp.2018.07.031>.
 - [24] R.W. Clough, J. Penzien, *Dynamics of structures*, Computers & Structures, Inc., Berkley, CA USA, 2003.
 - [25] J.S. Bendat, A.G. Piersol, *Engineering applications of correlation and spectral analysis*, Wiley-Interscience, New York, 1980.
 - [26] B. Peeters, *System identification and damage detection in civil engineering*, K.U.Leuven, 2000.
 - [27] H. Elci, R.W. Longman, Minh Phan, Jer-Nan Juang, R. Ugoletti, Discrete frequency based learning control for precision motion control, in: *Proc. IEEE Int. Conf. Syst. Man Cybern.*, IEEE, n.d.: pp. 2767–2773. <https://doi.org/10.1109/ICSMC.1994.400292>.
 - [28] P. Van Overschee, B. De Moor, Continuous-time frequency domain subspace system identification, *Signal Processing.* 52 (1996) 179–194. [https://doi.org/10.1016/0165-1684\(96\)00052-7](https://doi.org/10.1016/0165-1684(96)00052-7).
 - [29] P. Verboven, P. Guillaume, B. Cauberghe, S. Vanlanduit, E. Parloo, Modal parameter estimation from input–output Fourier data using frequency-domain maximum likelihood identification, *J. Sound Vib.* 276 (2004) 957–979. <https://doi.org/10.1016/j.jsv.2003.08.044>.
 - [30] J.-N. Juang, R.S. Pappa, An eigensystem realization algorithm for modal parameter identification and model reduction, *J. Guid. Control. Dyn.* 8 (1985) 620–627. <https://doi.org/10.2514/3.20031>.
 - [31] P. Guillaume, L. Hermans, H. Van der Auweraer, Maximum likelihood identification of

- modal parameters from operational data, in: 17th Int. Modal Anal. Conf. Modal Anal. - Reducing Time to Mark. Date 1999/02/08 - 1999/02/11, Locat. KISSIMMEE, FL, 1999: p. Vol. 3727; pp. 1887–1893.
- [32] R. Brincker, L. Zhang, P. Andersen, Modal identification of output-only systems using frequency domain decomposition, *Smart Mater. Struct.* 10 (2001) 441–445.
<https://doi.org/10.1088/0964-1726/10/3/303>.
 - [33] B. Peeters, G. De Roeck, Reference-based stochastic subspace identification for output-only modal analysis, *Mech. Syst. Signal Process.* 13 (1999) 855–878.
<https://doi.org/10.1006/mssp.1999.1249>.
 - [34] C. Devriendt, P. Guillaume, Identification of modal parameters from transmissibility measurements, *J. Sound Vib.* 314 (2008) 343–356. <https://doi.org/10.1016/j.jsv.2007.12.022>.
 - [35] F. Magalhães, Á. Cunha, Explaining operational modal analysis with data from an arch bridge, *Mech. Syst. Signal Process.* 25 (2011) 1431–1450.
<https://doi.org/10.1016/j.ymssp.2010.08.001>.
 - [36] A. Cabboi, F. Magalhães, C. Gentile, Á. Cunha, Automated modal identification and tracking: Application to an iron arch bridge, *Struct. Control Heal. Monit.* 24 (2017) e1854.
<https://doi.org/10.1002/stc.1854>.
 - [37] S.F. Stiemer, A.J. Felber, Object-Oriented Approach to Ambient Vibration Measurement Analysis, *J. Comput. Civ. Eng.* 7 (1993) 420–438. [https://doi.org/10.1061/\(ASCE\)0887-3801\(1993\)7:4\(420\)](https://doi.org/10.1061/(ASCE)0887-3801(1993)7:4(420)).
 - [38] A. Felber, R. Cantieni, Advances in Ambient Vibration Testing: Ganter Bridge, Switzerland, *Struct. Eng. Int.* 6 (1996) 187–190. <https://doi.org/10.2749/101686696780495671>.
 - [39] A.P. Brincker R, Zhang L, Modal identification from ambient responses using frequency domain decomposition, in: *Proc. 18th Int. Modal Anal. Conf. San Antonio, TX, Febr., San Antonio, Texas, 2000*: pp. 625–630.
 - [40] C.Y. Shih, Y.G. Tsuei, R.J. Allemang, D.L. Brown, Complex mode indication function and its applications to spatial domain parameter estimation, *Mech. Syst. Signal Process.* 2 (1988) 367–377. [https://doi.org/10.1016/0888-3270\(88\)90060-X](https://doi.org/10.1016/0888-3270(88)90060-X).
 - [41] P. Welch, The use of fast Fourier transform for the estimation of power spectra: A method based on time averaging over short, modified periodograms, *IEEE Trans. Audio Electroacoust.* 15 (1967) 70–73. <https://doi.org/10.1109/TAU.1967.1161901>.

- [42] R. Brincker, C.E. Ventura, P. Andersen, Damping Estimation by Frequency Domain Decomposition, in: *Proc. IMAC 19 A Conf. Struct. Dyn.* Febr. 5-8, 2001, Hyatt Orlando, Kissimmee, Florida, 2001, Kissimmee, Florida, 2001: pp. 698–703.
- [43] F. Magalhães, Á. Cunha, E. Caetano, R. Brincker, Damping estimation using free decays and ambient vibration tests, *Mech. Syst. Signal Process.* 24 (2010) 1274–1290.
<https://doi.org/10.1016/j.ymssp.2009.02.011>.
- [44] R.J. Allemang, D.L. Brown, A correlation coefficient for modal testing, in: *Proc. 1st Int. Modal Anal. Conf.*, 1983.
- [45] M. Pastor, M. Binda, T. Harčarik, Modal Assurance Criterion, *Procedia Eng.* 48 (2012) 543–548. <https://doi.org/10.1016/j.proeng.2012.09.551>.
- [46] F. Magalhães, Á. Cunha, E. Caetano, Dynamic monitoring of a long span arch bridge, *Eng. Struct.* 30 (2008) 3034–3044. <https://doi.org/10.1016/j.engstruct.2008.04.020>.
- [47] L. Ljung, System Identification, in: 1998: pp. 163–173. https://doi.org/10.1007/978-1-4612-1768-8_11.
- [48] E. Reynders, G. De Roeck, System Identification and Operational Modal Analysis with MACEC Enhanced, in: *2nd Int. Oper. Modal Anal. Conf. 2007*, 2007: pp. 325–331.
- [49] ARTeMIS Modal, (2018).
- [50] F. FNAIECH, L. LJUNG, Recursive identification of bilinear systems, *Int. J. Control.* 45 (1987) 453–470. <https://doi.org/10.1080/00207178708933743>.
- [51] J.N. Juang, *Applied system identification*, Prentice-Hall, Inc., 1994.
- [52] G. Standoli, E. Giordano, G. Milani, F. Clementi, Model Updating of Historical Belfries Based on Operational Identification Techniques, *Int. J. Archit. Herit.* (2020) 1–25.
<https://doi.org/10.1080/15583058.2020.1723735>.
- [53] G. Standoli, G.P. Salachoris, M.G. Masciotta, F. Clementi, Modal-based FE model updating via genetic algorithms: Exploiting artificial intelligence to build realistic numerical models of historical structures, *Constr. Build. Mater.* 303 (2021) 124393.
<https://doi.org/10.1016/j.conbuildmat.2021.124393>.
- [54] D. Foti, M. Diaferio, N.I. Giannoccaro, M. Mongelli, Ambient vibration testing, dynamic identification and model updating of a historic tower, *NDT E Int.* 47 (2012) 88–95.
<https://doi.org/10.1016/j.ndteint.2011.11.009>.

- [55] A. Bayraktar, T. Türker, B. Sevim, A.C. Altunişik, F. Yildirim, Modal Parameter Identification of Hagia Sophia Bell-Tower via Ambient Vibration Test, *J. Nondestruct. Eval.* 28 (2009) 37–47. <https://doi.org/10.1007/s10921-009-0045-9>.
- [56] G. Milani, R. Shehu, M. Valente, Role of inclination in the seismic vulnerability of bell towers: FE models and simplified approaches, *Bull. Earthq. Eng.* 15 (2017) 1707–1737. <https://doi.org/10.1007/s10518-016-0043-0>.
- [57] A. Pellegrinelli, A. Furini, P. Russo, Earthquakes and ancient leaning towers: Geodetic monitoring of the bell tower of San Benedetto Church in Ferrara (Italy), *J. Cult. Herit.* 15 (2014) 687–691. <https://doi.org/10.1016/j.culher.2013.12.005>.
- [58] J. Rodriguez, *Identificação Modal Estocástica: Métodos de Análise e Aplicações em Estruturas de Engenharia Civil*, 2004.
- [59] W. Torres, J.L. Almazán, C. Sandoval, R. Boroschek, Operational modal analysis and FE model updating of the Metropolitan Cathedral of Santiago, Chile, *Eng. Struct.* 143 (2017) 169–188. <https://doi.org/10.1016/j.engstruct.2017.04.008>.
- [60] A. Bajrić, J. Høgsberg, Identification of damping and complex modes in structural vibrations, *J. Sound Vib.* 431 (2018) 367–389. <https://doi.org/10.1016/j.jsv.2018.05.048>.
- [61] D.J. Ewins, H. Saunders, Modal Testing: Theory and Practice, *J. Vib. Acoust.* 108 (1986) 109–110. <https://doi.org/10.1115/1.3269294>.
- [62] S. Gade, N.B. Møller, H. Herlufsen, H. Konstantin-Hansen, Frequency domain techniques for operational modal analysis, in: *First Int. Oper. Modal Anal. Conf.*, Copenhagen, 2005: pp. 261–271.
- [63] F. Benedettini, M. Dilella, A. Morassi, Vibration analysis and structural identification of a curved multi-span viaduct, *Mech. Syst. Signal Process.* 54–55 (2015) 84–107. <https://doi.org/10.1016/j.ymssp.2014.08.008>.
- [64] M.I. Friswell, J.E. Mottershead, *Finite Element Model Updating in Structural Dynamics*, Springer Netherlands, Dordrecht, 1995. <https://doi.org/10.1007/978-94-015-8508-8>.
- [65] L.F. Ramos, L. Marques, P.B. Lourenço, G. De Roeck, A. Campos-Costa, J. Roque, Monitoring historical masonry structures with operational modal analysis: Two case studies, *Mech. Syst. Signal Process.* 24 (2010) 1291–1305. <https://doi.org/10.1016/j.ymssp.2010.01.011>.

- [66] V. Compan, P. Pachón, M. Cámara, Ambient vibration testing and dynamic identification of a historical building. Basilica of the Fourteen Holy Helpers (Germany)., *Procedia Eng.* 199 (2017) 3392–3397. <https://doi.org/10.1016/j.proeng.2017.09.572>.
- [67] Ministero delle Infrastrutture e dei Trasporti, D.M 17 gennaio 2018 “Aggiornamento delle Norme tecniche per le Costruzioni,” *Suppl. Ordin. Alla “Gazzetta Uff. n. 42 Del 20 Febbraio 2018- Ser. Gen. (2018) 1–198*.
- [68] Ministero delle Infrastrutture e dei Trasporti, Circolare 21 Gennaio 2019 n. 7 C.S.LL.PP. Istruzioni per l’applicazione Dell’aggiornamento Delle ‘Norme Tecniche per Le Costruzioni’ Di Cui Al D.M. 17/ 01/2018 (in Italian). *Suppl. Ord. Alla G.U. n. 35 Del 11/2/19., 2019*.
- [69] N. Cavalagli, G. Comanducci, F. Ubertini, Earthquake-Induced Damage Detection in a Monumental Masonry Bell-Tower Using Long-Term Dynamic Monitoring Data, *J. Earthq. Eng.* 22 (2018) 96–119. <https://doi.org/10.1080/13632469.2017.1323048>.
- [70] A. Elyamani, O. Caselles, P. Roca, J. Clapes, Dynamic investigation of a large historical cathedral, *Struct. Control Heal. Monit.* 24 (2017) e1885. <https://doi.org/10.1002/stc.1885>.
- [71] C. Gentile, A. Saisi, P. Borlenghi, FE modelling for seismic assessment of an ancient tower from ambient vibration survey, in: *8th IOMAC - Int. Oper. Modal Anal. Conf., Copenhagen, 2019: pp. 295–305*. <http://hdl.handle.net/11311/1124063>.
- [72] F. Clementi, A. Pierdicca, A. Formisano, F. Catinari, S. Lenci, Numerical model upgrading of a historical masonry building damaged during the 2016 Italian earthquakes: the case study of the Podestà palace in Montelupone (Italy), *J. Civ. Struct. Heal. Monit.* 7 (2017) 703–717. <https://doi.org/10.1007/s13349-017-0253-4>.
- [73] D. Pellegrini, M. Girardi, P.B. Lourenço, M.G. Masciotta, N. Mendes, C. Padovani, L.F. Ramos, Modal analysis of historical masonry structures: Linear perturbation and software benchmarking, *Constr. Build. Mater.* 189 (2018) 1232–1250. <https://doi.org/10.1016/j.conbuildmat.2018.09.034>.
- [74] T. Bartz-Beielstein, J. Branke, J. Mehnen, O. Mersmann, *Evolutionary Algorithms*, Wiley Interdiscip. Rev. Data Min. Knowl. Discov. 4 (2014) 178–195. <https://doi.org/10.1002/widm.1124>.
- [75] M.. Betti, G.. Bartoli, R.. Corazzi, V.. Kovacevic, Strumenti Open Source per l’ingegneria strutturale. Modellazione meccanica non lineare di edifici in muratura, *Boll. Ing.* 60 (2013) 3–15.

- [76] G. Bartoli, M. Betti, A.M. Marra, S. Monchetti, A Bayesian model updating framework for robust seismic fragility analysis of non-isolated historic masonry towers, *Philos. Trans. R. Soc. A Math. Phys. Eng. Sci.* 377 (2019) 20190024. <https://doi.org/10.1098/rsta.2019.0024>.
- [77] E. García-Macías, L. Ierimonti, I. Venanzi, F. Ubertini, Comparison of Surrogate Models for Handling Uncertainties in SHM of Historic Buildings, in: *Proc. XXIV AIMETA Conf.* 2019, 2020: pp. 1645–1657. https://doi.org/10.1007/978-3-030-41057-5_132.
- [78] K. Smarsly, K. Dragos, J. Wiggenbrock, Machine learning techniques for structural health monitoring, *8th Eur. Work. Struct. Heal. Monit. EWSHM 2016*. 2 (2016) 1522–1531.
- [79] Y. Ying, J.H. Garrett, I.J. Oppenheim, L. Soibelman, J.B. Harley, J. Shi, Y. Jin, Toward Data-Driven Structural Health Monitoring: Application of Machine Learning and Signal Processing to Damage Detection, *J. Comput. Civ. Eng.* 27 (2013) 667–680. [https://doi.org/10.1061/\(ASCE\)CP.1943-5487.0000258](https://doi.org/10.1061/(ASCE)CP.1943-5487.0000258).
- [80] M. Sanayei, E.S. Bell, C.N. Javdekar, J.L. Edelmann, E. Slavsky, Damage Localization and Finite-Element Model Updating Using Multiresponse NDT Data, *J. Bridg. Eng.* 11 (2006) 688–698. [https://doi.org/10.1061/\(ASCE\)1084-0702\(2006\)11:6\(688\)](https://doi.org/10.1061/(ASCE)1084-0702(2006)11:6(688)).
- [81] G.. Barchiesi, Ostra in Cartolina, Banca di Credito Cooperativo, 1994.
- [82] Guida storica artistica e turistica di Ostra, Ostra, 2015.
- [83] F.U. I Venanzi, A Kita, N Cavalagli, L Ierimonti, Continuous OMA for Damage Detection and Localization in the Sciri tower in Perugia, Italy, in: *8th IOMAC - Int. Oper. Modal Anal. Conf.*, Copenhagen, 2019.
- [84] E. Giordano, F. Clementi, A. Barontini, M. Giovanna, E. Chatzi, F. Luís, Damage detection and optimal sensor placement in health monitoring of “ Collegiata di Santa Maria ” in Visso (Central Italy) Damage detection and optimal sensor placement in health monitoring of “ Collegiata di Santa Maria ” in Visso (Central Italy), (2019) 44–53.
- [85] M.G. Masciotta, L.F. Ramos, Dynamic identification of historic masonry structures, in: P.B. Ghiassi, Bahman; Lourenco (Ed.), *Long-Term Perform. Durab. Mason. Struct.*, Woodhead, Publishing Series in Civil and Structural Engineering, Woodhead Publishing (2019), 2019: pp. 241–264. <https://doi.org/10.1016/B978-0-08-102110-1.00008-X>.
- [86] D.J. Ewins, *Modal Testing: Theory, Practice and Application*, Baldock, Hertfordshire, England, 2000.

- [87] L.F. Ramos, G. De Roeck, P.B. Lourenço, A. Campos-Costa, Damage identification on arched masonry structures using ambient and random impact vibrations, *Eng. Struct.* 32 (2010) 146–162. <https://doi.org/10.1016/j.engstruct.2009.09.002>.
- [88] M. Girardi, C. Padovani, D. Pellegrini, L. Robol, A finite element model updating method based on global optimization, *Mech. Syst. Signal Process.* (2020) 107372. <https://doi.org/10.1016/j.ymssp.2020.107372>.
- [89] R.S. Olivito, S. Porzio, A new multi-control-point pushover methodology for the seismic assessment of historic masonry buildings, *J. Build. Eng.* 26 (2019) 100926. <https://doi.org/10.1016/j.jobbe.2019.100926>.
- [90] A.B. S Bagchi, TB Roy, Multiple damage localization of gravity Dam: strain energy based approach using random data, in: *CSCE Annu. Conf.*, 2019.
- [91] A. Garcia-Gonzalez, A. Gonzalez-Herrera, A. Garcia-Cerezo, Damage Localization based on Modal Parameters using the Finite Element Method and Neural Networks, in: n.d. <https://doi.org/10.4203/ccp.93.48>.
- [92] F. Bianconi, G.P. Salachoris, F. Clementi, S. Lenci, A Genetic Algorithm Procedure for the Automatic Updating of FEM Based on Ambient Vibration Tests, *Sensors*. 20 (2020) 3315. <https://doi.org/10.3390/s20113315>.
- [93] J.P. Escallón, C. Wendeler, E. Chatzi, P. Bartelt, Parameter identification of rockfall protection barrier components through an inverse formulation, *Eng. Struct.* 77 (2014) 1–16. <https://doi.org/10.1016/j.engstruct.2014.07.019>.
- [94] S. Kokot, Z. Zembaty, Damage reconstruction of 3D frames using genetic algorithms with Levenberg–Marquardt local search, *Soil Dyn. Earthq. Eng.* 29 (2009) 311–323. <https://doi.org/10.1016/j.soildyn.2008.03.001>.
- [95] Á. Bautista-De Castro, L.J. Sánchez-Aparicio, P. Carrasco-García, L.F. Ramos, D. González-Aguilera, A multidisciplinary approach to calibrating advanced numerical simulations of masonry arch bridges, *Mech. Syst. Signal Process.* 129 (2019) 337–365. <https://doi.org/10.1016/j.ymssp.2019.04.043>.
- [96] A. Aloisio, I. Capanna, R. Cirella, R. Alaggio, F. Di Fabio, M. Fragiaco, Identification and Model Update of the Dynamic Properties of the San Silvestro Belfry in L’Aquila and Estimation of Bell’s Dynamic Actions, *Appl. Sci.* 10 (2020). <https://doi.org/10.3390/app10124289>.

- [97] C. Leyder, E. Chatzi, A. Frangi, Vibration-based model updating of a timber frame structure, *Procedia Eng.* 199 (2017) 2132–2139. <https://doi.org/10.1016/j.proeng.2017.09.141>.
- [98] Q. Sun, D. Dias, Global sensitivity analysis of probabilistic tunnel seismic deformations using sparse polynomial chaos expansions, *Soil Dyn. Earthq. Eng.* 141 (2021) 106470. <https://doi.org/10.1016/j.soildyn.2020.106470>.
- [99] S.R. Arwade, M. Moradi, A. Louhghalam, Variance decomposition and global sensitivity for structural systems, *Eng. Struct.* 32 (2010) 1–10. <https://doi.org/10.1016/j.engstruct.2009.08.011>.
- [100] F. Pianosi, F. Sarrazin, T. Wagener, A Matlab toolbox for Global Sensitivity Analysis, *Environ. Model. Softw.* 70 (2015) 80–85. <https://doi.org/10.1016/j.envsoft.2015.04.009>.
- [101] F. Benedettini, C. Gentile, Operational modal testing and FE model tuning of a cable-stayed bridge, *Eng. Struct.* 33 (2011) 2063–2073. <https://doi.org/10.1016/j.engstruct.2011.02.046>.
- [102] A. Kita, N. Cavalagli, F. Ubertini, Temperature effects on static and dynamic behavior of Consoli Palace in Gubbio, Italy, *Mech. Syst. Signal Process.* 120 (2019) 180–202. <https://doi.org/10.1016/j.ymssp.2018.10.021>.
- [103] R. Ceravolo, G. Pistone, L.Z. Fragonara, S. Massetto, G. Abbiati, Vibration-Based Monitoring and Diagnosis of Cultural Heritage: A Methodological Discussion in Three Examples, *Int. J. Archit. Herit.* 10 (2016) 375–395. <https://doi.org/10.1080/15583058.2013.850554>.
- [104] F. Magalhães, Á. Cunha, E. Caetano, Online automatic identification of the modal parameters of a long span arch bridge, *Mech. Syst. Signal Process.* 23 (2009) 316–329. <https://doi.org/10.1016/j.ymssp.2008.05.003>.
- [105] E. Reynders, J. Houbrechts, G. De Roeck, Fully automated (operational) modal analysis, *Mech. Syst. Signal Process.* 29 (2012) 228–250. <https://doi.org/10.1016/j.ymssp.2012.01.007>.
- [106] R.S. Pappa, K.B. Elliott, A. Schenk, Consistent-mode indicator for the eigensystem realization algorithm, *J. Guid. Control. Dyn.* 16 (1993) 852–858. <https://doi.org/10.2514/3.21092>.
- [107] A. Cabboi, C. Gentile, A. Saisi., Frequency tracking and FE model identification of a masonry tower, in: *5th Int. Oper. Modal Anal. Conf. IOMAC 2013*, 2013: pp. 1–11.
- [108] G. Marrongelli, F. Magalhães, Á. Cunha, Automated Operational Modal Analysis of an arch bridge considering the influence of the parametric methods inputs, *Procedia Eng.* 199 (2017) 2172–2177. <https://doi.org/10.1016/j.proeng.2017.09.170>.

- [109] F. Magalhaes, E. Reynders, A. Cunha, G. De Roeck, Online automatic identification of modal parameters of a bridge using the p-LSCF method, in: Proc. 3rd Int. Oper. Modal Anal. Conf., Portonovo, Italy, 2009: pp. 21–28.
- [110] C.R. Farrar, G.H. James III, SYSTEM IDENTIFICATION FROM AMBIENT VIBRATION MEASUREMENTS ON A BRIDGE, *J. Sound Vib.* 205 (1997) 1–18.
<https://doi.org/10.1006/jsvi.1997.0977>.
- [111] B. Peeters, G. De Roeck, One-year monitoring of the Z24-Bridge: environmental effects versus damage events, *Earthq. Eng. Struct. Dyn.* 30 (2001) 149–171.
[https://doi.org/10.1002/1096-9845\(200102\)30:2<149::AID-EQE1>3.0.CO;2-Z](https://doi.org/10.1002/1096-9845(200102)30:2<149::AID-EQE1>3.0.CO;2-Z).
- [112] E.J. Cross, K.Y. Koo, J.M.W. Brownjohn, K. Worden, Long-term monitoring and data analysis of the Tamar Bridge, *Mech. Syst. Signal Process.* 35 (2013) 16–34.
<https://doi.org/10.1016/j.ymssp.2012.08.026>.
- [113] H. Sohn, K. Worden, C.R. Farrar, Statistical Damage Classification Under Changing Environmental and Operational Conditions, *J. Intell. Mater. Syst. Struct.* 13 (2002) 561–574.
<https://doi.org/10.1106/104538902030904>.
- [114] J. Kullaa, Eliminating Environmental or Operational Influences in Structural Health Monitoring using the Missing Data Analysis, *J. Intell. Mater. Syst. Struct.* 20 (2009) 1381–1390. <https://doi.org/10.1177/1045389X08096050>.
- [115] A.-M. Yan, G. Kerschen, P. De Boe, J.-C. Golinval, Structural damage diagnosis under varying environmental conditions—Part I: A linear analysis, *Mech. Syst. Signal Process.* 19 (2005) 847–864. <https://doi.org/10.1016/j.ymssp.2004.12.002>.
- [116] A. Deraemaeker, E. Reynders, G. De Roeck, J. Kullaa, Vibration-based structural health monitoring using output-only measurements under changing environment, *Mech. Syst. Signal Process.* 22 (2008) 34–56. <https://doi.org/10.1016/j.ymssp.2007.07.004>.
- [117] S. Vanlanduit, P. Verboven, P. Guillaume, J. Schoukens, An automatic frequency domain modal parameter estimation algorithm, *J. Sound Vib.* 265 (2003) 647–661.
[https://doi.org/10.1016/S0022-460X\(02\)01461-X](https://doi.org/10.1016/S0022-460X(02)01461-X).
- [118] D.E. Newland, Harmonic wavelet analysis, *Proc. R. Soc. London. Ser. A Math. Phys. Sci.* 443 (1993) 203–225. <https://doi.org/10.1098/rspa.1993.0140>.
- [119] R.A. Johnson, D.W. Wichern, *Applied Multivariate Statistical Analysis*, Englewood Cliffs (NJ), 1992.

